experimental and numerical analysis of fast transient flows in the presence of obstacles

Filippo Bentivegna

Filippo Bentivegna. experimental and numerical analysis of fast transient flows in the presence of obstacles. Other. Ecole Centrale de Lyon, 2024. English. NNT : 2024ECDL0026 . tel-04772109

HAL Id: tel-04772109
https://theses.hal.science/tel-04772109v1

N° d'ordre NNT : 2024ECDL0026

THÈSE DE DOCTORAT DE L'ÉCOLE CENTRALE DE LYON
membre de l'Université de Lyon

École Doctorale N° 162
MEGA - Mécanique, Énergétique, Génie Civil, Acoustique

Spécialité de doctorat : Mécanique des fluides

Soutenue publiquement le vendredi 19 juillet 2024, par :

Filippo BENTIVEGNA

Experimental and numerical analysis of fast transient flows in the presence of obstacles

---

Devant le jury composé de :

Jean-Philippe MATAS	Professeur des Universités, Université Claude Bernard Lyon 1, LMFA	*Président*
Eric GONCALVES	Professeur des Universités, ISAE-ENSMA, Institut Pprime	*Rapporteur*
Annalisa MANERA	Full Professor, ETH Zürich, ML - Maschinenlaboratorium, D-MAVT	*Rapporteuse*
Vincent FAUCHER	Directeur de Recherche (HDR), CEA Cadarache, DNT	*Examinateur*
Christophe CORRE	Professeur des Universités, École Centrale de Lyon, LMFA	*Directeur de Thèse*
Alberto BECCANTINI	Ingénieur Chercheur, CEA Saclay, DYN	*Co-encadrant de Thèse*
Pascal GALON	Ingénieur Chercheur, CEA Saclay, DYN	*Invité, Co-encadrant de Thèse*

Unités de recherche : DYN - Laboratoire d'études de DYNamique, CEA Saclay
LMFA - Laboratoire de Mécanique des Fluides et Acoustique, ECL

Acknowledgements

First and foremost, I would like to express my deepest gratitude to my supervisors, Alberto and Pascal, as well as my thesis director, Christophe. Their immense support, guidance, and encouragement over the past three years have been invaluable. It has been a true privilege to work with them, and I look forward to continuing our collaboration in the future.

I am also profoundly grateful to the members of the defense jury, whose valuable insights and constructive discussion greatly contributed to the final refinement of my work.

A heartfelt thanks to everyone at the DYN laboratory, who welcomed me with open arms. I have had the pleasure of sharing both professional and personal moments with remarkable individuals, and I am excited to continue my career as an engineer-researcher alongside them for many more years.

I would also like to thank our industrial partners, EDF and Framatome, for their significant contributions to the realization of this project. I eagerly anticipate continuing our collaboration in the future.

To my friends in Paris and Italy, I am grateful for your companionship throughout my journey over the last three years and beyond. You have been a crucial part of my growth, both personally and professionally.

Lastly, but most importantly, I extend my infinite gratitude to my family. Your unwavering and constant support has been the foundation that brought me to this point. I could not have done it without you, and for that, I thank you from the bottom of my heart.

Résumé

Cette thèse de doctorat explore la dynamique de propagation des ondes de détente dans les circuits de réacteurs nucléaires, en se concentrant sur une configuration représentative d'un scénario de type Accident de Perte de Réfrigérant Primaire (APRP) dans les Réacteurs à Eau Pressurisée (REP). L'étude examine les charges de pression transitoires sur les structures internes, en particulier le cloisonnement du cœur du réacteur, induites par les ondes de détente générées par la rupture brutale et totale (rupture guillotine) d'une des tuyauteries du circuit primaire de refroidissement du REP. Cette analyse est menée en combinant des mesures expérimentales sur un banc d'essai de géométrie simplifiée mais représentatif du scénario APRP et des simulations numériques. Ces simulations sont réalisées en faisant appel à une hiérarchie de modèles numériques : 1D, 2D axisymétriques et 3D, avec ou sans prise en compte des mécanismes d'interaction fluide-structure. Les modèles 1D incluent des représentations simplifiées ou modèles d'impédance des obstacles présents dans l'écoulement, indispensables pour réduire les coûts de simulation de la propagation des ondes au travers d'un circuit complet. Ces obstacles sont des diaphragmes de diamètre et d'épaisseur variables, représentatifs des singularités géométriques présentes dans les circuits parcourus par les ondes de détente. La comparaison calcul/expérience permet d'évaluer le potentiel prédictif des différentes stratégies mises en œuvre.

Le Chapitre 1 introductif du mémoire détaille le contexte et la motivation de l'étude menée en mettant en évidence l'importance d'une compréhension approfondie des phénomènes physiques associés au scénario APRP et la nécessité de modèles simplifiés pour simuler l'écoulement de fluides dans les géométries complexes d'un REP. Une revue de la littérature récapitule les principaux travaux dans l'analyse par voie numérique des réacteurs nucléaires et les simulations d'écoulement transitoire. Une analyse des approches numériques développées pour la propagation d'ondes en présence d'obstacles avec description simplifiée est également menée pour des applications hors contexte nucléaire.

Les Chapitres 2 et 3 présentent respectivement i) la plateforme expérimentale MADMAX utilisée pour produire les mesures de référence ainsi que l'évolution de ses configurations au cours de la thèse, ii) les modèles disponibles au sein du logiciel EUROPLEXUS et utilisés pour mener les simulations numériques des configurations étudiées expérimentalement.

Le Chapitre 4 détaille les résultats des expériences et des simulations de la propagation des ondes de détente à travers un unique diaphragme de géométrie modulaire. L'impact de la géométrie des obstacles sur la propagation des ondes est analysé et les capacités prédictives de modèles numériques de complexité (et de coût) variable sont évaluées pour cette configuration de base.

Le Chapitre 5 élargit l'analyse à la configuration complète de MADMAX, incorporant une conduite de dérivation avec plusieurs diaphragmes positionnés dans cette conduite. La comparaison détaillée des données expérimentales et des résultats des simulations révèle un bon accord dans la capture du comportement transitoire et des différentiels de pression entre les conduites du cœur et de la dérivation. Des configurations alternatives de MADMAX sont explorées dans le Chapitre 6, mettant en évidence les effets de variation du nombre des diaphragmes et de leur emplacement.

Les expériences sur la plateforme MADMAX et les simulations EUROPLEXUS réalisées dans le présent travail contribuent à une meilleure compréhension des phénomènes d'écoulement transitoire dans les circuits de réacteurs nucléaires. Les comparaisons calcul/expérience proposées fournissent des indications quantitatives sur la capacité prédictive des codes de simulation selon les choix de description des singularités géométriques présentes dans l'écoulement. La conclusion du mémoire propose quelques pistes d'analyses et d'améliorations pour l'avenir.

Mots-clés : Accident par Perte de Réfrigérant Primaire (APRP), Réacteur à Eau Pressurisée (REP), onde de raréfaction, interaction fluide-structure, simulation numérique, validation expérimentale, EUROPLEXUS, installation MADMAX, diaphragme, écoulement transitoire, sûreté des réacteurs nucléaires.

Abstract

This doctoral thesis explores the dynamics of rarefaction wave propagation in nuclear reactor circuits, focusing on a configuration representative of a Loss of Coolant Accident (LOCA) scenario in Pressurized Water Reactors (PWR). The study examines transient pressure loads on internal structures, particularly the reactor core baffle, induced by rarefaction waves generated by the sudden and complete rupture (guillotine break) of one of the pipes in the primary cooling circuit of the PWR. This analysis is conducted by combining experimental measurements on a test bench with simplified geometry but representative of the LOCA scenario and numerical simulations. These simulations employ a hierarchy of numerical models: 1D, 2D axisymmetric, and 3D, with or without taking into account fluid-structure interaction mechanisms. The 1D models include simplified representations or impedance models of the obstacles in the flow, essential for reducing the simulation costs of wave propagation through an entire circuit. These obstacles are orifice plates of varying diameter and thickness, representative of the geometric singularities present in the circuits traversed by rarefaction waves. The comparison between calculations and experiments allows for evaluating the predictive potential of the various strategies implemented.

Chapter 1 of the thesis introduces the context and motivation of the study, highlighting the importance of a thorough understanding of the physical phenomena associated with the LOCA scenario and the necessity of simplified models for simulating fluid flow in the complex geometries of a PWR. A literature review summarizes the main works in the numerical analysis of nuclear reactors and transient flow simulations. An analysis of the numerical approaches developed for wave propagation in the presence of obstacles with simplified descriptions is also conducted for applications outside the nuclear context.

Chapters 2 and 3 respectively present i) the MADMAX experimental platform used to produce the reference measurements and the evolution of its configurations during the thesis, ii) the models available within the EUROPLEXUS software and used to perform the numerical simulations of the experimentally studied configurations.

Chapter 4 details the results of the experiments and simulations of rarefaction wave propagation through a single modular orifice plate. The impact of obstacle geometry on wave propagation is analyzed, and the predictive capabilities of numerical models of varying complexity (and cost) are evaluated for this basic configuration.

Chapter 5 expands the analysis to the complete MADMAX configuration, incorporating a by-pass pipe with several orifice plates positioned in this pipe. The detailed comparison of experimental data and simulation results reveals good agreement in capturing transient behavior and pressure differentials between the core and by-pass pipes. Alternative configurations of MADMAX are explored in Chapter 6, highlighting the effects of varying the number and placement of the orifice plates.

The experiments on the MADMAX platform and the EUROPLEXUS simulations conducted in this work contribute to a better understanding of transient flow phenomena in nuclear reactor circuits. The proposed calculations/experiments comparisons provide quantitative indications on the predictive capacity of the simulation codes based on the choices of geometric singularity descriptions present in the flow. The thesis conclusion proposes some avenues for future analysis and improvements.

Keywords: Loss of Coolant Accident (LOCA), Pressurized Water Reactor (PWR), rarefaction wave, fluid-structure interaction, numerical simulation, experimental validation, EUROPLEXUS, MADMAX facility, orifice plate, transient flow, nuclear reactor safety.

Contents

Résumé **i**

Abstract **iii**

Contents **v**

List of Symbols **ix**

List of Figures **xi**

List of Tables **xv**

1 Introduction **1**
- 1.1 Context and motivation . . . 1
- 1.2 State of the Art . . . 3
- 1.3 Outline of the thesis . . . 7

2 MADMAX experimental facility: original set-up and new features **9**
- 2.1 Original set-up . . . 9
  - 2.1.1 General description . . . 9
  - 2.1.2 Mock-up modifications in 2010 . . . 11
- 2.2 Evolutions of the experiment and new experimental campaigns in 2022-2024 . . . 13
  - 2.2.1 Experimental set-up without by-pass pipe, with modular orifice plate . . . 13
  - 2.2.2 Experimental set-up with by-pass pipe and multiple orifice plates . . . 14
  - 2.2.3 Historical overview of experimental campaigns 2022-2024 . . . 17

3 EUROPLEXUS: simulation framework and hierarchy of numerical models **21**
- 3.1 Theoretical foundations . . . 22
  - 3.1.1 Fluid-Structure Interaction . . . 22
    - 3.1.1.1 Fluid modelling . . . 22
    - 3.1.1.2 Structural analysis . . . 24
  - 3.1.2 Euler equations for fluids . . . 24
    - 3.1.2.1 Mass Conservation Equation . . . 25
    - 3.1.2.2 Momentum Equation . . . 25
    - 3.1.2.3 Energy Conservation Equation . . . 26

3.1.2.4 Equation of state 27
3.1.3 Dynamic Equilibrium for Structures 28
3.1.4 Boundary conditions and impedances 28
3.2 Numerical models: spatial and temporal discretization 30
3.3 Models used in our simulations 31
3.3.1 Details of numerical resolution 33

4 MADMAX without by-pass pipe, with single modular orifice plate 35
4.1 Experimental campaign 35
4.2 Numerical simulations 37
4.2.1 2D axisymmetric calculations 38
4.2.2 1D with impedances calculations 41
4.3 Simulation-experiment comparison 44
4.3.1 Evolution of the pressure variation through the orifice plate: effects of the geometry 44
4.3.2 Accuracy of numerical models compared to experiments 46
4.3.3 Numerical prediction of the velocity evolution 51
4.3.3.1 Physical interpretation 51
4.3.3.2 Evaluation of numerical model accuracy 51
4.4 Fluid-Structure Interaction (FSI) calculations 53
4.4.1 Motivation 53
4.4.2 2D axisymmetric FSI calculations 54
4.4.2.1 Set-up of the simulations 54
4.4.2.2 Qualitative observation of the computed flow 56
4.4.2.3 Quantitative analysis of the pressure evolution 58
4.5 Conclusions 65

5 MADMAX with by-pass pipe and multiple orifice plates 67
5.1 Experimental campaign 67
5.1.1 Overview of tested configurations 67
5.1.2 Pressure evolution and flow description 68
5.2 Numerical simulations 78
5.2.1 Overview of the hierarchy of models 78
5.2.2 3D/3D FSI calculations 79
5.2.2.1 Design and refinement of the 3D mesh 79
5.2.2.2 3D FSI calculations 82
5.2.3 1D/1D FSI calculations 89
5.3 Simulation-experiment comparison 90
5.3.1 Analysis of absolute pressure evolutions 91
5.3.2 Analysis of relative pressure evolutions 91
5.3.3 Error analysis 92
5.4 Conclusions 96

6 Alternative configurations of MADMAX with by-pass pipe 97
6.1 Experimental campaign 97
6.1.1 Analysis of measurements for Configuration 2 98
6.1.2 Analysis of measurements for Configuration 3 99

6.2 Simulation-experiment comparison 100
6.2.1 Configuration 2: MADMAX with 4 orifice plates in by-pass pipe 100
6.2.2 Configuration 3: MADMAX with 6 orifice plates in by-pass pipe and 1 orifice plate in core pipe 106
6.3 Conclusions 111

Conclusions and Perspectives **113**

Bibliography **117**

A Finite Element Method **123**
A.1 Spatial Discretization 123
A.2 Temporal Discretization 127

B Finite Volume Method **131**

C Implementation of the IMPEDANCE GRID model in EUROPLEXUS **135**

List of Symbols

Acronyms

ALE	Arbitrary Lagrangian Eulerian
APRP	Accident de Perte de Réfrigérant Primaire (= LOCA in English)
CCFV	Cell Centered Finite Volumes
CEA	Commissariat à l'énergie atomique et aux énergies alternatives (French Alternative Energies and Atomic Energy Commission)
CFD	Computational Fluid Dynamics
CFL	Courant–Friedrichs–Lewy condition
DYN	Laboratoire d'études de DYNamique (Laboratory of DYNamic studies)
EPX	EuroPleXus
ESF	Element Size Factor
FE	Finite Element
FEM	Finite Element Method
FSI	Fluid-Structure Interaction
FV	Finite Volume
FVM	Finite Volume Method
GCL	Geometric Conservation Law
HLLC	Harten–Lax–van Leer Contact
LDV	Laser Doppler Velocimetry
LOCA	Loss-Of-Coolant Accident
MADMAX	Modélisation de l'Accident de Dépressurisation - Maquette Analytique-eXpérimentale (Depressurisation Accident Modelling - Analytical-Experimental Mock-up)
PIV	Particle Image Velocimetry
PTV	Particle Tracking Velocimetry
PWR	Pressurized Water Reactor
UDV	Ultrasound Doppler Velocimetry

List of Figures

1.1 PWR vessel and internal components [1]. 1
1.2 (a) Baffle and perforated reinforcement plates [1]. (b) Simplified scheme. 2

2.1 Original design of the MADMAX experimental facility at DYN (CEA Saclay, France). Dimensions in millimeters. Pipe diameters given are internal diameters. 10
2.2 (a) Petal bursting disk used in the first tests (2000-2001) and (b) graphite fragmentation disk used from 2010. 11
2.3 MADMAX configuration in 2010. Dimensions in millimeters. Pipe diameters given are internal diameters. 12
2.4 Experimental set-up (all dimensions in millimeters): (a) thin orifice plates, (b) thick modular orifice plate. 13
2.5 MADMAX configurations 1 and 2 with by-pass pipe. 15
2.6 MADMAX configuration 3 with by-pass pipe. 16
2.7 Bursting disk metrology. 17

3.1 Scheme of the Lagrangian description. [2] 23
3.2 Scheme of the Eulerian description. [2] 23
3.3 Scheme of the ALE description. [2] 23
3.4 Fluid domain. 24
3.5 Orifice plate scheme. 30
3.6 Finite Element and Cell Centered Finite Volume mesh schemes. 30

4.1 Experimental pressure evolution for all experiments and for all sensors. 36
4.2 Actual pressure sensor size and position compared with the corresponding mesh cell representing the pressure sensor in the 2D axisymmetric simulations. 38
4.3 Scheme of the 2D axisymmetric mesh. 39
4.4 2D axisymmetric mesh convergence for ΔP_{7-6}. Configuration: [$e = 50\,\mathrm{mm}$, $d = 50\,\mathrm{mm}$]. 40
4.5 1D mesh scheme. The 1D element between the nodes corresponds to a 1D mesh for a pipe of constant diameter. Each node corresponds to a change of pipe section or diameter. In the present case, the mesh would correspond to 3 connected pipes of various diameters. 41
4.6 Scheme of the 1D with impedances mesh. 42
4.7 1D with impedances mesh convergence for ΔP_{7-6}. Configuration: [$e = 50\,\mathrm{mm}$, $d = 50\,\mathrm{mm}$]. 43

4.8 Pressure difference between sensors C6 and C7, ΔP_{7-6}, for all thin orifice plates ($e = 10\,\mathrm{mm}$). . . . 45
4.9 Pressure difference between sensors C6 and C7, ΔP_{7-6}, for thick modular orifice plate ($e = 50\,\mathrm{mm}$). . . . 45
4.10 Pressure evolution for sensor C1, P_{C1}, for all orifice plates. . . . 48
4.11 Pressure evolution for sensor C5, P_{C5}, for all orifice plates. . . . 49
4.12 Pressure evolution for sensor C8, P_{C8}, for all orifice plates. . . . 50
4.13 y-velocity at positions C6 (a) and C7 (b). . . . 52
4.14 (a) Pressure evolution for sensor C6, P_{C6}, for all thick modular orifice plate configurations and (b) x-velocity at positions C6. . . . 53
4.15 2D axisymmetric FLUID density profile for configuration [$e = 50\,\mathrm{mm}$, $d = 10\,\mathrm{mm}$] below the orifice plate. . . . 54
4.16 Scheme of the 2D axisymmetric mesh for FSI calculations. In the close-up on the right (top: in the vicinity of the orifice plate, bottom: in the vicinity of the connection between the junction pipe and the core pipe), the fluid domain is pictured in red while the solid domain is pictured in blue. . . . 55
4.17 2D axisymmetric WATER void ratio profile for configuration [$e = 50\,\mathrm{mm}$, $d = 10\,\mathrm{mm}$] below the orifice plate. . . . 57
4.18 2D axisymmetric WATER velocity y-component, v_y, profile for configuration [$e = 50\,\mathrm{mm}$, $d = 10\,\mathrm{mm}$] below the orifice plate. In dark grey: $0 < v_y < 2.5\,\mathrm{m/s}$. . . . 57
4.19 Pressure difference between sensors C6 and C7, ΔP_{7-6}, for all thin orifice plates ($e = 10\,\mathrm{mm}$). . . . 59
4.20 Pressure difference between sensors C6 and C7, ΔP_{7-6}, for thick modular orifice plate ($e = 50\,\mathrm{mm}$). . . . 59
4.21 Pressure difference between sensors C6 and C7, ΔP_{7-6}, for all orifice plates. Focus on $0 < t < 4\,\mathrm{ms}$. . . . 60
4.22 Pressure evolution for sensor C5, P_5, for all thin orifice plates ($e = 10\,\mathrm{mm}$). . . . 61
4.23 Pressure evolution for sensor C5, P_5, for thick modular orifice plate ($e = 50\,\mathrm{mm}$). 61
4.24 Pressure evolution for sensor C8, P_8, for all thin orifice plates ($e = 10\,\mathrm{mm}$). . . . 62
4.25 Pressure evolution for sensor C8, P_8, for thick modular orifice plate ($e = 50\,\mathrm{mm}$). 62
4.26 2D axisymmetric thin orifice plate [$e = 10\,\mathrm{mm}$, $d = 10\,\mathrm{mm}$] displacement profiles at $t = 7\,\mathrm{ms}$. In violet, the profile of the undeformed orifice plate at $t = 0\,\mathrm{ms}$. . . . 63
4.27 2D axisymmetric mesh deformation for thin orifice plate [$e = 10\,\mathrm{mm}$, $d = 10\,\mathrm{mm}$] at $t = 7\,\mathrm{ms}$. . . . 64

5.1 Experimental pressure evolution for all sensors for Configuration 1. . . . 68
5.2 Experimental pressure evolution for sensors C4-C8 and D1-D5 for Configuration 1. 71
5.3 Pressure evolution in the lower part of MADMAX for $0 \leq t \leq 0.7\,\mathrm{ms}$ (cross section of 3D simulation). . . . 72
5.4 Pressure evolution in the lower part of MADMAX for $0.8 \leq t \leq 2.0\,\mathrm{ms}$ (cross section of 3D simulation). . . . 73
5.5 Pressure evolution in the middle part of MADMAX for $2.0 \leq t \leq 3.5\,\mathrm{ms}$. . . . 74
5.6 Pressure evolution in the middle part of MADMAX for $3.75 \leq t \leq 8.0\,\mathrm{ms}$. . . . 75
5.7 Pressure evolution in the upper part of MADMAX for $4.5 \leq t \leq 7.0\,\mathrm{ms}$. . . . 76
5.8 Pressure evolution in the upper part of MADMAX for $10 \leq t \leq 20\,\mathrm{ms}$. . . . 77
5.9 Accumulators' average nitrogen pressure and pistons y-displacement for Configuration 1 - 3D calculation. . . . 78

5.10 3D mesh. 80
5.11 3D mesh generating process on a sample geometry (cylinder). 81
5.12 3D mesh sensitivity analysis on the mesh size for $\Delta P_{\text{D3-C6}}$. 82
5.13 3D FSI mesh. 83
5.14 Structure displacement (visually amplified by a factor 1000) along y and z following water depressurization. 86
5.15 Structure displacement along y and z following water depressurization. 87
5.16 Structure displacement along y and z following water depressurization. 88
5.17 1D/1D FSI mesh scheme. 89
5.18 Configuration 1 pressure evolution comparison for sensors C1 and C2. 92
5.19 Configuration 1 pressure evolution comparison for sensors C4, D1, C6, D3, C8 and D5. 93
5.20 Configuration 1 pressure difference between sensors D2 and C5, ΔP_{D2-C5}, and sensors D4 and C7, ΔP_{D4-C7}. 94
5.21 Configuration 1 mean absolute error for the junction pipe sensor and the core pipe sensors. 94
5.22 Configuration 1 mean absolute error for the by-pass pipe sensors. 95
5.23 Configuration 1 mean absolute error for pressure differences between core and by-pass pipe sensors. 95
5.24 Configuration 1 computational cost of the four calculations with respect to their precision. 96

6.1 Experimental pressure evolution for all sensors for Configuration 2. 98
6.2 Experimental pressure evolution for sensors C4-C8 and D1-D5 for $t \leq 6\,\text{ms}$. Comparison between Configuration 2 (a) and Configuration 1 (b). 99
6.3 Experimental pressure evolution for all sensors for Configuration 3. 99
6.4 Configuration 2 pressure evolution comparison for sensors C1, C2, C4 and D1. . 101
6.5 Configuration 2 pressure evolution comparison for sensors C6, D3, C8 and D5. . 102
6.6 Configuration 2 pressure difference between sensors D2 and C5, ΔP_{D2-C5}, and sensors D4 and C7, ΔP_{D4-C7}. 103
6.7 Configuration 2 mean absolute error for the junction pipe sensor and the core pipe sensors. 104
6.8 Configuration 2 mean absolute error for the by-pass pipe sensors. 104
6.9 Configuration 2 mean absolute error for pressure differences between core and by-pass pipe sensors. 105
6.10 Configuration 3 pressure evolution comparison for sensors C1 and C2. 106
6.11 Configuration 3 pressure evolution comparison for sensors C4, D1, C6, D3, C8 and D5. 107
6.12 Configuration 3 pressure difference between sensors D2 and C5, ΔP_{D2-C5}, and sensors D4 and C7, ΔP_{D4-C7}. 108
6.13 Configuration 3 mean absolute error for the junction pipe sensor and the core pipe sensors. 109
6.14 Configuration 3 mean absolute error for the by-pass pipe sensors. 109
6.15 Configuration 3 mean absolute error for pressure differences between core and by-pass pipe sensors. 110
6.16 Multi-orifice plates examples. 114
6.17 MADMAX configuration with pseudo fuel assembly and mixing grids. 115

C.1 Orifice plate scheme. 136
C.2 Simplified scheme of the orifice plate. 137
C.3 Elements extracted from the 1D mesh. 139

List of Tables

2.1 History of MADMAX experiments without by-pass pipe. 18
2.2 History of MADMAX experiments with by-pass pipe. 20

3.1 Hierarchy of numerical models used for the simulations of MADMAX simplified configuration without by-pass pipe. 32
3.2 Hierarchy of numerical models used for the simulations of MADMAX complete configuration with by-pass pipe. 33

4.1 Experimental bursting pressure for MADMAX simplified set-up. 35
4.2 2D axisymmetric mesh characteristics for sensitivity analysis. 40
4.3 Characteristic time and head loss coefficient for IMPEDANCE GRID. 43

5.1 Experimental bursting pressure for MADMAX complete set-up. 68
5.2 3D mesh characteristics for sensitivity analysis. 82

6.1 Experimental bursting pressure for MADMAX complete set-up (alternative configurations). 98

Chapter 1

Introduction

1.1 Context and motivation

Loss Of Coolant Accident (LOCA) in a Pressurized Water Nuclear Reactor (PWR) consists in a brutal and total opening (guillotine break) of one of the main coolant pipes. The transient rarefaction wave generated by the break propagates within the primary circuit and, when reaching the reactor core (see Figure 1.1), crosses two zones displaying different geometric characteristics: the reactor core itself (fuel assemblies) and the by-pass zone between the baffle and the core barrel where several perforated reinforcement plates are arranged. This difference leads to non-identical travel times of the rarefaction wave in the two zones, causing a transient pressure load between the two sides of the baffle (see Figure 1.2). This phenomenon generates such stresses on the baffle that it can cause the structure to deform, thus no longer guaranteeing its structural integrity. These structures are of primary importance since internals are designed to ensure the cooling of the fuel and the movement of the emergency control assemblies during the accident (see for instance [3]; [4]; [5]).

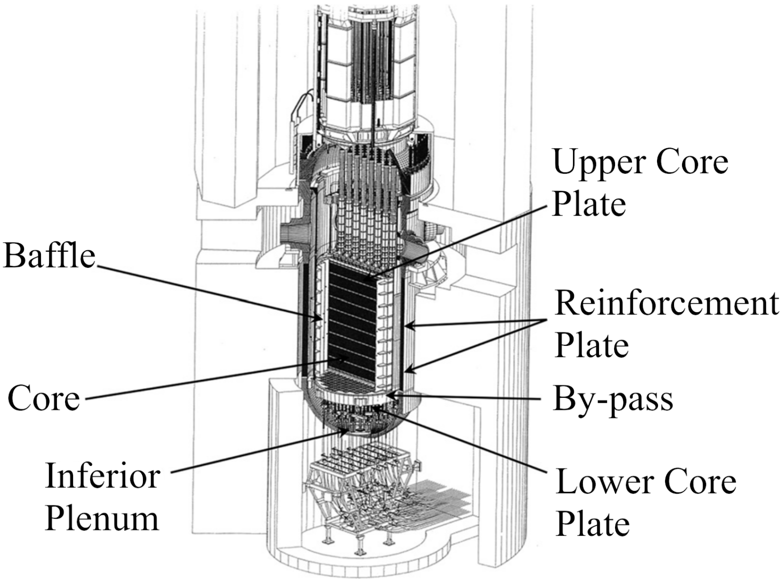

Figure 1.1: PWR vessel and internal components [1].

As all the details of the primary circuit cannot be modeled, simplified models are used to represent the flow in some areas, such as between the perforated plates. Some of these models are implemented in the fast-transient fluid-structure dynamics software EUROPLEXUS [6], developed at DYN (Laboratory of Dynamics Studies at CEA Saclay in France), and validated through experimental facilities.

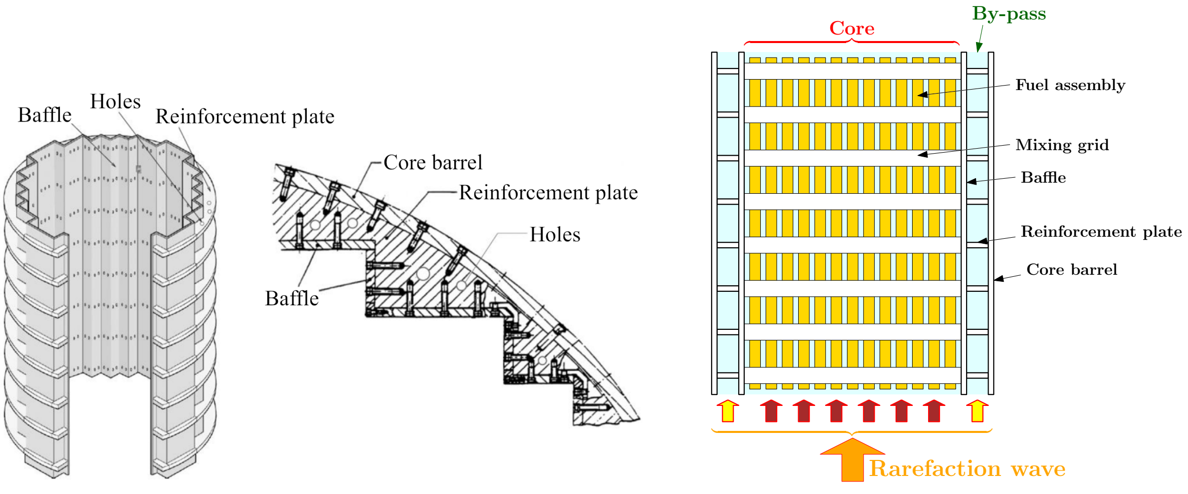

(a) (b)

Figure 1.2: (a) Baffle and perforated reinforcement plates [1]. (b) Simplified scheme.

The MADMAX facility has been developed at DYN with a focus on the study of a LOCA scenario: MADMAX stands in French for “Modélisation de l’Accident de Dépressurisation - Maquette Analytique-eXpérimentale”, which can be translated as “Depressurisation Accident Modelling - Analytical-Experimental Mock-up”. More precisely the MADMAX experiment, detailed in Chapter 2, has been designed 20 years ago to provide experimental results which could be used to calibrate and/or to assess the accuracy of Finite Elements (FE) and Finite Volumes (FV) simulations (including or not the Fluid-Structure Interaction (FSI) dynamics) when applied to the numerical prediction of a rarefaction wave propagating across different obstacles positioned in pipes, thus reproducing some key features of a LOCA configuration.

The phenomenon we intend to observe and analyze is a very rapid transient and we are particularly interested in observing the first $10 \div 20$ ms of the transient.

This work aims to significantly expand the validation scope of numerical models implemented in EUROPLEXUS for representing obstacles by conducting unprecedented experimental campaigns and numerical simulations on the MADMAX experiment. Previous seminal works, particularly those by V. Faucher and colleagues (2012) [1], have influenced the current state-of-the-art in nuclear reactor analysis and transient flow simulations, focusing on transient wave propagation through perforated plates relevant to LOCA scenarios in PWRs. Faucher’s research utilized a single orifice plate configuration and employed only a 1D model in EUROPLEXUS, comparing it with experimental results and a simplified 3D model from another software.

Our work extends this foundation by exploring six different orifice plate configurations, performing a sensitivity analysis on geometric characteristics, and incorporating 2D axisymmetric calculations and Fluid-Structure Interaction (FSI). These new orifice plates were designed, manufactured, and installed with significant personal involvement, and experiments were conducted personally with technical assistance. This research was initially presented at ICONE30 [7] and later expanded in a 2024 publication [8].

Additionally, the study evolved to include scenarios with multiple orifice plates in three configurations including not only the core pipe but also a by-pass pipe. These configurations were simulated using EUROPLEXUS with various models, including a simplified 1D model, a novel 1D model with FSI effects, and two innovative 3D reference models, one with fixed structures and the other incorporating FSI dynamics. Each experimental setup modification and the subsequent experiments were conducted with hands-on involvement.

1.2 State of the Art

Reference works in the context of nuclear applications

The recent state-of-the-art in the field of nuclear reactor analysis and transient flow simulations remains significantly influenced by several seminal works, notably those by V. Faucher and colleagues. As mentioned in the previous Section, Faucher et al. (2012) [1] conducted a comprehensive numerical and experimental analysis of transient wave propagation through perforated plates, particularly relevant for simulating Loss of Coolant Accidents (LOCA) in Pressurized Water Reactors (PWRs). Their work provided valuable insights into the fluid loading on internal structures, such as the reactor core baffle, under LOCA conditions. The analysis was carried out on a single orifice plate configuration on the MADMAX device while an EUROPLEXUS numerical simulation was carried out using only a 1D model for the representation of pipes and obstacles, similar to the ones which will be developed and assessed in the present work. A comparison was then made between the experimental result, the EUROPLEXUS calculation and a simplified 3D model performed with another commercial software. Some limitations of this seminal work were: the assessment of the simplified 1D model for a single geometry of obstacle; a limited instrumentation for the platform; the lack of assessment of the pressure differential between a core pipe and a by-pass pipe, an important feature in the LOCA context.

The present work extends [1] by addressing the above mentioned limitations: the relevance of simplified models is assessed for various orifice plate configurations, with a sensitivity analysis on the geometric characteristics of the obstacle (thickness and diameter); the experimental platform is equipped with a larger set of sensors; the experiment/simulation comparison is enriched with new 2D axisymmetric calculations and the account of 2D/3D Fluid-Structure Interaction (FSI); configurations involving the propagation of an expansion wave through a core pipe and a by-pass pipe are experimentally and numerically investigated.

Faucher et al. (2014) [9] contributed to the further understanding of the fast transient mechanical consequences of LOCA on PWR internal structures. The coupled 1D/3D simulations with fluid-structure interaction developed in this other seminal work offered a robust methodology for representing small geometric details, such as perforated plates near the reactor core, crucial for industrial applications. This work was taken as a reference for the presentation of the equations related to structural dynamics in Chapter 3 and the proper way to account for Fluid-Structure Interaction in the analysis of the flow configurations.

Additionally, research conducted at the Commissariat à l'énergie atomique et aux énergies alternatives (CEA) has been instrumental in advancing the understanding of transient flow phenomena. Gibert and Schwab (1983) [10] investigated the reaction between sodium and water, focusing on representing perforated plates traversed by a plane wave. Similarly, Izquierdo and Valin (2011) [11] provided experimental results on depressurization wave propagation through singularities, offering insights into the comparison between experimental data and EUROPLEXUS calculations. The latter served as preliminary work to the results subsequently presented by Faucher et al. (2012) [1].

Numerous studies in the literature have addressed the pressure drop induced by geometric obstacles under steady flow conditions. For instance, Idel'Cik (1969) [12] compiled a comprehensive database on this topic and we extensively used his work for calculating localized head losses in the modeling of our simplified simulations. Additionally, several models have been proposed to account for acoustic inertial corrections when waves propagate in a stationary flow, as demonstrated by Baylac et al. (1971) [13] and Gibert (1988) [14]. However, these existing models fall short of providing a complete representation of phenomena spanning from initial pressurized steady state to final stationary leak flow in pipe break simulations, indicating the potential benefit of combining different approaches.

Furthermore, computational tools and methodologies developed for fluid-structure interaction analysis, as demonstrated by Pedroso (1986) [15] and Daru and Tenaud (2009) [16], have facilitated the qualification of calculation methods for nuclear reactor components, ensuring their structural integrity under transient conditions.

The works of Gibert (1988) [14] and Pedroso (1986) [15] were of particular interest in this thesis for understanding and introducing the formulation of acoustic impedance for our simplified model in Chapter 3.

One of the most significant developments pertains to the simulation of two-phase flows within nuclear reactors. Radman et al. (2021) [17] proposed a segregated algorithm for simulating dispersed two-phase flows in porous media, implemented within the OpenFOAM programming library. This approach offers an efficient and accurate method for modeling physical interactions in complex engineering systems.

Recent advancements in computational fluid dynamics have led to the development of sophisticated numerical methods for simulating aeroacoustic phenomena. Feuchter (2021) [18] presented a lattice Boltzmann cumulant method for direct aeroacoustic simulation, offering a promising tool for investigating aeroacoustic effects in nuclear reactor systems.

Mokhtari et al. (2020) [19] developed a wavelet-based approach for multiscale filtering of compressible wave propagation in complex geometries in the framework of pressurized water reactors depressurization transient analysis, contributing to the understanding of transient flow phenomena in nuclear reactor systems. Radaideh et al. (2019) [20] analyzed loss of coolant accident scenarios under the restriction of reverse flow, providing insights into flow behavior and transient phenomena in nuclear reactor safety analysis.

Recent advancements by Faucher et al. (2021) [21] introduced a novel numerical framework for solving strongly coupled fluid-structure dynamic problems, particularly applicable to PWR fuel assemblies under axial flow and dynamic loading conditions. Their work emphasized the importance of porous approaches and computational efficiency in simulating hydraulic coupling between fuel assemblies.

The present contribution to the efficient simulation of transient flows in the presence of obstacles has obviously benefited from the experimental and numerical frameworks developed in the works we have briefly reviewed. The manuscript will detail in Chapter 2 how the experimental set-up has been evolved and enhanced to produce an enriched set of validation measurements. The state-of-the-art numerical treatments available in EUROPLEXUS and reviewed in Chapter 3 will be applied in Chapters 4, 5 and 6 to an extended set of flow configurations in order to provide a thorough assessment of the predictive power of simplified models.

Fast transient flows in the presence of obstacles outside the nuclear field

Many other works, not related to the nuclear domain, have been investigated throughout the thesis in order to keep track of the various numerical strategies developed to simulate fast transient flows in the presence of obstacles. These works cover a wide range of interesting application fields, from aeroacoustics to gas dynamics and the analysis of shock waves (rather than expansion waves) interacting with various types of obstacles. Unfortunately, very few of these studies address the propagation of pressure waves in water or liquids in general; they focus predominantly on air or gases. Additionally, the fluid-structure interaction phenomena we are interested in do not produce the violent shocks considered in some if not most of the works cited below.

Regarding the response of an orifice plate in an aeroacoustic regime, studies by Rienstra and Hirschberg (2006) [22] and Hofmans et al. (2001) [23] offer valuable insights. Nonetheless, the methodologies outlined in these studies are not directly applicable to the transient flows under consideration here. Efforts have been made to extend head loss concepts to unsteady flows, particularly in the context of friction losses in pipes. Two primary approaches have emerged: one where the friction coefficient depends on the mean instantaneous velocity and its spatial and temporal derivatives, exemplified by Brunone et al. (1991) [24], and another where it depends on a weighted sum of mean velocity variations, as proposed by Zielke (1968) [25]. Further details and variations on these approaches can be found in studies by Adamkowski and Lewandowski (2006) [26] and Vitkovsky et al. (2006) [27]. Despite these advancements, none of these approaches directly addresses the physics of transient flows. However, they provide valuable avenues for research, particularly in cases where combined stationary head loss and acoustic correction impedance models are inadequate.

Numerical studies, such as those conducted by Mohsen et al. (2013) [28], have explored the effects of area contraction on shock tube performance, providing insights into transient flow behavior in test structures. Similarly, Britan et al. (2006) [29] investigated shock wave attenuation by porous barriers, offering guidelines for mitigating shock wave effects in refuge ventilation systems.

Experimental and theoretical investigations into shock wave interaction with orifice plates have been conducted. Dadone and Pandolfi (1971) [30] proposed a theoretical model for estimating shock wave effects on orifices within ducts, with experimental validation demonstrating good agreement with numerical predictions. Additionally, Eckenfels (2021) [31] studied explosion mitigation via perforated plates using an explosively driven shock tube, highlighting the role of geometric effects and plate number in attenuating shock waves.

The transient behavior of pressurized pipelines with in-line valves has been examined by Meniconi et al. (2014) [32], who analyzed energy dissipation and pressure decay during transients. Their study provides insights into the dynamics of pressurized flow systems and factors influencing pressure fluctuations during transient events.

Furthermore, recent experimental work by Laffay et al. (2020) [33] investigated noise radiated from airflow channeled through diaphragms and perforated plates, providing information on acoustic modifications and sources in practical applications. Ciccarelli et al. (2018) [34] conducted experiments to study detonation propagation in a circular tube fitted with repeated orifice plates, contributing to the understanding of detonation phenomena and propagation mechanisms. Cummings (1984) described acoustic power losses in orifices in the absence of mean flow, offering insights into the interaction between high-amplitude sound waves and orifice structures. Igra et al. (2001) [35] conducted experimental and theoretical studies on shock wave propagation through double-bend ducts, providing valuable information on shock wave attenuation and flow behavior in complex geometries.

Moreover, numerical investigations conducted by Igra et al. (1996) [36] on the interaction of a planar shock wave with a square cavity provide insights into complex time-dependent processes and offer a reliable physical model for similar shock wave interactions with other complex boundaries.

Colas et al. (2019) [37] developed an implicit integral formulation to model inviscid fluid flows in obstructed media, providing a technique for computing compressible fluid flows in physical domains cluttered up with many small obstacles. Abate and Shyy (2002) [38] reviewed experimental and numerical results to highlight the flow phenomena and main physical mechanisms associated with confined shocks undergoing sudden expansion, contributing to the understanding of dynamic structure in such scenarios. Additionally, Romenski et al. (2019) [39] discussed a multiphase model for wavefields numerical simulation in the context of compressible fluid flows in elastic porous media, offering insights into modeling wave propagation in saturated elastic porous media based on thermodynamically compatible system theory for multiphase mixtures.

Furthermore, recent studies by Igra et al. (2016) [40] have numerically investigated the mitigation of shock waves by different combinations of plate barriers, showing their effectiveness in attenuating transmitted shock waves. The propagation of shock waves within circular cross-section shock tubes with sudden area changes has been studied by Jiang et al. (1997) [41], providing insights into transient shock-wave phenomena and interactions in such configurations. Kroner and Mai (2005) [42] presented numerical solutions to compressible flows in nozzles with variable cross-section, contributing to the understanding of flow behavior in variable geometry ducts.

Moreover, Rudinger (1960) [43] investigated the passage of shock waves through ducts of variable cross-section, providing insights into the wave patterns and transient processes involved in such configurations. Loske (2016) [44] studied shock wave interaction with abrupt area changes, shedding light on the effects produced on fluid flow dynamics. Schulze et al. (2016) [45] investigated linearized Euler equations for the determination of scattering matrices for orifice and perforated plate configurations in the high Mach number regime, contributing to the understanding of aeroacoustic phenomena.

Igra and Gottlieb (1985) [46] studied the interaction of rarefaction waves with area enlargements in ducts, providing analytical and numerical insights into wave patterns and flow behavior in such configurations. Emanuel et al. (2005) [47] investigated the performance of a shock tube with a large-area contraction, offering insights into shock wave behavior in shock tube configurations with sudden area changes.

Falcovitz and Igra (2008) [48] proposed a model for shock interaction with sharp area reductions, contributing to the understanding of shock wave behavior in configurations with abrupt area changes. Alligne et al. (2014) [49] proposed an integer linear programming (ILP) approach for optimizing real-time pump schedules in water distribution systems, considering various constraints such as capacity, demand satisfaction, water quality, and maximum power consumption.

Menina et al. (2011) [50] developed a quasi-1D model to account for variations in section in gas dynamics, particularly in ducts with abrupt area changes. Payri et al. (2004) [51] conducted a comparative study of numerical schemes to solve one-dimensional fluid-dynamic equations in tapered pipes under impulsive flow conditions, highlighting the importance of scheme selection and equation arrangement for mass conservation. Rochette and Clain (2006) [52] proposed a finite volume method with a VFRoe solver to simulate compressible gas flow in a variable porous medium for two-dimensional geometries, considering non-conservative terms to account for porosity variation.

Erez et al. (2000) [53] investigated the membrane effect on turbulent mixing measurements in shock tubes, highlighting the influence of the membrane on the evolution of the mixing zone during different stages. Berger et al. (2015a) [54] conducted experimental and numerical investigations of shock wave attenuation by geometrical means, particularly focusing on the dependence of shock wave attenuation on various barrier geometries in corridor-like structures. Ram et al. (2018) [55] experimentally studied the pressure buildup behind an array of perforated plates impinged by a normal shock wave, considering factors such as the number of plates, porosity, and gas type.

Sha et al. (2012) [56] numerically investigated blast wave attenuation by obstacles using a 5th-order WENO scheme and immersed boundary method, analyzing the effect of obstacle shape on blast wave attenuation. Berger et al. (2015) [57] experimentally and numerically investigated shock wave attenuation by dynamic barriers, demonstrating the feasibility of dynamic barriers that adjust their orientation in response to shock wave loads, thereby reducing shock-induced pressure downstream.

This analysis of the literature on fast transient flows over obstacles with a simplified geometric description of the obstacles which was performed at the start of the PhD (and the scientific watch keep during the PhD) did not lead eventually to the selection and implementation in EUROPLEXUS of alternative simplified models with respect to those already available and preliminary assessed in previous works.

1.3 Outline of the thesis

This section provides a comprehensive outline of the thesis. Chapters 2 and 3 deal respectively with the experimental and the numerical tools applied to the present analysis of fast transient flows in the presence of obstacles, while Chapters 4, 5, and 6 present the results and their discussions.

Chapter 2: Evolution of Experimental Set-up

- **Historical Context:** Trace the evolution of the MADMAX experimental facility from its inception in the early 2000s to recent modifications undertaken during the PhD thesis.
- **Experimental Enhancements:** Detail the modifications made to the experimental set-ups, including introduction of modular orifice plates and changes in set-up configurations.

Chapter 3: Numerical Modeling Framework

- **Theoretical Foundations:** Explore the theoretical underpinnings of the numerical models used in simulations, focusing on fluid-structure interaction concepts, fluid and structural behavior models, and equations of state.
- **Computational Techniques:** Examine the spatial and temporal discretization methods employed in numerical simulations, such as finite element and finite volume methods.
- **Hierarchy of Simulation Models:** Present a hierarchical overview of the numerical models utilized in simulations, ranging from simplified 1D representations to more intricate 2D axisymmetric and 3D models.

Chapter 4: Experimental and Numerical Results (Simplified Configuration)

- **Evaluation of Predictive Capabilities:** Analyze experimental and numerical results for the simplified configuration of the MADMAX experiment. Assess the predictive capabilities of EUROPLEXUS in simulating rarefaction wave propagation through a single obstacle.
- **Comparative Analysis:** Compare experimental data with simulation outputs, highlighting agreements and discrepancies. Discuss the strengths and limitations of 1D and 2D axisymmetric models in replicating experimental observations.

Chapter 5: Experimental and Numerical Results (Complete Configuration)

- **Pressure Evolution Analysis:** Investigate pressure evolution and dynamics in the complete configuration of the MADMAX experiment. Examine experimental findings and numerical simulations to understand the effects of multiple obstacles on wave propagation.
- **Insights into Model Performance:** Provide insights into the performance of numerical models in simulating complex fluid-structure interactions. Discuss the implications of simulation results for optimizing experimental set-ups and refining numerical models.

Chapter 6: Experimental and Numerical Results (Alternative Configurations)

- **Exploration of Novel Configurations:** Explore experimental and numerical results for alternative MADMAX configurations, including configurations with different numbers of obstacles and simultaneous presence of obstacles in core and by-pass pipes.
- **Comparative Assessment:** Conduct comparative analyses between experimental data and numerical simulations for alternative configurations. Evaluate the accuracy and computational efficiency of different numerical models in capturing system behavior.

Chapter 7: Conclusions and Perspectives

Chapter 2

MADMAX experimental facility: original set-up and new features

This chapter delves into the evolution of the MADMAX experimental facility, initially designed in the early 2000s to analyze pressure loads induced by depressurization waves in parallel pipelines. The original set-up featured a main pipe with a bursting disk and an auxiliary branch mimicking a PWR vessel's core and by-pass. Modifications in 2010 simplified the mock-up, focusing on studying wave passage through an orifice plate. Recent experimental campaigns (2022-2024), carried out in the framework of this PhD thesis, expanded on these modifications, introducing setups with and without a by-pass pipe and incorporating modular orifice plates of varying thickness and diameter or the presence of multiple orifice plates, to analyze their impact on wave propagation. These developments aim to enhance the understanding of wave dynamics and validate simulation codes for fluid dynamics research in the context of nuclear safety, reflecting the facility's continuous quest for accurate experimental data.

2.1 Original set-up

2.1.1 General description

The MADMAX experiment, originally called SMART and later Maquette APRP (LOCA Mock-up), has been designed in the early 2000s to analyze the pressure loads on the structure generated by different travel times of a depressurization wave in two parallel pipelines. Much of the historical information regarding the experiment up to 2010 is derived from the internal technical report by CEA authored by Faucher, Galon, and Izquierdo (2010) [58].

Figure 2.1 provides an overview of the experimental platform. It consists of a main pipe, arranged vertically and fitted at its lower end with a bursting disk designed to cause a sudden opening of the circuit. An auxiliary branch, of smaller cross-section and equipped with several orifice plates, is connected to this main pipe. In analogy with the geometry of the core and by-pass in a PWR vessel, the main pipe plays the role of the core, while the auxiliary pipe plays the role of the by-pass and perforated reinforcement plates.

In the generic experiment the pipes are initially filled with water that is then pressurized until it triggers the opening of a bursting disk (failure pressure at about 70 bar) located at the bottom of the core pipe.

The orifice plates arranged at different heights in the by-pass pipe, to simulate the effect of the baffle reinforcement plates in the PWR core, have an orifice diameter of 17 mm and a thickness of 5 mm.

Two water accumulators are disposed at the top end of the core pipe to supply the system with water during several milliseconds. On the one hand, they speed up the fluid, to study the combined effects of pressure drops and acoustic impedances at the orifice plates, and on the other, they prevent the system from draining too quickly, enabling us to monitor the effects of wave propagation in the water.

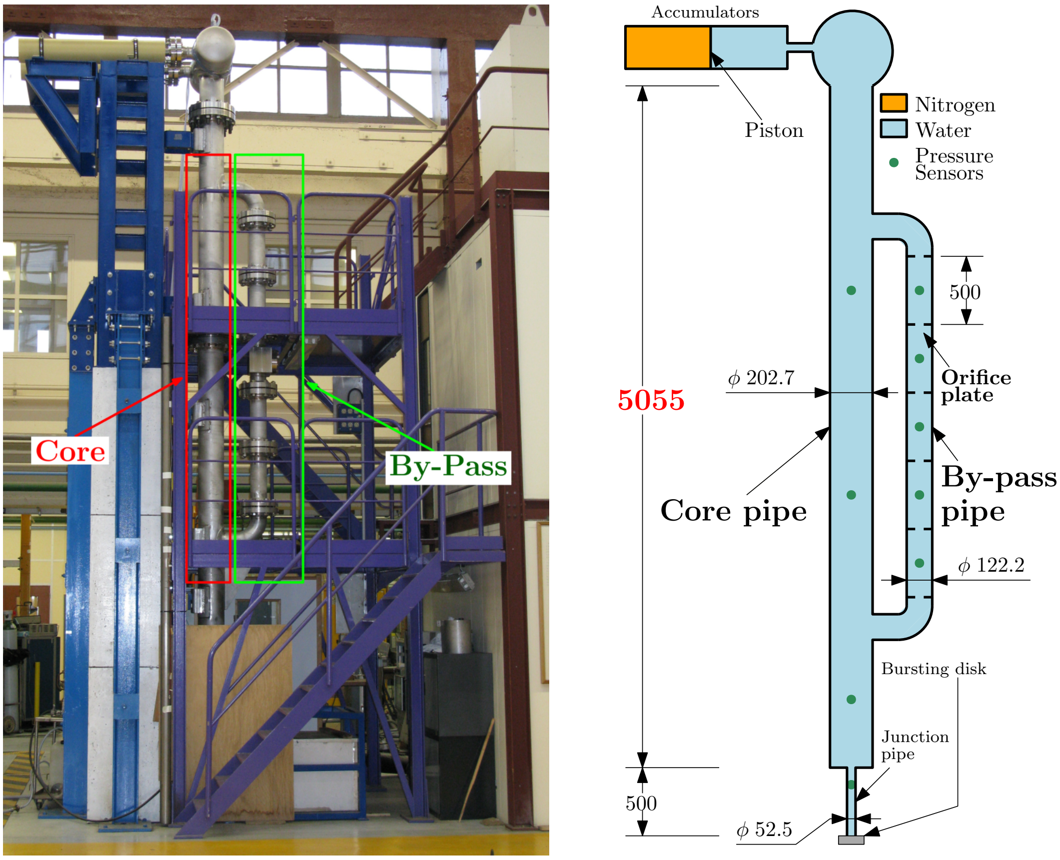

Figure 2.1: Original design of the MADMAX experimental facility at DYN (CEA Saclay, France). Dimensions in millimeters. Pipe diameters given are internal diameters.

The bursting disks used for the initial tests on the mock-up were precast metal disks, with 4-petal opening kinematics (see Fig. 2.2 (a)) once the maximum resistance pressure had been exceeded. The opening time and effective opening cross-section obtained with such discs are unknown parameters with a major influence on the measurements obtained from these tests.

In the initial mock-up configuration, there was also a Helmholtz resonator installed on the junction pipe in order to smooth the profile of the depressurization wave. This component, however, perturbed the measurements too much and was therefore removed.

In the first tests carried out between 2000 and 2001, some of the results measured on the experiment deviated too much from some simplified calculations made with EUROPLEXUS, which were closer to the analytical solution instead.

This suggested the hypothesis of perturbations in the experiment, due to the opening kinematics of the petal discs or to the presence in the junction pipe of the spigot designed to accommodate the Helmholtz resonator when in use. In particular, the actual cross-sectional area of fluid flow through the petal disk seemed uncertain, insofar as tests with a reduced leakage cross-section led to satisfactory correlations with the simulation, in contrast to those where the entire cross-sectional area of the nozzle should be open.

This led to the resumption of experimental work on the mock-up, with prior simplification of its geometry and improvement of the opening process under pressure, in order to remove the uncertainties arising from the last series of tests and obtain a reliable and correctly interpreted experimental reference solution.

(a)

(b)

Figure 2.2: (a) Petal bursting disk used in the first tests (2000-2001) and (b) graphite fragmentation disk used from 2010.

2.1.2 Mock-up modifications in 2010

In 2010, as well as seeking to reduce uncertainties to facilitate test interpretation, some modifications of the mock-up also reflected a change in the purpose of the experiments. In its initial configuration, the mock-up was designed to quantitatively measure the pressure forces between the two branches, which were then being sought to reproduce with EUROPLEXUS, in order to validate the program's capabilities for calculating the loading on the baffle screws in the event of a LOCA (see Chapter 1).

Instead, with the modifications came the search for a reference solution for the passage of a depressurization wave through an orifice plate. This solution must be as simple as possible, so that it can be used for rigorous validation of a high-precision simulation code.

In the final configuration (see Figure 2.3), a single orifice plate was placed in the middle of the main pipe. It is relatively thick compared with the diameter of the opening (50 mm thick for a diameter of 30 mm), so that the delay in wave propagation it induces was clearly measurable. The junction pipe is retained, to limit the flow at the opening at the bottom of the mock-up, but the original tube, fitted with the resonator spigot, is replaced by a straight tube with no geometric peculiarities. For these new tests, the by-pass is either open, with all the orifice plates it originally contained then removed, or closed, at the locations of the lower and upper orifice plates.

The petal-type rupture disks are replaced by fragmentation graphite disks. As soon as the rupture pressure is reached, a rupture cone is released into the flow, freeing the entire opening cross-section (see Fig. 2.2 (b)).

The insertion of an orifice plate in the middle of the main pipe was foreseen in the initial design of the model and did not require any structural modifications. As far as the by-pass is concerned, it could be closed at the locations of the upper and lower orifice plates without modification. What remains are the two elbows, shown in Figure 2.3. Their presence can disrupt the propagation of the depressurization wave in the main pipe, but their removal would require costly cutting and welding work, and has therefore not been carried out.

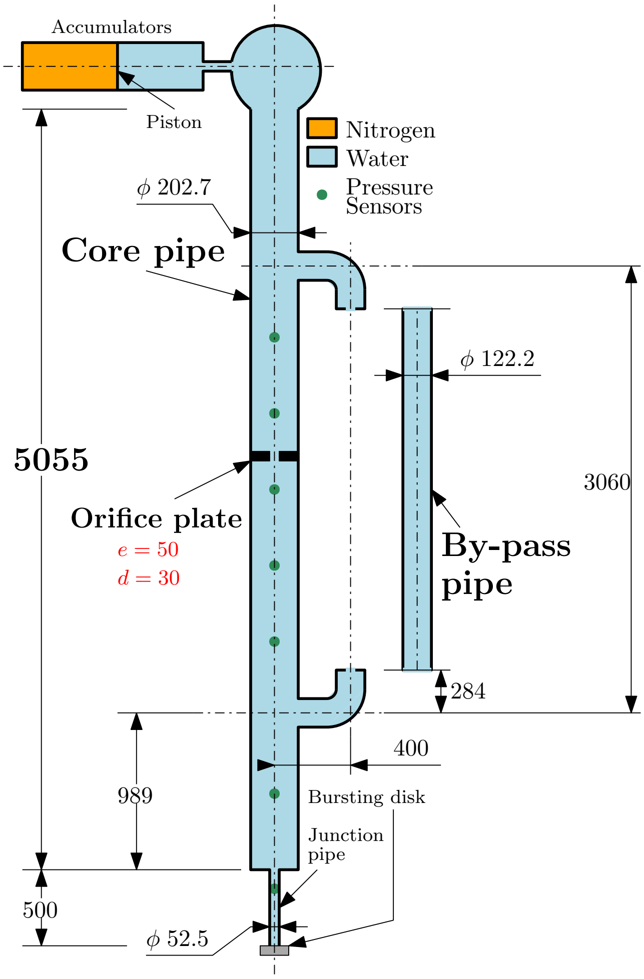

Figure 2.3: MADMAX configuration in 2010. Dimensions in millimeters. Pipe diameters given are internal diameters.

The experimental campaign realized in 2010 consisted of five tests. Some were carried out with the by-pass in place, featuring either a fragmentation rupture disk or a petal disk, enabling the behavior of the two types of disk to be compared. One test was carried out with a fragmentation disk and the by-pass closed.

For each test, an interpretation calculation with EUROPLEXUS is proposed. Some of the results are presented and discussed in [1].

After this experimental campaign, the mock-up suffered an 8-year stop. Then in 2018, in preparation for new experimental campaigns, the mock-up was put back into service and requalified, and the last experiment carried out in 2010 was reproduced to check its repeatability.

2.2 Evolutions of the experiment and new experimental campaigns in 2022-2024

2.2.1 Experimental set-up without by-pass pipe, with modular orifice plate

In the novel 2022/2023 experiments the overall setup remains very similar to the one of 2010, but new orifice plates are now installed (see Fig. 2.4) with thickness and diameter that can be changed to parametrically assess the geometry influence on wave propagation. The plate thickness e can be set at 10 or 50 mm, while the diameter d can be set to three different sizes (10, 30 and 50 mm). So, we have a total of six different configurations.

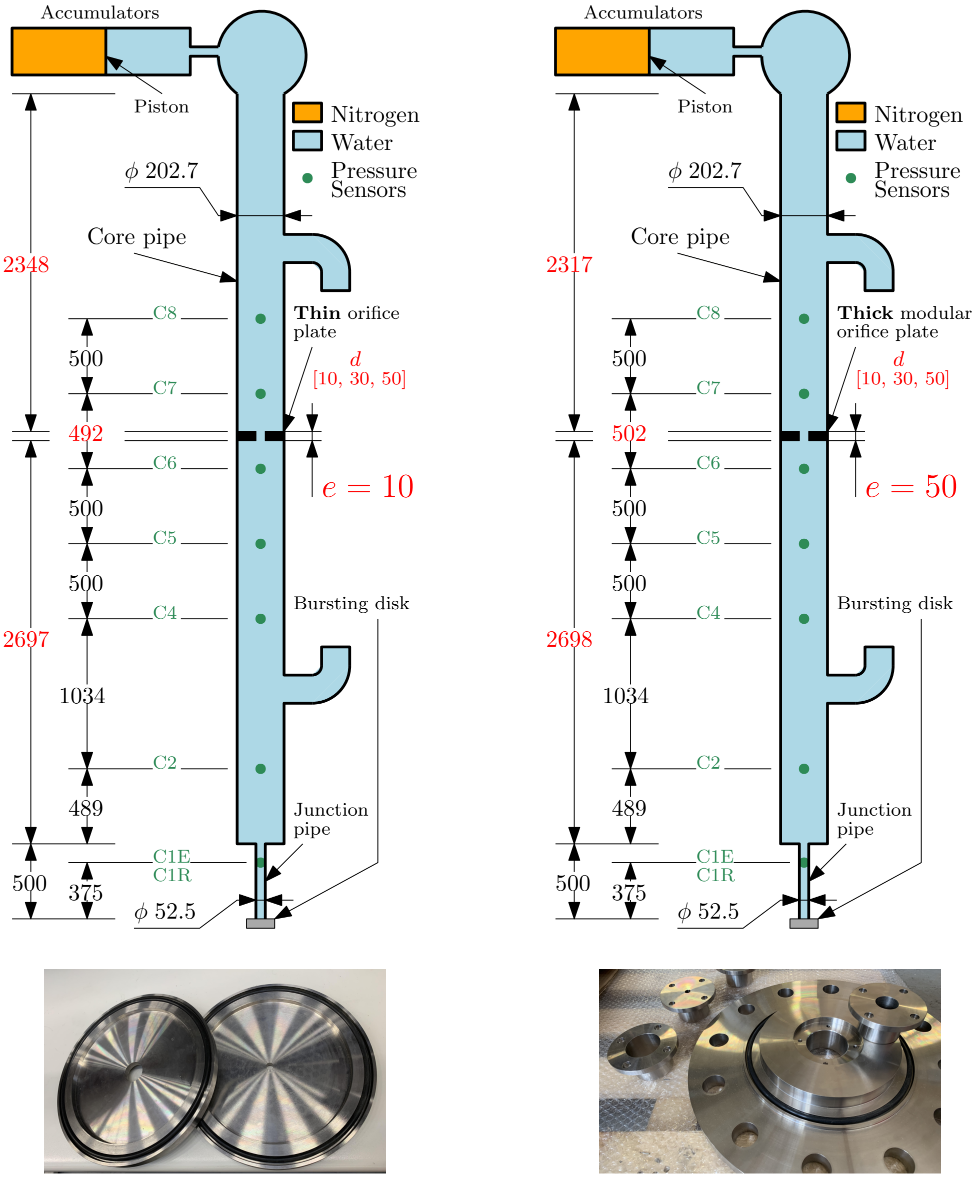

(a)

(b)

Figure 2.4: Experimental set-up (all dimensions in millimeters): (a) thin orifice plates, (b) thick modular orifice plate.

The new orifice plates were entirely designed in the context of the present thesis work, with the assistance of the person in charge of the experimental platform in the DYN Laboratory at CEA Saclay, Engineer Thibaut Gay-Peiller. Subsequently, they were manufactured by an external company. The tasks performed in the present work included the installation of these plates on the experimental device, with the support of the laboratory technician, Mr. Lehsen Tarmoul, and the management of the full set of experiments presented and analyzed in this manuscript, again with the assistance of the laboratory technician.

In order to investigate the influence of these geometric obstacles on wave propagation, eight pressure sensors are placed along the pipes to measure the pressure of the fluid at the inner wall of the pipe: a piezoelectric pressure sensor (C1E) and a piezoresistive pressure sensor (C1R) are positioned at the same height in the junction pipe; six piezoelectric pressure sensors are positioned along the core pipe, four below (C2, C4, C5 and C6) and two above (C7 and C8) the orifice plate (see Fig. 2.4). The C1R sensor, providing a continuous measurement of absolute pressure (unlike piezoelectric sensors, which are dynamic sensors detecting only rapid pressure changes), is used to trigger the activation of the measurement acquisition system. Additionally, it provides a dual verification measure for that point in the junction pipe.

2.2.2 Experimental set-up with by-pass pipe and multiple orifice plates

The experimental campaign on the simplified MADMAX configuration without by-pass pipe concluded in February 2023. Subsequently, during the months of June and July 2023, the experimental team, comprised of platform supervisors - including the present PhD candidate - and technicians, proceeded with the re-installation of the by-pass pipe along with its six orifice plates. This endeavor aimed primarily at replicating the original experiment configuration as conceived during its design phase.

Due to the depletion of the available stock of bursting disks (the last disk was used in the final experiment of February 2023) and a significant delay in the delivery of the new stock (ordered in December 2022 and delivered almost a year later), the new experimental campaign was launched in December 2023 and concluded at the end of February 2024.

During this experimental campaign, three different configurations of MADMAX with by-pass pipe were tested, as depicted in Figures 2.5 and 2.6, and summarized as follows:

1. **Configuration 1:** free core pipe and 6 orifice plates in the by-pass pipe,
2. **Configuration 2:** free core pipe and 4 orifice plates in the by-pass pipe,
3. **Configuration 3:** 1 orifice plate [$e = 10\,\mathrm{mm}$, $d = 30\,\mathrm{mm}$] in the core pipe and 6 orifice plates in the by-pass pipe.

The orifice plates in the by-pass pipe all have a thickness $e = 5\,\mathrm{mm}$ and an orifice diameter $d = 17\,\mathrm{mm}$, spaced 500 mm apart from each other. In Configurations 1 and 3, all six orifice plates are retained, while in Configuration 2, the bottom and top ones have been removed, leaving the four central ones.

Five new piezoelectric pressure sensors (D1, D2, D3, D4, and D5) are installed on the by-pass pipe, positioned exactly midway between each pair of orifice plates. Consequently, they are located at the same height as the sensors on the core pipe (C4, C5, C6, C7, and C8), which remain installed on the device. All these sensors are identical. Sensor C2 is the same one used in the previous experimental campaign. However, for the sensors on the junction pipe, it was necessary to remove the piezoelectric sensor C1E due to damaged threading in its housing, causing water leakage and pressure loss in the device. This sensor was temporarily replaced by a threaded steel plug to ensure tightness. Fortunately, at the same height as the removed sensor, there is also a second piezoresistive pressure sensor, previously labeled C1R in the configuration without the by-pass, which we will now simply refer to as sensor C1.

Configuration 1 is chosen first because it is the complete configuration with which the experiment was originally designed. Configuration 2 is designed to investigate the effect of a different number of obstacles placed in series within the by-pass pipe, while Configuration 3 incorporates the same number of orifice plates in the by-pass as Configuration 1, but an additional orifice plate is added in the core pipe to analyze the effect of the simultaneous presence of obstacles in both branches of the experiment, thus approaching even closer to the real industrial case (see Figure 1.2). In the actual industrial case, there is the simultaneous presence of perforated plate-type obstacles in the by-pass zone and fuel assemblies with mixing grids in the core zone. The orifice plate in the core pipe of Configuration 3 of MADMAX is intended to represent the core zone's geometry in a simplified manner.

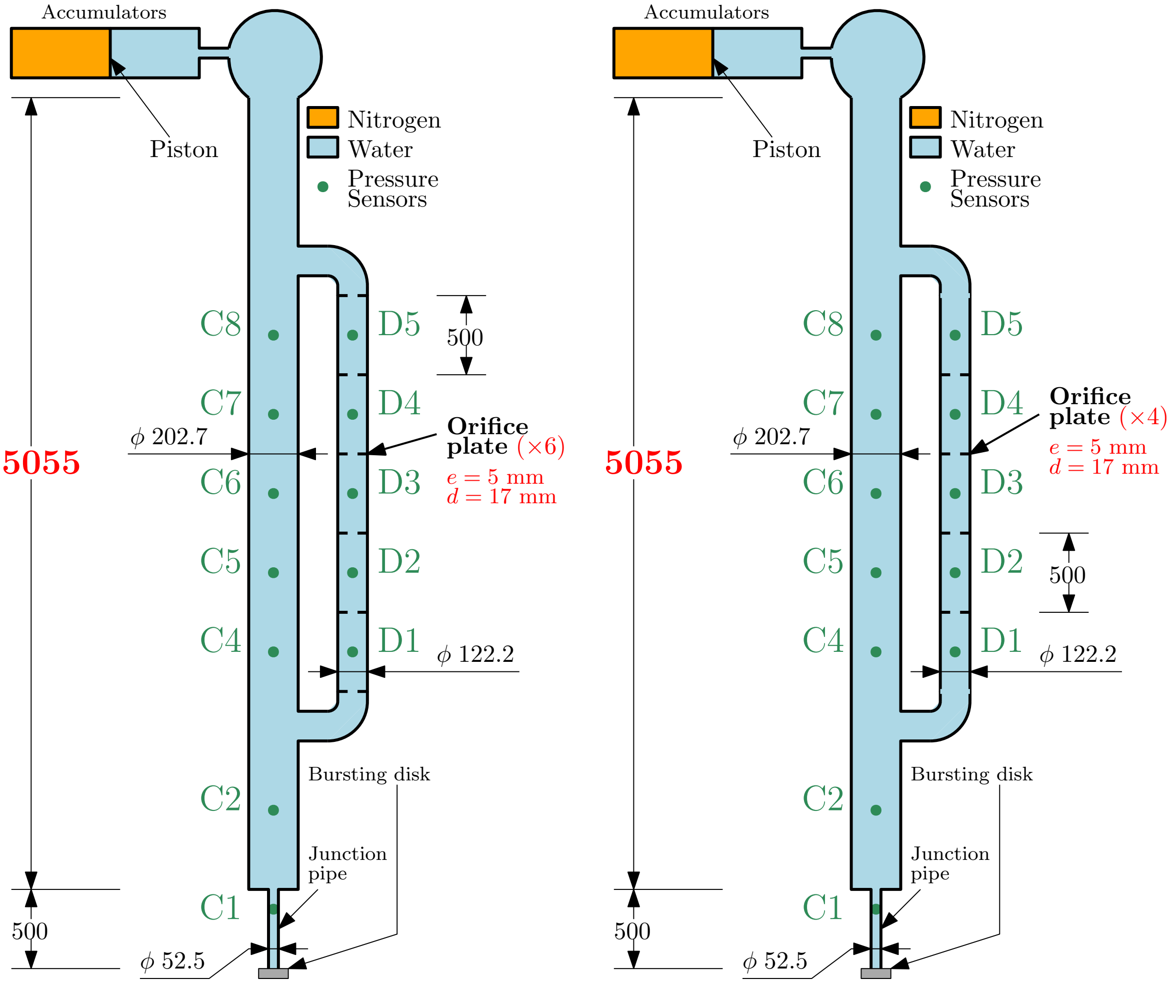

(a) Configuration 1

(b) Configuration 2

Figure 2.5: MADMAX configurations 1 and 2 with by-pass pipe.

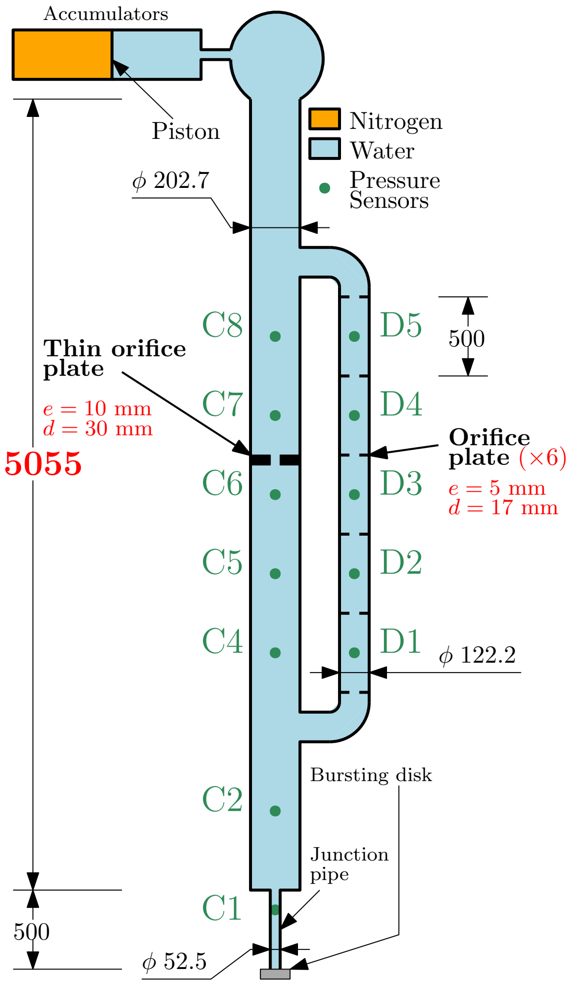

(a) Configuration 3

Figure 2.6: MADMAX configuration 3 with by-pass pipe.

2.2.3 Historical overview of experimental campaigns 2022-2024

The results analyzed in Chapters 4, 5 and 6 of this thesis work correspond to a total of 9 experiments: 6 configurations for the MADMAX set-up without by-pass pipe and 3 configurations for the complete set-up with by-pass pipe. As is typical in most experimental studies, the presented results constitute only a part of all the experimental tests conducted during the campaign. Many tests are indeed reiterated to verify repeatability or need to be conducted again due to issues such as data acquisition system malfunction, device damage, etc.

In the present work, an experiment is deemed successful if the following conditions are met:

- Sharp rupture of the bursting disk (complete separation of the failure cone and full opening of the outlet section) within the range $[60, 80]$ bar with some added tolerance to the factory tolerance of the bursting disk, which would be $[63, 77]$ bar.
- Full operation of the acquisition system, meaning that all sensors have recorded the signal.

If a bursting disk proves to be more resistant than expected, a pressure relief safety system installed on the device prevents the pressure from exceeding 80 bar. In this case, the experiment is interrupted and possibly retried later on the same disk a second time. If the disk does not rupture on the second attempt, it is replaced with a new one.

The characteristic parameter determining the bursting pressure of the bursting disk is the thickness e, as indicated in Figure 2.7. Before installing the disk on the experimental set-up, we always perform a metrological measurement to verify the actual thickness: using a caliper, we measure the thicknesses e_1, e_2, and e_3, from which we derive the thickness e using the formula provided in the figure.

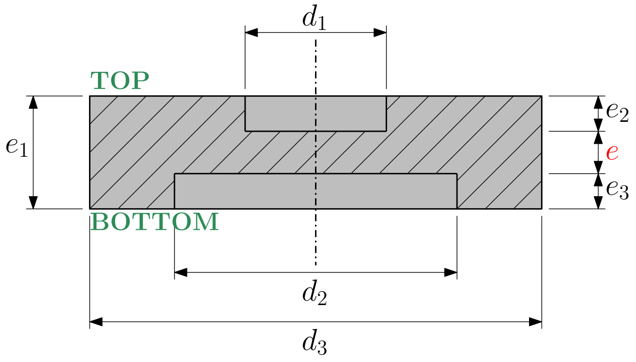

Fixed dimensions

$d_1 = 52.5$ mm
$d_2 = 100$ mm
$d_3 = 160$ mm
$e_1 = 40$ mm

Bursting disk thickness

$$e = e_1 - e_2 - e_3$$

Figure 2.7: Bursting disk metrology.

In this thesis work, a total of 21 experiments were conducted during the period 2022-2024: 17 of these tests resulted in a bursting disk rupture, while 4 were terminated due to reaching the maximum acceptable pressure without rupturing the bursting disk.

Out of these 17 tests, 10 pertained to the simplified configuration of MADMAX without by-pass pipe. Among these, 3 tests were discarded due to total or partial malfunctioning of the data acquisition system, leaving us with 7 valid tests for this configuration. Table 2.1 provides an overview of all the 10 experiments conducted on this set-up. For each experiment, we indicate the date, the configuration of the orifice plates used, the bursting pressure, the thickness of the bursting disk, and whether the experiment was retained or discarded (with motivation). The first entry in the table was a valid test, but it was excluded from the results because it was the first test conducted since 2018, performed solely to verify the proper functioning of the entire system without changing the configuration (the device had the old orifice plate used in the 2010 experimental campaign installed).

Table 2.1: History of MADMAX experiments without by-pass pipe.

Date (dd/mm/yyyy)	**Configuration**	P_{burst} (bar)	**Bursting disk** e (mm)	**Retained**
01/06/2022	$e = 50\,\text{mm}$ $d = 30\,\text{mm}$ (original set-up)	68.4	14.4	NO (recommissioning test)
20/07/2022	$e = 50\,\text{mm}$ $d = 30\,\text{mm}$ (modular)	67.5	14.4	NO (acquisition system total malfunctioning)
21/07/2022	$e = 50\,\text{mm}$ $d = 30\,\text{mm}$ (modular)	78.0	14.4	NO (acquisition system partial malfunctioning)
21/07/2022	$e = 50\,\text{mm}$ $d = 30\,\text{mm}$ **(modular)**	**74.3**	14.4	**YES**
25/07/2022	$e = 50\,\text{mm}$ $d = 10\,\text{mm}$ **(modular)**	**73.3**	14.4	**YES**
25/07/2022	$e = 50\,\text{mm}$ $d = 10\,\text{mm}$ (modular)	76.3	14.4	NO (acquisition system partial malfunctioning)
26/07/2022	$e = 50\,\text{mm}$ $d = 50\,\text{mm}$ **(modular)**	**62.3**	13.2	**YES**
25/01/2023	$e = 10\,\text{mm}$ $d = 30\,\text{mm}$	**66.8**	14.4	**YES**
23/02/2023	$e = 10\,\text{mm}$ $d = 10\,\text{mm}$	**67.8**	14.4	**YES**
27/02/2023	$e = 10\,\text{mm}$ $d = 50\,\text{mm}$	**68.7**	14.4	**YES**

The remaining 7 tests resulting in bursting disk rupture were conducted on the complete configuration of MADMAX with by-pass pipe: 2 of these tests were discarded due to non-net rupture of the bursting disk (failure cone fractured into multiple pieces causing a non-instantaneous complete opening of the exit section), 1 was discarded due to total malfunctioning of the data acquisition system (no sensor recorded the pressure signal), and another was discarded because the bursting pressure was below the range $[60, 80]$ bar. This leaves us with 3 valid experiments for this configuration. Four additional experiments were conducted on the complete configuration of MADMAX, but they did not result in the rupture of the bursting disk.

Table 2.2 provides an overview of all the 11 experiments conducted on this set-up. For each experiment, we indicate the date, the configuration of the orifice plates used, the bursting pressure, the thickness of the bursting disk, and whether the experiment was retained or discarded (with motivation).

As previously mentioned in Paragraph 2.2.2, we experienced a significant delay in the delivery of the new stock of bursting disks for the implementation of the new experimental campaign. This delay was due to the inability of the disk manufacturer to perform qualification tests on the new disks using their test bench. The reasons provided by the company were multiple, in order: replacement of a defective gasket on the test bench, breakdown of the device during testing, workplace injury to the maintenance worker operating the device.

It is important to note that these disks need to be qualified as they are initially intended as safety devices used in pressurized circuits to act as a kind of fuse in case of circuit overpressure. In our specific case, however, these disks are used solely for scientific research purposes.

It should be noted that these new disks cannot be automatically certified using the data from the disks used in the previous experimental campaign because they are manufactured from a different batch of graphite, which may produce different mechanical characteristics.

The use of alternative solutions was not possible because the section of our experimental device housing the bursting disk had been specifically modified to accommodate exactly that model of bursting disk with those precise dimensions. Any alternative solution would have required a modification of the device. Consequently, after months of delivery date delays, we (the MADMAX platform management team composed of the PhD candidate and the DYN laboratory experimental platform supervisor) proposed as a solution to the manufacturing company to carry out ourselves the qualification tests of the bursting disks directly on MADMAX.

The qualification test involves initially using a bursting disk with a thickness derived from tabulated data (which should ensure the desired bursting pressure within the tolerance range), gradually pressurizing it until it ruptures. If the bursting pressure falls within the desired range, the thickness is deemed valid; otherwise, further disks with different thicknesses are tested until the desired range is achieved.

In November 2023, the company provided us with an initial trial disk (non-certified) with a thickness of 14.5 mm for an initial test: two tests conducted with this disk (the first two in the Table 2.2) did not rupture before reaching 80 bar (the maximum limit set by our device). Subsequently, another five non-certified disks were sent to us with different thicknesses: 12.48, 13.36, 13.33, 12.99, and 13.45 mm. Tests on these five disks were conducted between December 14, 2023, and January 22, 2024, as described in the Table 2.2. Following the results of these tests, we communicated the data to the manufacturing company, which was then able to send us the stock of certified disks, all with a thickness of 13.49 mm, used in the last three experiments.

As can be seen from the table, a total of 9 experiments were conducted on Configuration 1, out of which only 5 resulted in the rupture of the bursting disk, with only one yielding exploitable results, that of December 14, 2023. Despite the success of this test, further tests were conducted on the same configuration simply in an attempt to achieve another valid test with a bursting pressure within the range $[63, 77]$ bar. Unfortunately, this objective was not met, and it was decided to consider the result of December 14, 2023, as definitive, as it still fell within the range $[60, 80]$ bar. Subsequently, by the end of February 2024, it was decided to move on to directly testing Configurations 2 and 3, which fortunately yielded immediately satisfactory results. The repeatability of these tests was not attempted simply due to a lack of time.

Table 2.2: History of MADMAX experiments with by-pass pipe.

Date (dd/mm/yyyy)	**Configuration**	P_{burst} (bar)	**Bursting disk** e (mm)	**Retained**
27/11/2023	1	-	14.5	NO (no burst till 78.3 bar)
28/11/2023	1	-	14.5 (same disk as 27/11/2023)	NO (no burst till 80.1 bar)
14/12/2023	**1**	**61.6**	12.48	**YES**
15/12/2023	1	≈ 67.0	13.36	NO (acquisition system total malfunctioning)
15/12/2023	1	77.5	13.33	NO (non-net rupture of the bursting disk)
11/01/2024	1	-	12.99	NO (cracked disk around 70 bar)
12/01/2024	1	-	13.45	NO (no burst till 77.6 bar)
22/01/2024	1	57.7	13.45 (same disk as 12/01/2024)	NO (P_{burst} too low)
23/01/2024	1	78.8	13.49	NO (non-net rupture of the bursting disk)
23/02/2024	**2**	**68.0**	13.49	**YES**
28/02/2024	**3**	**76.5**	13.49	**YES**

Duly equipped with the experimental tool which will provide reference measurements, we proceed to review in the next Chapter the key components of the simulation tool which will be used to numerically reproduce and thoroughly analyze the various MADMAX experiments.

Chapter 3

EUROPLEXUS: simulation framework and hierarchy of numerical models

In this chapter, we aim to present the general framework of the simulation tool (EUROPLEXUS software) used to perform the numerical simulations of the MADMAX experiments and to give an overview of the hierarchy of numerical models utilized in our simulations.

EUROPLEXUS (EPX) [6] is a simulation software tailored for analyzing fast transient phenomena involving structural-fluid interactions. It utilizes a conditionally stable explicit scheme for time integration and employs a fully nonlinear solving algorithm capable of handling geometric and material complexities.

In terms of *structural dynamics*, EPX offers specialized finite element models for analyzing shocks, impacts, explosions, and wave propagation phenomena. It supports various material models catering to both brittle and non-brittle materials.

For *fluid dynamics*, EPX features advanced finite element fluid models and finite volume schemes for multi-component, reactive, or multi-phase flows. It allows for the study of blast effects from explosions using methodologies like pressure-time curves and balloon models.

EPX excels in simulating *fluid-structure interaction* with techniques like direct coupling via Lagrange multipliers or fluid pressure forces transmitted to the structure. It supports Lagrangian, Eulerian, and mixed Arbitrary Lagrange Eulerian (ALE) mesh descriptions, with automatic rezoning algorithms to address mesh distortion issues. Furthermore, EPX offers an alternative FSI approach where the structural mesh is embedded in the fluid mesh, facilitating the modeling of severe structural damage without mesh rezoning.

The present chapter is organized as follows:

- we start by introducing the theoretical foundations of our models, introducing Fluid-Structure Interaction (FSI) concepts and outlining fluid and structural behavior models.
- Euler equations for the fluid under different descriptions (Lagrangian, Eulerian, ALE) are

presented. The discussion extends to the equation of state, detailing its application to determine fluid pressure, considering various fluid materials.

- The integration of fluid modeling with dynamic equilibrium equations for structures in FSI problems is explored, alongside the representation of specific elements using impedances and boundary conditions.
- Finally, spatial and temporal discretization methods are briefly reviewed, including Finite Element and Finite Volume methods, essential for numerical simulations in EUROPLEXUS.
- The chapter concludes with a presentation of the hierarchy of models used for conducting simulations, progressing from simplified 1D models to novel and more detailed 2D axisymmetric and 3D reference models, including FSI.

3.1 Theoretical foundations

In this section, we aim to furnish a theoretical framework underpinning the models integrated within EUROPLEXUS for scrutinizing the dynamics of pipeline circuits during transient accidental scenarios [59].

The term “Fluid-Structure Interaction” (FSI) is conventionally employed to depict the coupled behavior of fluid and structures, encompassing various singularities inherent in both fluidic (pressure drops, intricate components) and structural domains (junctions, supports).

In the following, we briefly present the models used to describe fluid and structure behaviors: Euler equations with ALE description for the fluid and dynamic equilibrium equations for the structure. Finally, we also briefly describe the boundary condition and impedance models used in this study.

3.1.1 Fluid-Structure Interaction

Fast transient fluid-structure interaction (FSI) calculations can be performed with the EUROPLEXUS code. The structural calculation is always based on a Lagrangian description (mesh deforming with the structure), whereas three different descriptions are possible for modelling the fluid, depending on the application: Lagrangian as for structures; Eulerian, the most commonly used for fluids, in which the mesh is fixed; and finally a mixed description called Arbitrary Lagrangian-Eulerian (ALE) suitable for the specific case of FSI, in which the mesh deforms arbitrarily and therefore its velocity can be different from that of the material points.

3.1.1.1 Fluid modelling

The fluid modeling [59] outlined below is based on the following assumptions:

- Compressible fluid
- Negligible heat conduction
- Negligible viscous forces compared to pressure and inertia forces

The model describing the fluid behavior consists of:

- Euler equations
  - Mass conservation equation
  - Momentum equation
  - Total energy conservation equation
- Equation of state for the fluid material

Three different descriptions are possible to describe the fluid:

1. **Lagrangian**: the most suitable description for calculating structures (if deformations are not excessive), as the reference domain (mesh) is attached to the material of the structure. It can also be applied to describe a fluid, with some interesting properties when discretized (*e.g.* no dissipation of wakes). The mesh nodes (or grid) follow the material points.

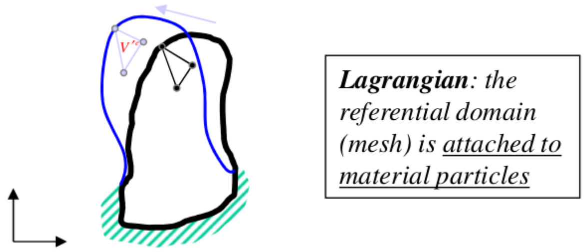

Figure 3.1: Scheme of the Lagrangian description. [2]

2. **Eulerian**: the most intuitive description for the fluid problem. The mesh remains fixed, allowing the calculation of the movement parameters (velocity, acceleration, etc.) of the material point at each instant.

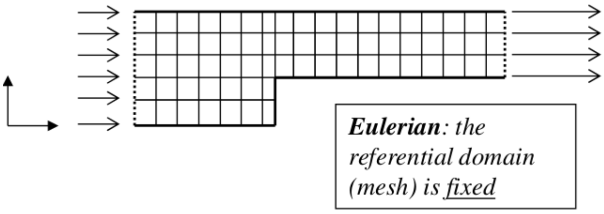

Figure 3.2: Scheme of the Eulerian description. [2]

3. **Arbitrary Lagrangian-Eulerian** (ALE): a mixed description suitable for problems with movements of both fluids and structures. The mesh deforms arbitrarily: the mesh velocity is arbitrary and can be different from the velocity of the material particles.

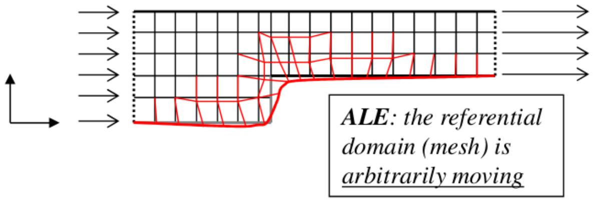

Figure 3.3: Scheme of the ALE description. [2]

As the general context we are dealing with is that of FSI, the Euler equations will be presented in the following for the ALE description. This description can then be adapted, through appropriate assumptions, to a Lagrangian or Eulerian description.

3.1.1.2 Structural analysis

The structural analysis in EUROPLEXUS is based on a Lagrangian description, which is suitable for deformable structures. This approach allows for a mesh that is attached to the structure, meaning it deforms simultaneously with the structure as it moves [59].

Once the momentum equation is formulated for the structure, it is discretized as follows:

- **Spatial Discretization**: Finite Element Method (FEM)
- **Temporal Discretization**: Centered Differences Method

The constraints are handled using the method of Lagrange multipliers. In EUROPLEXUS, the penalty method is also available.

3.1.2 Euler equations for fluids

The general assumptions adopted in this study for the fluid modeling are the following ones: compressible fluid; heat conduction and viscous forces negligible. These simplifications can be justified by the nature and characteristic time of the phenomenon we aim to observe. We analyze a phenomenon occurring at room temperature in a confined space, where there are no significant temperature variations, allowing us to disregard thermal effects. Additionally, we are dealing with a very rapid transient, and we are particularly interested in observing the first $10 \div 20$ ms of the transient, during which the fluid does not move sufficiently to exhibit significant viscous phenomena. The primary objective of this study is to observe the acoustic phenomena generated by the abrupt depressurization of the circuit, for which the chosen model proves to be quite adequate.

The governing Euler Equations are presented below in integral form using the ALE description. Figure 3.4 shows the fluid domain Φ, in which $V(t)$ is the control volume, $S(t)$ is the control surface, $\underline{n}$ is the unit vector normal to the control surface, $\underline{v}$ is the velocity of the fluid (i.e. of its particles), $\underline{w}$ is the velocity of the control volume interface.

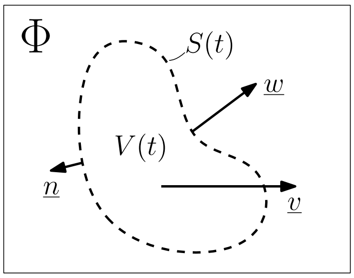

Figure 3.4: Fluid domain.

Based on the relationship between $\underline{v}$ and $\underline{w}$, considering a function $f(\underline{x}, t)$ scalar or vector-valued defined on the domain Φ, and using the notation adopted by Letellier (see [60] for details on the notation), we can distinguish the three descriptions as follows:

- If $\boxed{\underline{w} = \text{arbitrary}}$, we refer to it as the **ALE description**.

  We can write
  $$\frac{d}{dt} f(\underline{x}, t) = \frac{\delta}{\delta t} f(\underline{x}, t) + \frac{\partial f(\underline{x}, t)}{\partial \underline{x}} \cdot (\underline{v} - \underline{w}) \tag{3.1}$$
  where d/dt is the derivative with respect to time in the direction of velocity $\underline{v}$, and $\delta/\delta t$ is the derivative with respect to time in the direction of the velocity $\underline{w}$ of the control volume interface.

- If $\boxed{\underline{w} = \underline{v}}$ (the velocity of the control volume coincides with the material velocity), it is referred to as the **Lagrangian description**.

  We can write
  $$\frac{d}{dt} f(\underline{x}, t) = \frac{\partial f(\underline{x}, t)}{\partial t} \tag{3.2}$$

- If $\boxed{\underline{w} = 0}$ (the grid is fixed), it is referred to as the **Eulerian description**.

  We can write
  $$\frac{d}{dt} f(\underline{x}, t) = \frac{\partial f(\underline{x}, t)}{\partial t} + \frac{\partial f(\underline{x}, t)}{\partial \underline{x}} \cdot \underline{v} \tag{3.3}$$

3.1.2.1 Mass Conservation Equation

If we consider the volume $V(t)$ that follows the movement of material particles, the mass M is conserved within the volume, which can be expressed as:

$$\frac{dM}{dt} = \frac{d}{dt} \int_{V(t)} \rho(\underline{x}, t)\, dV = 0 \tag{3.4}$$

Consequently, according to equation (3.1), we deduce:

$$\frac{\delta}{\delta t} \int_{V(t)} \rho(\underline{x}, t)\, dV = \oint_{S(t)} \rho(\underline{x}, t)(\underline{w} - \underline{v}) \cdot \underline{n}\, dS \tag{3.5}$$

where $\rho(\underline{x}, t)$ is the fluid density.

3.1.2.2 Momentum Equation

We consider that the variation of momentum of the volume $V(t)$ is equal to the sum of *volumetric forces* and *surface forces*. Therefore, we can write:

$$\frac{d\underline{Q}}{dt} = \frac{d}{dt} \int_{V(t)} \rho(\underline{x}, t)\underline{v}\, dV = \int_{V(t)} \rho(\underline{x}, t)\underline{g}\, dV + \oint_{S(t)} \underline{\underline{\sigma}} \cdot \underline{n}\, dV \tag{3.6}$$

where $\underline{Q}$ is the momentum of the control volume, $\underline{\underline{\sigma}}$ is the stress tensor, $\underline{g}$ is the gravitational field.

We then deduce, still according to equation (3.1), that:

$$\frac{\delta}{\delta t} \int_{V(t)} \rho(\underline{x}, t)\underline{v}\, dV + \oint_{S(t)} [\rho(\underline{x}, t)\underline{v} \otimes (\underline{w} - \underline{v})] \cdot \underline{n}\, dS = \int_{V(t)} \rho(\underline{x}, t)\underline{g}\, dV + \oint_{S(t)} \underline{\underline{\sigma}} \cdot \underline{n}\, dV \tag{3.7}$$

Now, we aim to obtain a **variational formulation** associated with the conservation of momentum. To do this, we start from the fundamental equation of dynamics expressed in the Lagrangian formalism:

$$\nabla \cdot \underline{\underline{\sigma}} + \rho \underline{g} = \rho(\underline{x}, t)\frac{d\underline{v}}{dt} \tag{3.8}$$

where $(\nabla \cdot)$ is the divergence operator.

If we now apply the principle of virtual power for a virtual velocity field $\underline{v}^*$ (by multiplying the above equation by $\underline{v}^*$ and integrating it over the volume V), we obtain:

$$\int_V (\nabla \cdot \underline{\underline{\sigma}}) \cdot \underline{v}^* \, dV + \int_V \rho(\underline{x}, t)\underline{g} \cdot \underline{v}^* \, dV = \int_V \rho(\underline{x}, t)\frac{d\underline{v}}{dt} \cdot \underline{v}^* \, dV \tag{3.9}$$

Using equation (3.1), we obtain:

$$\int_V (\nabla \cdot \underline{\underline{\sigma}}) \cdot \underline{v}^* \, dV + \int_V \rho(\underline{x}, t)\underline{g} \cdot \underline{v}^* \, dV = \int_V \rho(\underline{x}, t)\frac{\delta \underline{v}}{\delta t} \cdot \underline{v}^* \, dV - \int_V \rho(\underline{x}, t)\left((\underline{w} - \underline{v}) \cdot \frac{\partial \underline{v}}{\partial \underline{x}}\right) \cdot \underline{v}^* \, dV \tag{3.10}$$

By integrating by parts, we obtain:

$$\int_V (\nabla \cdot \underline{\underline{\sigma}}) \cdot \underline{v}^* \, dV = \oint_S \underline{\underline{\sigma}} \cdot \underline{n} \cdot \underline{v}^* \, dS - \int_V \underline{\underline{\sigma}} : \frac{\partial \underline{v}^*}{\partial \underline{x}} \, dV \tag{3.11}$$

where the operator $\ll : \gg$ represents a double contraction product.

Finally:

$$\begin{aligned} \int_V \rho(\underline{x}, t)\frac{\delta \underline{v}}{\delta t} \cdot \underline{v}^* \, dV = &\int_V \rho(\underline{x}, t)\underline{g} \cdot \underline{v}^* \, dV + \oint_S \underline{\underline{\sigma}} \cdot \underline{n} \cdot \underline{v}^* \, dS - \int_V \underline{\underline{\sigma}} : \frac{\partial \underline{v}^*}{\partial \underline{x}} \, dV \\ &+ \int_V \rho(\underline{x}, t)\left((\underline{w} - \underline{v}) \cdot \frac{\partial \underline{v}}{\partial \underline{x}}\right) \cdot \underline{v}^* \, dV \end{aligned} \tag{3.12}$$

3.1.2.3 Energy Conservation Equation

Considering the control volume $V(t)$, the variation of the total energy per unit mass e (= specific internal energy i + specific kinetic energy) is equal to the work of external forces. Therefore, we can write:

$$\frac{dE}{dt} = \frac{d}{dt}\int_{V(t)} \rho(\underline{x}, t)e \, dV = \int_{V(t)} \rho(\underline{x}, t)\underline{g} \cdot \underline{v} \, dV - \oint_{S(t)} p\underline{v} \cdot \underline{n} \, dS \tag{3.13}$$

where E and e are respectively the total energy and the specific total energy of the control volume.

Using equation (3.1), we obtain:

$$\frac{\delta}{\delta t}\int_{V(t)} \rho(\underline{x}, t)e \, dV = \oint_{S(t)} \rho(\underline{x}, t)e(\underline{w} - \underline{v}) \cdot \underline{n} \, dS + \int_{V(t)} \rho(\underline{x}, t)\underline{g} \cdot \underline{v} \, dV - \oint_{S(t)} p\underline{v} \cdot \underline{n} \, dS \tag{3.14}$$

For a compressible fluid, the specific total energy e is:

$$e = i + \frac{1}{2}v^2 \tag{3.15}$$

where i is the specific internal energy.

Equation (3.14) can then be rewritten as follows:

$$\begin{aligned}\frac{\delta}{\delta t}\int_{V(t)} \rho(\underline{x},t)\left(i+\frac{1}{2}v^2\right)dV = \oint_{S(t)} \rho(\underline{x},t)\left(i+\frac{1}{2}v^2\right)(\underline{w}-\underline{v})\cdot\underline{n}\,dS + \int_{V(t)} \rho(\underline{x},t)\underline{g}\cdot\underline{v}\,dV \\ - \oint_{S(t)} p\underline{v}\cdot\underline{n}\,dS\end{aligned} \tag{3.16}$$

We can equivalently write the previous equation in terms of the internal energy I of the control volume (valid if the flow is steady, meaning there are no shocks [61]):

$$\frac{\delta I}{\delta t} = \frac{\delta}{\delta t}\int_{V(t)} \rho(\underline{x},t)i\,dV = \oint_{S(t)} \rho(\underline{x},t)i(\underline{w}-\underline{v})\cdot\underline{n}\,dS - \oint_{S(t)} p\underline{v}\cdot\underline{n}\,dS \tag{3.17}$$

3.1.2.4 Equation of state

The pressure p can be determined via an equation of state as a function of the density ρ and the specific internal energy i:

$$p = p(\rho, i) \tag{3.18}$$

In the present study two fluid materials are involved: water and nitrogen.

In the EUROPLEXUS calculations, water can be described using the FLUID model that enables a fluid (liquid-like) behavior for continuous elements as an input option [62]. The fluid (isothermal) can be perfect (non-viscous) or viscous. The expression used to compute the absolute pressure p in the fluid is:

$$p = p(\rho) = p_{\text{ini}} + (\rho - \rho_{\text{ini}})c^2 \tag{3.19}$$

where p_{ini} is the fluid pressure in the initial state, ρ is the current density, ρ_{ini} is the initial density and c is the sound speed, which is considered constant. An absolute minimum pressure p_{min} attainable by the fluid must be declared (by default, $p_{\text{min}} = 0$), such that $p_{\text{min}} \leq p_{\text{ini}}$. If it is verified during the simulation that $p < p_{\text{min}}$ then $p = p_{\text{min}}$ is automatically imposed (constant absolute pressure imposed to the fluid by the calculation in the event of cavitation) [62]. In this model, equation (3.17) is thus decoupled from equations (3.5) and (3.7), the pressure being calculated via the barotropic hypothesis (3.19).

To more accurately consider water vaporization and possible cavitation, it is possible to use another model to represent the fluid, namely the WATER model [62], which uses tabulated Equations of State (EoS) [63] to calculate the properties of water. In this work, this model is particularly used to perform FSI calculations.

To represent nitrogen instead, the GAZP (perfect gas) model [62] is used and its absolute pressure p is calculated using the perfect gas formulation:

$$p = \rho(\gamma - 1)i \tag{3.20}$$

where γ is a constant and is the ratio between the specific heat at constant pressure c_p and the specific heat at constant volume c_v.

Finally, it should be pointed out that in our calculations, the fluids in the accumulators are always modeled by means of an ALE description: ALE-liquid and an ALE-gas separated by a Lagrangian interface (representing the piston, $\underline{w} = \underline{v}$). The water in the rest of the of the pipes is also modeled with ALE description in the case of the WATER model for FSI calculations, while a purely Eulerian description (ALE description but with $\underline{w} = 0$) is used in the case of FLUID model calculations with fixed structures (non-deformable pipes).

3.1.3 Dynamic Equilibrium for Structures

In EUROPLEXUS, to solve a FSI problem, the Euler equations for the fluid described earlier are coupled with the dynamic equilibrium equation for the structures [9; 64].

The dynamic equilibrium for structures can be described by the equation [9]:

$$\rho(\underline{x}, t)\frac{\delta^2 \underline{q}}{\delta t^2} + \nabla \cdot \left\{\underline{\underline{\sigma}}\left[\underline{\varepsilon}\left(\underline{q}\right)\right]\right\} = \underline{f}^{\mathrm{str}}_{\mathrm{vol}} \tag{3.21}$$

where $\rho(\underline{x}, t)$ represents the local density for structures, $\underline{q}$ is the structural displacement, $\underline{\underline{\sigma}}$ is the structural Cauchy stress tensor, $\underline{\varepsilon}$ is the structural Almansi-Euler strain tensor and $\underline{f}^{\mathrm{str}}_{\mathrm{vol}}$ are the structural body forces.

In our work, to represent the structures (specifically, the steel piping), we use a solid material model called LINE (see EPX User's manual [62]), which allows us to represent a solid material with linear elastic behavior. EPX numerically handles this model using the Finite Element Method (FEM) with a Lagrangian description. We then associate the model with the actual mechanical properties of the material under study (for steel: density $\rho = 7800\,\mathrm{kg/m^3}$, Young's modulus $E = 200\,\mathrm{GPa}$, and Poisson's coefficient $\nu = 0.3$).

3.1.4 Boundary conditions and impedances

To simulate the MADMAX experiment, in addition to the behavior of fluids and structures, it is necessary to represent the presence of two specific elements in particular:

- the bursting disk,
- the geometric obstacles (the sudden changes in cross section, such as the presence of the orifice plate).

These elements can be represented by a suitable directive called IMPEDANCES that enables to input boundary conditions or impedance conditions.

Bursting disk It can be represented by an impedance called MEMBRANE, which introduces a safety membrane to the extremity of a pipeline (1D), or on the axis of an axisymmetric reservoir (2D). The membrane rupture occurs either when the pressure in the neighboring element exceeds the rupture pressure, or when the time exceeds a prescribed value [62]. In the calculations, the inputs provided are the initial pressure p_{ini} (equal to the pressure at which bursting disk rupture occurs), the final pressure p_{end} (atmospheric pressure) and the time constant ξ of the exponential function that drives the initial pressure to the final pressure, shown in Eq. (3.22). The time constant used was calibrated according to the experiments in [1].

$$p_{\text{memb}}(t) = p_{\text{ini}} e^{-\frac{t}{\xi}} + p_{\text{end}} \left(1 - e^{-\frac{t}{\xi}}\right) \qquad \text{with} \quad 0 \leq t \leq \xi \tag{3.22}$$

Orifice plate Geometric obstacles can be represented by means of an impedance called GRID, which enables to model the influence of grids or rigid perforated plates on a fluid [62]. Initially, under the acoustic assumption (non-linear entrainment terms and viscosity terms are neglected), it can be shown that the pressure difference between the two sides of the obstacle, Δp, is related to the acceleration effect of the fluid at the hole of the orifice plate [15]. This effect can be represented by means of an equivalent length L_{eq} such that:

$$\Delta p = -\frac{L_{\text{eq}}}{s} \dot{q} \tag{3.23}$$

where s is the cross-sectional area of the orifice and $\dot{q} = dq/dt$ where q is the mass flow rate.

Considering, in addition, the effects of drag and viscosity and assuming that the methods used for permanent flows at a singularity still apply, we can write (superposition of the effects):

$$\Delta p = -\frac{L_{\text{eq}}}{s} \dot{q} - \frac{1}{2} k \frac{q^2}{\rho_0 S_{\text{t}}^2} \tag{3.24}$$

where k is the head loss coefficient, ρ_0 is the average density of the fluid, S_{t} is the cross-sectional area of the pipe.

In summary, it can be said that the modeling of the singularity consists of two terms: an inertial acoustic term and a classic head loss term. In the calculations, we must provide as input to the model, in addition to the fluid density and the speed of sound, two fundamental parameters: the characteristic time τ and the head loss coefficient k.

The characteristic time τ can be computed, in the case of a perforated plate, through an analytical formulation [14]:

$$\tau = \frac{S_{\text{t}}}{s} \frac{L_{\text{eq}}}{2c} \tag{3.25}$$

where L_{eq} can be calculated using

$$L_{\text{eq}} = 2 \left[0.85 - \frac{r}{R} + 0.15 \left(\frac{r}{R}\right)^2\right] r + e \tag{3.26}$$

where r is the radius of the orifice plate hole, R is the inner radius of the pipe and e is the thickness of the orifice plate (see Fig. 3.5). In the case of a single cross-sectional change (sudden enlargement or shrinkage), L_{eq} reduces to:

$$L_{\text{eq}} = \left[0.85 - \frac{r}{R} + 0.15 \left(\frac{r}{R}\right)^2\right] r \tag{3.27}$$

The head loss coefficient k can be obtained from Idel'Cik correlations [12] for an orifice plate or for single cross-sectional changes.

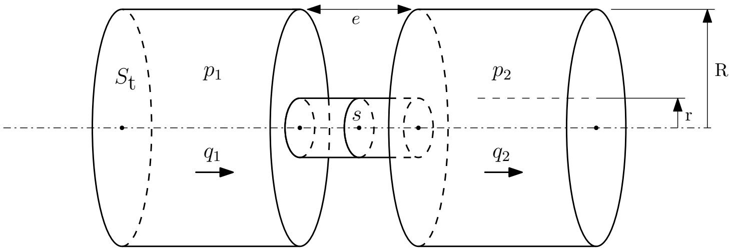

Figure 3.5: Orifice plate scheme.

The reader is referred to the Appendix C for more details on numerical implementation of the impedance GRID in EUROPLEXUS.

3.2 Numerical models: spatial and temporal discretization

As already mentioned, different approaches are available in EPX to perform the spatial discretization of the FSI problem: the Finite Element Method (FEM), used mainly for the structural component, but also suitable for fluids, and the Finite Volume Method (FVM); in particular we will see here the Cell Centered Finite Volume (CCFV) formulation, used especially for the treatment of the fluid component.

Time-discretization is operated using a second order explicit central differences scheme for the FEM calculations, while a second order explicit Runge-Kutta scheme is used for the FVM simulations.

In both FEM and FVM, the domain is divided into elements connected by nodes. In FEM, certain quantities (such as density, internal energy, pressure, etc.) are defined at the mesh Gauss points within the elements (in our FE simulations, we use elements with a single Gauss point), while others (typically velocity, acceleration, etc.) are defined at the nodes. Conversely, in FVM, all quantities are defined at the Finite Volume centroid. For a schematic view, refer to Fig. 3.6.

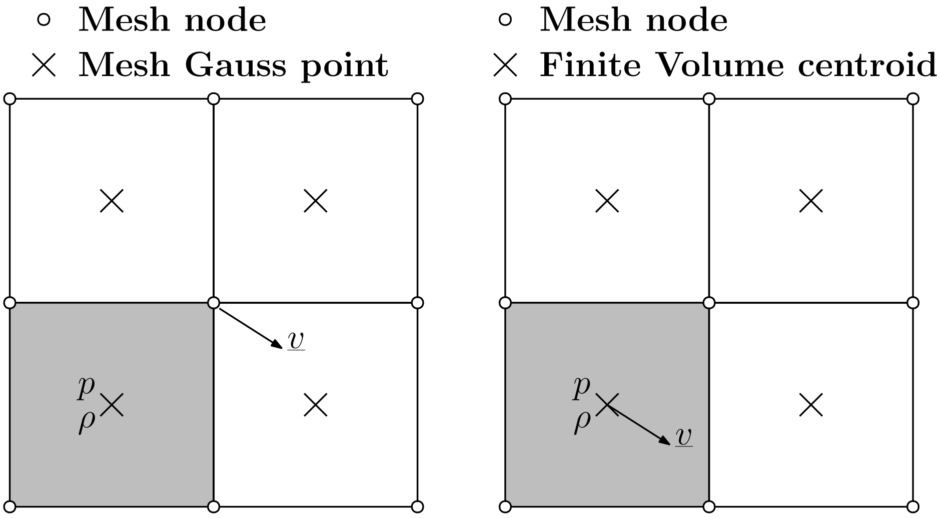

(a) FE mesh.

(b) CCFV mesh.

Figure 3.6: Finite Element and Cell Centered Finite Volume mesh schemes.

More details on numerical modeling can be found in the Appendices of the manuscript:

- Appendix A provides more information on the Finite Element Method (FEM) such as implemented in EUROPLEXUS,
- Appendix B provides more information on the Finite Volume Method (FVM) such as implemented in EUROPLEXUS,
- Appendix C details the numerical implementation of the IMPEDANCE GRID model used in the simplified 1D approach to describe the orifice(s) implemented in the core pipe or/and in the by-pass pipe of the MADMAX platform.

3.3 Models used in our simulations

This section aims to succinctly provide the hierarchy of numerical models used in this PhD thesis for conducting simulations of the experimental configurations presented in Chapter 2.

We can first distinguish between two main set-ups of our experiment:

1. **MADMAX simplified configuration:** experimental set-up without by-pass pipe, with modular orifice plate;
2. **MADMAX complete configuration:** experimental set-up with by-pass pipe and multiple orifice plates.

For each of the two set-ups, simulations are conducted using 1D models, referred to as **Simplified models**, and more complex 2D axisymmetric or 3D models, referred to as **Reference models**. It is important to remember that the primary objective of this work is to assess the relevance and accuracy of the simplified 1D models in reproducing the rapid transient phenomenon under investigation. To achieve this, we rely on a dual comparison for these 1D models:

- with experimental results, which include the full physics and constitute an absolute reference;
- and with the reference models, which share the same physical assumptions (inviscid compressible flows) and constitue a numerical reference.

In Table 3.1, we provide a summary of the models used for simulations of the simplified configuration of MADMAX. A simplified 1D model utilizing the IMPEDANCE GRID (introduced in Paragraph 3.1.4) to represent the presence of an obstacle (the orifice plate) in the pipeline is employed. This model will be detailed in Paragraph 4.2.2 in the subsequent chapter. Two reference models are utilized in this case: a 2D axisymmetric model with fixed structures and a 2D axisymmetric model with Fluid-Structure Interaction (FSI). These two models will be detailed upon in Paragraphs 4.2.1 and 4.4.2, respectively. For the 1D model and the 2D axisymmetric model with fixed structures, we use the Finite Element Method (FEM) for spatial discretization, while for the 2D axisymmetric model with Fluid-Structure Interaction (FSI), we employ a mixed approach, using the Finite Volume Method (FVM) for the fluid and FEM for the structure. The reasons for these choices are as follows: for the 1D model, EUROPLEXUS provides an IMPEDANCE GRID model only with a FEM discretization, making the choice of FEM obligatory in this case; the 2D axisymmetric model with fixed structures was initially chosen as the reference model for comparison with the 1D model, and for consistency, FEM was initially selected. The FVM is also available in EPX for the 2D axisymmetric model, and it was tested to observe differences with FEM, but the results were very similar, so it was decided to keep the FEM results as the reference.

Table 3.1: Hierarchy of numerical models used for the simulations of MADMAX simplified configuration without by-pass pipe.

Model	**Materials**	**Description**	**Numerical method**
1D with impedances **(simplified)**	FLUID	Eulerian	FEM
	FLUID (accumulators)	ALE	FEM
	GAZP (accumulators)	ALE	FEM
2D axisymmetric **(reference)**	FLUID	Eulerian	FEM
	FLUID (accumulators)	ALE	FEM
	GAZP (accumulators)	ALE	FEM
2D axisymmetric + FSI **(reference)**	WATER	ALE	FVM
	WATER (accumulators)	ALE	FVM
	GAZP (accumulators)	ALE	FVM
	Linear elastic (steel pipe)	Lagrangian	FEM

Table 3.2 provides a summary of the models used for simulations of the complete configuration of MADMAX with by-pass pipe. This time, two simplified 1D models are employed, one with fixed structures and the other incorporating Fluid-Structure Interaction (FSI), as presented together in Paragraph 5.2.3. Both utilize the IMPEDANCE GRID (introduced in Section 3.1.4) to represent the presence of the orifice plates in the pipeline. Again, two reference models are utilized in this case, but with the installation of the by-pass pipe, the axisymmetric assumption is no longer valid. Therefore, we opted for 3D models: one with fixed structures and one with FSI. These two models will be reviewed together in Section 5.2.2. In this case, we consistently employ the Finite Element Method (FEM) for the 1D models for the same reasons described earlier for the simplified configuration. For the 3D model with fixed structures and the one with FSI, it was decided upfront to adopt the Finite Volume Method (FVM) and the mixed

FVM/FEM approach, respectively.

Table 3.2: Hierarchy of numerical models used for the simulations of MADMAX complete configuration with by-pass pipe.

Model	Materials	Description	Numerical method
1D with impedances **(simplified)**	FLUID	Eulerian	FEM
	FLUID (accumulators)	ALE	FEM
	GAZP (accumulators)	ALE	FEM
1D with impedances + FSI **(simplified)**	WATER	ALE	FEM
	WATER (accumulators)	ALE	FEM
	GAZP (accumulators)	ALE	FEM
3D **(reference)**	FLUID	Eulerian	FVM
	FLUID (accumulators)	ALE	FVM
	GAZP (accumulators)	ALE	FVM
3D + FSI **(reference)**	WATER	ALE	FVM
	WATER (accumulators)	ALE	FVM
	GAZP (accumulators)	ALE	FVM
	Linear elastic (steel pipe)	Lagrangian	FEM

3.3.1 Details of numerical resolution

FEM The following resolution schemes are used for simulations using the Finite Element Method:

- Upwind scheme in space for the mass and energy conservation equations,
- Second order in space for the momentum equation,

- Second order explicit central differences scheme for time integration.

FVM The following resolution schemes are used for simulations using the Finite Volume Method:

- Second order in space,
- Second order explicit Runge-Kutta scheme for time integration,
- HLLC (Harten–Lax–van Leer Contact) Riemann solver for the calculation of numerical fluxes at interfaces between volumes,
- Green-Gauss reconstruction of the primitive variables (density, velocity, internal energy per unit mass, mass fraction) at the inter-volume interfaces starting from the values at the centroids and from the (spatial) gradients at the centroids,
- Limitation of Dubois for the reconstruction of the various quantities to adjust the value of the gradient in order to ensure that the reconstructed values at the interfaces do not violate some conditions.

FSI The coupling between the fluid (ALE and treated with FVM) and the structure (Lagrangian and treated with FEM) is realized by an FSI algorithm with the following characteristics:

- Basic algorithm suitable for large motion and large deformation of structures (but moderate rotations), but only provided these do not fail,
- Conforming spatial discretization for Fluid-Structure meshes (meshes at the interface between fluid and structure are perfectly coincident),
- Direct application of fluid pressure forces to the structure; the structure motion provides weak feedback on fluid. The two calculations are performed in a staggered approach (non-monolithic approach).

Chapter 4

MADMAX without by-pass pipe, with single modular orifice plate

This chapter discusses numerical and experimental results regarding the most simplified configuration of the MADMAX experiment which has been presented in Chapter 2, that without a by-pass pipe and with a single orifice plate (with the possibility of changing its diameter and thickness to perform a parametric study) located in the middle of the core pipe. The numerical simulations are performed using EUROPLEXUS and the hierarchy of models described in Chapter 3. The purpose, as already anticipated, is to evaluate the predictive capabilities of EUROPLEXUS regarding the passage of a rarefaction wave through a single obstacle as simple as an orifice plate. As anticipated in the introductory chapter, compared with previous works, particularly that of Faucher et al. (2012) [1], we extend the study to six different orifice plate configurations to perform a sensitivity analysis on the geometric characteristics of the obstacle (thickness and diameter). In addition, the simulation/experiment comparison are enriched by new 2D axisymmetric calculations and consideration of Fluid-Structure Interaction (FSI).

4.1 Experimental campaign

In the following, the results of the experimental campaign carried out by myself with the assistance of the laboratory technicians and the person in charge of the experimental platform in 2022/2023 with the six different geometric configurations of the orifice plate mentioned in Subsection 2.2.1 are presented and analyzed. Each experiment is characterized not only by the different geometric configuration of the orifice plate, but also by a specific bursting pressure P_{burst} of the bursting disk (see Table 4.1).

Table 4.1: Experimental bursting pressure for MADMAX simplified set-up.

EXP	$e = 10\,\text{mm}$ $d = 10\,\text{mm}$	$e = 10\,\text{mm}$ $d = 30\,\text{mm}$	$e = 10\,\text{mm}$ $d = 50\,\text{mm}$	$e = 50\,\text{mm}$ $d = 10\,\text{mm}$	$e = 50\,\text{mm}$ $d = 30\,\text{mm}$	$e = 50\,\text{mm}$ $d = 50\,\text{mm}$
P_{burst} (bar)	**67.8**	**66.8**	**68.7**	**73.3**	**74.3**	**62.3**

From the factory data, each bursting disk is designed to open at 70 bar ± 10%, depending on manufacturing tolerances and the environmental conditions of each experiment (actual thickness of the disk, speed at which the device is pressurized, etc.). It can be observed from Table 4.1 the range [63, 77] bar is indeed almost the one covered in the experimental campaign (see Paragraph 2.2.3 for details).

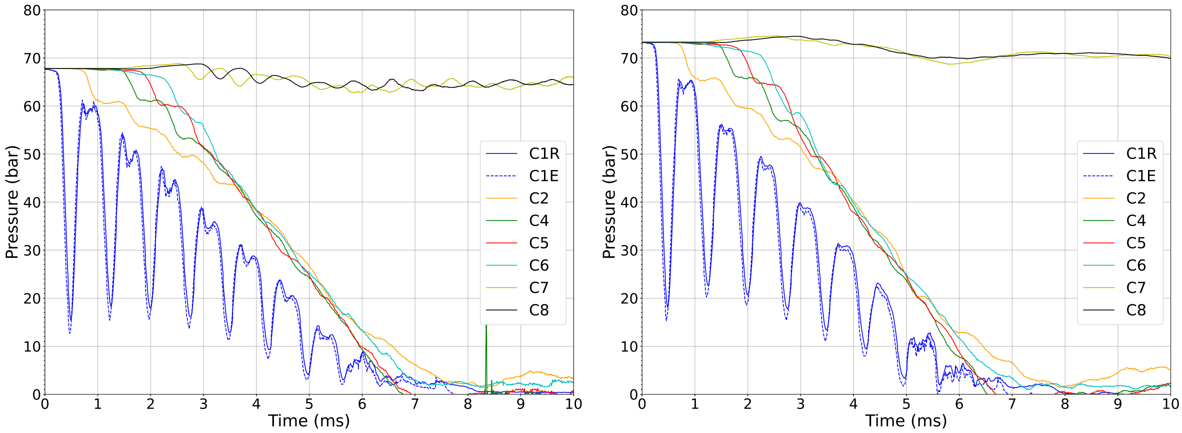

(a) $e = 10\,\text{mm},\ d = 10\,\text{mm}$ (b) $e = 50\,\text{mm},\ d = 10\,\text{mm}$

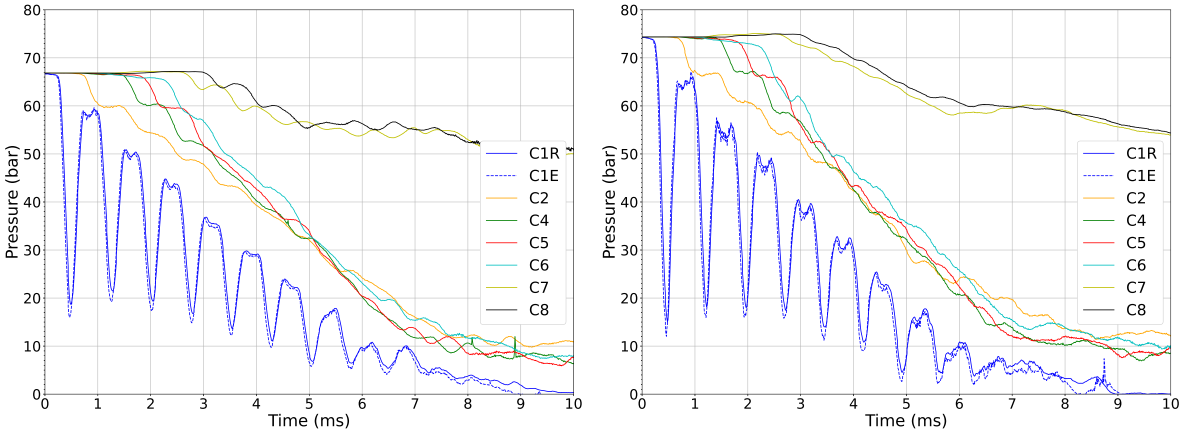

(c) $e = 10\,\text{mm},\ d = 30\,\text{mm}$ (d) $e = 50\,\text{mm},\ d = 30\,\text{mm}$

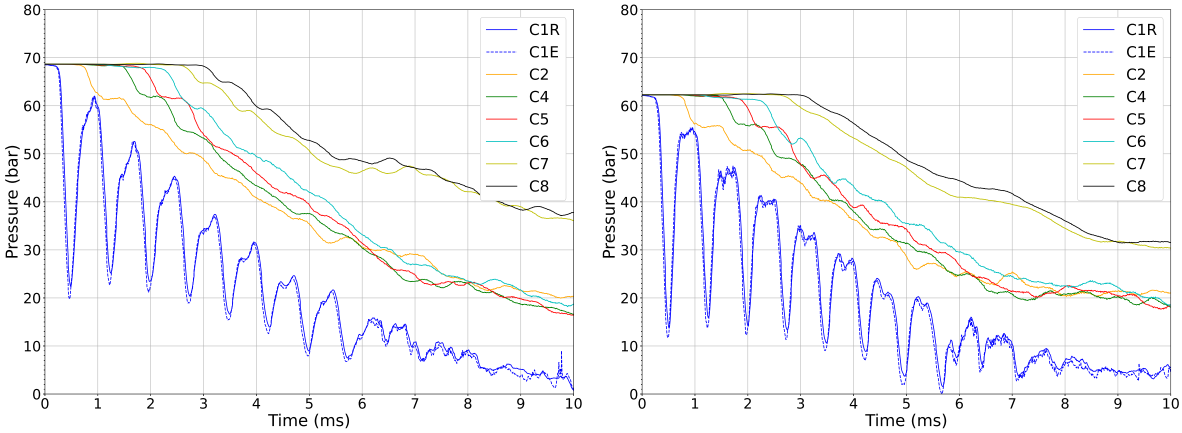

(e) $e = 10\,\text{mm},\ d = 50\,\text{mm}$ (f) $e = 50\,\text{mm},\ d = 50\,\text{mm}$

Figure 4.1: Experimental pressure evolution for all experiments and for all sensors.

Fig. 4.1 shows the pressure evolution for all eight sensors positioned along the device (see Fig. 2.4) during the first 10 ms after opening the bursting disk for all the experiments. At the opening of the bursting disk a rarefaction wave is produced and propagates upwards in the junction pipe; at the moment it reaches the connection with the core pipe the wave is partly reflected back and partly transmitted into the core pipe depending on the ratio of the cross sections of the two pipes.

As the junction pipe is relatively short, multiple transmissions/reflections can therefore be observed in the 10 ms of observation, as can clearly be seen from the C1R/C1E sensors in Fig. 4.1. The signal is consequently cascaded to the sensors in the lower part of the core pipe (C2, C4, C5 and C6), the measured pressure of which decreases following a sequence of steps. Before reaching sensors C7 and C8, the signal encounters the orifice plate from which it is partly reflected back and partly transmitted through the orifice. The signal transmitted through the orifice plate to sensors C7 and C8 is influenced by the geometry of the obstacle. It can be seen that the pressure also decreases for these two sensors, but less significantly than the sensors at the upstream (with respect to the direction of propagation of the rarefaction wave) of the orifice plate.

It can be qualitatively deduced that this difference between the pressure signals for sensors upstream and downstream of the orifice plate grows with a factor inversely proportional to the diameter of the hole. By comparing the graphs in Fig. 4.1, the influence of varying orifice plate thickness on wave propagation can also be deduced: for the same orifice diameter we can deduce that by decreasing the thickness of the orifice plate the pressure signal is transmitted more effectively and is less diffused when crossing the obstacle. In fact we can clearly see on the C7 and C8 sensors the characteristic pressure steps of the sensors upstream of the orifice plate. On the other hand, the thickness e does not significantly affect the pressure difference between the two sides of the obstacle.

4.2 Numerical simulations

Experiments are simulated using EUROPLEXUS with two different models of varying complexity and computational cost:

- a 2D axisymmetric reference model with the obstacle fully described,
- a 1D model with the obstacle replaced by suitable impedance relations (see the description provided in Paragraph 3.1.4)

All calculations are performed using the FLUID model (with fixed structures) described in Paragraph 3.1.2.4.

For both models, the time constant involved in the aforementioned boundary condition which drives the opening of the bursting disk (IMPEDANCE MEMBRANE, see Paragraph 3.1.4) is equal to 0.12 ms and it was calibrated according to the experiments in [1] (calibration also confirmed by the results of our experimental campaign). The value used for the speed of sound in the fluid c takes into account the flexibility of the pipes, by means of the Allievi correction [65], as well as the presence of gas dissolved in water (Wood formula [66; 67]). The average value observed experimentally for c is 1310 m/s. In order to verify the accuracy of the experimental value, c is calculated by Allievi's correction that takes into account the geometric (diameter and thickness) and mechanical (density $\rho = 7800\,\mathrm{kg/m^3}$, Young's modulus $E = 200\,\mathrm{GPa}$ and Poisson's coefficient $\nu = 0.3$) characteristics of the steel pipe. If we do not initially consider the presence of dissolved gases in water (thus considering a water density of 1000 kg/m^3 and Bulk modulus of 2.231 GPa), we obtain a value of c equal to 1335 m/s, already very close to the experimental value. In order to precisely fit the experimental measurements, we assume a very small volume fraction of gas (air) dissolved in water of approximately 2.6×10^{-5} (air volume/water volume), which allows us to calculate, via Wood's formula, the mean density (999.974 kg/m^3) and mean Bulk modulus (2.128 GPa) of the water/air mixture to be used in Allievi's correction, thus obtaining a value of c equal to 1310 m/s.

Simulations are performed for all six geometric configurations using both models in which the experimental device is represented in a simplified way, in particular by neglecting the presence of the two connecting elbows between the core pipe and the by-pass pipe. In each simulation, the initial fluid pressure is set equal to the experimental bursting pressures P_{burst} summarized in Table 4.1 and its initial density is set to 1000 kg/m^3. The initial pressure of the gas in the accumulator is also set equal to P_{burst} as it is in equilibrium with the fluid.

4.2.1 2D axisymmetric calculations

A schematic of the mesh used for the 2D axisymmetric calculations is displayed in Fig. 4.3. The mesh used is composed of quadrilateral elements of different sizes depending on the area. The first region of quasi-uniform mesh size corresponds radially to the orifice diameter while the second region of (larger) quasi-uniform mesh size corresponds to the core of the pipe. Both regions are connected through a geometric progression for the radial mesh size, with a factor close to 1.1.

The pressure sensors shown in Figure 4.3 correspond to the mesh elements that best reproduce the position of the actual sensors mounted on the experimental device. The real sensors have a diameter of about 10 mm, and we approximate its vertical position (along y in the Figure 4.3) with that of its axis of symmetry: the numerical sensor corresponds to the single mesh cell that is closest to this position. For the mesh chosen to perform the simulations after convergence analysis (see 1 mm mesh in the Table 4.2) such a cell is 10 times thinner (1 mm side) than the sensor, as shown in Figure 4.2.

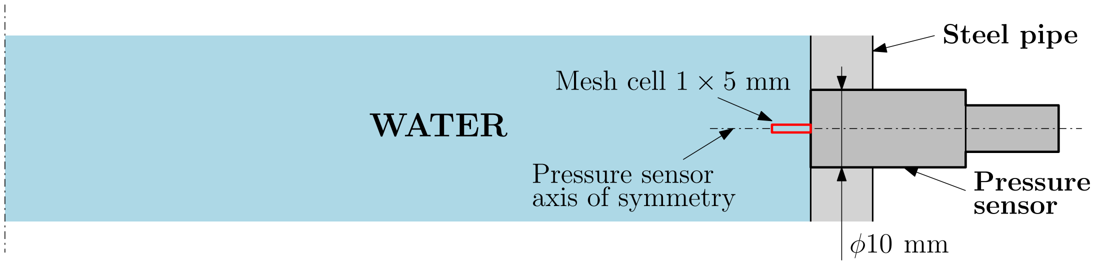

Figure 4.2: Actual pressure sensor size and position compared with the corresponding mesh cell representing the pressure sensor in the 2D axisymmetric simulations.

Due to the nature of the 2D axisymmetric mesh, it is impossible to faithfully reproduce the topmost zone of the device, where the core pipe and the accumulators are connected (see Figure 2.4). This area has therefore been reproduced in a simplified manner (e.g. the two accumulators are reduced to a single, larger accumulator), as shown in Fig. 4.3, while maintaining the actual volumes (25 liters per accumulator and about 20 kg per piston).

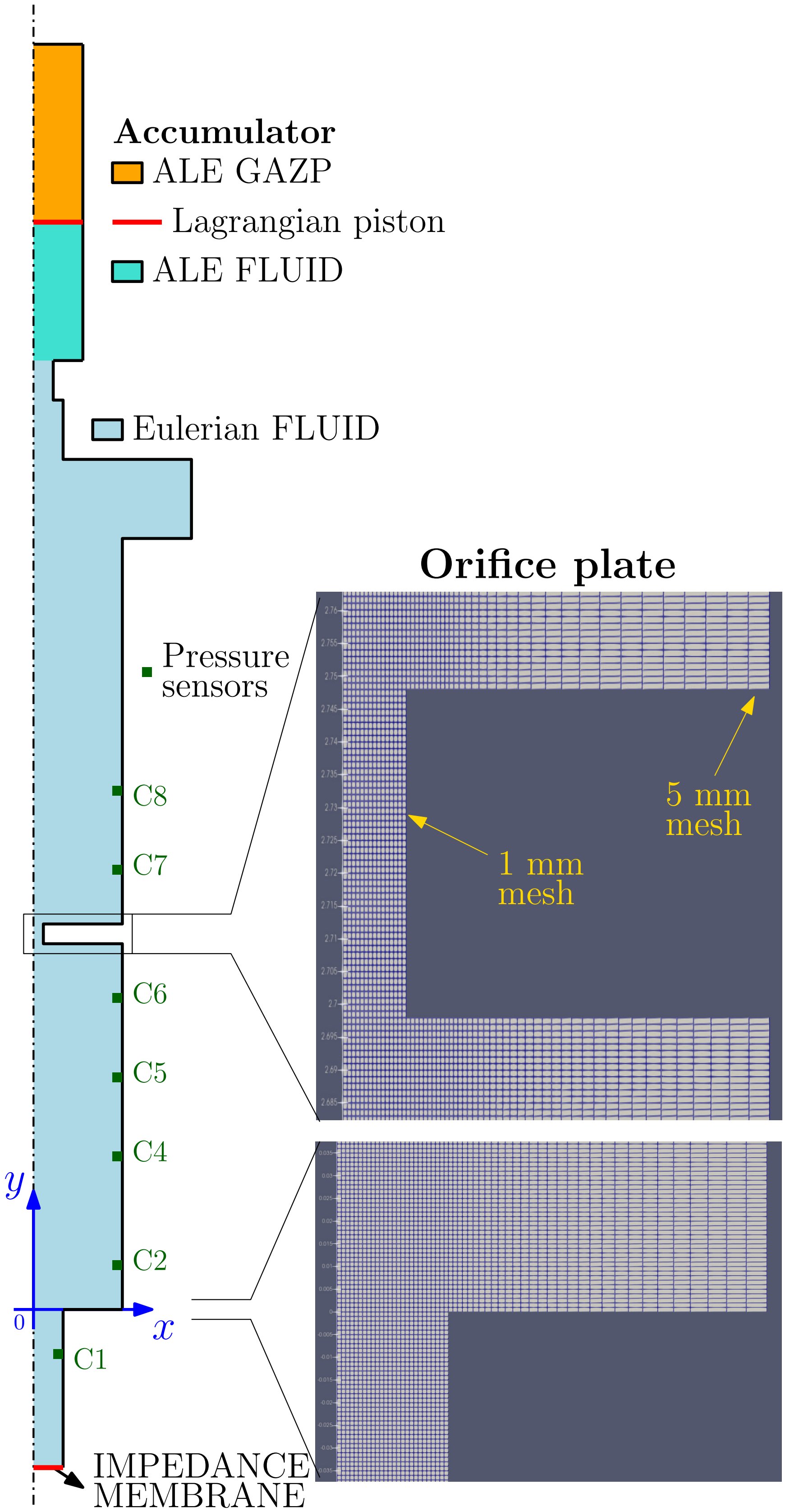

Figure 4.3: Scheme of the 2D axisymmetric mesh.

As usual in numerical calculations, a mesh convergence analysis was carried out for all six geometric configurations of orifice plate using meshes finer or coarser than the one shown in Fig. 4.3. Four different meshes were tested and we summarize their characteristics in Table 4.2.

Referring to Table 4.2, the 1 mm mesh corresponds exactly to that shown in Fig. 4.3. It should be noted that the Progressive type only refers to non-uniformity in the radial (x) direction, while all four meshes are uniform in the axial (y) direction. Only the 10 mm mesh is uniform in both directions, the elements of which will therefore all be squares of 10 mm side. The analysis is performed on all sensors for each geometric configuration. As an example, Fig. 4.4 shows the sensitivity analysis with respect to the cell size performed on the evolution of the pressure difference between sensors C7 and C6, ΔP_{7-6}, for the orifice plate configuration [$e = 50\,\text{mm}$, $d = 50\,\text{mm}$]. It can be concluded from this comparison that the 1 mm mesh (mesh of approximately 230000 elements) is sufficient to achieve grid convergence of the calculations for ΔP_{7-6}. Since a systematic analysis performed for various sensors and orifice geometries leads to the same observation, the 1 mm mesh is the one retained in this chapter for the 2D axisymmetric calculations.

Table 4.2: 2D axisymmetric mesh characteristics for sensitivity analysis.

Mesh name	**Mesh type**	**Smallest element** (mm × mm)	**Largest element** (mm × mm)
0.5 mm mesh	Progressive	0.5×0.5	5.0×0.5
1 mm mesh	Progressive	1.0×1.0	5.0×1.0
3.3 mm mesh	Progressive	3.3×3.3	5.0×3.3
10 mm mesh	Uniform	10.0×10.0	10.0×10.0

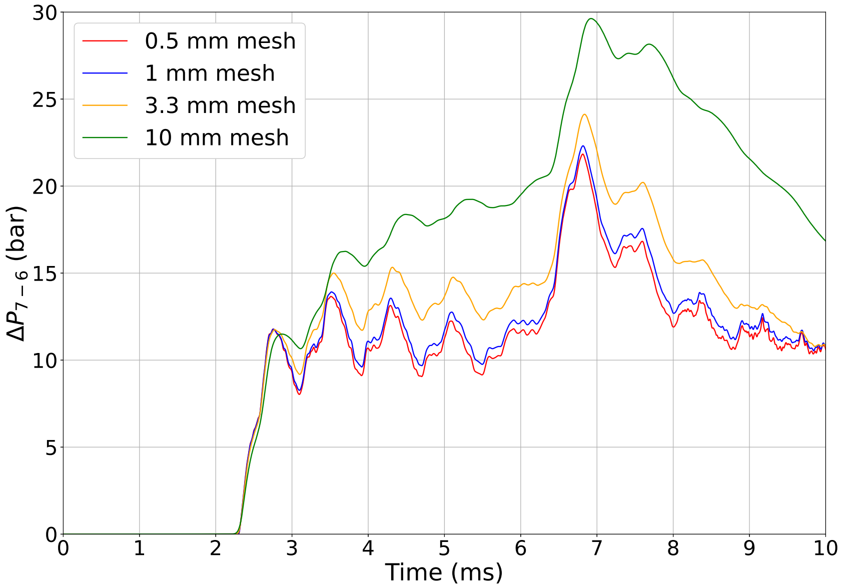

Figure 4.4: 2D axisymmetric mesh convergence for ΔP_{7-6}. Configuration: [$e = 50\,\text{mm}$, $d = 50\,\text{mm}$].

4.2.2 1D with impedances calculations

The 1D with impedances mesh consists of linear elements connected via point nodes (see Fig. 4.5). Each set of elements, representing a pipe section, is associated with its diameter, thus enabling a change in section to be represented via a junction element. Figure 4.6 shows the schematic of the 1D impedance mesh used in our simulations.

The main feature that distinguishes it from the 2D axisymmetric model is that this time the orifice plate is not represented geometrically, but is replaced by the impedance called IMPEDANCE GRID to which a characteristic time τ and a head loss coefficient k are then associated. The values of these coefficients are summarized in Table 4.3 for the six geometric configurations of the orifice plate, computed as described in Subsection 3.1.4.

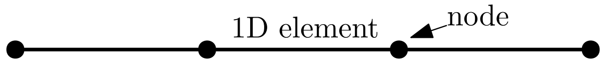

Figure 4.5: 1D mesh scheme. The 1D element between the nodes corresponds to a 1D mesh for a pipe of constant diameter. Each node corresponds to a change of pipe section or diameter. In the present case, the mesh would correspond to 3 connected pipes of various diameters.

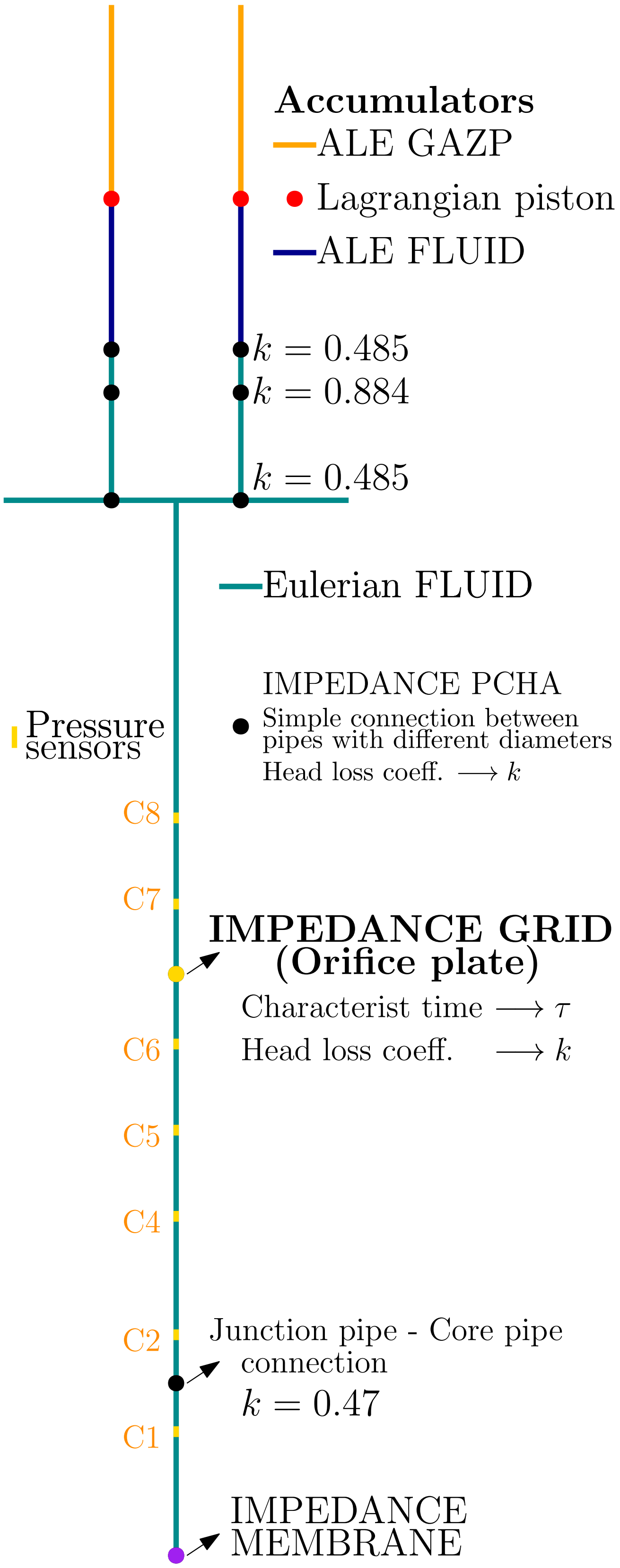

Figure 4.6: Scheme of the 1D with impedances mesh.

Table 4.3: Characteristic time and head loss coefficient for IMPEDANCE GRID.

Orifice plate geometry	$e = 10\,\mathrm{mm}$ $d = 10\,\mathrm{mm}$	$e = 10\,\mathrm{mm}$ $d = 30\,\mathrm{mm}$	$e = 10\,\mathrm{mm}$ $d = 50\,\mathrm{mm}$	$e = 50\,\mathrm{mm}$ $d = 10\,\mathrm{mm}$	$e = 50\,\mathrm{mm}$ $d = 30\,\mathrm{mm}$	$e = 50\,\mathrm{mm}$ $d = 50\,\mathrm{mm}$
τ (ms)	2.47	0.47	0.22	7.94	1.08	0.44
k (-)	294503	5399	666	261874	3178	427

All other cross-sectional changes, represented with black dots in Fig. 4.6, are associated with another type of impedance called IMPEDANCE PCHA, which corresponds to imposing only a classical head loss without the acoustic contribution present in IMPEDANCE GRID (see Paragraph 3.1.4. This choice is based on the fact that the other section changes in question are single cross-sectional changes (sudden enlargement or shrinkage). Consequently, the contribution of the acoustic term in Equation (3.24) does not have the same significance as in the case of the orifice plate (a sudden shrinkage immediately followed by a sudden enlargement). For the orifice plate the frequency of the transmission/reflection phenomenon within its thickness plays a crucial role in delaying the pressure signal transmission from one side of the obstacle to the other (need to use the IMPEDANCE GRID). It is, however, much less significant in the case of single cross-sectional changes, where the term for classical head loss (IMPEDANCE PCHA) makes the most important contribution and is sufficient for their representation. As can be seen in Figure 4.6, no impedance is associated with the single junction node between the core pipe and the horizontal element of the accumulator zone. This is because, despite being a cross-sectional change, the ratio between the two sections is very close to 1, making both the acoustic effect and the head loss negligible.

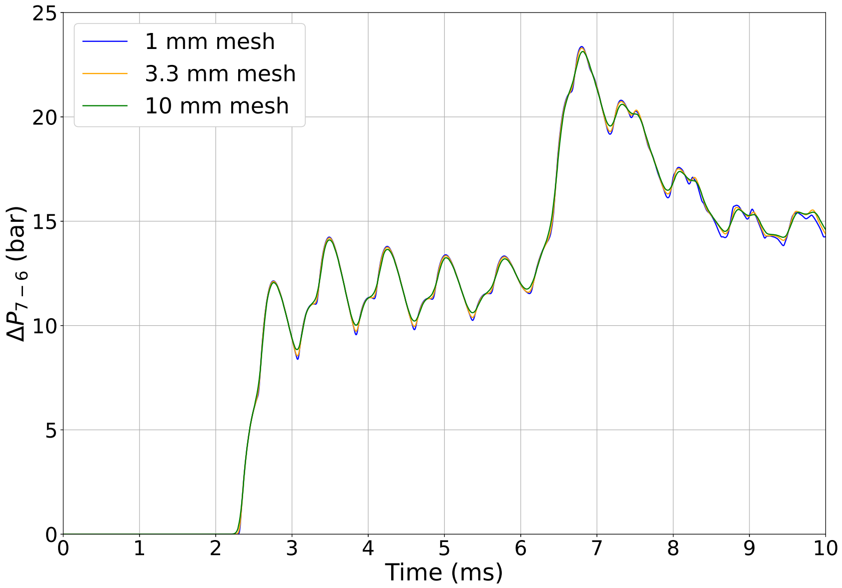

Figure 4.7: 1D with impedances mesh convergence for ΔP_{7-6}. Configuration: [$e = 50\,\mathrm{mm}$, $d = 50\,\mathrm{mm}$].

With the 1D with impedances model, unlike the 2D axisymmetric model, it is possible to break free from the axisymmetry assumption and thus obtain a more accurate geometric representation of two accumulators and their connection to the core pipe, allowing for the representation of two accumulators with directional changes as in reality.

As done for 2D axisymmetric simulations, a mesh convergence analysis is also performed for the 1D model with impedances. Since there is obviously no radial dimension for the 1D mesh, in this case all the tested meshes are uniform (the cells belonging to the 1D element between two nodes are all of the same length or size). For this grid convergence study, it was sufficient to test only three cell sizes: 1 mm, 3.3 mm and 10 mm. All three meshes are actually sufficient for the convergence of the simulations, as can be seen from Fig. 4.7, which shows the convergence analysis for the pressure difference between sensors C7 and C6, ΔP_{7-6}, for the orifice plate configuration [$e = 50\,\mathrm{mm}$, $d = 50\,\mathrm{mm}$]. This analysis led us to choose the coarsest 10 mm mesh, thus consisting of around 1500 cells.

4.3 Simulation-experiment comparison

In this section, we aim to present a comparison between the numerical simulation results and the experimental data. We will initially focus on the evolution of pressure variation across the orifice plate to evaluate the effect of its geometry. Subsequently, we will analyze the difference in accuracy between the two numerical models. Finally, we will present a numerical-to-numerical comparison of the two models in predicting flow velocity, introducing a further novelty compared to previous works, notably that of Faucher et al. (2012).

4.3.1 Evolution of the pressure variation through the orifice plate: effects of the geometry

As previously done at the beginning of the chapter when we analyzed the experimental results, we now aim to provide a qualitative assessment of the effect of the orifice plate geometry on the evolution of the pressure variation through it, this time comparing the experimental results with those of the two numerical models. It is important to recall that the orifice plate is installed between the two sensors C6 and C7, located upstream and downstream of the orifice plate, respectively. We are therefore interested in the transient pressure difference created between these two sensors, ΔP_{7-6}.

Figures 4.8 and 4.9 show the pressure difference between sensors C7 and C6, ΔP_{7-6}, for all the orifice plate configurations, comparing the results of the simulations with the experimental results. The results are in good agreement with the experiments and one can clearly deduce the effect of the orifice plate geometry: the smaller the diameter of the orifice plate hole, the greater the pressure difference between the two sensors; the thickness does not significantly affect the pressure difference between the two sides of the obstacle.

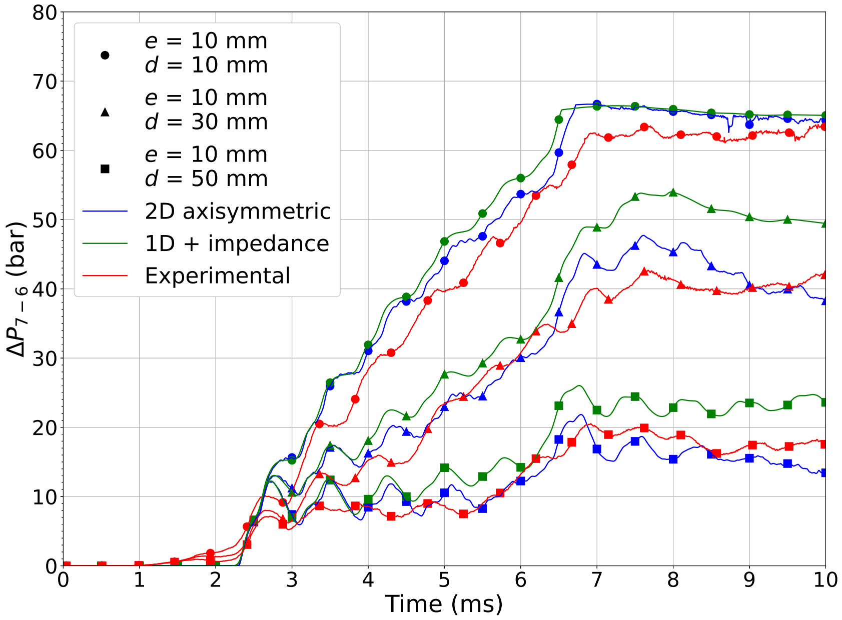

Figure 4.8: Pressure difference between sensors C6 and C7, ΔP_{7-6}, for all thin orifice plates ($e = 10\,\text{mm}$).

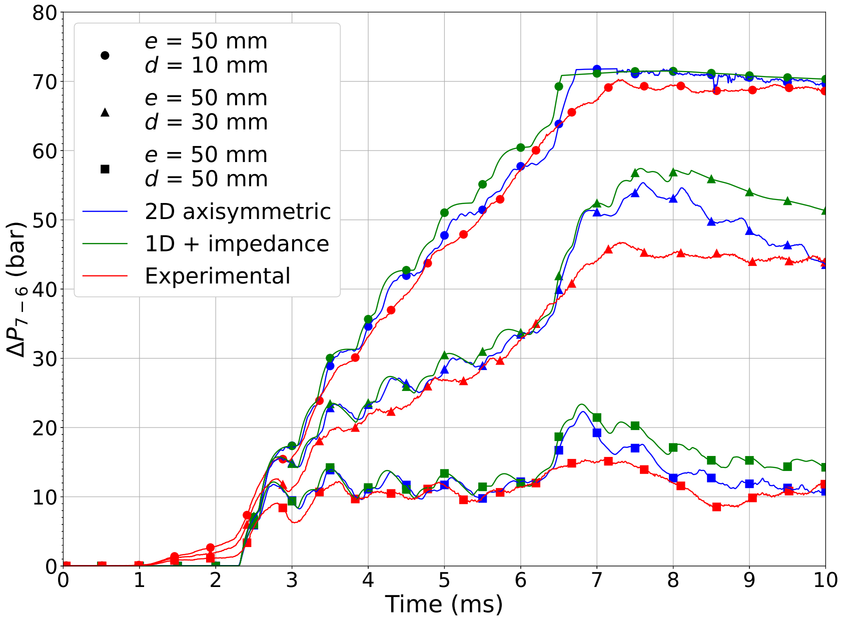

Figure 4.9: Pressure difference between sensors C6 and C7, ΔP_{7-6}, for thick modular orifice plate ($e = 50\,\text{mm}$).

4.3.2 Accuracy of numerical models compared to experiments

As previously mentioned, observing Figures 4.8 and 4.9, it can be seen that both models are in good agreement with the experimental results regarding the transient pressure difference generated between the two sides of the orifice plate.

To provide a more comprehensive evaluation of the accuracy of the two models compared to the experimental results, we present below a simulation/experiment comparison of pressure evolutions on three specific sensors for all orifice plate configurations:

- the C1 sensor of the junction pipe in Figure 4.10, to assess the accuracy in reproducing the bursting disk opening,
- and two sensors of the core pipe, the C5 sensor in Figure 4.11 and the C8 sensor in Figure 4.12, located upstream and downstream of the orifice plate, respectively. We chose sensors C5 and C8 instead of C6 and C7 in this case for two reasons: to provide additional information compared to Figures 4.8 and 4.9, and to evaluate the pressure evolution in regions slightly further from the orifice plate, where we are closer to a condition of plane wave propagation in the experiment and in the 2D axisymmetric simulation.

For sensor C1, looking at Figure 4.10, it is evident that both models are capable of accurately reproducing the transmission/reflection mechanism generated in the junction pipe by the opening of the bursting disk. In particular, during the first 3 ms, the two models are almost perfectly superimposed, with the 1D model better capturing the first four peaks. Subsequently, from the fifth peak (at around 4 ms) to 6 ms, the 2D axisymmetric model proves to be the most accurate. In the final part ($t \geq 6$ ms), the pressure tends to zero more rapidly as the diameter of the orifice plate decreases, suggesting that a larger orifice diameter allows for a greater flow from the upper part of the device, thereby maintaining higher pressure in the junction pipe. In this latter case, both models continue to show increasingly pronounced peaks as the orifice plate diameter increases, whereas the experimental signal tends towards a plateau. In all cases, a slight phase shift can be observed, which can be attributed to a not sufficiently accurate bottom outlet condition (the opening of the bursting disk in the numerical models is driven by a simple exponential function, as presented in Paragraph 3.1.4).

From Figure 4.11, we can deduce that for sensor C5, the two numerical models overlap almost perfectly up to 4 ms, while accurately following the experimental curve up to 3 ms. The two numerical models begin to diverge from each other for $t \geq 4$ ms, with the 1D model showing an underestimated pressure compared to both the 2D axisymmetric model and the experimental curve. In general, for $t \geq 4$ ms, the 2D axisymmetric model is the one that best follows the experimental curve.

By looking at the pressure evolution for the individual sensor C8, P_{C8}, in Figure 4.12 we can again deduce the effect of the orifice plate thickness on the wave propagation through it: by decreasing the thickness of the orifice plate the pressure signal is transmitted more effectively and is less diffused when crossing the obstacle. In fact we can clearly see on the C8 sensor the characteristic pressure footprint (the pressure steps) transmitted from the upstream of the orifice plate. Regarding the accuracy of the models, in the first 3 ms, we observe that for the cases with orifice diameters of 30 and 50 mm (Figures 4.12 (c)-(d)-(e)-(f)), the two models overlap and follow the experimental curve with reasonable accuracy. In the case of $d = 10\,\mathrm{mm}$ (Figures 4.12 (a)-(b)), neither model is able to reproduce the slight pre-increase in pressure observed experimentally between 2 and 3 ms. This phenomenon will be explained in Paragraph 4.4.2.3 when we consider the FSI mechanisms. For $3 \leq t \leq 5$ ms, the models closely follow the trend of the experimental curve, except for the cases with $d = 10\,\mathrm{mm}$, where they fail to reproduce the same acoustic imprint (peaks) of the experimental curve (which we will see when considering FSI mechanisms). Between 5 and 7 ms, there is a small plateau due to the return of the reflected wave from the topmost part of the device (the first rarefaction wave traveled the entire height of the device, slightly over 5 meters, in about 4 ms), after which the pressure starts to decrease again. The plateau is accurately reproduced by both models only for configurations (c), (e), and (f); for configuration (d), the 1D model is more accurate; in configurations (a) and (b), both models slightly overestimate the pressure value, with the 1D model again showing greater accuracy.

For both models, a major influence is also played by the value of the speed of sound, which is considered uniform throughout the fluid, but which actually depends not only on the material of the pipe, but also on its diameter and thickness (when taking pipes flexibility into account to correct the value of the speed of sound in the fluid). We will explore this effect in detail in Section 4.4 when considering the FSI mechanisms.

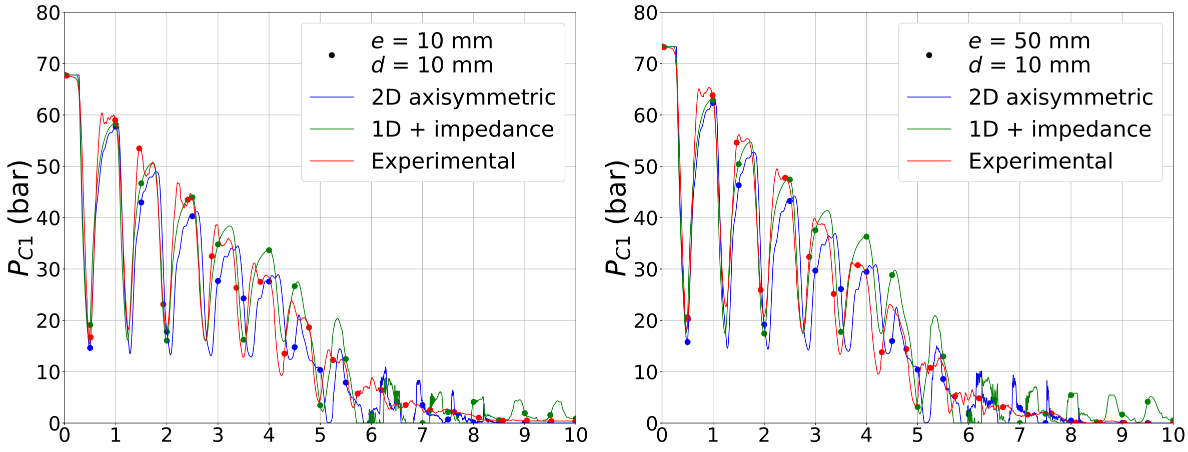

(a) $e = 10\,\mathrm{mm},\ d = 10\,\mathrm{mm}$

(b) $e = 50\,\mathrm{mm},\ d = 10\,\mathrm{mm}$

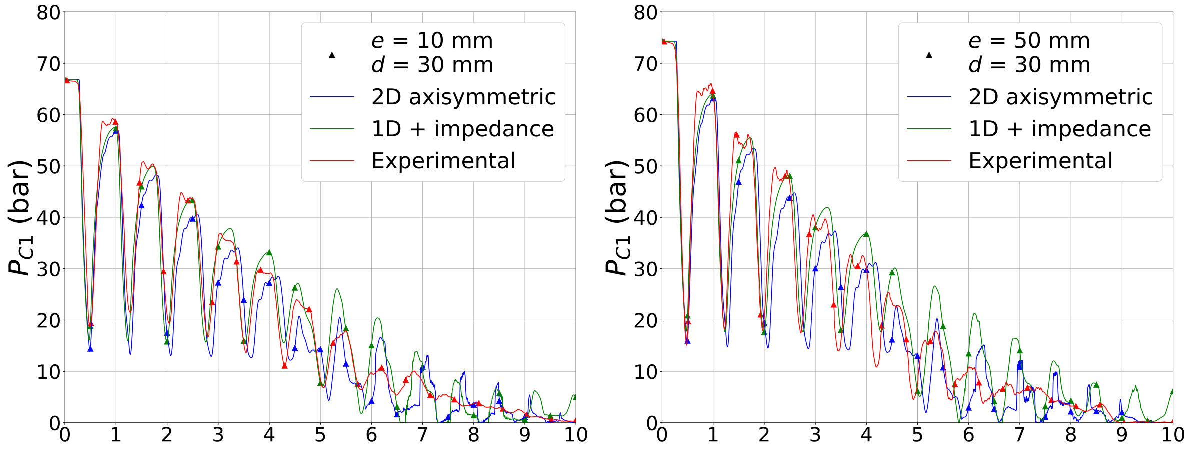

(c) $e = 10\,\mathrm{mm},\ d = 30\,\mathrm{mm}$

(d) $e = 50\,\mathrm{mm},\ d = 30\,\mathrm{mm}$

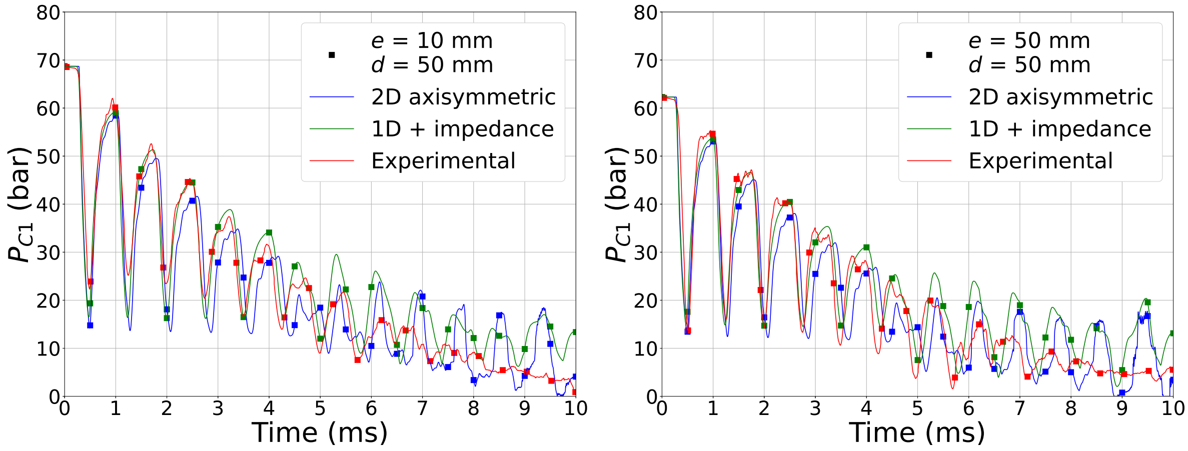

(e) $e = 10\,\mathrm{mm},\ d = 50\,\mathrm{mm}$

(f) $e = 50\,\mathrm{mm},\ d = 50\,\mathrm{mm}$

Figure 4.10: Pressure evolution for sensor C1, P_{C1}, for all orifice plates.

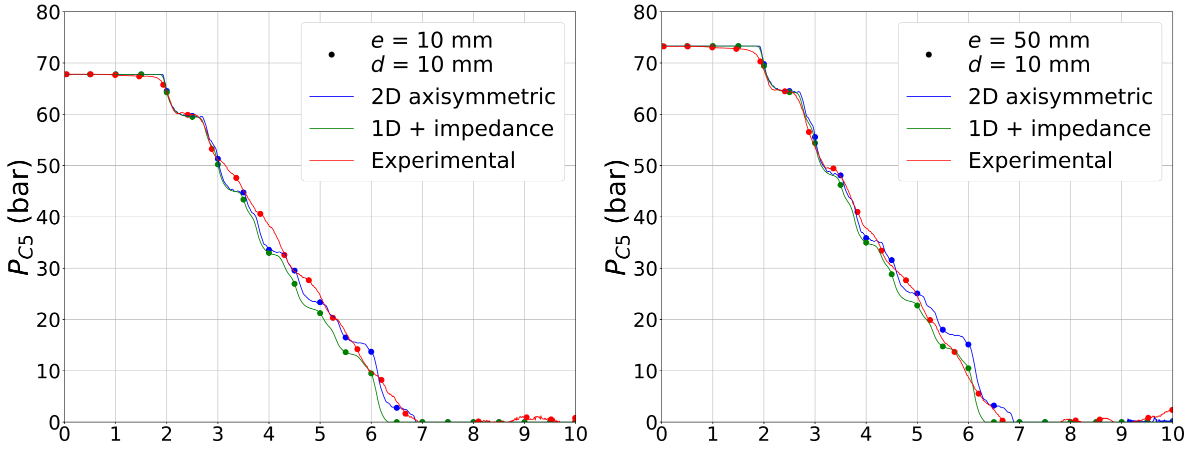

(a) $e = 10\,\mathrm{mm}$, $d = 10\,\mathrm{mm}$ (b) $e = 50\,\mathrm{mm}$, $d = 10\,\mathrm{mm}$

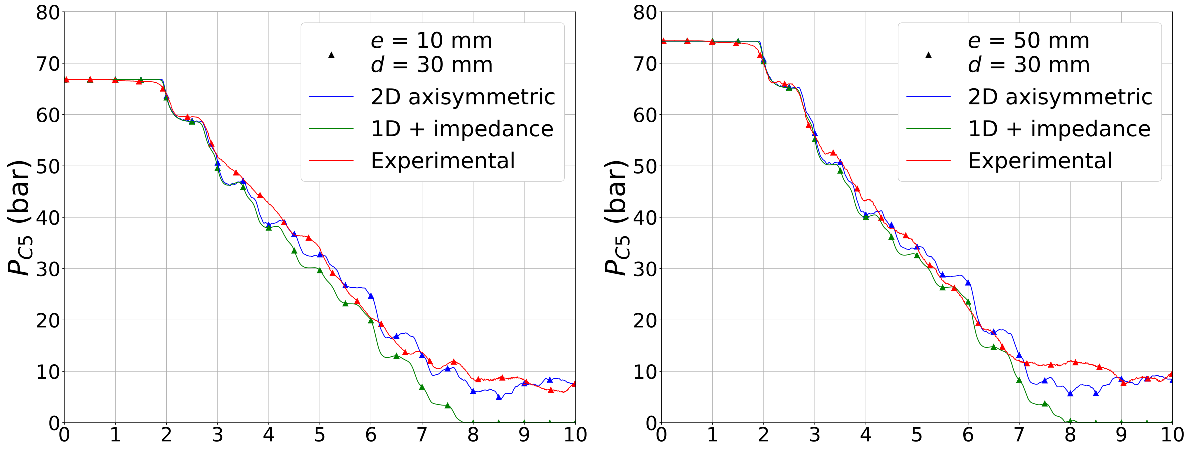

(c) $e = 10\,\mathrm{mm}$, $d = 30\,\mathrm{mm}$ (d) $e = 50\,\mathrm{mm}$, $d = 30\,\mathrm{mm}$

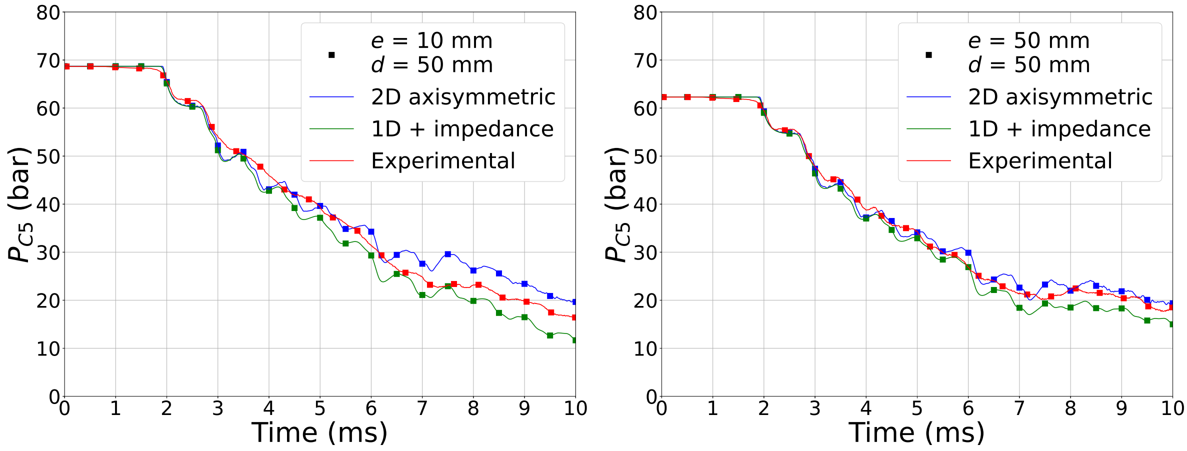

(e) $e = 10\,\mathrm{mm}$, $d = 50\,\mathrm{mm}$ (f) $e = 50\,\mathrm{mm}$, $d = 50\,\mathrm{mm}$

Figure 4.11: Pressure evolution for sensor C5, P_{C5}, for all orifice plates.

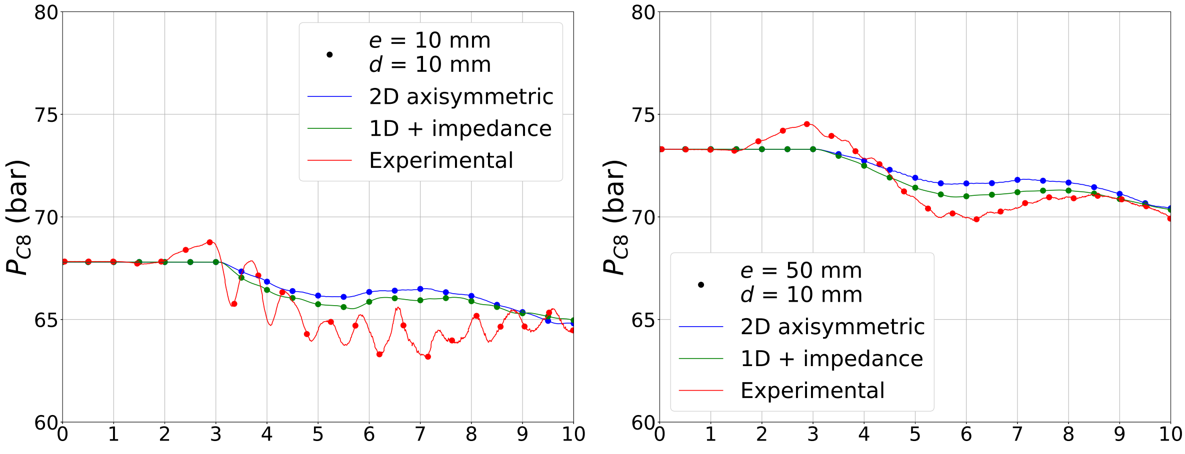

(a) $e = 10\,\text{mm},\ d = 10\,\text{mm}$ (b) $e = 50\,\text{mm},\ d = 10\,\text{mm}$

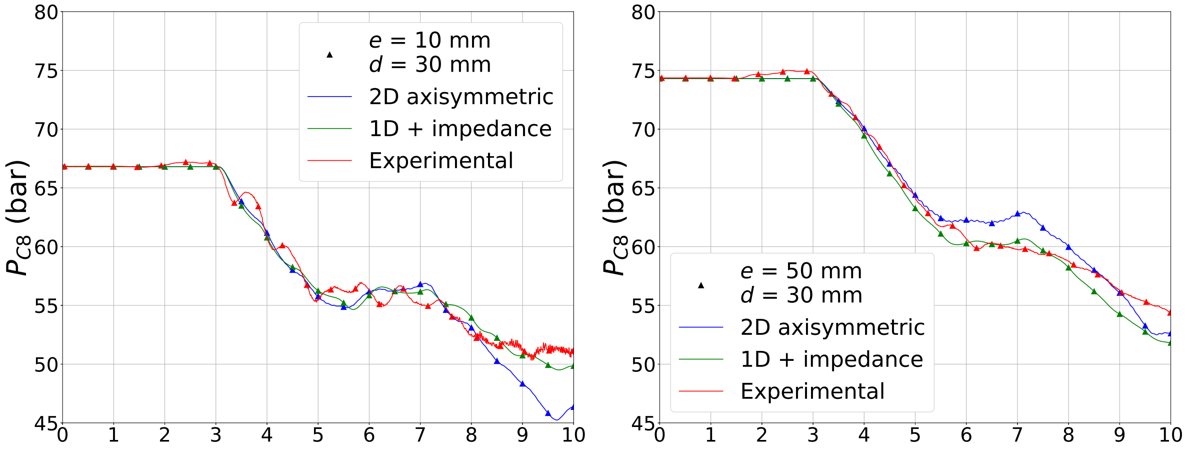

(c) $e = 10\,\text{mm},\ d = 30\,\text{mm}$ (d) $e = 50\,\text{mm},\ d = 30\,\text{mm}$

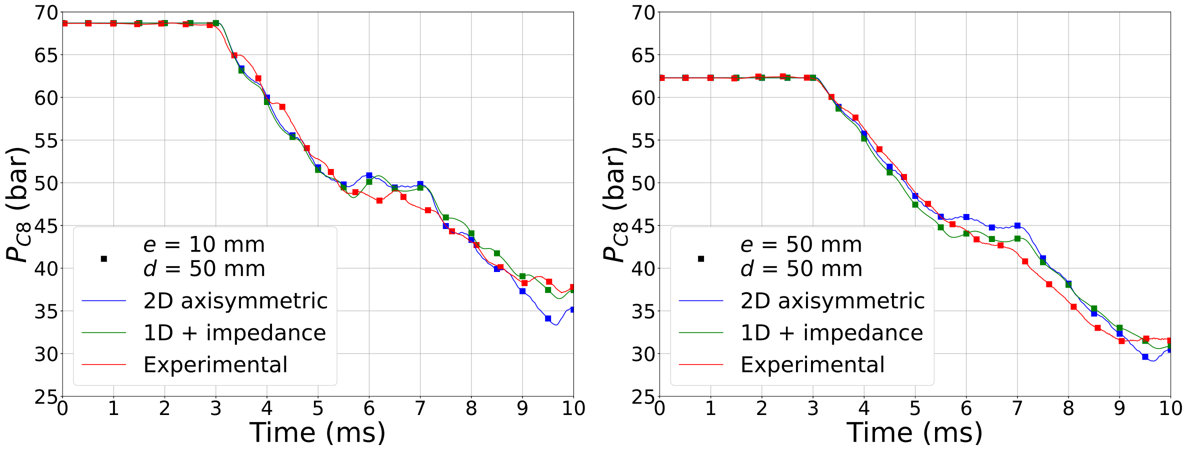

(e) $e = 10\,\text{mm},\ d = 50\,\text{mm}$ (f) $e = 50\,\text{mm},\ d = 50\,\text{mm}$

Figure 4.12: Pressure evolution for sensor C8, P_{C8}, for all orifice plates.

4.3.3 Numerical prediction of the velocity evolution

From the simulations, in addition to the pressure field, it is possible to extract the values of the fluid velocity for each node of the mesh. Unfortunately, no experimental measurements are currently available for the velocity (how to perform such a measurement is being investigated and perspectives will be given in the conclusion of the manuscript), but a comparison is made between the results of the two models for the velocities at the same position of the pressure sensors. For the 2D axisymmetric model, two velocity components are associated with each node, one radial (along x) and one axial (along y), whereas the velocities of the 1D model have one spatial component in the direction of flow. Therefore, to compare the two models, we chose to extract only the y-components of the velocity for each node of the 2D axisymmetric model and average them in the radial direction (weighted average over the mass).

4.3.3.1 Physical interpretation

Figure 4.13 shows the velocity evolution (y-component) at positions C6 and C7, for all geometric configurations of the thick modular orifice plate and for the two numerical models. Velocities have negative values because the flow is clearly going downwards with respect to the reference system (y-axis pointing upwards). By comparing the two figures with each other, it can be qualitatively deduced that the momentum conservation is respected above and below of the orifice plate, apart from oscillations due to acoustics. Finally, regarding the effect of orifice plate geometry, it can be seen that the larger the hole the higher the velocities and the more effectively the signal is transmitted from position C6 to position C7.

4.3.3.2 Evaluation of numerical model accuracy

The two models are in good agreement for the first few milliseconds after the arrival of the pressure signal, after which the curves tend slightly to diverge, with the 2D axisymmetric model displaying lower velocities that tend to zero at some point, while for the 1D model it appears that the velocity reaches a plateau. This latter behavior, which is particularly pronounced for position C6 in configurations [$e = 50\,\mathrm{mm}$, $d = 10\,\mathrm{mm}$] and [$e = 50\,\mathrm{mm}$, $d = 30\,\mathrm{mm}$] (see Fig. 4.13 (a)), can be explained by observing the pressure evolution for sensor C6 (Fig. 4.14 (a)): for the 1D model, we observe that at a certain time, which depends on the orifice diameter (at approximately 6.5 ms for [$e = 50\,\mathrm{mm}$, $d = 10\,\mathrm{mm}$]-bullets, and 8.2 ms for [$e = 50\,\mathrm{mm}$, $d = 30\,\mathrm{mm}$]-triangles) the pressure reaches approximately 0 bar (limit imposed by the calculation, see Eq. (3.19) in subsection 3.1.2) and remains stable for a certain period of time, thus indicating the presence of cavitation in the actual flow. Since the numerical models used in the present calculations do not allow a proper description of the phyical cavitation we will refer to the occurrence of the regime where the computed pressure reaches approximately 0 bar as a “numerical cavitation”; for the configuration [$e = 50\,\mathrm{mm}$, $d = 30\,\mathrm{mm}$] only the 1D model shows numerical cavitation, unlike the 2D axisymmetric model which agrees more closely with the experimental curve.

For the 2D axisymmetric model, on the other hand, the y-component of the velocity for sensor C6, $v_{y,\mathrm{C6}}$, (Fig. 4.13 (a)) tends to zero in presence of numerical cavitation (velocity is radially weight averaged over the mass; as will be discussed in Section 4.4, a localized density drop is observed, Fig. 4.15, in the area of higher fluid velocity, Fig. 4.18, thus explaining why $v_{y,\mathrm{C6}}$ tends to zero), but at the same time a significant x-component of the velocity, $v_{x,\mathrm{C6}}$, appears (Fig. 4.14 (b)), highlighting a subsequent fluid acceleration in the radial direction (x) towards the pipe wall.

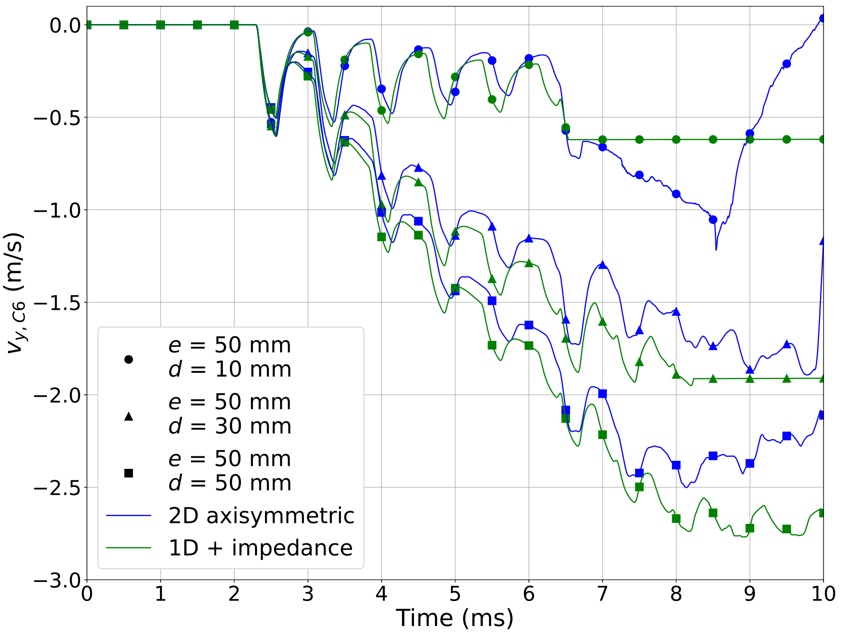

(a)

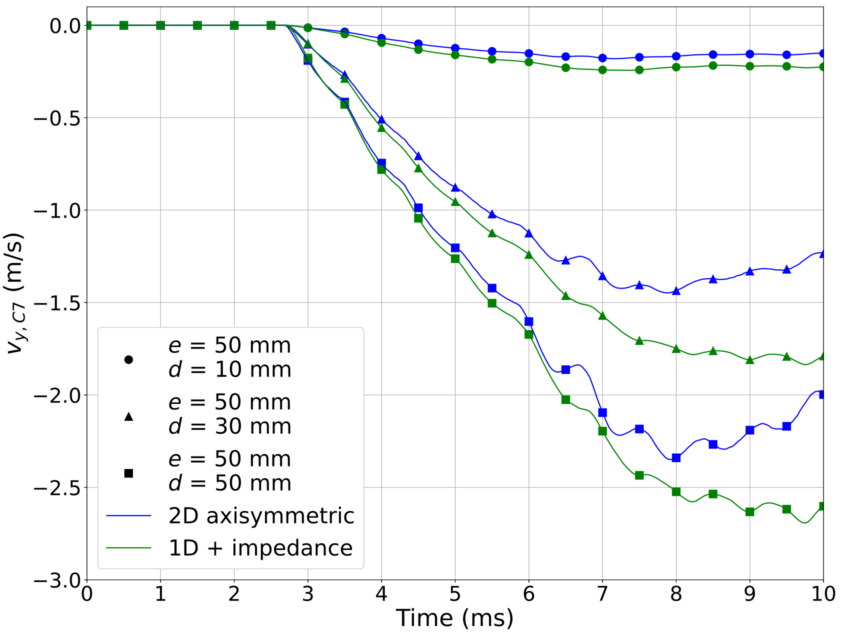

(b)

Figure 4.13: y-velocity at positions C6 (a) and C7 (b).

In the observation period presented here, [0, 10] ms, we do not observe the same effects on the configuration [$e = 50\,\text{mm}$, $d = 50\,\text{mm}$], but looking at the tendency of the curves we can expect to find similar behavior for observation periods longer than 10 ms.

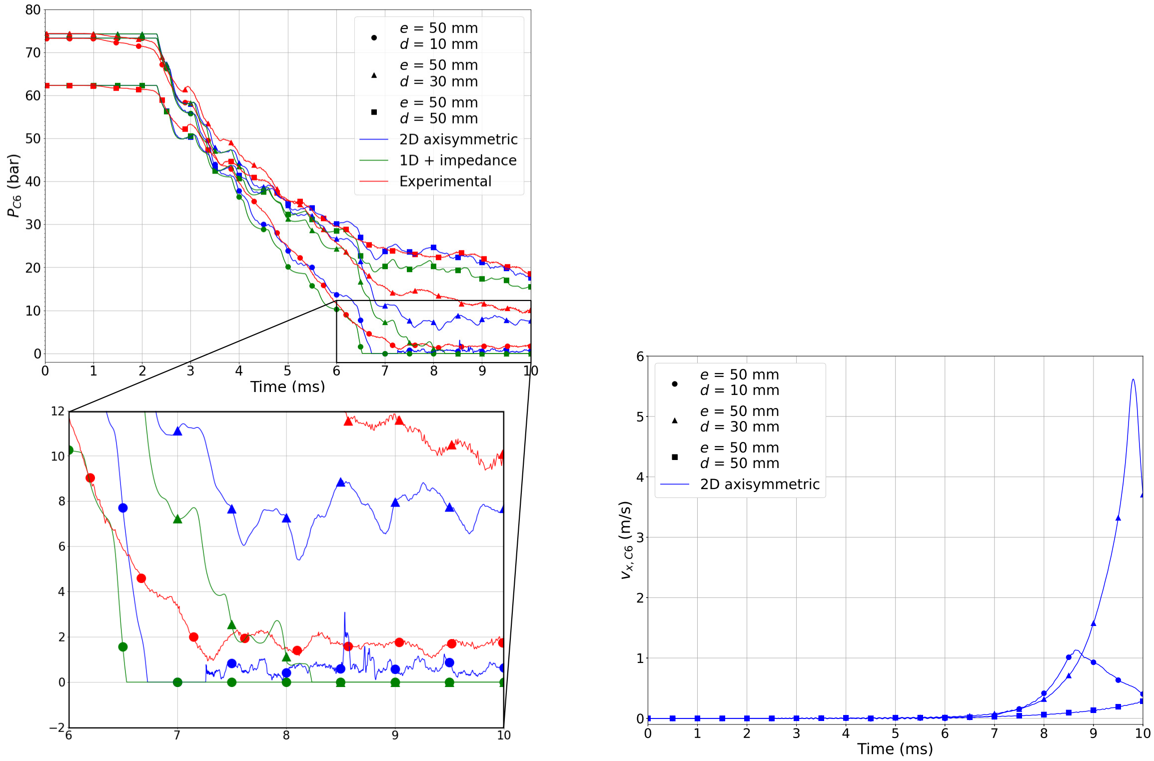

(a) (b)

Figure 4.14: (a) Pressure evolution for sensor C6, P_{C6}, for all thick modular orifice plate configurations and (b) x-velocity at positions C6.

Finally, considering the 2D axisymmetric model as reference and the difference with respect to the 1D model with impedances on the prediction of velocity evolution, it can be deduced that, despite the latter's ability to reproduce pressure evolution in a somewhat satisfactory manner, the same cannot be said about its predictive capacity for velocity evolution, particularly when more complex and/or more realistic configurations are taken into account.

4.4 Fluid-Structure Interaction (FSI) calculations

In order to investigate in more detail the numerical cavitation phenomenon observed in some of the simulations carried out so far and analysed in particular in the previous section, we show below the results of some FSI calculations carried out with EUROPLEXUS on the case study under consideration in this Chapter and explain the necessity of such calculations.

4.4.1 Motivation

In the 2D axisymmetric and 1D calculations performed so far with the FLUID model (no phase change, fluid pressure calculated using Eq. (3.19)) and fixed structures (Eulerian description for the fluid), numerical cavitation is produced locally (just below the orifice plate, observed at sensor C6) by the attainment of a minimum threshold value for the fluid pressure, as already explained in the previous section. This has an effect on the fluid velocity, as already described, but a localised decrease in density can also be observed (see Fig. 4.15).

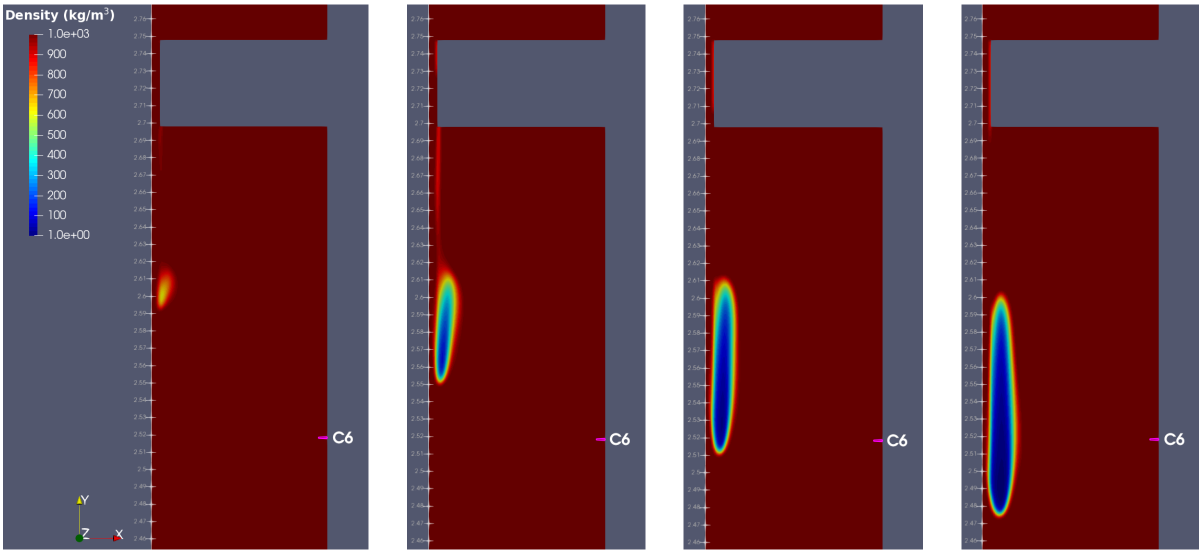

(a) $t = 7\,\text{ms}$ (b) $t = 8\,\text{ms}$ (c) $t = 9\,\text{ms}$ (d) $t = 10\,\text{ms}$

Figure 4.15: 2D axisymmetric FLUID density profile for configuration [$e = 50\,\text{mm}$, $d = 10\,\text{mm}$] below the orifice plate.

The localised drop in density suggests the possible presence of cavitation but the FLUID model does not allow a more accurate prediction since it does not take phase change into account. The occurrence of fluid vaporization could be observed experimentally on the test-rig but the current experimental device prevents such an observation since no porthole has been fitted along the core pipe. It was therefore decided to perform complementary numerical simulations using again EUROPLEXUS but with a new model to represent the fluid, namely the WATER model [62], which uses tabulated Equations of State (EoS) [63] to calculate the properties of water and allows phase change to be taken into account.

With the FLUID model, the value of the speed of sound in the fluid was adjusted by means of the Allievi correction to take into account the flexibility of the pipe and the presence of dissolved gases in the water (as explained in Section 4.2). On top of having a validity limited to simple configurations, this description does not allow to represent the occurrence of cavitation in the flow. Using the WATER model, on the other hand, employing the EoS and FSI calculations to take into account the flexibility of the pipe, we obtain the correct value of the speed of sound without applying the Allievi correction. In the WATER model, the equations (3.5), (3.7) and (3.17) are solved in a coupled manner and the water properties calculated through the tabulated EoS, giving us the possibility to take the phase change into account. The energy equation is then solved for a homogeneous equilibrium water/steam model in which pressure is this time both a function of density and internal energy.

4.4.2 2D axisymmetric FSI calculations

4.4.2.1 Set-up of the simulations

To perform 2D axisymmetric FSI calculations on the case under investigation, we first added a mesh layer around the fluid to represent the pipe (see Fig. 4.16). The thickness of this layer varies over the length of the pipe respecting the actual pipe thickness. In this case we used a uniform squares mesh (cell characteristic size ≈ 1 mm) to facilitate a perfectly coherent coupling between the fluid and the pipe (nodes and faces of the two meshes coinciding at the interface between them).

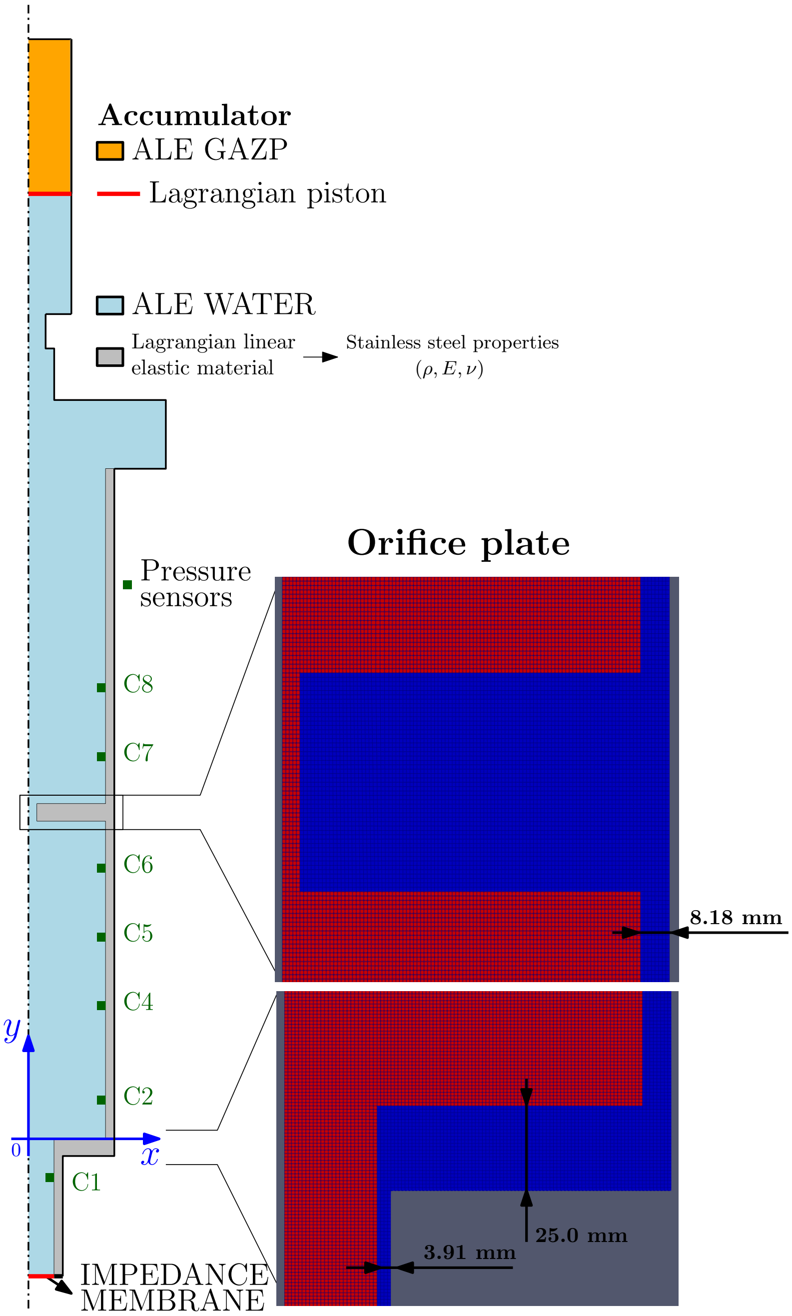

Figure 4.16: Scheme of the 2D axisymmetric mesh for FSI calculations. In the close-up on the right (top: in the vicinity of the orifice plate, bottom: in the vicinity of the connection between the junction pipe and the core pipe), the fluid domain is pictured in red while the solid domain is pictured in blue.

From a physical and numerical point of view, the two components, steel pipe and water, are described as follows:

- **Pipe** (structure): spatial discretization using Finite Element Model (FEM), Lagrangian description (the mesh deforms following the deformation of the solid), linear elastic material model with associated steel properties (density $\rho = 7800\,\mathrm{kg/m^3}$, Young's modulus $E = 200\,\mathrm{GPa}$ and Poisson's coefficient $\nu = 0.3$).
- **Water** (fluid): spatial discretization using Finite Volume Model (FVM), ALE description (the fluid mesh can deform to follow the displacements of the surrounding structure, see Section 3.1.2), WATER model to which we only give as input the initial pressure of the fluid (corresponding to the bursting pressure) and the initial temperature (equal to the ambient temperature), all other properties being calculated by EUROPLEXUS via the tabulated EoS.

4.4.2.2 Qualitative observation of the computed flow

As mentioned above, by means of FSI calculations with the WATER model, it is possible to assess whether a phase change actually occurs in the fluid (water vaporization): Fig. 4.17 shows the 2D axisymmetric profile of the void ratio (vapour volume/total volume) in the section just below the orifice plate.

It can clearly be deduced that cavitation is indeed generated as a vapour bubble that begins to form near the axis of symmetry of the pipe a few tens of centimeters below the orifice plate and that enlarges and elongates in the axial direction over time, moving in the direction of flow (fluid flow downwards). The location of the phenomenon corresponds almost perfectly with that observed in the calculations with the FLUID model shown in Fig. 4.15.

The occurrence of this phenomenon is very likely correlated with the strong acceleration of the fluid at this location, as displayed in Fig. 4.18: at the axis of symmetry of the pipe, and thus at the orifice plate hole, a high-speed wall-jet is created in the negative y-direction (maximum velocity magnitude of 125 m/s) with cavitation appearing roughly at the head of this wall-jet.

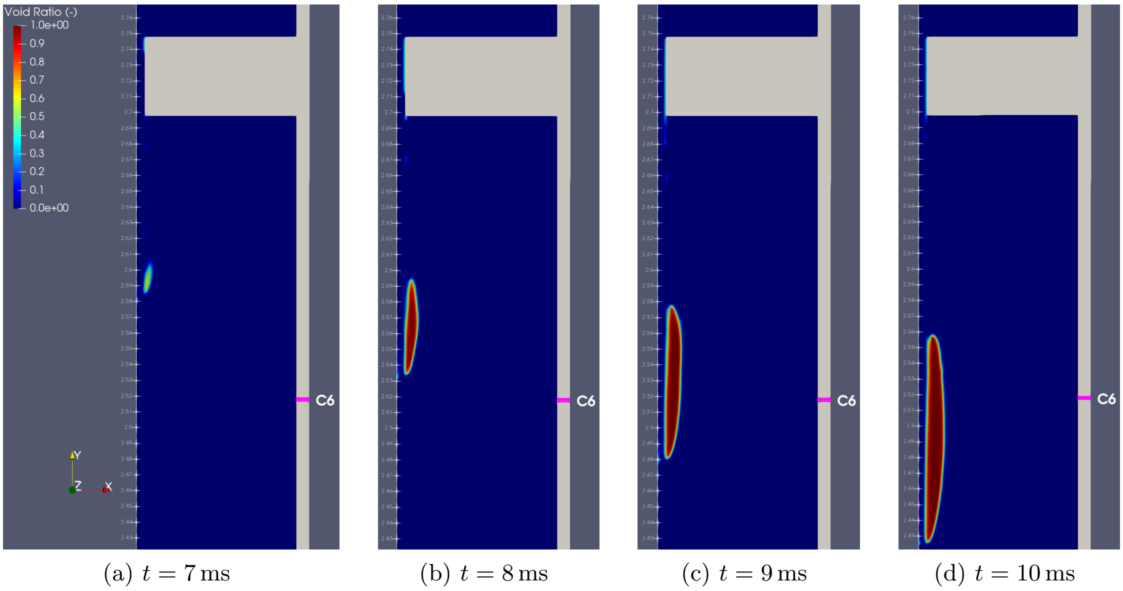

(a) $t = 7\,\mathrm{ms}$ (b) $t = 8\,\mathrm{ms}$ (c) $t = 9\,\mathrm{ms}$ (d) $t = 10\,\mathrm{ms}$

Figure 4.17: 2D axisymmetric WATER void ratio profile for configuration [$e = 50\,\mathrm{mm}$, $d = 10\,\mathrm{mm}$] below the orifice plate.

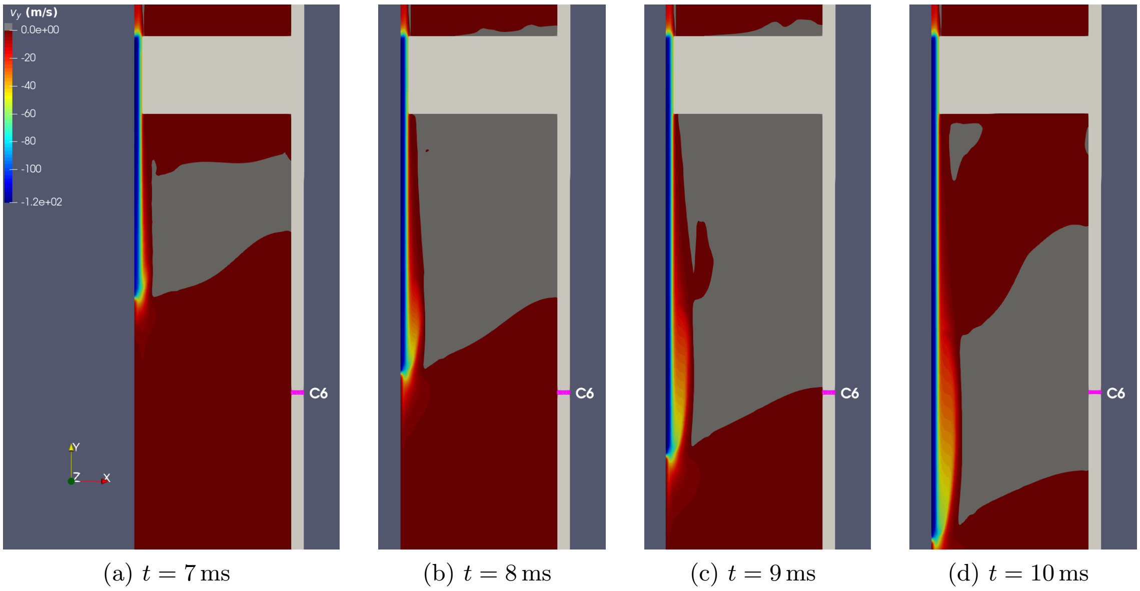

(a) $t = 7\,\mathrm{ms}$ (b) $t = 8\,\mathrm{ms}$ (c) $t = 9\,\mathrm{ms}$ (d) $t = 10\,\mathrm{ms}$

Figure 4.18: 2D axisymmetric WATER velocity y-component, v_y, profile for configuration [$e = 50\,\mathrm{mm}$, $d = 10\,\mathrm{mm}$] below the orifice plate. In dark grey: $0 < v_y < 2.5\,\mathrm{m/s}$.

4.4.2.3 Quantitative analysis of the pressure evolution

Figures 4.19 and 4.20 display the evolution of the pressure difference between sensors C6 and C7, ΔP_{7-6}, respectively for the thin orifice plates ($e = 10\,\mathrm{mm}$) and the thick orifice plates ($e = 50\,\mathrm{mm}$). The evolution computed using the 2D axisymmetric calculations with non-deformable structure (2D axi - blue line) previously analyzed in 4.3 are compared with the new calculations with FSI (2D axi FSI - green line) and the reference experimental measurements. Figure 4.21 also provides the same comparison but with a focus on the first 4 ms of the time evolution; distinct plots are proposed for each geometric configuration (defined by the values of e and d) to allow a clear comparison between the 2 simulations and the corresponding experiment.

Early stage of the time evolution From Fig. 4.21 one can clearly see that calculations with FSI are able to follow the experimental curve more closely in the first 4 ms. FSI simulations allow us indeed to reproduce a particular phenomenon that we have always observed in experiments but which could not be observed in simulations without taking the flexibility of the structure into account: referring to Fig. 4.19, 4.20 and 4.21 we can see that for $1 < t < 2.3\,\mathrm{ms}$ the experimental pressure difference ΔP_{7-6} (red curve) undergoes a slight pre-increase before rising abruptly at about $t = 2.3\,\mathrm{ms}$, a trend that is nearly also followed by the FSI calculation (green curve), but not by the 2D axisymmetric calculation with fixed structures (blue curve), which maintains a ΔP_{7-6} equal to zero up to 2.3 ms and then directly undergoes a brutal increase.

The aforementioned behavior can be explained by considering that the acoustic rarefaction wave, generated as a result of the rupture of the bursting disk, not only propagates through the fluid but also traverses the structure, albeit at a different velocity. To be more precise, in the case of steel, the speed of sound is approximately 5100 m/s, which is more than three times greater than the speed of sound in water. This discrepancy leads to the structural deformation occurring prior to the arrival of the same acoustic signal in the water.

This pre-deformation causes the section of the pipe below the orifice plate to slightly expand radially as the wave passes through it, resulting in a localized decrease in fluid pressure. Conversely, in the section of the pipe above the orifice plate, the opposite effect takes place as the wave propagating within the structure encounters the discontinuity formed by the orifice plate itself. Consequently, a slight pressure difference is established between the two sides of the orifice plate in the initial moments, causing the upper portion to undergo a minor depressurization. This, in turn, induces a slight radial constriction in that part of the pipe, leading to a minor localized increase in pressure in the fluid located above the orifice plate.

Time evolution after 5 ms From Figures 4.19 and 4.20 one could say the FSI prediction between 5 and 6 ms for the 2D axi FSI seems further away from the experiment than the baseline 2D axi, except for configurations [$e = 10\,\mathrm{mm}$, $d = 30\,\mathrm{mm}$] and [$e = 10\,\mathrm{mm}$, $d = 50\,\mathrm{mm}$], where the models yield very similar results instead. This effect could be due to an inaccurate response of the structure to the return of the wave reflected from the upper part of the device (the first rarefaction wave traveled the entire height of the device, slightly over 5 meters, in about 4 ms): the connection between the core pipe and the accumulators is simplified in 2D modeling (a single accumulator placed on the same axis as the core pipe) compared to reality (two accumulators connected at 90 degrees to the core pipe), thus not ensuring the same transmission/reflection mechanisms and consequently a different response of the structure, which, when deforming in the 2D axi FSI simulation, has a consequent effect on the local pressure.

After 6 ms, the 2D axi FSI model generally appears to be closer to the experimental curve compared to the 2D axi model with fixed structures.

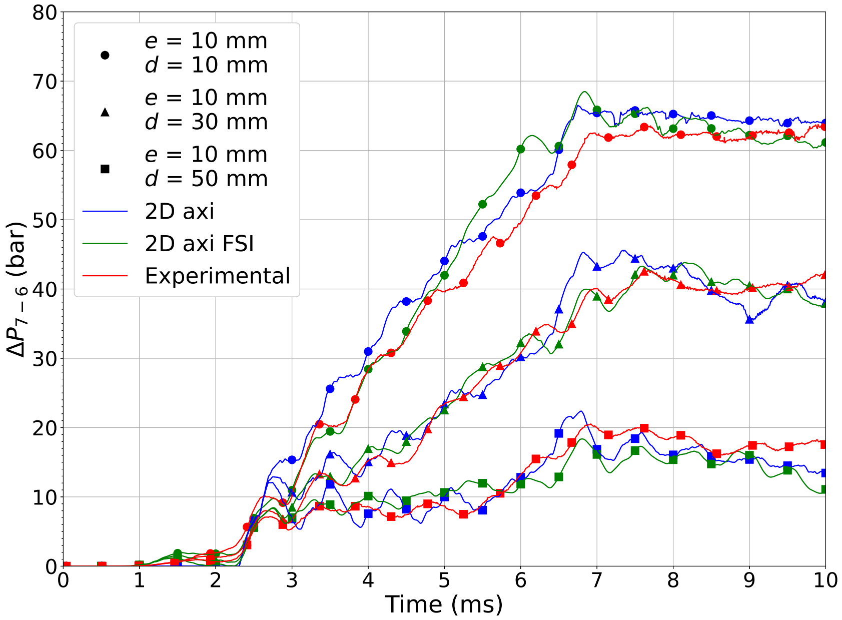

Figure 4.19: Pressure difference between sensors C6 and C7, ΔP_{7-6}, for all thin orifice plates ($e = 10\,\mathrm{mm}$).

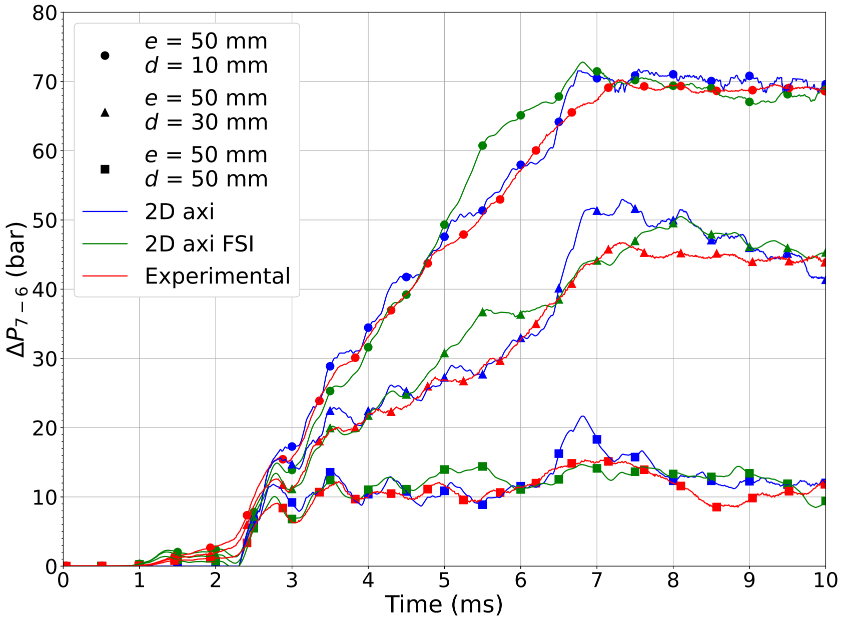

Figure 4.20: Pressure difference between sensors C6 and C7, ΔP_{7-6}, for thick modular orifice plate ($e = 50\,\mathrm{mm}$).

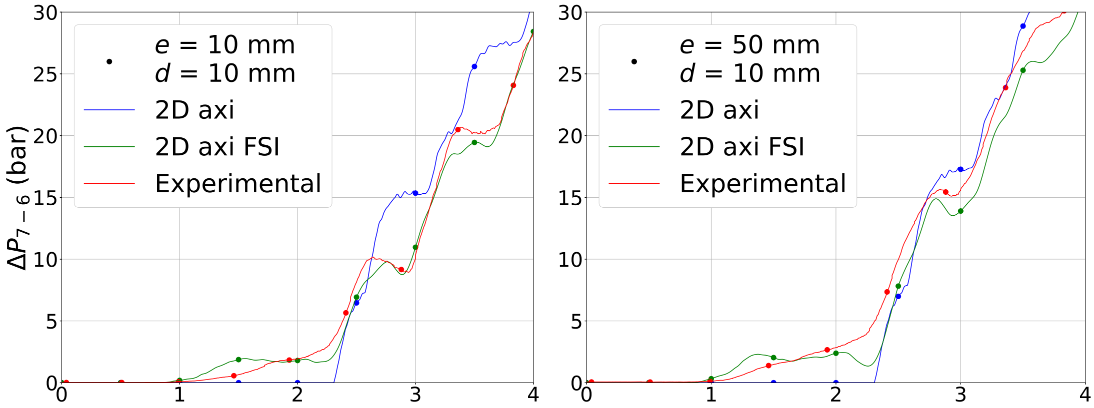

(a) $e = 10\,\text{mm},\ d = 10\,\text{mm}$ (b) $e = 50\,\text{mm},\ d = 10\,\text{mm}$

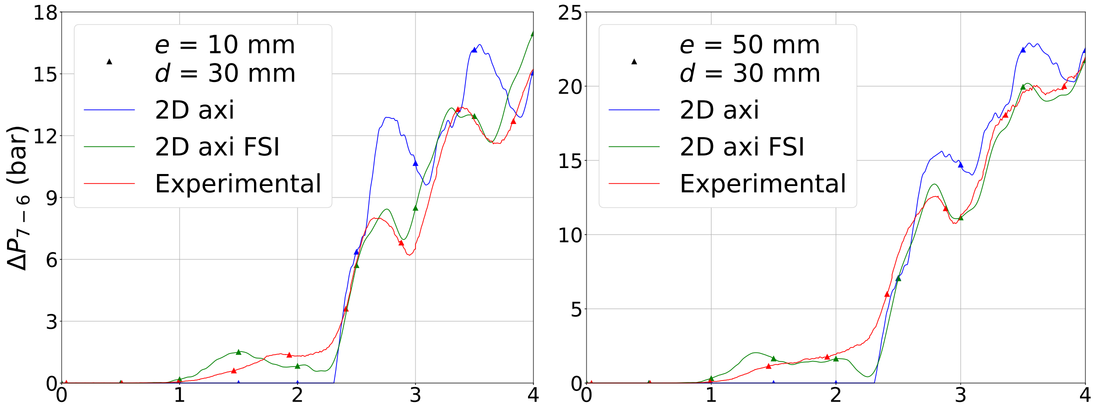

(c) $e = 10\,\text{mm},\ d = 30\,\text{mm}$ (d) $e = 50\,\text{mm},\ d = 30\,\text{mm}$

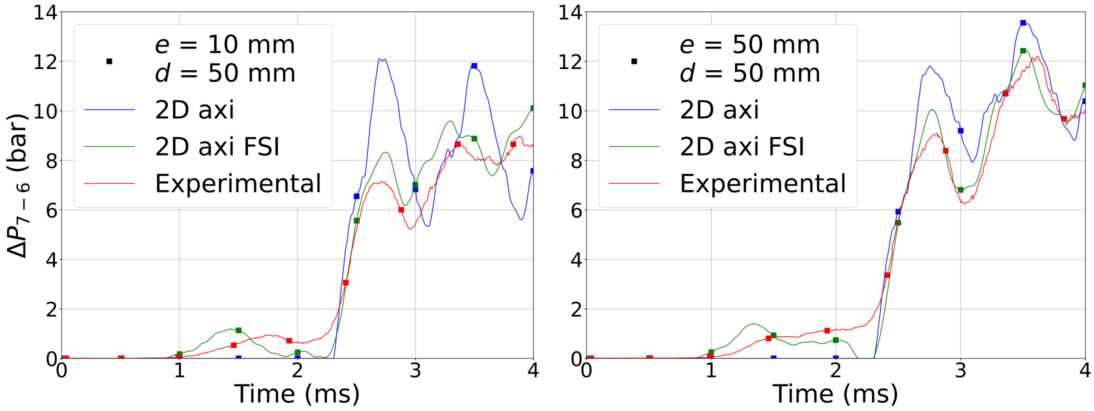

(e) $e = 10\,\text{mm},\ d = 50\,\text{mm}$ (f) $e = 50\,\text{mm},\ d = 50\,\text{mm}$

Figure 4.21: Pressure difference between sensors C6 and C7, ΔP_{7-6}, for all orifice plates. Focus on $0 < t < 4\,\text{ms}$.

Full time evolution at sensors C5 and C8 Figures 4.22, 4.23, 4.24 and 4.25 depict the evolution of pressure at sensors C5 (below the orifice plate) and C8 (above the orifice plate) for all geometric configurations. These trends further corroborate the presence of the phenomenon described previously: a slight, anticipated decrease in pressure for the fluid located below the orifice plate (sensor C5) and a slight, anticipated increase for the fluid above it (sensor C8). As previously explained, it is evident that the FSI simulation successfully replicates this phenomenon, closely tracking the experimental curve. Conversely, in the fixed-structure simulation, this phenomenon is absent. Notably, for sensor C8, the FSI simulation for thin orifice plates (Fig. 4.24) excellently reproduces the experimental pressure oscillations observed for $t > 3\,\text{ms}$, in contrast to the fixed-structure simulation.

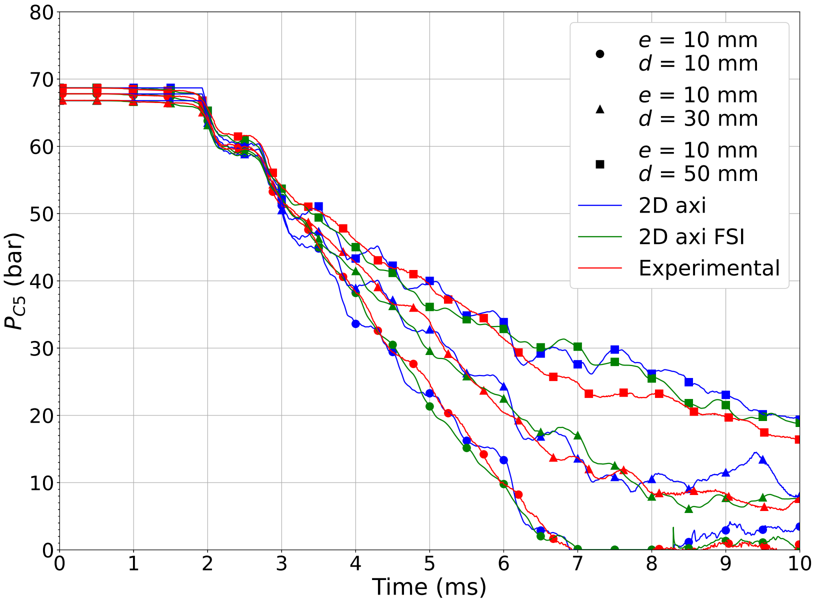

Figure 4.22: Pressure evolution for sensor C5, P_5, for all thin orifice plates ($e = 10\,\text{mm}$).

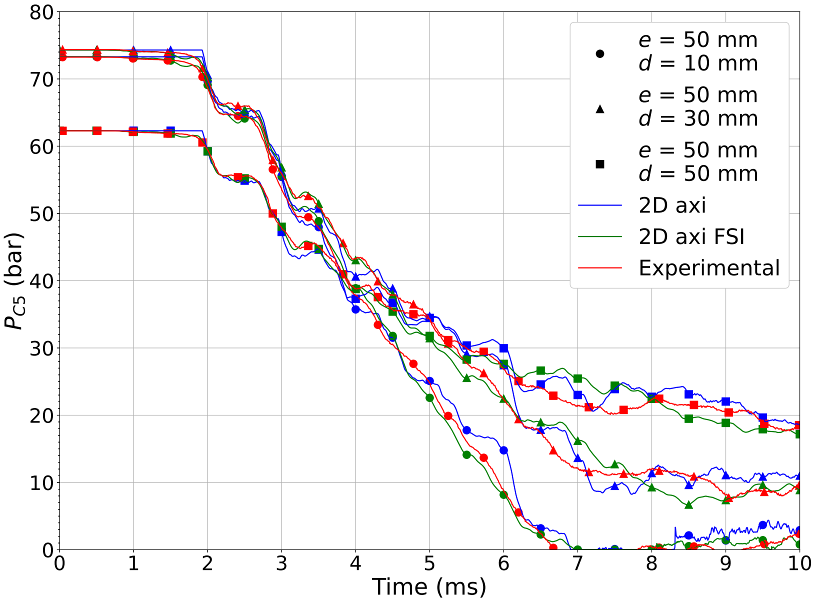

Figure 4.23: Pressure evolution for sensor C5, P_5, for thick modular orifice plate ($e = 50\,\text{mm}$).

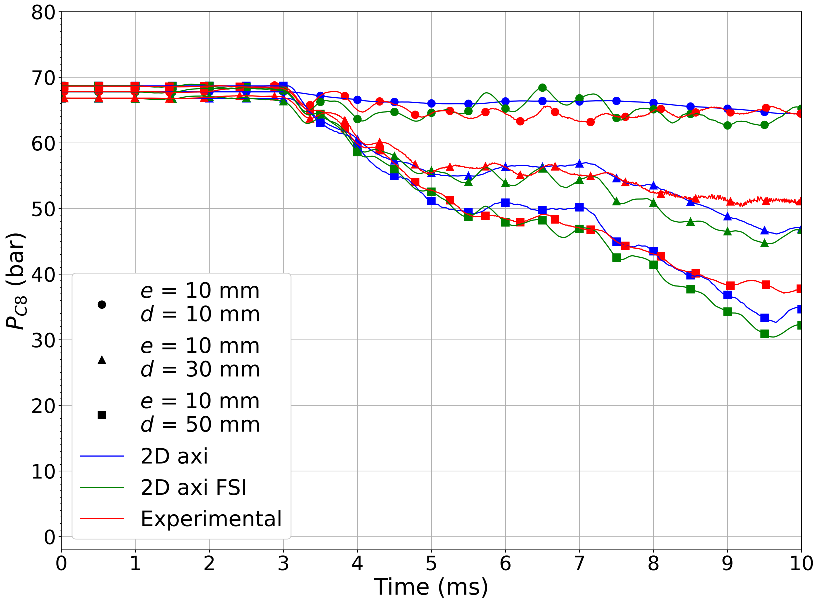

Figure 4.24: Pressure evolution for sensor C8, P_8, for all thin orifice plates ($e = 10\,\mathrm{mm}$).

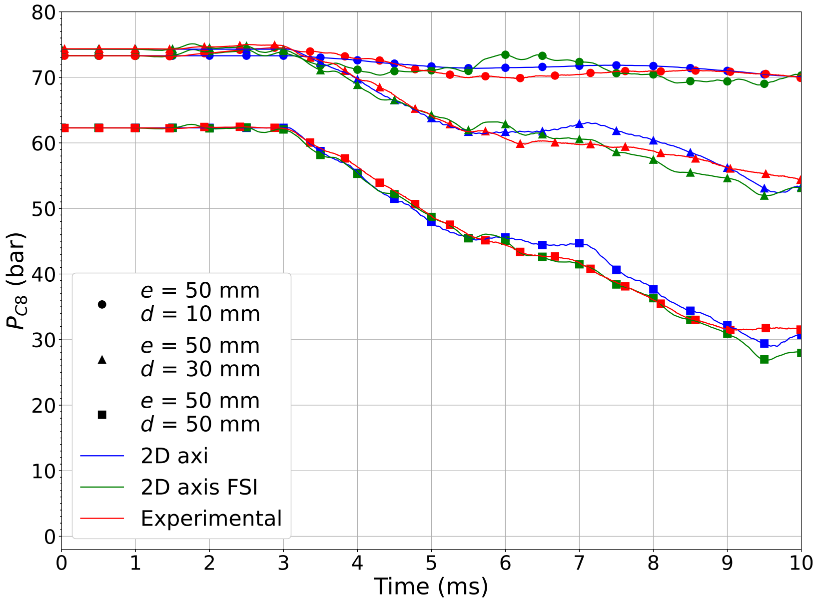

Figure 4.25: Pressure evolution for sensor C8, P_8, for thick modular orifice plate ($e = 50\,\mathrm{mm}$).

Pipe deformation By conducting the FSI calculations, it becomes possible not only to account for the deformation of the pipe and assess its impact on wave propagation in the fluid but also to evaluate the mechanical stress exerted on the structure. Specifically, the component experiencing the greatest stress is the orifice plate, which, as observed thus far, undergoes an increasingly abrupt transient pressure differential, especially as its orifice size decreases.

The geometric configuration of orifice plate that is most penalising from the point of view of deformation is the one with the smallest thickness (lower stiffness) and smallest orifice diameter (higher generated pressure difference), i.e. configuration [$e = 10\,\text{mm}$, $d = 10\,\text{mm}$].

Figure 4.26 shows, as an example, the deformation undergone by the above-mentioned configuration, at $t = 7\,\text{ms}$, in terms of radial (x-component) and axial (y-component) displacement. It is evident that the orifice plate is subjected to a bending stress directed downward due to the pressure differential existing between its two sides. To provide an order of magnitude, the maximum displacements experienced by the orifice plate in the radial direction are of the order of a few tens of micrometers, whereas in the axial direction, they are approximately in the millimeter range (that is two orders of magnitude larger than the radial component).

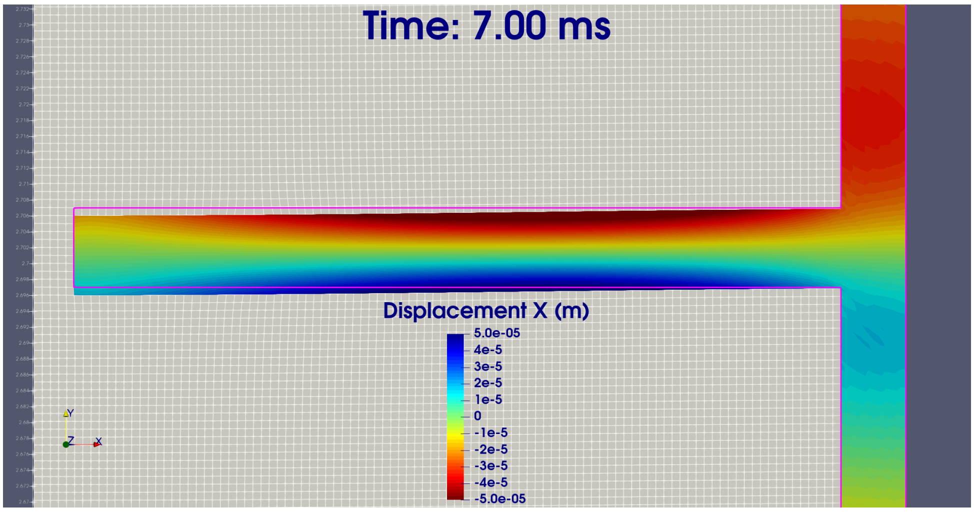

(a) Displacement x-component.

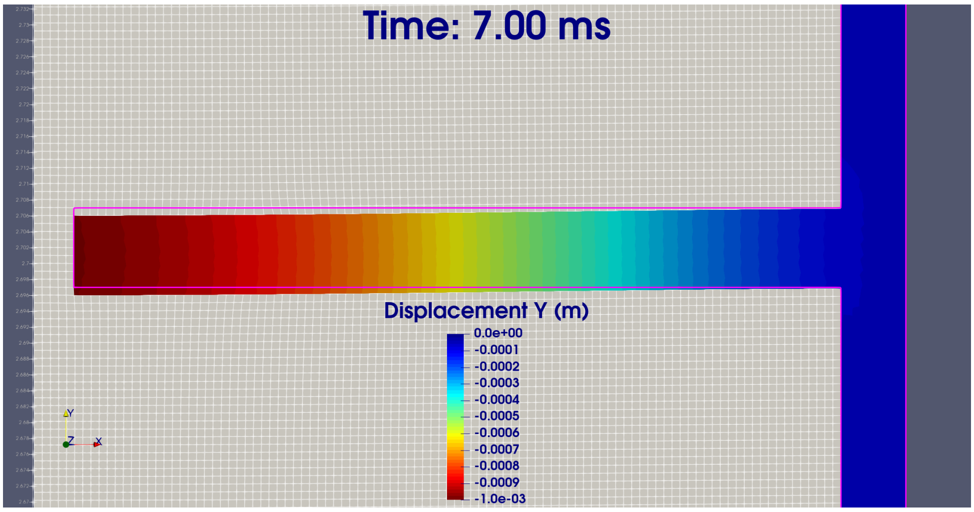

(b) Displacement y-component.

Figure 4.26: 2D axisymmetric thin orifice plate [$e = 10\,\text{mm}$, $d = 10\,\text{mm}$] displacement profiles at $t = 7\,\text{ms}$. In violet, the profile of the undeformed orifice plate at $t = 0\,\text{ms}$.

The x-component of displacement highlights how the upper fibers of the orifice plate are subjected to tensile stress (displacements in the negative x-direction), while conversely, the lower fibers are subject to compressive stress (displacements in the positive x-direction), almost symmetrically. Simultaneously, the y-component of displacement clearly illustrates the extent to which the orifice plate undergoes deformation in the axial direction, downward (negative y-direction), with a maximum displacement occurring at the orifice plate's hole and progressively decreasing to zero moving radially towards the junction area between the orifice plate and the pipe.

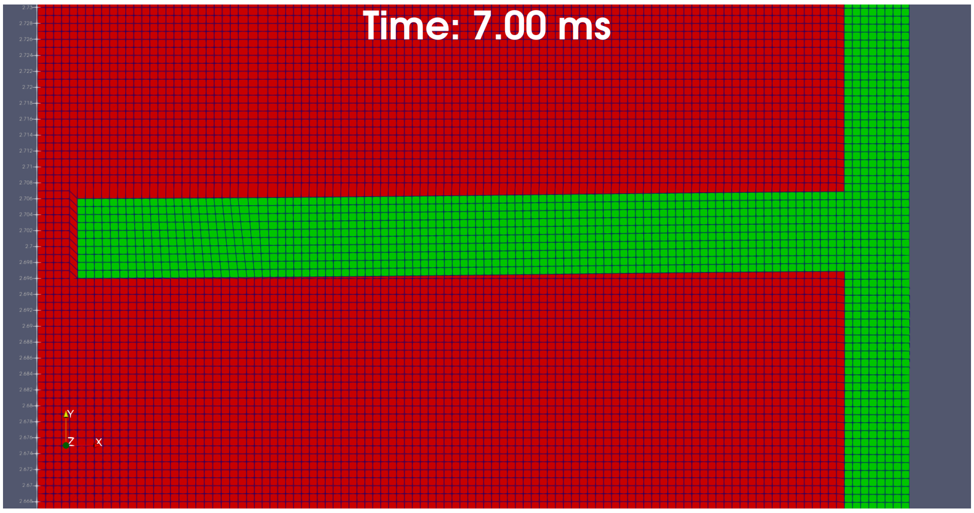

(a) Without automatic rezoning.

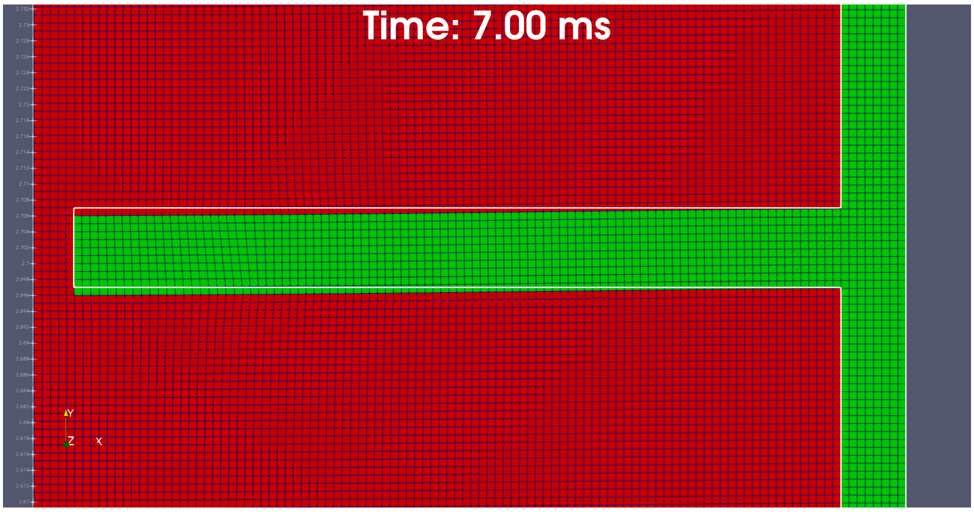

(b) With automatic rezoning. In white, the profile of the undeformed orifice plate at $t = 0\,\mathrm{ms}$.

Figure 4.27: 2D axisymmetric mesh deformation for thin orifice plate [$e = 10\,\mathrm{mm}$, $d = 10\,\mathrm{mm}$] at $t = 7\,\mathrm{ms}$.

Lastly, it is noteworthy to mention that in the conducted FSI computations, an automatic mesh rezoning algorithm available in EUROPLEXUS [62] was employed to control the grid motion in the ALE computation. As previously explained, these FSI calculations utilize both a Lagrangian description and an ALE description for the structure and the fluid, respectively. This approach enables the structural mesh to deform in accordance with the solid's deformation and allows the fluid mesh to deform in response to the structural displacement with which it is coupled.

Figure 4.27 presents the deformation of the 2D axisymmetric mesh for the FSI computation at $t = 7\,\mathrm{ms}$ in the vicinity of the orifice plate, an area where the grid is most perturbed. In the case where the mesh rezoning algorithm is not employed (Fig. 4.27 (a)), the coupling approach applied at the interface between the fluid and the structure (not detailed here for the sake of simplicity) causes the grid motion in the ALE description (fluid mesh) to apply solely to the elements in direct contact with the solid mesh, resulting in substantial distortions. As a consequence, the fluid elements directly above the orifice plate progressively expand to follow the structure's displacement, while those below are squeezed. In particular, the latter, if too much reduced in size, may lead to convergence issues in explicit numerical computations. The time-step used in the temporal discretization is progressively adjusted during the simulation to comply with the imposed stability condition, and it is directly proportional to the size of the smallest mesh element. Consequently, if at any point, a mesh element becomes infinitely small, a very small time-step will be calculated, such that the simulation will not converge.

As depicted in Figure 4.27 (b), the automatic rezoning algorithm effectively addresses the issue described earlier, as it manages grid motion for the ALE calculation and successfully maintains a nearly uniform fluid mesh throughout the simulation.

4.5 Conclusions

The propagation of a transient rarefaction wave through a pipe equipped with a diaphragm of varying thickness and inner diameter has bee studied both experimentally on the MADMAX platform and numerically using a hierarchy of model implemented in the EUROPLEXUS code. The experiment provides reference results allowing to assess the accuracy of the numerical prediction, depending on the level of simplification introduced in the simulation framework. At this stage, no full 3D simulation has been performed (this will be investigated in the next chapter) because it has been considered a 2D axisymmetric description of the core pipe and its environment could provide a "reference" numerical result with which a truly simplified numerical description could be compared. The geometry simplification introduced by the 2D asymmetric simulation is limited to the description of the accumulator in the upper part of the core pipe; the diaphragm is fully described. In the 1D numerical model with impedances, all section changes are described using impedance conditions; the IMPEDANCE GRID condition described in 3.1.4 with complements in C is applied to describe the diaphragm.

The two numerical models investigated are both quite reliable for the simulation of the case study under consideration, particularly with regard to the reproduction of the correct pressure values at the sensors. As one would expect, the 2D axisymmetric model is generally in better agreement with the experimental results, but the 1D model with impedances nonetheless produces satisfactory results, while at the same time allowing a significant gain in terms of greater simplicity of representation (mesh creation) and shorter calculation time required: for simulations up to a physical time of 10 ms, 1D calculations take about 3 minutes each, performed on a single CPU, while 2D axisymmetric calculations, performed in parallel on multiple processors (between 12 and 24 CPUs) take about 100 minutes on average, while the most precise calculations, 2D axisymmetric calculations with FSI, have come to take as long as nearly 24 hours while performed in parallel on 36 processors.

Both models imply a simplified representation of the real geometry of the experimental device, but despite this they can be considered quite valid: the presence of the two connecting elbows on the core pipe is negligible in agreement with the experimental results and makes the choice of an axisymmetric approximation reasonable; the simplified representation of accumulators does not adversely affect the numerical results at least over the observation period considered in this study, but could turn out to lead to significant differences between numerical and experimental results over longer observation periods.

Lastly, the FSI calculations with the WATER model and tabulated EoS enable us to comprehensively assess the phenomenon of cavitation and provide an initial evaluation of the deformations and mechanical stresses experienced by the structure, particularly the orifice plate.

Chapter 5

MADMAX with by-pass pipe and multiple orifice plates

The present chapter discusses numerical and experimental results regarding the complete configuration of the MADMAX experiment which has been presented in Chapter 2. In this configuration, the by-pass pipe has been reinstalled and multiple orifice plates can be arranged there in series up to a maximum of six. The core pipe, at the same time, can be left free or one of the orifice plates used for the simplified configuration can be installed in the middle of it. In this chapter we specifically discuss the configuration with free core pipe and 6 orifice plates in the by-pass pipe: it is the complete configuration for which the experiment was originally designed. The numerical simulations are performed again using EUROPLEXUS following the hierarchy of models presented in Chapter 3. The purpose is to evaluate the predictive capabilities of EUROPLEXUS regarding the passage of multiple rarefaction waves through multiple obstacles and to estimate the pressure difference generated between the core pipe and the by-pass pipe. For the first time, experimental results pertaining to this configuration are presented, along with novel simulations that account for Fluid-Structure Interaction.

5.1 Experimental campaign

5.1.1 Overview of tested configurations

The complete configuration of MADMAX with 6 orifice plates (each of thickness $e = 5\,\mathrm{mm}$ and orifice diameter $d = 17\,\mathrm{mm}$) in the by-pass pipe and the free core pipe will be referred to as **Configuration 1**. Two other configurations, respectively **Configuration 2** and **Configuration 3** will be analyzed in the next chapter. The characteristics of the three configurations can be summarized as follows:

1. **Configuration 1:** free core pipe and 6 orifice plates in the by-pass pipe,
2. **Configuration 2:** free core pipe and 4 orifice plates in the by-pass pipe,
3. **Configuration 3:** 1 orifice plate [$e = 10\,\mathrm{mm}$, $d = 30\,\mathrm{mm}$] in the core pipe and 6 orifice plates in the by-pass pipe.

Configuration 2 is designed to investigate the effect of a different number of obstacles placed in series within the by-pass pipe, while Configuration 3 incorporates the same number of orifice plates in the by-pass as Configuration 1, but an additional orifice plate is added in the core pipe to analyze the effect of the simultaneous presence of obstacles in both branches of the experiment, thus approaching even closer to the real industrial case. Details on the key steps of the experimental campaign leading to the results analyzed hereafter can be found in Paragraph 2.2.2. An important parameter for the proper setup of the numerical simulations is the bursting pressure. The bursting pressures corresponding to the three experiments are collected in Table 5.1.

Table 5.1: Experimental bursting pressure for MADMAX complete set-up.

EXP	**Configuration 1** (6 o.p. in by-pass)	**Configuration 2** (4 o.p. in by-pass)	**Configuration 3** (6 o.p. in by-pass + 1 o.p. e10d30 in core)
P_{burst} (bar)	**61.6**	**68.0**	**76.5**

5.1.2 Pressure evolution and flow description

Figure 5.1 shows the experimental measurements of pressure temporal evolution in the first 20 ms of transient for all installed sensors for Configuration 1. One piezoresistive pressure sensor (C1) is installed on the junction pipe, six piezoelectric pressure sensors (C2, C4, C5, C6, C7, and C8) are installed on the core pipe, and five piezoelectric pressure sensors (D1, D2, D3, D4, and D5) are installed on the by-pass pipe. As visible from the diagrams in Paragraph 2.2.2, the five sensors D1-D5 are at the same respective elevations as sensors C4-C8.

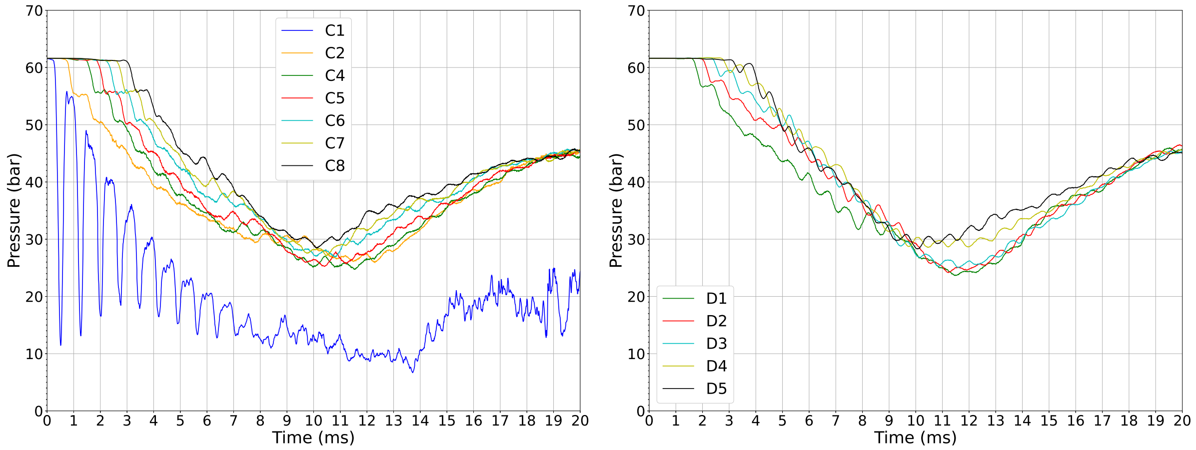

(a) Junction pipe (C1) and core pipe (C2-C8).

(b) By-pass pipe (D1-D5).

Figure 5.1: Experimental pressure evolution for all sensors for Configuration 1.

To achieve a better understanding of the physics at work in the experiment, we also provide in this section snapshots of the flow taken from the 3D numerical simulations conducted on this configuration. The purpose at this stage is merely to complement the local information provided by the sensors with a global view of the flow features provided by the simulation - a quantitative comparison between experiment and simulations will be performed in the next section.

Three zones can be distinguished in the experiment:

- the lower part, which ranges from the junction pipe to sensors C4-D1. Figures 5.3 and 5.4) provide pressure contours in this lower part at successive time instants;
- the middle part, which comprises the entire by-pass pipe and the corresponding part of the core pipe, thus sensors C4-C8 and D1-D5. Figures 5.5 and 5.6) provide pressure contours in this middle part at successive time instants;
- the upper part, above sensors C8 and D5 and which also includes the accumulators. Figures 5.7 and 5.8) provide pressure contours in this upper part at successive time instants.

The snapshots provided in Figures 5.3 to 5.8 display the pressure distribution along a vertical section of the experiment at various time instants, focusing on four wave fronts propagating:

- the first at 61.6 bar corresponds to the initial rarefaction wave directly produced by the bursting disk opening;
- the second, third and fourth take respectively place at 54 bar, 49 bar and 45 bar.

Of course, it should be noted that there is not an exact correspondence between the results of the 3D simulation and the experimental ones. In particular, some differences are observed in the acoustic signal propagation, especially in the by-pass pipe, as will be seen in the Section 5.3 (Simulation-experiment comparison) later on. Nevertheless, the overall trends of the pressure evolution are reproduced quite satisfactorily so that these numerical flow fields can be used here to provide a qualitative description of the experiment's physics.

The physical interpretation of the experimental results for the junction pipe/core pipe part is roughly the same as that presented for the simplified configuration of MADMAX in Section 4.1. At the opening of the bursting disk a rarefaction wave is produced and propagates upwards in the junction pipe; at the moment it reaches the connection with the core pipe the wave is partly reflected back and partly transmitted into the core pipe depending on the ratio of the cross sections of the two pipes; as the junction pipe is relatively short, multiple transmissions/reflections can therefore be observed in the first 10 ms of observation, as can clearly be seen from the C1 sensor in Figure 5.1 (a).

Referring to the results of the 3D simulation in Figures 5.3 and 5.4, we can clearly identify the key moments concerning the propagation of the first rarefaction wave at 61.6 bar and how the transmission/reflection mechanism acts in the junction pipe. Already at $t = 0.1$ ms, the formation of multiple wave fronts can be observed: there is not a single wave front at 61.6 bar because the bursting disk opening is not instantaneous but is controlled by an exponential function (as described in Paragraph 3.1.4) that gradually opens the bursting disk over a characteristic time imposed by the user (0.12 ms in our case). The front at 61.6 bar reaches the connection between the junction pipe and the core pipe at $t \approx 0.38$ ms (propagating at approximately 1310 m/s in water according to Allievi's correction and therefore having to travel the 50 cm length of the junction pipe). There, part of the wave is transmitted, as mentioned, to the core pipe, while the majority returns back, reaching the opening of the junction pipe in double the time (at the level of the opening, with no bursting disk, we are in ambient conditions and with a ratio between the opening section and the external environment equal to zero, causing a complete reflection of the wave which will then propagate upwards again). The second wave front at 54 bar starts to propagate in the core pipe at $t \approx 1.15$ ms, when the wave has thus traveled back up through the junction pipe, and so on for the subsequent wave fronts.

Meanwhile, the first rarefaction wave propagating in the core pipe, the one at 61.6 bar, reaches sensor C2 shortly after 0.7 ms and sensor C4 at around 1.5 ms, while it enters the by-pass pipe at around 1.1 ms to encounter the first orifice plate at around 1.5 ms and subsequently sensor D1 at about 1.8 ms.

The signal is cascaded to the sensors in the core pipe (C2, C4, C5, C6, C7 and C8), the measured pressure of which decreases following a sequence of steps. The pressure signal between one sensor and the following one in the core pipe (C2-C8) is simply delayed by the distance that physically separates them.

Note that in this case, unlike the simplified configuration (Chapter 4), we do not observe any significant transient pressure difference between sensors C2-C4 and sensors C7-C8, since there are no obstacles in the core pipe. Instead, we only find, as mentioned, the delay due to the distance between the sensors. However, we will encounter this behavior in Configuration 3, which will be analyzed in the next chapter.

Regarding the evolution of pressure in the by-pass pipe (see Figures 5.1 (b) and 5.2), several effects can be observed: for sensors D1-D5, firstly, there is a delay in the arrival of the pressure signal compared to the corresponding sensors C4-C8. This delay is due to the longer path the signal must travel due to the presence of the lower elbow pipe. Additionally, the effect of the presence of the orifice plates is clearly visible, as the pressure in the by-pass for each sensor is not only shifted forward but also remains slightly higher. This is because part of the pressure signal is partly reflected by each orifice plate. Also, the change in section and direction between the core pipe and the by-pass pipe has an effect on the pressure drop, but it can be considered negligible compared to the effect of the orifice plates.

From Figures 5.1 (b) and 5.2, it can be observed that for sensors D4-D5, there is a peculiar behavior: after the first pressure drop, the steps between successive pressure drops are wider compared to those of sensors located lower (D1-D3). This is because while the rarefaction wave propagates upward in the by-pass, it also continues to propagate in the core pipe, covering less distance and entering the by-pass pipe from the upper elbow tube at around 3.5 ms (as shown in Figure 5.5 (h)). Consequently, the wave entering from the top will interfere with the one traveling through the by-pass from below, amplifying the pressure drop for the sensors located higher in the by-pass, particularly D5. From Figure 5.6, it can be seen how the pressure gradually equalizes across the various sections of the by-pass pipe, eventually reaching a nearly uniform distribution around 8-10 ms.

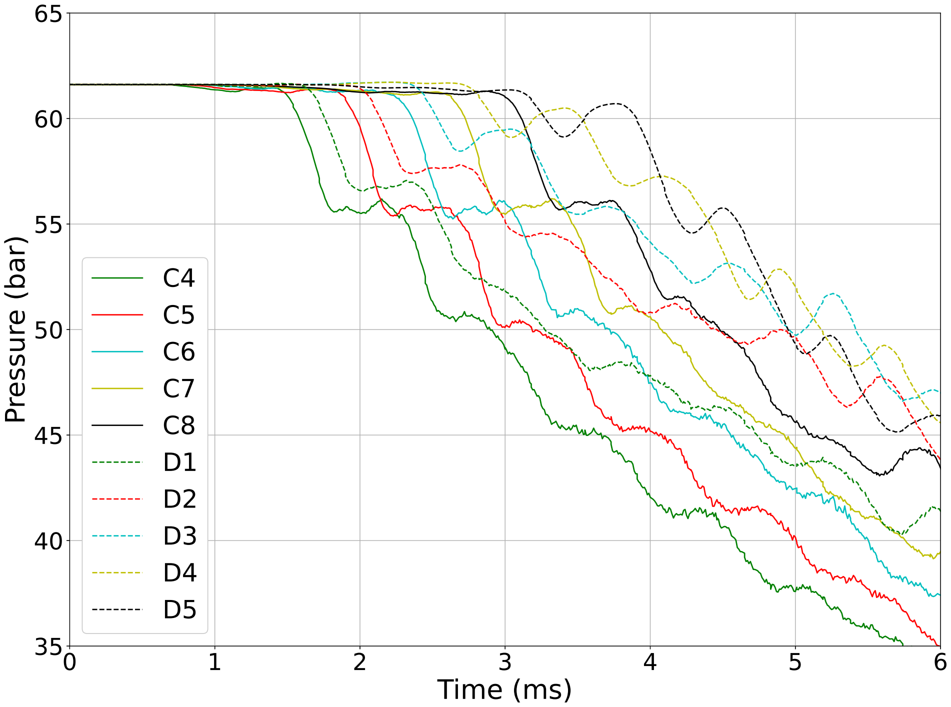

Figure 5.2: Experimental pressure evolution for sensors C4-C8 and D1-D5 for Configuration 1.

Finally, from Figure 5.1, we can observe around 10-11 ms that the pressure for all sensors begins to rise again. This is due to the effect of the accumulators, which continue to inject water into the pipes.

Figures 5.7 and 5.8 depict the pressure evolution in the upper part of the experiment, including the accumulators: at $t \approx 5$ ms, the first rarefaction wave reaches the accumulators, and the pistons begin to move due to the depressurization on the fluid side, which disrupts the equilibrium with the nitrogen on the other side. Consequently, the nitrogen expands in an attempt to maintain pressure equilibrium with the fluid, thereby pushing the pistons (see Figure 5.9, which shows the average nitrogen pressure evolution and the displacement in the y direction of the two pistons relative to the initial position). By the end of the transient, in 20 ms, the two pistons moved approximately 30 mm and the nitrogen pressure has dropped to approximately 57.8 bar, gradually increasing the pressure in the pipes.

Equipped with this knowledge of the main flow features associated with Configuration 1, let us now proceed to the description of the numerical simulations also applied to the analysis of this configuration.

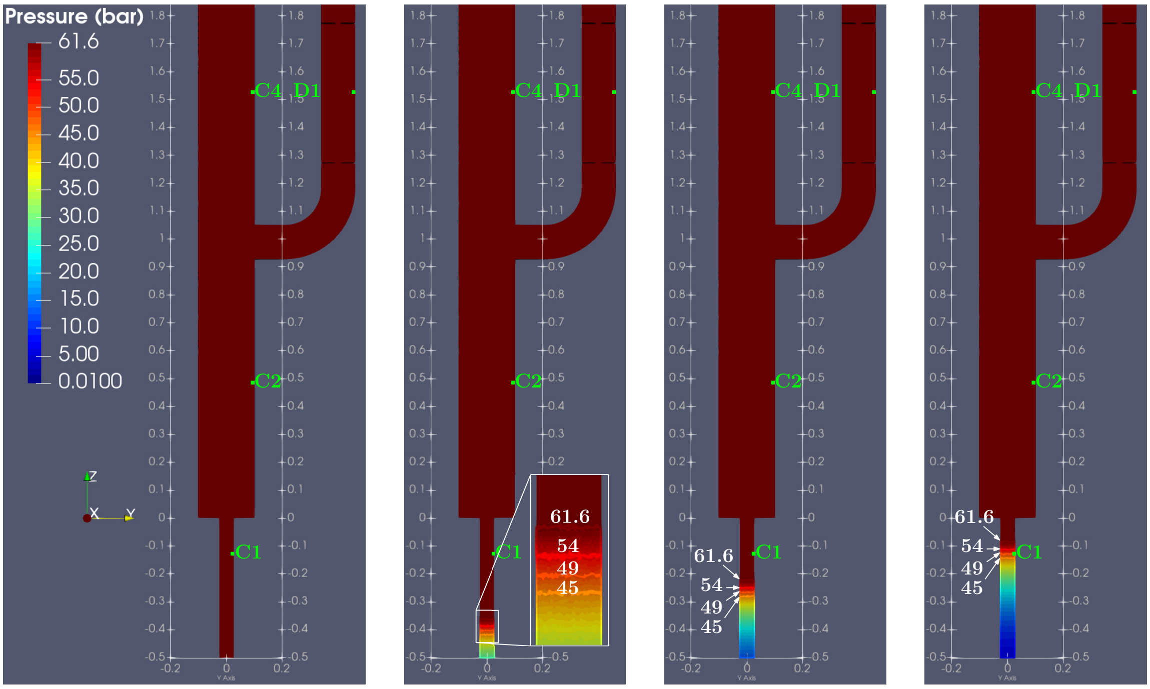

(a) $t = 0.0\,\mathrm{ms}$ (b) $t = 0.1\,\mathrm{ms}$ (c) $t = 0.2\,\mathrm{ms}$ (d) $t = 0.3\,\mathrm{ms}$

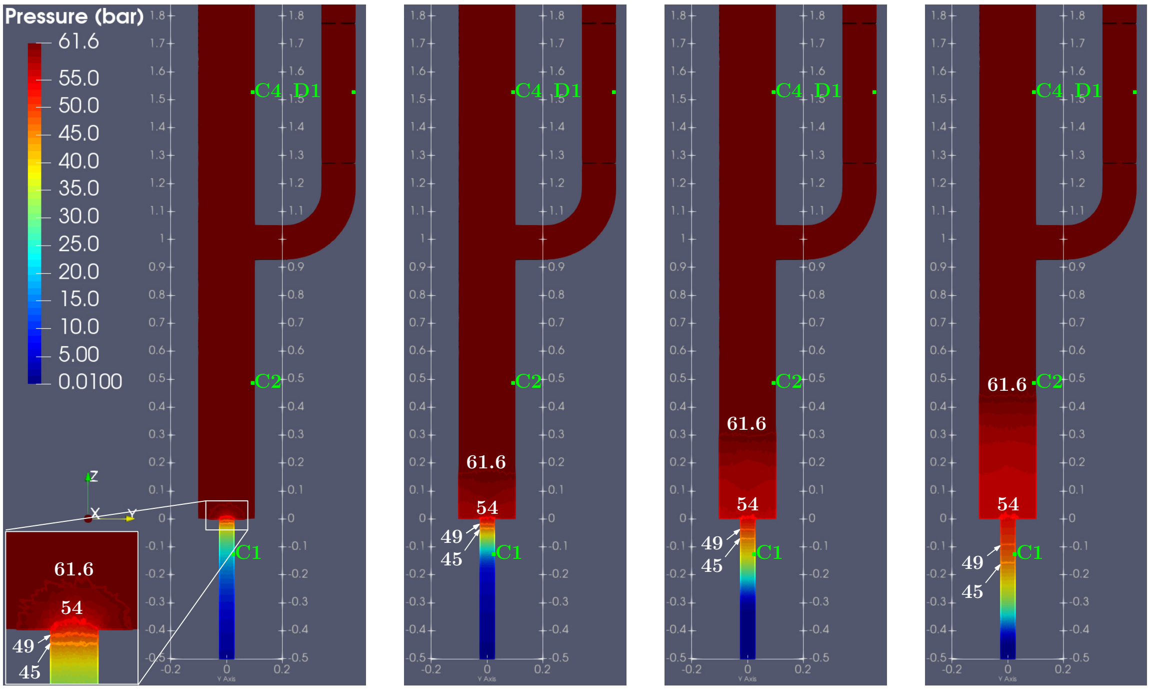

(e) $t = 0.4\,\mathrm{ms}$ (f) $t = 0.5\,\mathrm{ms}$ (g) $t = 0.6\,\mathrm{ms}$ (h) $t = 0.7\,\mathrm{ms}$

Figure 5.3: Pressure evolution in the lower part of MADMAX for $0 \leq t \leq 0.7\,\mathrm{ms}$ (cross section of 3D simulation).

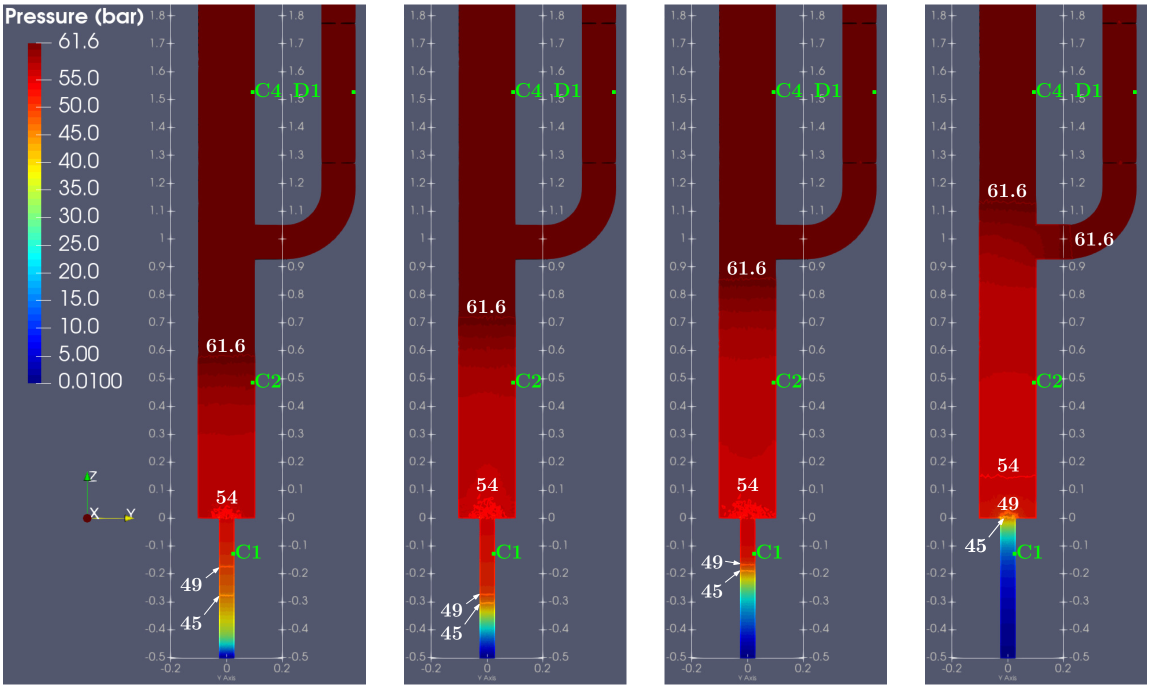

(a) $t = 0.8\,\mathrm{ms}$ (b) $t = 0.9\,\mathrm{ms}$ (c) $t = 1.0\,\mathrm{ms}$ (d) $t = 1.2\,\mathrm{ms}$

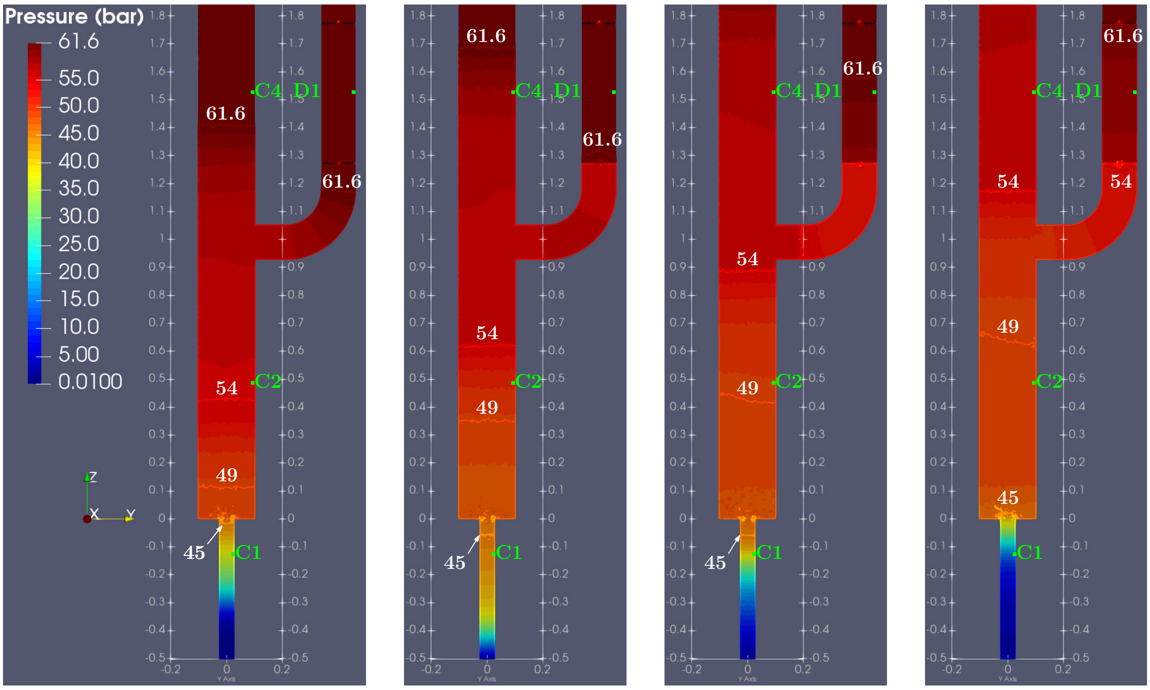

(e) $t = 1.4\,\mathrm{ms}$ (f) $t = 1.6\,\mathrm{ms}$ (g) $t = 1.8\,\mathrm{ms}$ (h) $t = 2.0\,\mathrm{ms}$

Figure 5.4: Pressure evolution in the lower part of MADMAX for $0.8 \leq t \leq 2.0\,\mathrm{ms}$ (cross section of 3D simulation).

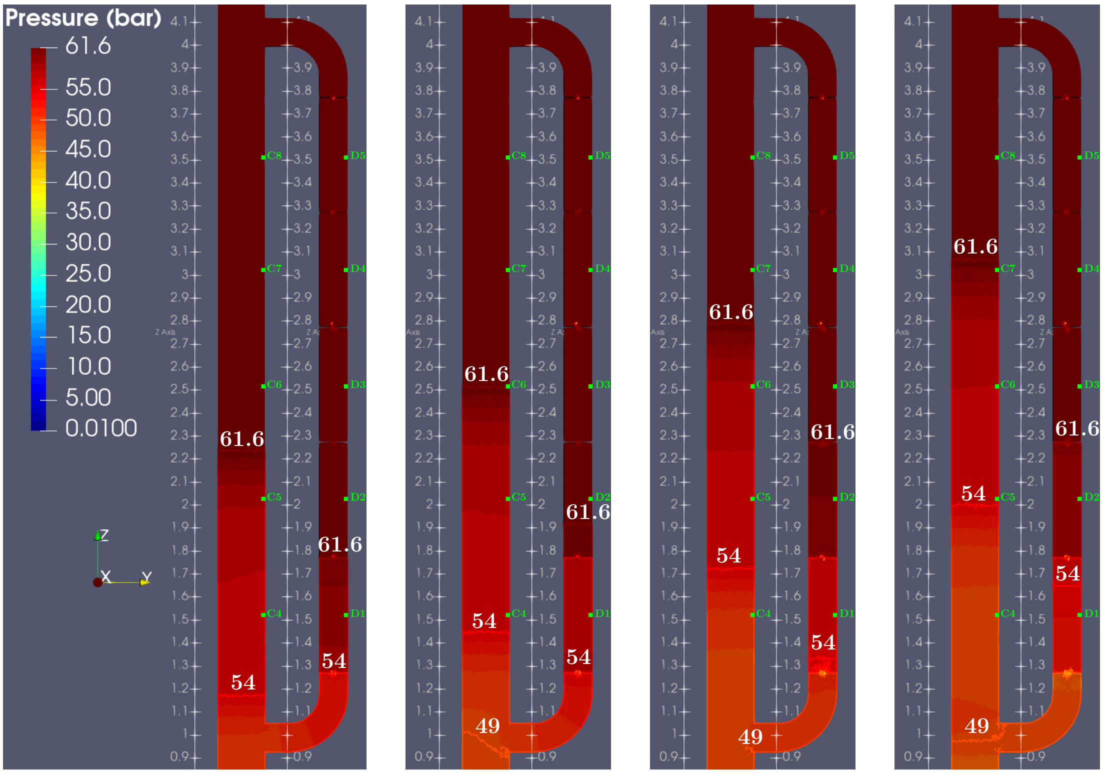

(a) $t = 2.0\,\mathrm{ms}$ (b) $t = 2.2\,\mathrm{ms}$ (c) $t = 2.4\,\mathrm{ms}$ (d) $t = 2.6\,\mathrm{ms}$

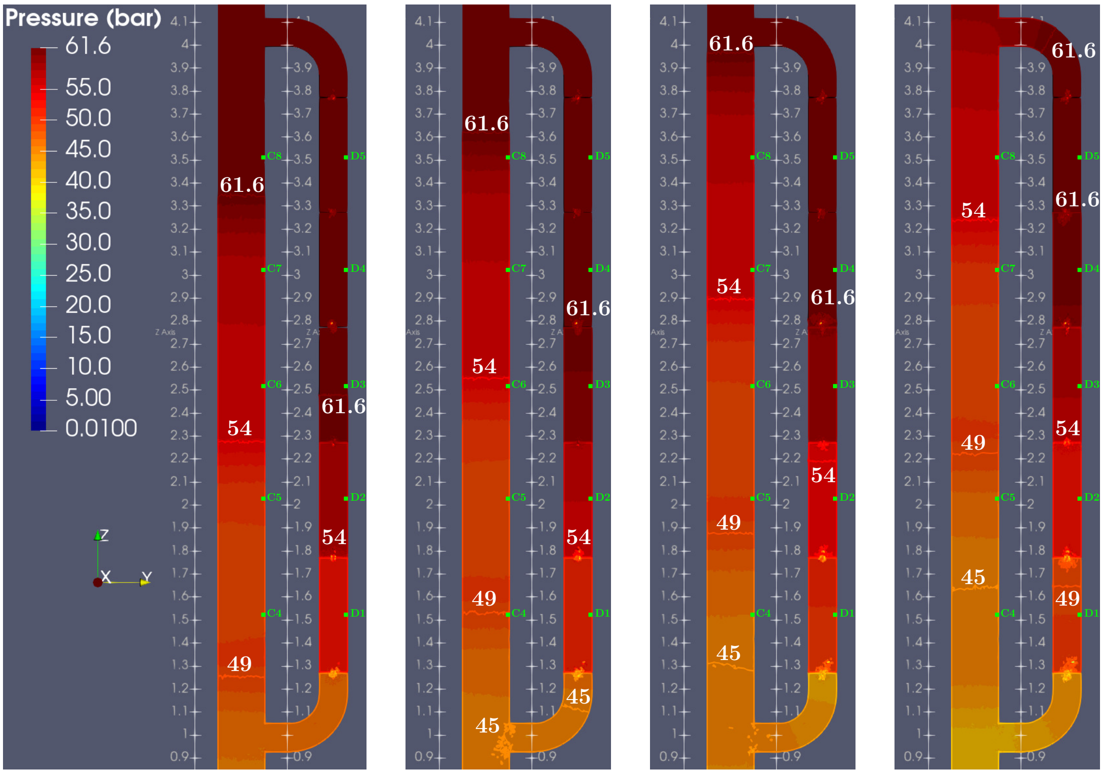

(e) $t = 2.8\,\mathrm{ms}$ (f) $t = 3.0\,\mathrm{ms}$ (g) $t = 3.25\,\mathrm{ms}$ (h) $t = 3.5\,\mathrm{ms}$

Figure 5.5: Pressure evolution in the middle part of MADMAX for $2.0 \leq t \leq 3.5\,\mathrm{ms}$.

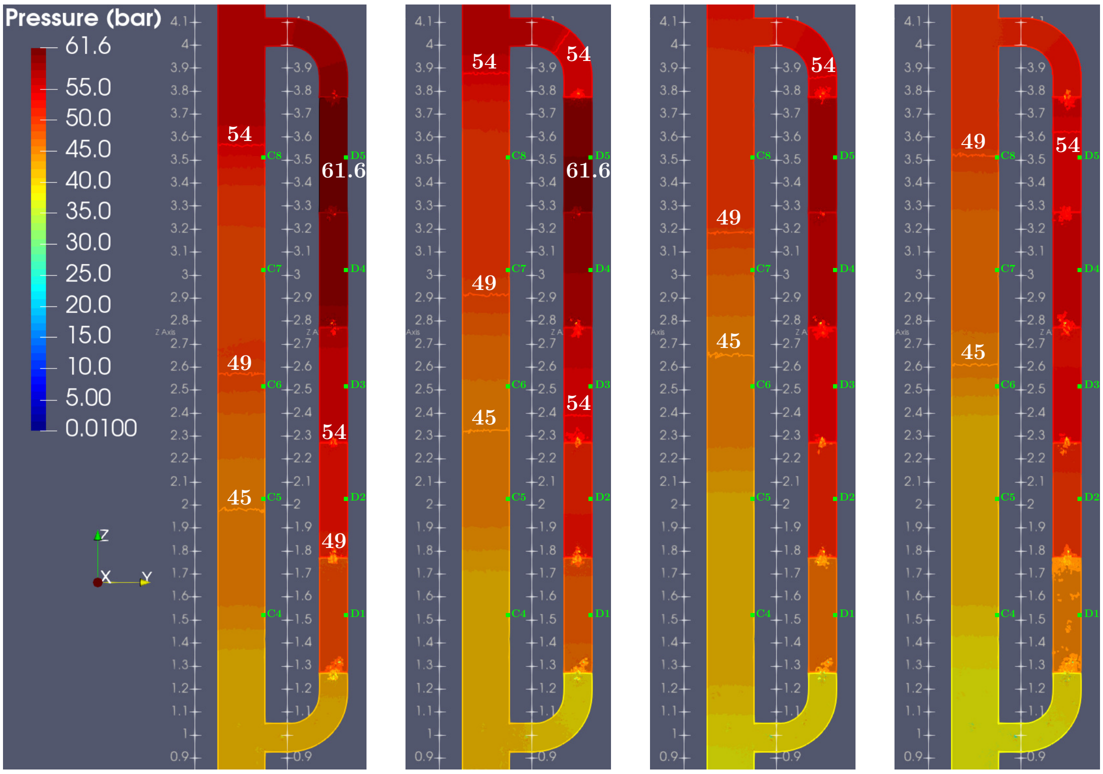

(a) $t = 3.75\,\mathrm{ms}$ (b) $t = 4.0\,\mathrm{ms}$ (c) $t = 4.25\,\mathrm{ms}$ (d) $t = 4.5\,\mathrm{ms}$

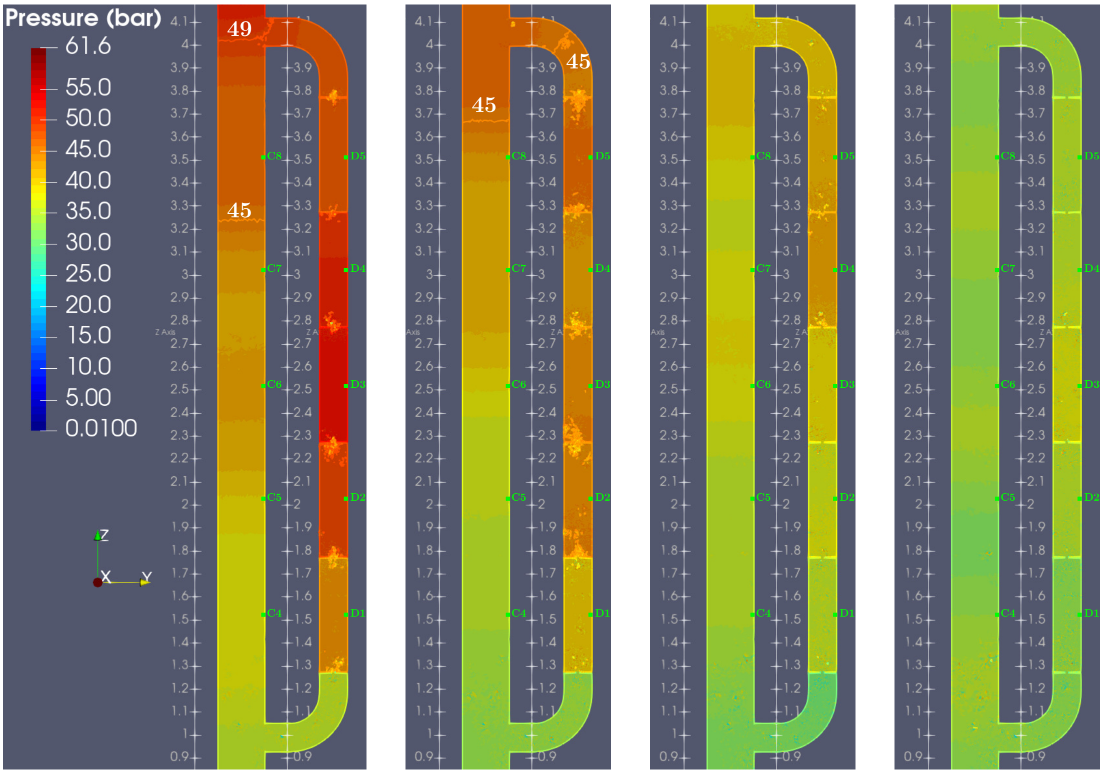

(e) $t = 5.0\,\mathrm{ms}$ (f) $t = 6.0\,\mathrm{ms}$ (g) $t = 7.0\,\mathrm{ms}$ (h) $t = 8.0\,\mathrm{ms}$

Figure 5.6: Pressure evolution in the middle part of MADMAX for $3.75 \leq t \leq 8.0\,\mathrm{ms}$.

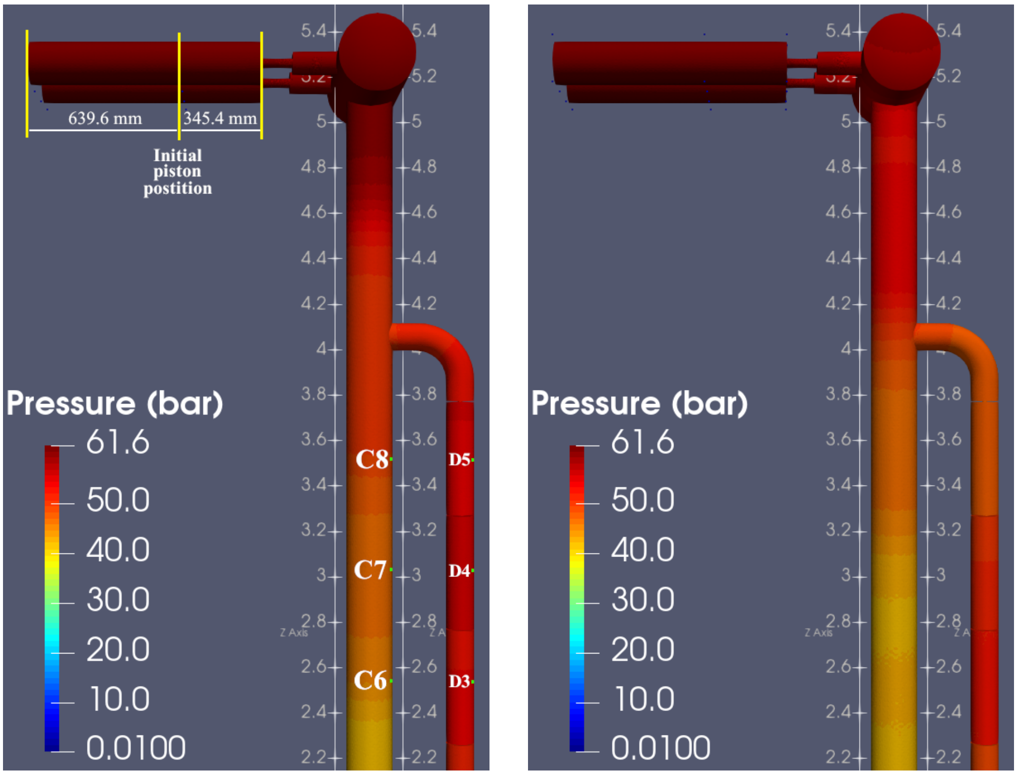

(a) $t = 4.5\,\text{ms}$ (b) $t = 5.0\,\text{ms}$

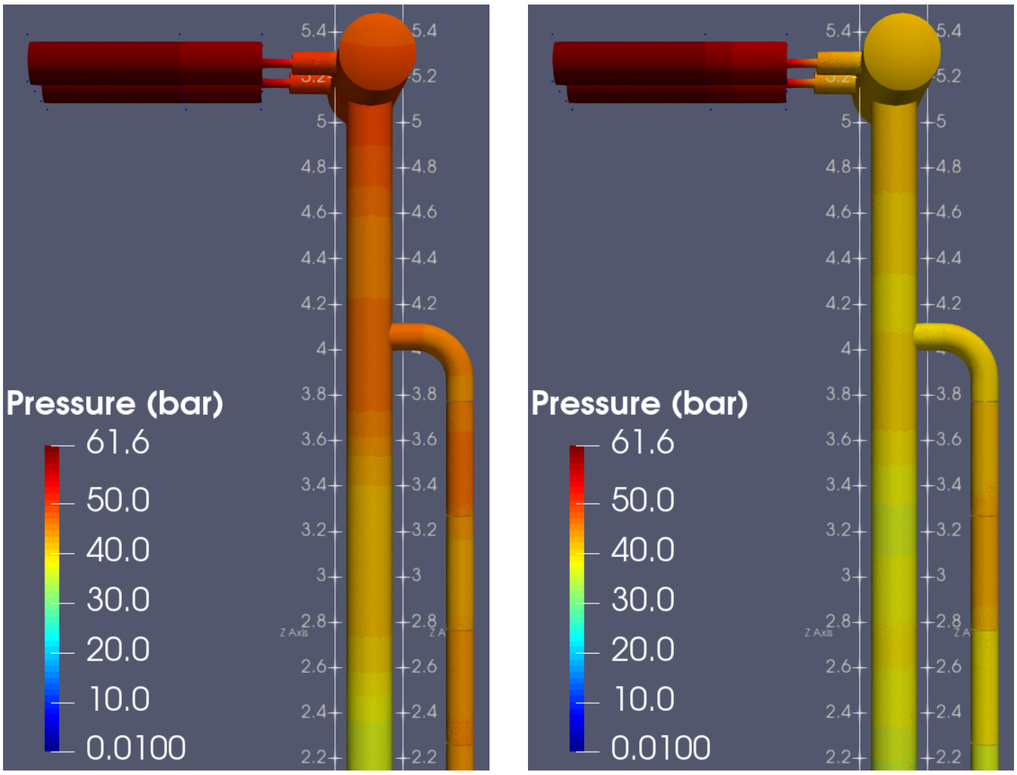

(c) $t = 6.0\,\text{ms}$ (d) $t = 7.0\,\text{ms}$

Figure 5.7: Pressure evolution in the upper part of MADMAX for $4.5 \leq t \leq 7.0\,\text{ms}$.

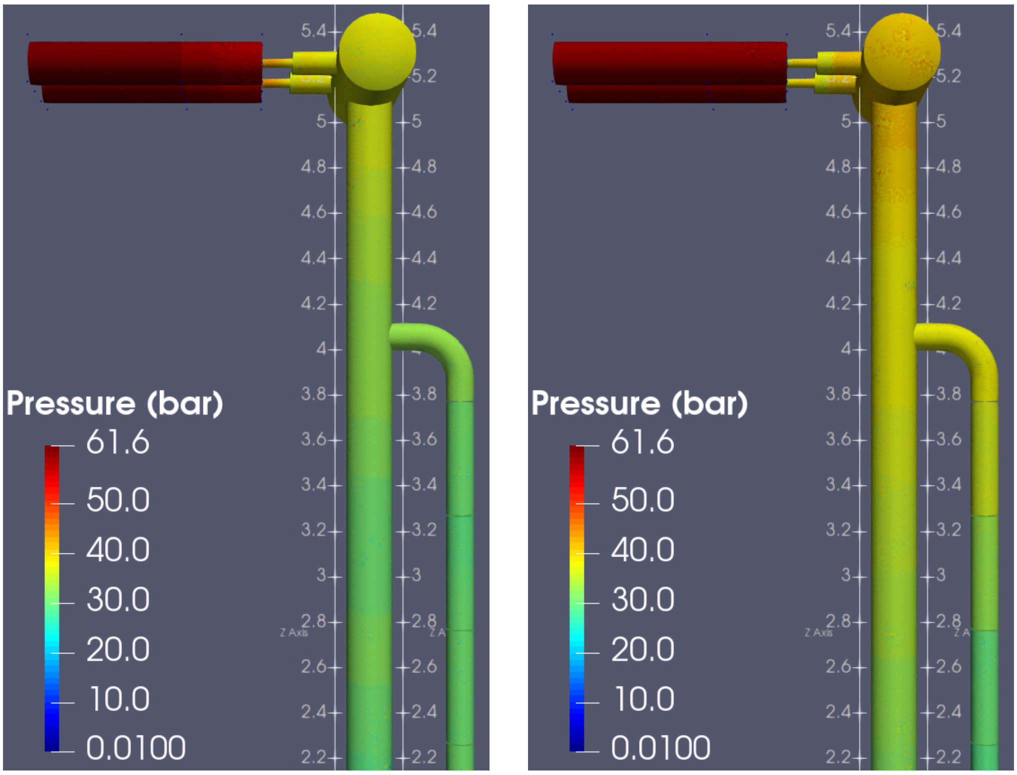

(a) $t = 10.0\,\mathrm{ms}$

(b) $t = 12.5\,\mathrm{ms}$

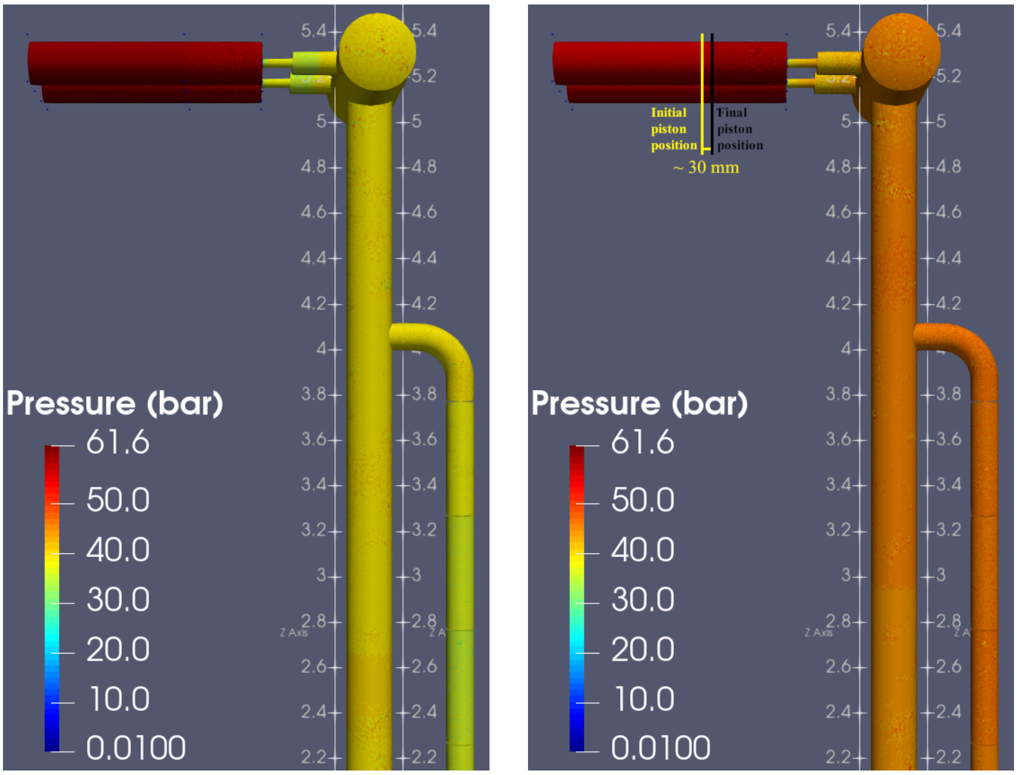

(c) $t = 15.0\,\mathrm{ms}$

(d) $t = 20.0\,\mathrm{ms}$

Figure 5.8: Pressure evolution in the upper part of MADMAX for $10 \leq t \leq 20\,\mathrm{ms}$.

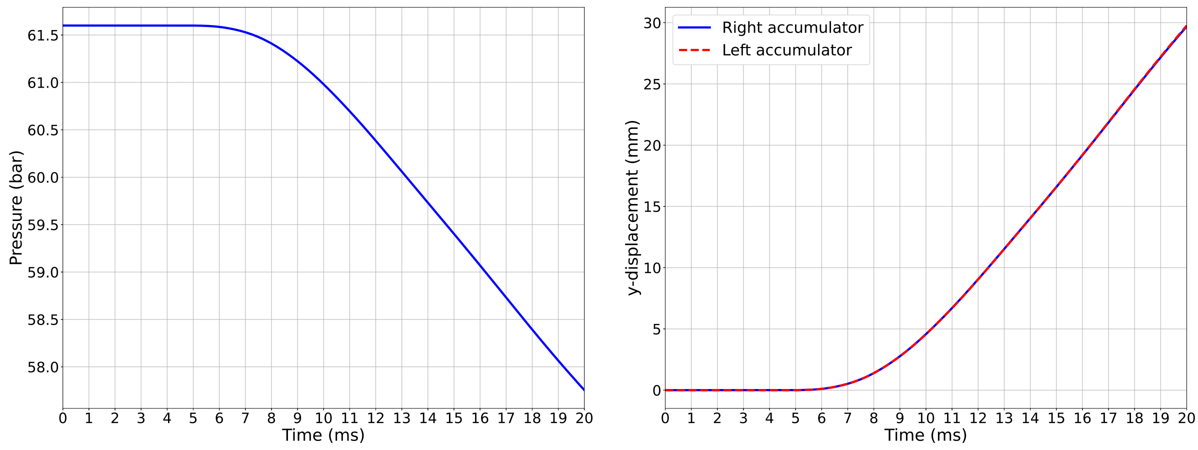

(a) Nitrogen pressure.

(b) Piston y-displacement.

Figure 5.9: Accumulators' average nitrogen pressure and pistons y-displacement for Configuration 1 - 3D calculation.

5.2 Numerical simulations

5.2.1 Overview of the hierarchy of models

Four numerical models (summarized in Section 3.3) are employed to simulate the MADMAX experiment using EUROPLEXUS. Specifically, two 3D models are used as numerical reference models:

- a 3D FLUID model with fixed structures
- a 3D WATER model with Fluid-Structure Interaction (FSI)

Additionally, two simplified (and low-cost) 1D models are also investigated:

- one with fixed structures (similar to the one used in the 1D simulations of the previous chapter on the simplified MADMAX configuration, see Paragraph 4.2.2),
- the other using WATER material, incorporating FSI without directly applying the Allievi correction to the material.

In all four models, the time constant associated with the boundary condition governing the bursting disk opening (IMPEDANCE MEMBRANE, see Paragraph 3.1.4), is configured to be 0.12 ms. For the two fixed-structure models utilizing the FLUID material (see Paragraph 3.1.2.4), the user sets the speed of sound in the fluid, denoted as c, to 1310 m/s after applying the Allievi correction [65].

As explained in Section 4.4, to observe phase change phenomena in the fluid such as cavitation, it is necessary to use the WATER model and perform FSI calculations. In this case, the speed of sound in the fluid is not directly imposed by the user but is calculated through tabulated EoS. For 3D FSI simulations, similar to what was done for the 2D axisymmetric case with FSI (see Paragraph 4.4.2), a solid mesh is physically added externally to the fluid mesh, representing the steel piping, as detailed in the following paragraph. However, for the 1D FSI model, a solid mesh is not added; instead, elastic properties dependent on the geometry and material of the piping are assigned to the 1D elements constituting the fluid. With knowledge of these properties, EUROPLEXUS can calculate how much the piping will deform following the passage of the pressure wave and consequently obtain the corrected speed of sound in the fluid through the tabulated EoS [63].

Simulations are conducted for Configuration 1 using all four models, which will be also applied in the next chapter to Configuration 2 and Configuration 3. In each simulation, the initial fluid pressure is set to the experimental bursting pressures P_{burst} summarized in Table 5.1. The initial density is set to $1000\,\text{kg/m}^3$ for the models with fixed structures, while it is calculated through the tabulated EoS for the FSI simulations, by knowing the initial pressure P_{burst} and the initial temperature (set equal to $20\,^{\circ}\text{C}$). The initial pressure of the gas in the accumulator is also set to P_{burst} to maintain equilibrium with the fluid.

5.2.2 3D/3D FSI calculations

Let us outline the modeling choices regarding the implementation of 3D and 3D FSI simulations.

5.2.2.1 Design and refinement of the 3D mesh

Overview of the mesh structure In Figure 5.10, the 3D mesh constructed (using the software Gmsh [68]) for MADMAX Configuration 1 is displayed, highlighting its key elements:

- both the fluid and gas in the two accumulators are treated with an ALE description and separated by a Lagrangian piston having the mass of the actual piston in the device (approximately 20 kg);

- the remainder of the fluid is treated with an Eulerian description; characteristic dimensions are provided (see Paragraph 2.2.2 for more details);

- the mesh is made of hexahedra, with a refinement increasing proportionally to the geometry's curvature. In the mesh generation process, the algorithm initially generates a mesh composed of tetrahedra, each of which is subsequently subdivided into four hexahedra. The choice to use hexahedra is motivated by EUROPLEXUS's greater capability to handle this type of element when employing the Finite Volume Method (FVM) for spatial discretization.

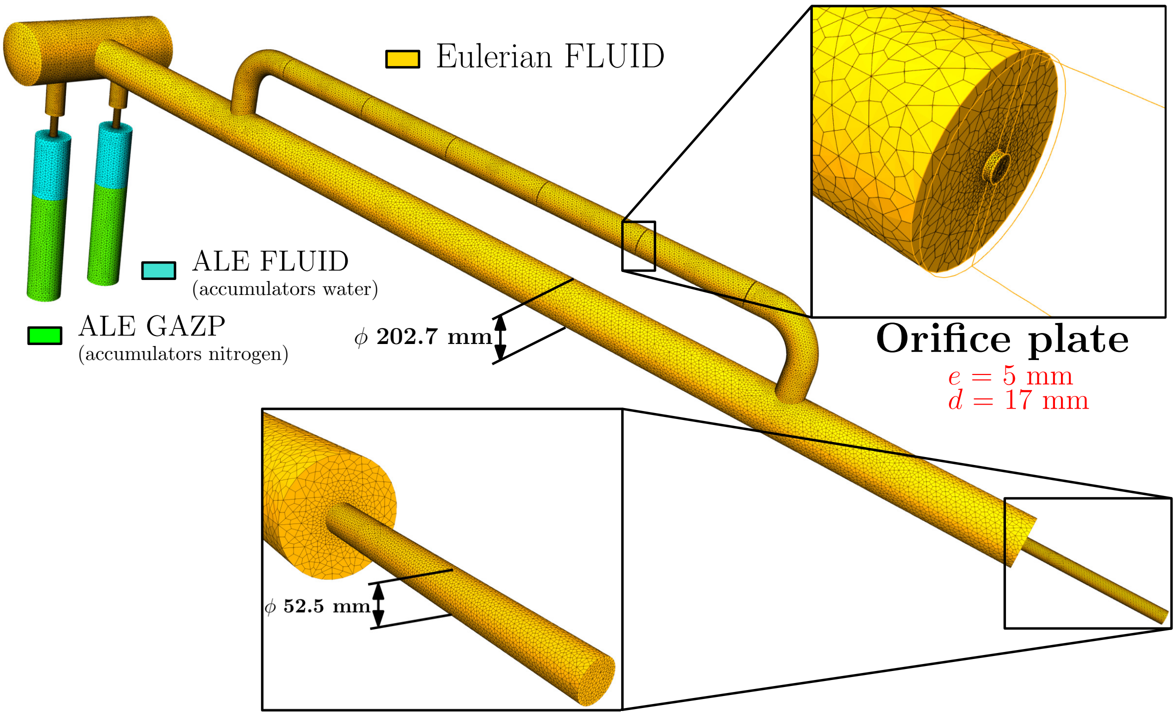

Figure 5.10: 3D mesh.

Mesh generation process and choice of refinement level Starting from the 1D discretization of each edge of the geometry, the algorithm generates the 2D surface mesh composed of triangles for the tetrahedral mesh, which are then subdivided into three quadrangles for the hexahedral mesh. Finally, the respective 3D elements are generated inside the volume of the geometry. Figure 5.11 illustrates the process of generating a 3D hexahedral mesh starting from a simple initial geometry, such as a cylinder.

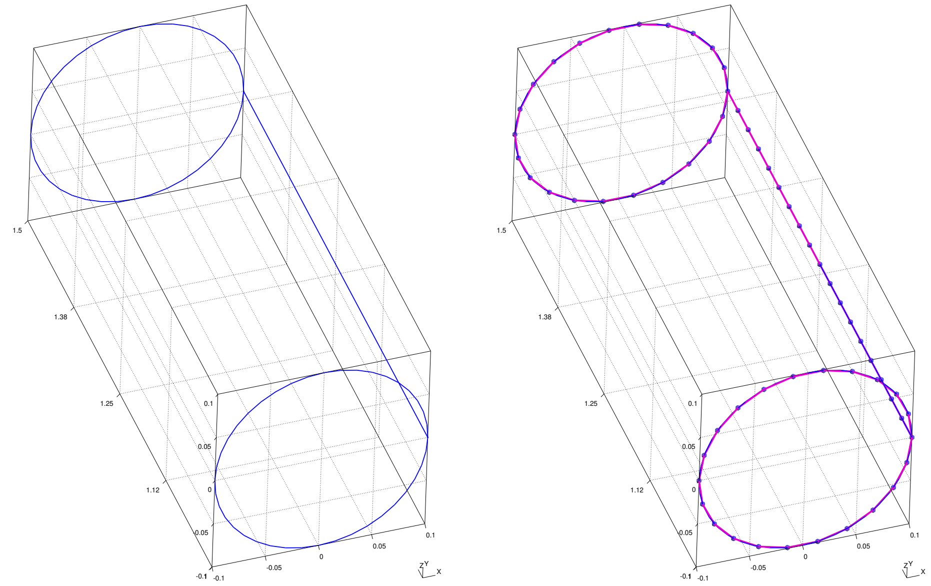

(a) Initial geometry

(b) 1D discretization

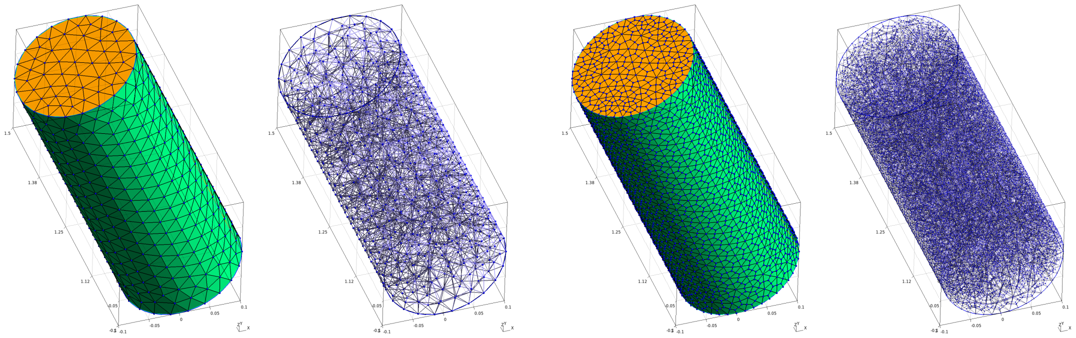

(c) 2D/3D tetrahedral discretization

(d) 2D/3D hexahedral discretization

Figure 5.11: 3D mesh generating process on a sample geometry (cylinder).

The sensitivity analysis on the mesh size is conducted by varying a parameter in the Gmsh software called the Element Size Factor (ESF), which allows us to determine how many parts each segment (circles, curves resulting from the intersection between cylinders, etc.) should be discretized. In the generation of the tetrahedral mesh, each circle representing an edge of the geometry is discretized into approximately 1/ESF 1D elements, which consequently become 2/ESF for the hexahedral mesh. For example, with ESF=0.04, each circle will be discretized into 25 1D elements for the tetrahedral mesh and consequently into 50 elements for the hexahedral mesh.

This approach logically results in larger elements corresponding to less significant curvatures (outer diameter of the core pipe and the by-pass pipe) and smaller elements corresponding to major curvatures (orifice plates and junction pipe). Table 5.2 summarizes the characteristics of the meshes used for the sensitivity analysis in terms of the ESF for the 3D simulations of MADMAX Configuration 1.

Table 5.2: 3D mesh characteristics for sensitivity analysis.

ESF	**# of elements**	**Smallest element edge** (mm)	**Largest element edge** (mm)
0.1	77 276	2.67	31.8
0.08	150 236	2.13	25.5
0.05	495 636	1.34	15.9
0.04	914 272	1.07	12.7
0.03	2 123 980	0.80	9.6

Figure 5.12 illustrates the sensitivity analysis for the pressure difference between sensors D3 and C6, $\Delta P_{\text{D3-C6}}$, conducted on 3D preliminary calculations for MADMAX Configuration 1 (performed before the experiment, assuming $P_{\text{burst}} = 70\,\text{bar}$). This analysis allowed us to choose, in advance, the mesh with ESF $= 0.04$ as the mesh for conducting simulations, considered the optimal solution in terms of the trade-off between computational cost and accuracy.

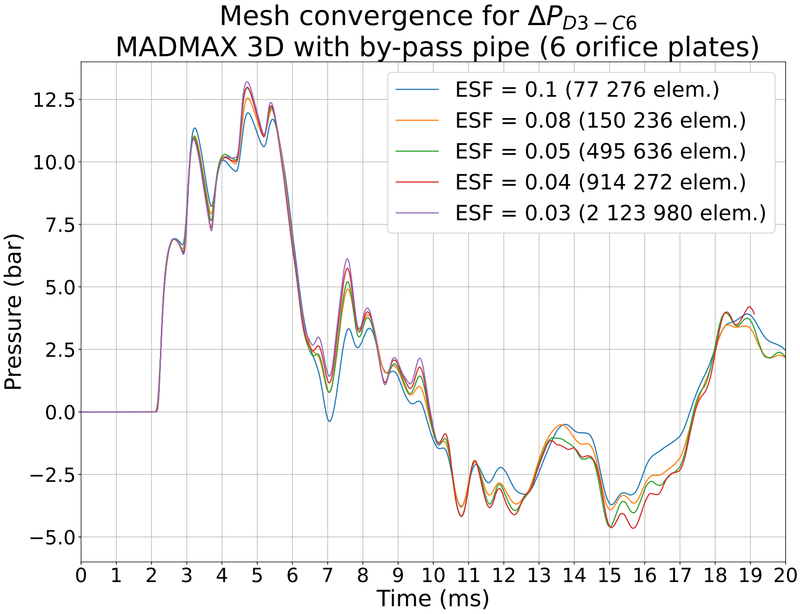

Figure 5.12: 3D mesh sensitivity analysis on the mesh size for $\Delta P_{\text{D3-C6}}$.

5.2.2.2 3D FSI calculations

Modeling choices In Figure 5.13, the 3D FSI mesh, created using Gmsh [68], is depicted. As can be easily observed, for the fluid part and the accumulators, it is practically the same mesh as in the 3D case. However, outside the fluid, the mesh representing the steel piping structure has been added (shown in red in the figure). For the sake of simplicity in mesh generation, the presence of the connecting flanges (visible in Figure 2.1) between the components of the core pipe and the by-pass pipe has been neglected. Once again, the main geometric features and modeling choices adopted are summarized in the figure. The mesh of the structure is perfectly coherent with that of the fluid, with nodes and faces of the two meshes coinciding at the interface between them.

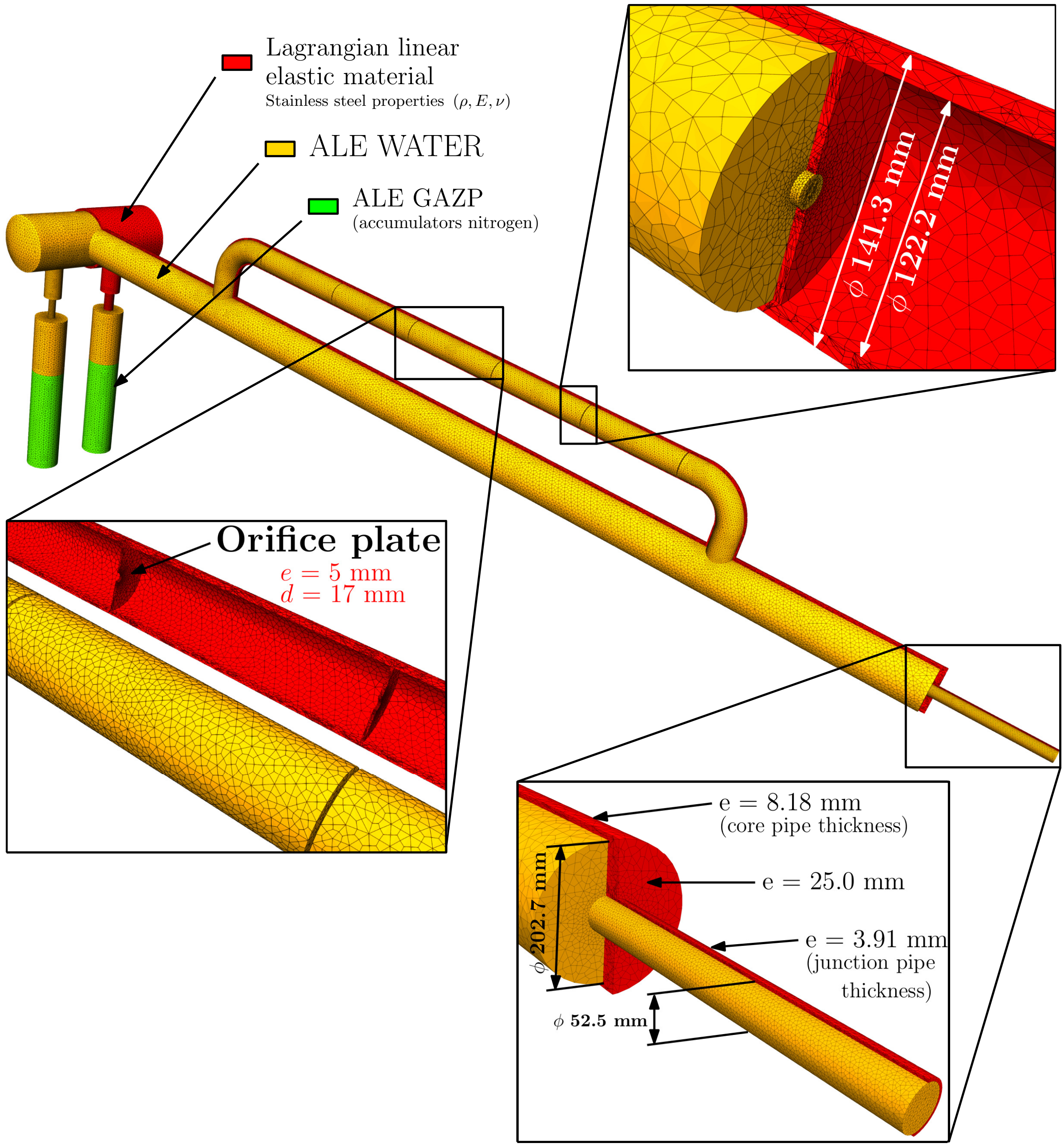

Figure 5.13: 3D FSI mesh.

From a numerical and mathematical standpoint, the characteristics of the two main components, the steel tube and water, are exactly the same as those adopted for the 2D axisymmetric FSI simulations (see Paragraph 4.4.2).

The structure is left completely free to deform in all directions, but it is numerically anchored by blocking the displacements of the nodes located at the actual five vertical anchoring positions of the experimental device. All five anchoring points are located on the outer surface of the core pipe on the side opposite to the by-pass pipe (as seen in Figure 2.1, the device is anchored to the steel structure and concrete blocks located on the left side in the photo). The five points are located respectively, from bottom to top:

1. at the same height as sensor C2,
2. at the same height as the first connection between the core pipe and the by-pass pipe,
3. at the same height as sensor C5,
4. at the same height as sensor C7,
5. just before the flanges connecting the core pipe with the accumulator section.

Only the nodes on the outer surface of the structure mesh that are located at these five positions are constrained in all directions, while the rest of the structure is free to move and deform. The effects of gravity are neglected. The pre-load of the structure during the pressurization phase has been assessed through static structural calculations, which show pre-deformations on the order of tenths of a micron, thus considered negligible compared to the deformations subsequently calculated with EUROPLEXUS.

Unfortunately, there are currently no sensors installed on the experimental setup to measure the dynamic deformation of the structure (in the perspectives of device improvement and evolution) and thus validate the corresponding 3D FSI numerical results through a quantitative comparison with experiment. Since section 5.3 of the present chapter is focused on a quantitative comparison between simulation and experiment, it is decided to analyze in the next paragraph the flow fields computed using the 3D FSI approach so as to assess the effects of the structure deformation on the rarefaction wave propagation. We emphasize that for lack of reference measurements this analysis should be considered as a qualitative interpretation of what the real deformations undergone by the device would be.

Numerical results The potential of 3D simulations with FSI includes the ability to evaluate and visualize how the structure actually deforms in response to the rarefaction wave. In Figures 5.14, 5.15 and 5.16, the displacements of the structure along the y and z directions during the water depressurization are shown for various time instances, with a focus on different areas of the device. In all three figures, the displacements have been visually amplified by a factor 1000 to make them more appreciable and are displayed on the cross-sectional view of the structure on the $y-z$ plane. The z direction coincides with the axis of symmetry of the core pipe and is directed upwards, while the y axis is radially directed towards the by-pass pipe (to the left in the figures). The x direction is obviously perpendicular to these two and points out of the plane, but we do not show the displacement values along x here as, for the by-pass pipe, they are negligible compared to those in the other two directions.

Figure 5.14 focuses on the area of the junction pipe and its connection with the core pipe in the first millisecond of the transient. It is observed that up to 0.5 ms, the junction pipe tends to elongate longitudinally downwards and to contract radially due to the passage of the first rarefaction wave. Instead, with the subsequent transmissions/reflections, the junction pipe tends to rise upwards alternating phases of radial shrinkage and widening. The sheet steel that connects the junction pipe to the core pipe undergoes significant deformations upwards in the region closest to the axis of symmetry, while tending to bulge outwards in the radial direction.

Figures 5.15 and 5.16, instead, mainly focus on the analysis of the deformations simultaneously undergone by the core pipe and the by-pass pipe, from 2.5 ms until the end of the transient at 20 ms. As anticipated, the absence of connecting flanges in the structure mesh does not allow for the reproduction of the actual rigidity of the experimental device. In particular, the by-pass pipe features six pairs of flanges, one pair for each orifice plate, which undoubtedly significantly influence the inertia and rigidity of the system. Consequently, it is highly probable that the by-pass pipe deformations shown by the 3D FSI simulation are overestimated compared to reality. Nevertheless, we can observe that the core pipe, being anchored, undergoes much less significant deformations compared to the by-pass pipe: a progressive radial constriction is observed in the areas between the anchoring points during the depressurization phase (up to about 10 ms), followed by a dilation effect due to the pressure increase caused by the accumulators (after 10 ms). The by-pass pipe undergoes a succession of bending modes at different time instances, as if it were subjected to whip-like motions. It is interesting to note the deformation of the orifice plates in the first 5 ms: the three lower-positioned orifice plates logically bend downward due to the rarefaction wave entering from the first elbow pipe; whereas the two upper-positioned orifice plates experience the opposite effect due to the rarefaction wave reaching them from above.

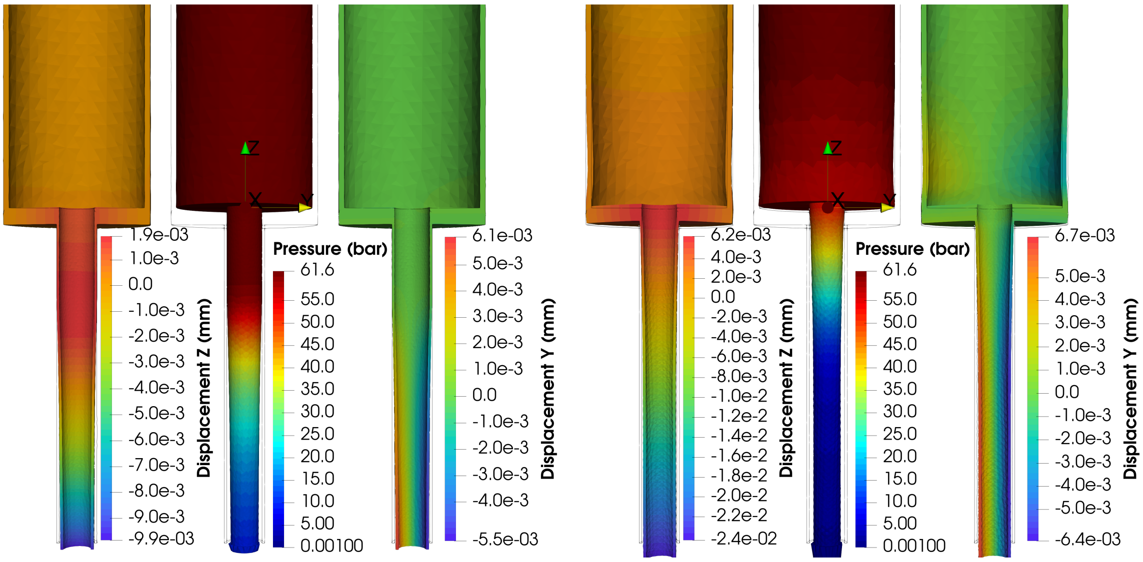

(a) $t = 0.25\,\mathrm{ms}$ (b) $t = 0.5\,\mathrm{ms}$

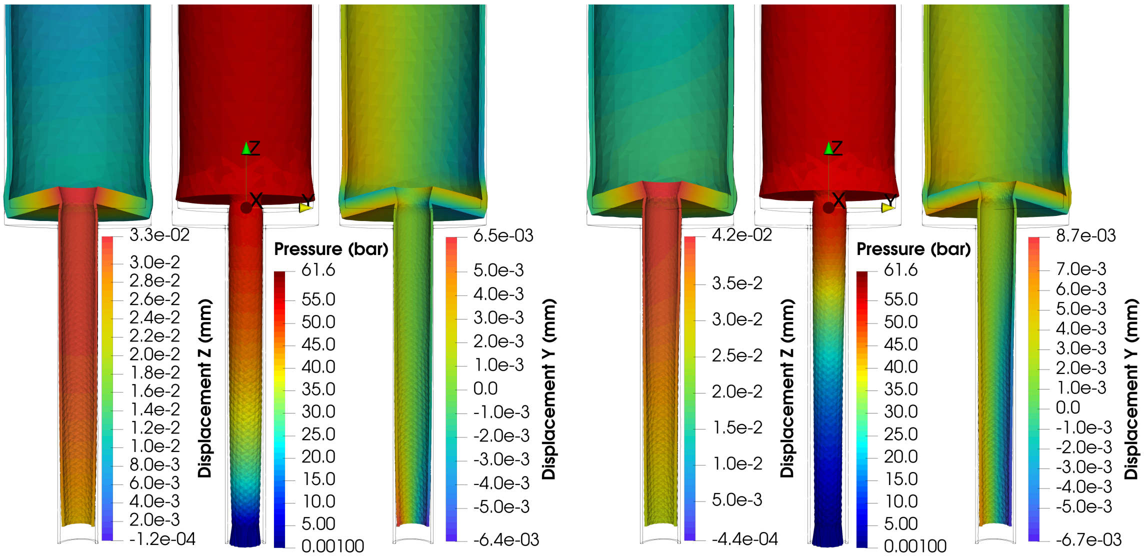

(c) $t = 0.75\,\mathrm{ms}$ (d) $t = 1.0\,\mathrm{ms}$

Figure 5.14: Structure displacement (visually amplified by a factor 1000) along y and z following water depressurization.

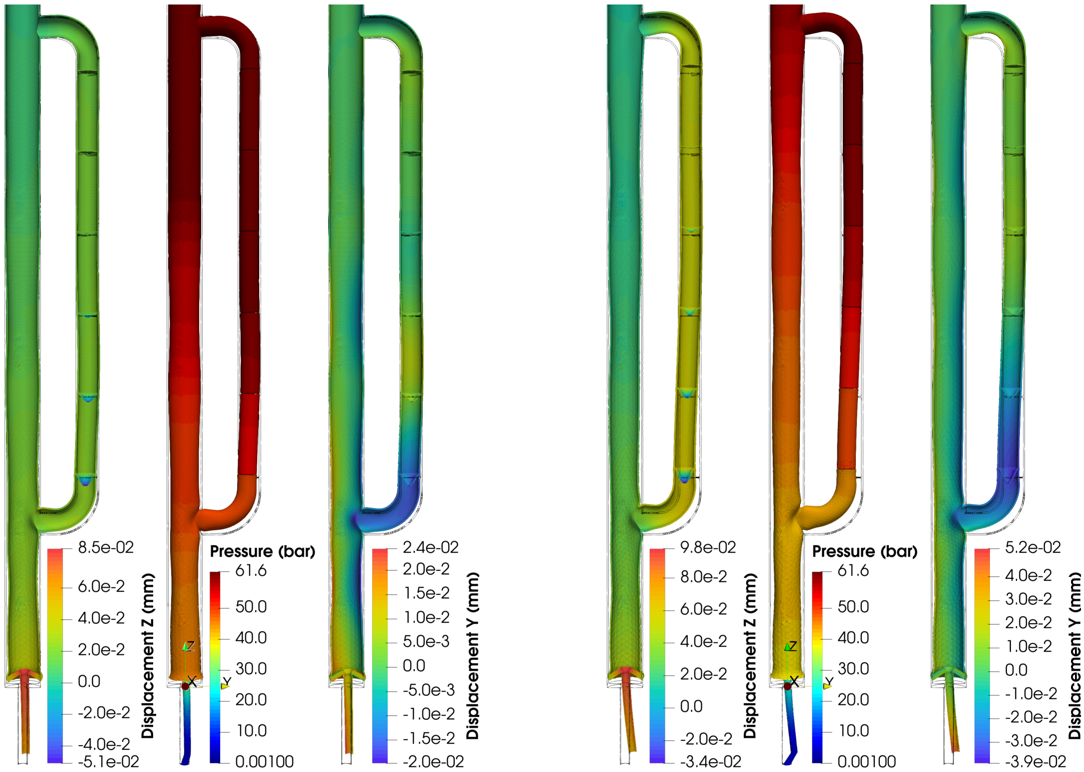

(a) $t = 2.5\,\mathrm{ms}$ (b) $t = 3.5\,\mathrm{ms}$

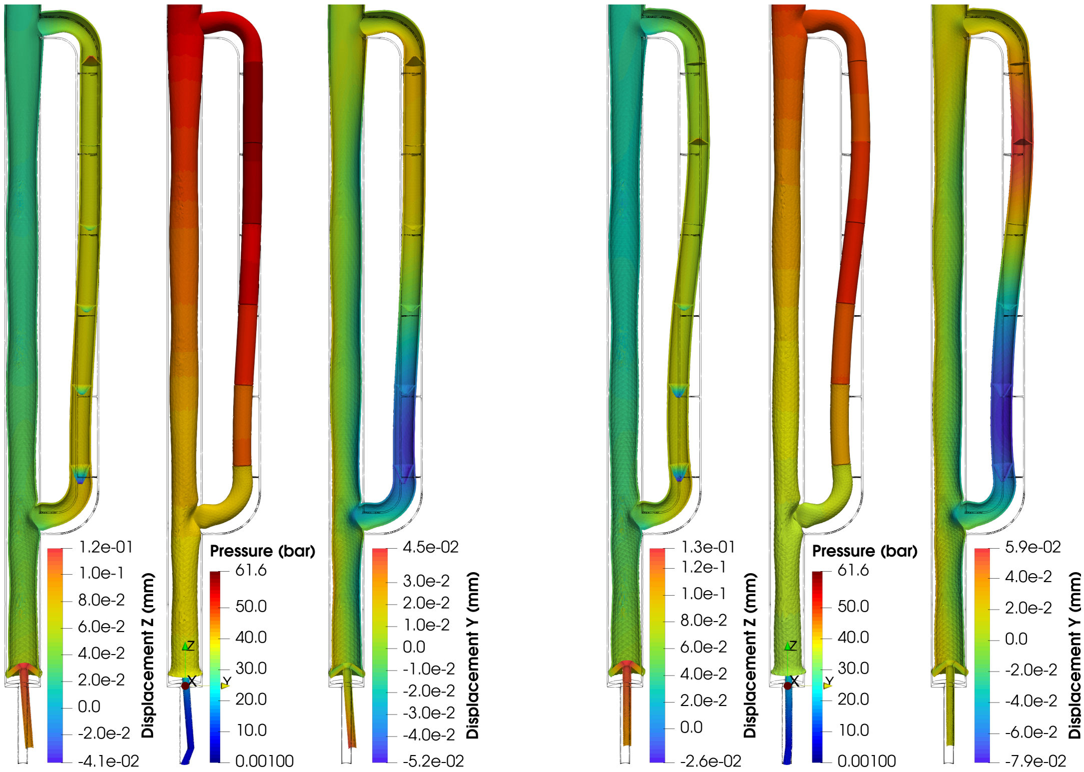

(c) $t = 4.0\,\mathrm{ms}$ (d) $t = 5.0\,\mathrm{ms}$

Figure 5.15: Structure displacement along y and z following water depressurization.

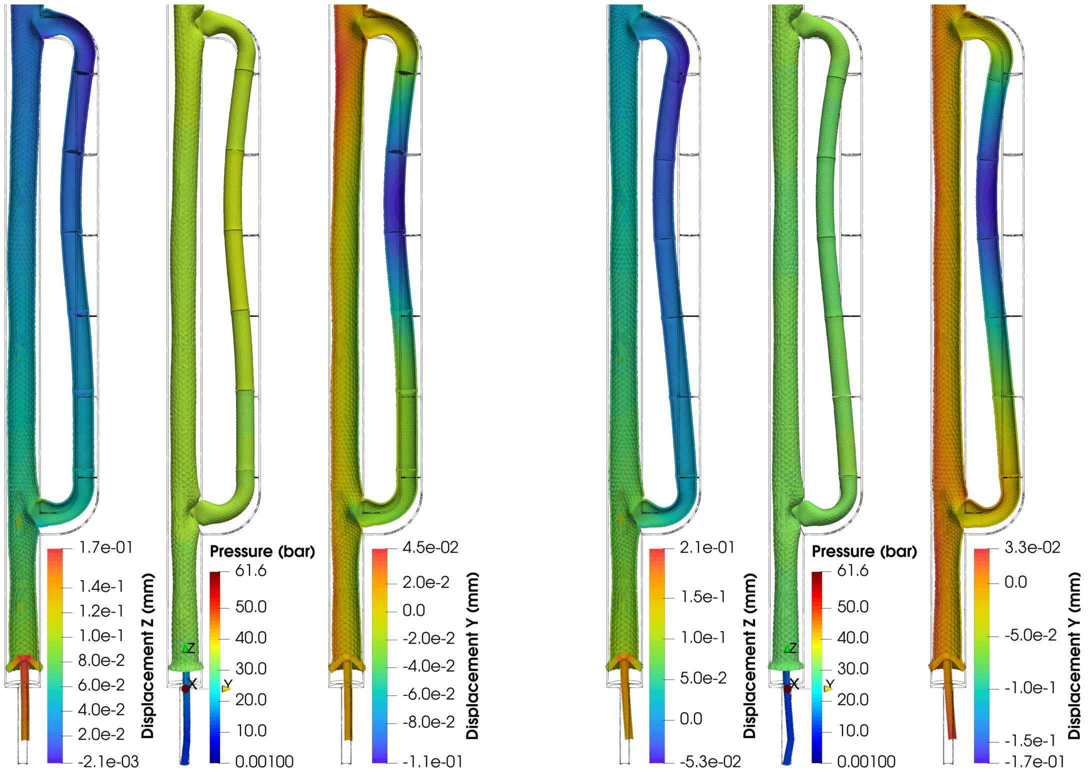

(a) $t = 8.0\,\mathrm{ms}$ (b) $t = 10.0\,\mathrm{ms}$

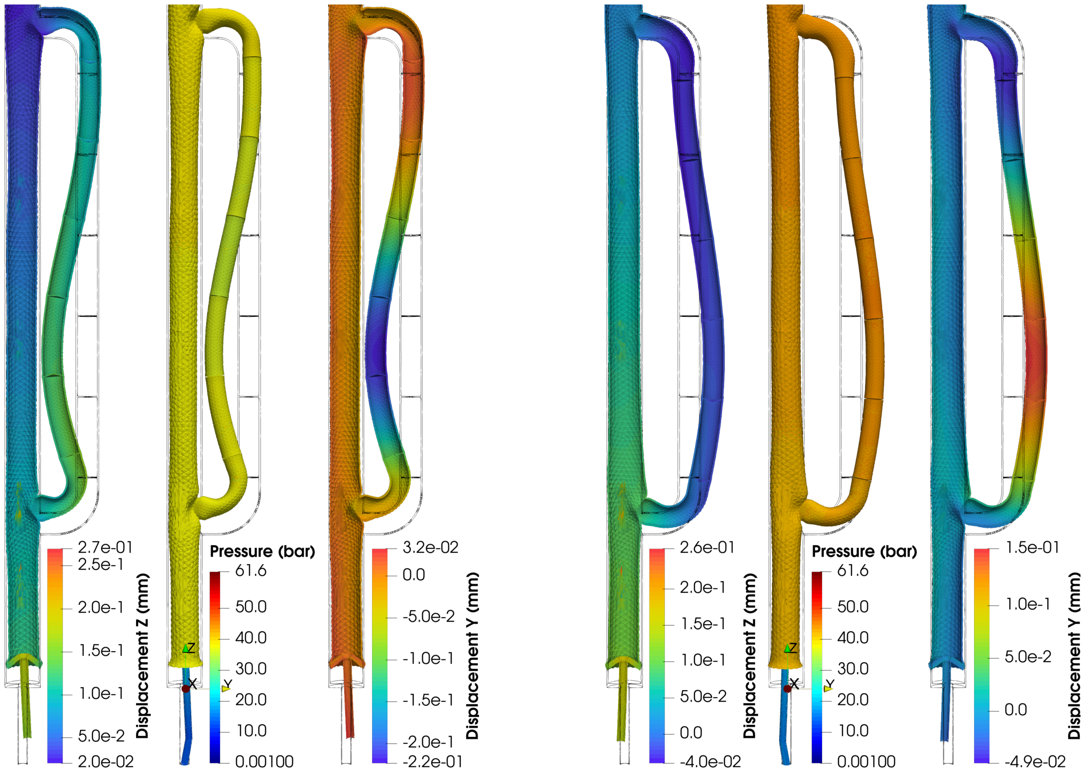

(c) $t = 15.0\,\mathrm{ms}$ (d) $t = 20.0\,\mathrm{ms}$

Figure 5.16: Structure displacement along y and z following water depressurization.

5.2.3 1D/1D FSI calculations

The 1D/1D FSI mesh for the MADMAX configuration with the by-pass pipe (shown in Figure 5.17) is simply an extension of the 1D mesh used for the simplified configuration presented in Paragraph 4.2.2. In order to build it, the by-pass pipe was simply added in the form of a 1D pipeline straddling the C4-C8 sensors with 90-degree direction changes representing the two elbow pipes in a simplified manner.

As in the case of the simplified configuration without a by-pass pipe, the presence of the orifice plates is no longer represented geometrically as for 2D axisymmetric and 3D calculations, but is replaced by impedance relations of IMPEDANCE GRID type (see Paragraph 3.1.4) to which the characteristic time τ and the head loss coefficient k are associated. This relation is assigned to the mesh node where the orifice plate is located. The orifice plates installed in the by-pass pipe all have a thickness $e = 5\,\text{mm}$ and an orifice diameter of $d = 17\,\text{mm}$. This results in a characteristic time $\tau = 0.297\,\text{ms}$ and a head loss coefficient $k = 6962$.

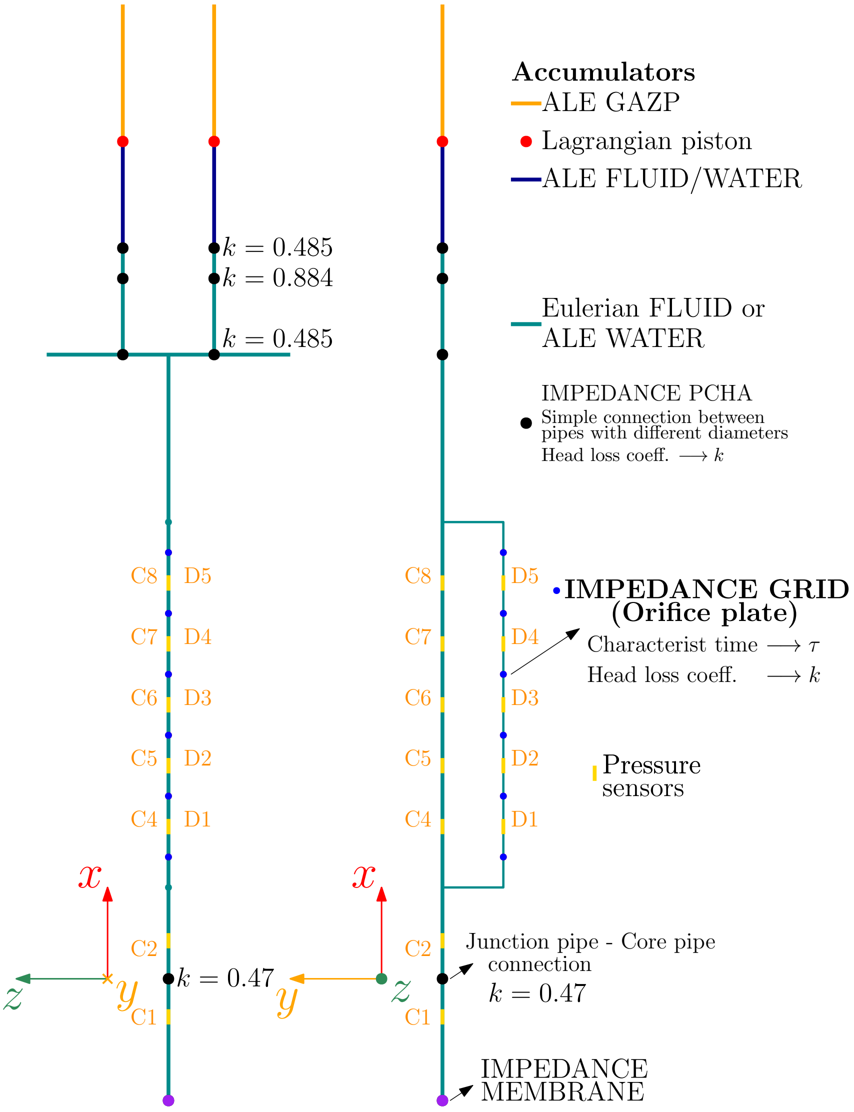

Figure 5.17: 1D/1D FSI mesh scheme.

All other cross-sectional changes, represented with black dots, are associated with another type of impedance called IMPEDANCE PCHA, which corresponds to imposing only a classical head loss without the acoustic contribution present in IMPEDANCE GRID (see Paragraph 3.1.4. This choice, as already discussed in Paragraph 4.2.2, is based on the fact that the other section changes in question are single cross-sectional changes (sudden enlargement or shrinkage). Consequently, the contribution of the acoustic term in Equation (3.24) does not have the same significance as in the case of the orifice plate (a sudden shrinkage immediately followed by a sudden enlargement). For the orifice plate the frequency of the transmission/reflection phenomenon within its thickness plays a crucial role in delaying the pressure signal transmission from one side of the obstacle to the other (need to use the IMPEDANCE GRID). It is, however, much less significant in the case of single cross-sectional changes, where the term for classical head loss (IMPEDANCE PCHA) makes the most important contribution and is sufficient for their representation. As can be seen in Figure 5.17, no impedance is associated with the junction nodes between the core pipe and the by-pass pipe, nor with the single junction node between the core pipe and the horizontal element of the accumulator zone. This is because, despite being cross-sectional changes, the ratio between the two sections is very close to 1, making both the acoustic effect and the head loss negligible.

The mesh used for the 1D simulations with fixed structures is exactly the same as the one used in the 1D FSI simulations, which is why only one scheme is shown for both in Figure 5.17. As anticipated, no mesh is materially added to represent the structure in the FSI case. One of the differences is in the type of material used to represent the water: FLUID model with Eulerian description for the case with fixed structures (except for the water in the accumulators which always uses an ALE description), while the WATER model with ALE description is used for the FSI case.

As mentioned at the beginning of the Section 5.2, in the FSI case, to take into account the flexibility of the structure elastic properties dependent on the geometry and material of the piping are assigned to the 1D elements constituting the fluid. With knowledge of these properties, EUROPLEXUS can calculate how much the piping will deform following the passage of the pressure wave and consequently obtain the corrected speed of sound in the fluid through the tabulated EoS.

Similarly to what was done for the simplified configuration, a sensitivity analysis on mesh size again allowed us to select a mesh composed of 1D elements of 10 mm in length, totaling about 2000 elements.

5.3 Simulation-experiment comparison

The 4 numerical models which have been previously described are now compared with the reference experimental measurements. This quantitative comparison is first focused on the analysis of the computed and measured pressure evolutions for the various sensors in the core pipe and in the by-pass pipe. Since the prediction of the pressure difference between the core pipe and the by-pass pipe is a quantity of interest particularly relevant for safety analysis (in the industrial case, the transverse stress generated on the core baffle - see Figure 1.2 - is directly due to the pressure difference created between the core zone and the by-pass zone), a quantitative comparison is also provided for such pressure differences. Finally, a synthetic view of the accuracy of each numerical model is proposed through selected plots of errors (computed using a L_1 norm) between the numerical predictions and the measurements. These errors are also put in perspective by a 2-criteria analysis including the computational cost as another criterion, complementing the accuracy criterion.

5.3.1 Analysis of absolute pressure evolutions

Figures 5.18 and 5.19 show the pressure evolution for the four models in comparison with the experimental results for sensors C1, C2, C4, D1, C6, D3, C8 and D5. For all sensors, it is observed that the behavior is satisfactorily reproduced by all models in the first half of the transient, up to 6 ms. Surprisingly, between 6 and 12 ms, 1D simulations yield higher accuracy compared to 3D simulations. After that, the two 1D models tend to deviate slightly from the experimental results, while the 3D models continue to be more accurate.

For the sensors in the core pipe (C2, C4, C6, C8), a common factor among all models is that they perform well not only in reproducing the overall pressure trend but also in capturing the acoustic characteristics of the signal, namely the pressure steps generated and propagated by each transmission/reflection in the junction pipe. Unfortunately, the same cannot be said for the sensors in the by-pass pipe (D1, D3, D5), where none of the four models manage to reproduce the pressure step features satisfactorily, although they adequately capture the overall trend.

The fact that the signal reaching the sensors in the by-pass pipe appears smoothed in simulations can be attributed to two factors: the double change in direction of the elbow pipe, which causes numerical diffusion due to a likely insufficient refinement of the mesh in those areas; or the signal is numerically smoothed as it passes through the orifice plates, but given their small thickness, this should not be the case. This latter hypothesis will be excluded in the next chapter when discussing the configuration with four orifice plates, where the removed orifice plates are the bottom and top ones, and we will see that even in their absence, the signal entering the by-pass pipe has still lost its acoustic footprint when it reached sensor D1. However, it should be emphasized that for the by-pass pipe sensors, the 3D FSI model is the one that best reproduces the very first instants of the transient in terms of closeness to the experimental curve. This latter observation, as previously explained for the 2D axisymmetric FSI model in Paragraph 4.4.2.3, is justified by the fact that the presence of a deformable structure allows for the reproduction of the pipe's pre-deformation phenomenon. This phenomenon occurs because the speed of sound in steel is approximately three times higher than in the fluid (refer to Paragraph 4.4.2.3 for further details).

5.3.2 Analysis of relative pressure evolutions

To complete the information on all the experiment's sensors, Figure 5.20 shows the transient pressure difference between sensors D2-C5 and sensors D4-C7. It can be observed that in both cases, during the first half of the transient phase, the pressure difference is positive, with peaks around 10 bar, indicating that in this phase, as expected, the core pipe, not containing obstacles, depressurizes more quickly than the by-pass pipe. Afterward, the pressure difference tends to balance out around the midpoint of the transient, and then becomes negative (pressure in the core pipe greater than pressure in the by-pass pipe), because in that phase the effect of the accumulators is predominant in the core pipe and has more difficulty manifesting in the by-pass pipe due to the presence of the orifice plates.

5.3.3 Error analysis

To obtain a more quantitative assessment of the accuracy of the four models, we calculated for each sensor the absolute error of each model with respect to the experimental measurement and then calculated the average over the entire transient. Figures 5.22 and 5.23 show the mean absolute error for the junction pipe sensor C1, for the core pipe sensors C2-C8 and for the by-pass sensors D1-D5.

It can be inferred that, in general, the 3D/3D FSI simulations are more accurate than the 1D/1D FSI simulations for all sensors, but in particular for sensors C1, C2, D4, and D5. Contrary to expectations, the FSI models consistently exhibit slightly lower overall precision with respect to their fixed structure counterpart, particularly the 1D WATER+FSI model, which appears significantly less accurate for sensors D1-D5. Even the 3D WATER+FSI model generally demonstrates lower precision compared to the 3D FLUID model (except for sensors C1 and C2), although the difference is small. If we instead consider the pressure difference between the sensors of the by-pass pipe D1-D5 and the corresponding sensors in the core pipe C4-C8, we observe from Figure 5.23 that the models incorporating FSI yield the smallest errors. The prediction of the pressure difference between the core pipe and the by-pass pipe is the quantity of major interest being particularly relevant for safety analysis in the industrial case, since the transverse stress generated on the core baffle - see Figure 1.2 - is directly due to the pressure difference created between the core zone and the by-pass zone.

Finally, we took the errors shown in Figure 5.23 and calculated their average across all five pairs of sensors for each model, in order to construct the cost-accuracy graph shown in Figure 5.24. The computational cost is expressed in terms of computational time, but it should be noted that both 3D calculations were performed in parallel on 64 processors, while for the 1D calculations, it was sufficient to perform them on a single processor. As expected, 1D calculations allow for a significant reduction in computational costs while still maintaining an acceptable level of accuracy and definitely providing greater simplicity in mesh creation.

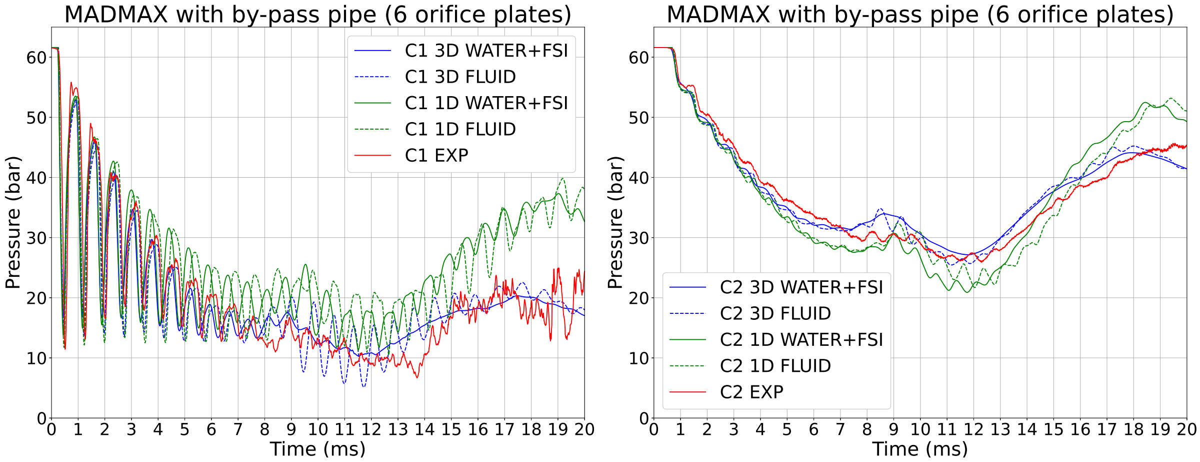

(a) C1

(b) C2

Figure 5.18: Configuration 1 pressure evolution comparison for sensors C1 and C2.

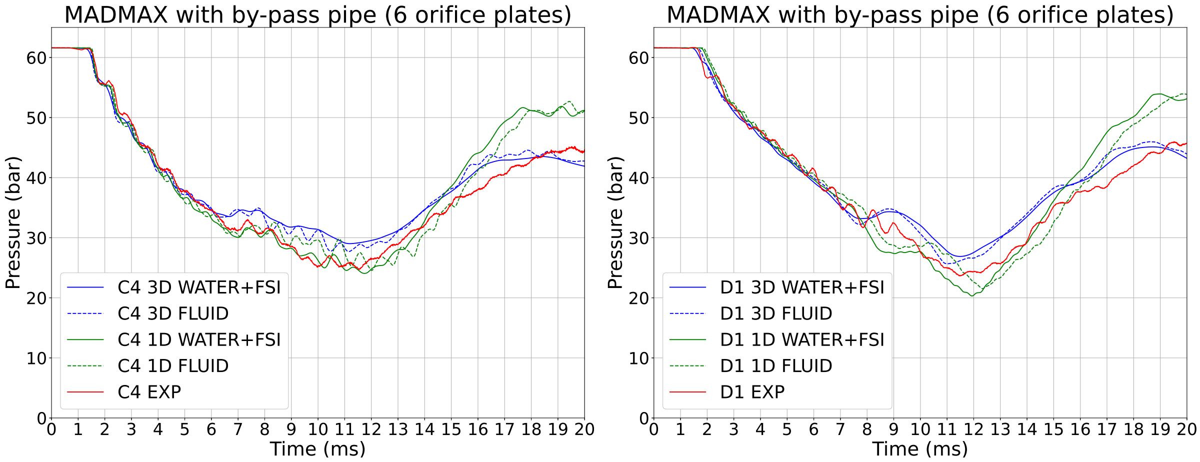

(a) C4 (b) D1

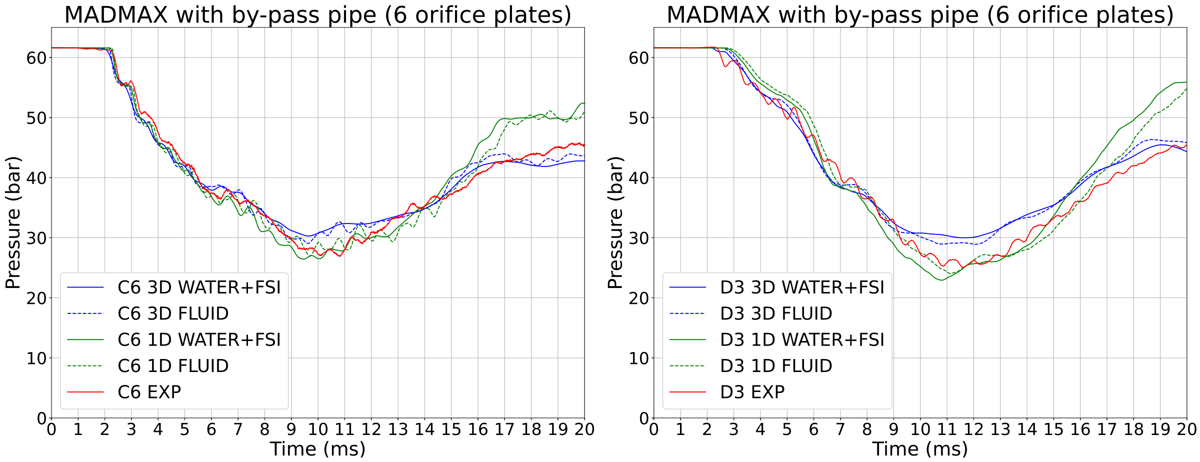

(c) C6 (d) D3

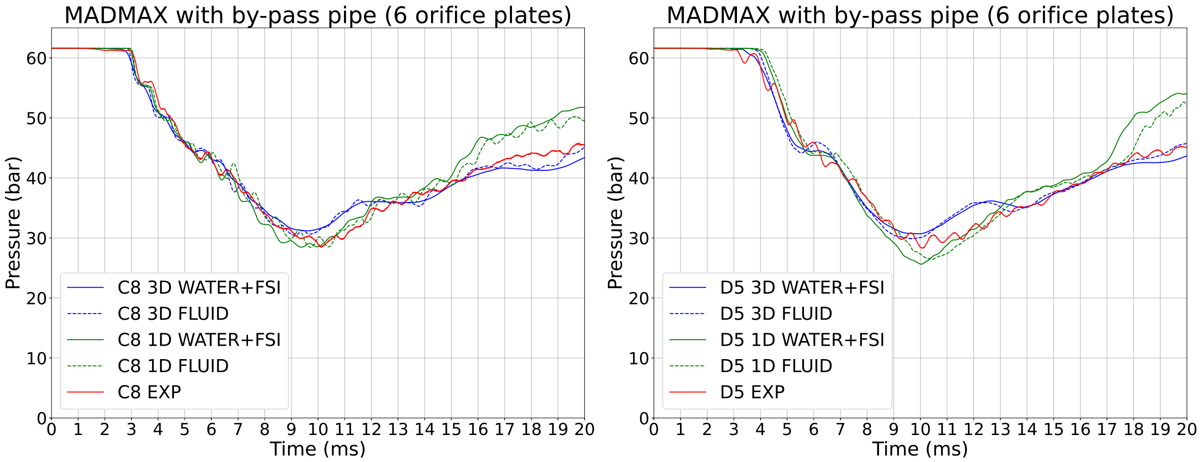

(e) C8 (f) D5

Figure 5.19: Configuration 1 pressure evolution comparison for sensors C4, D1, C6, D3, C8 and D5.

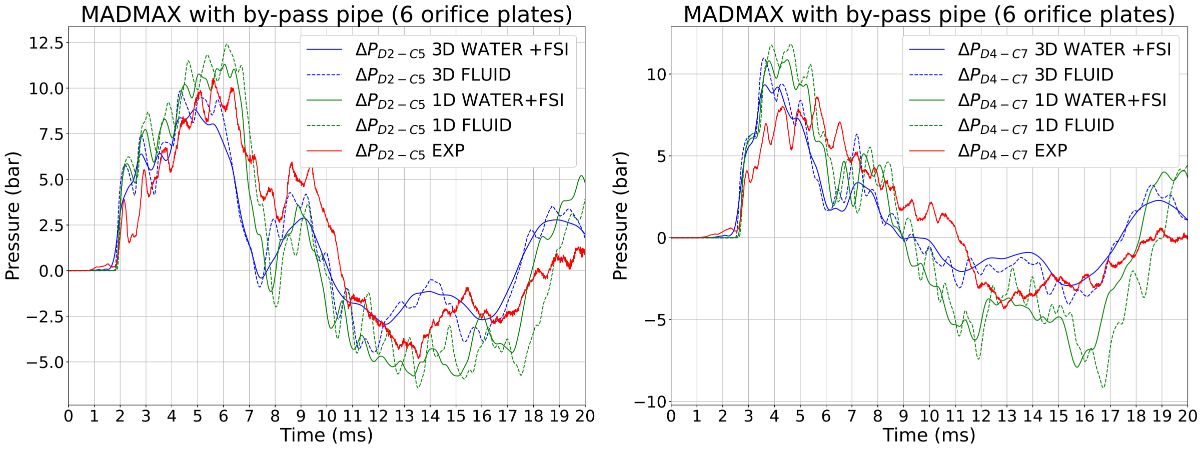

(a) D2-C5 (b) D4-C7

Figure 5.20: Configuration 1 pressure difference between sensors D2 and C5, ΔP_{D2-C5}, and sensors D4 and C7, ΔP_{D4-C7}.

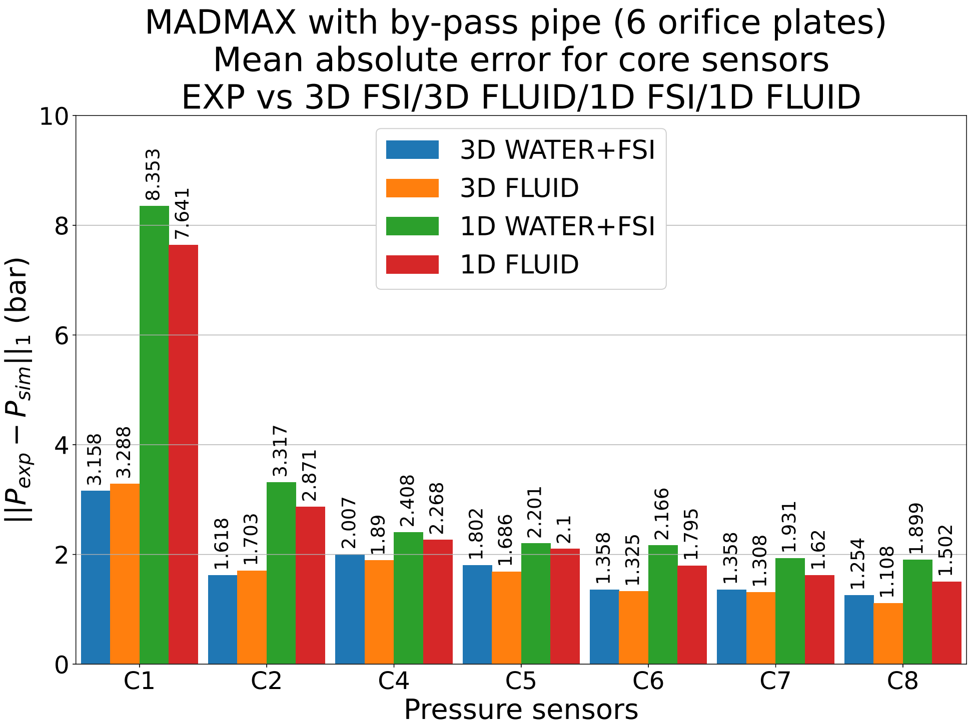

Figure 5.21: Configuration 1 mean absolute error for the junction pipe sensor and the core pipe sensors.

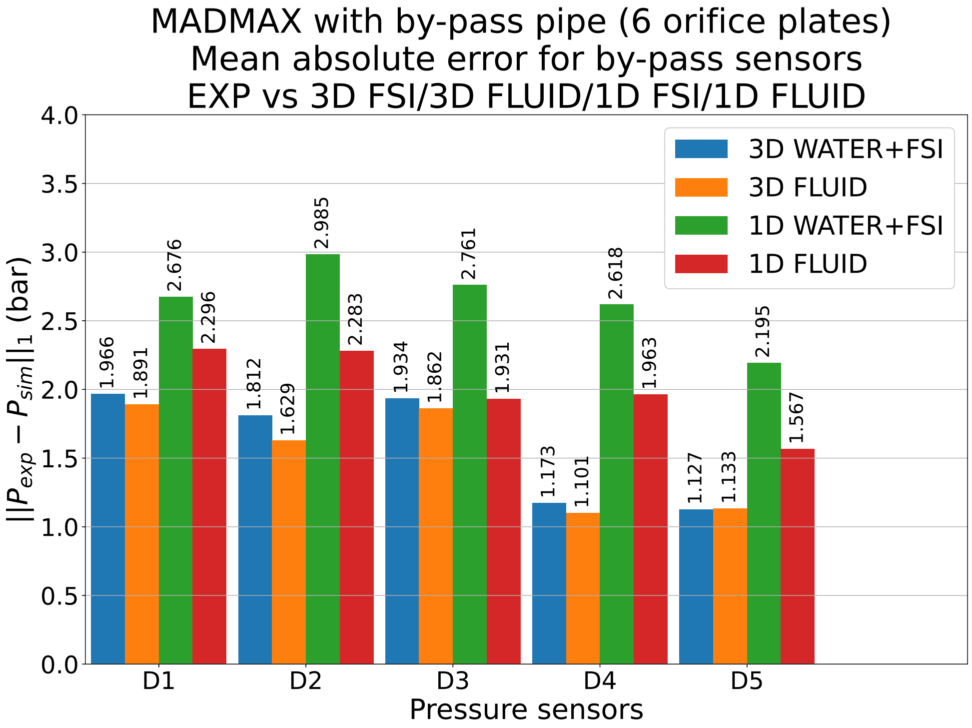

Figure 5.22: Configuration 1 mean absolute error for the by-pass pipe sensors.

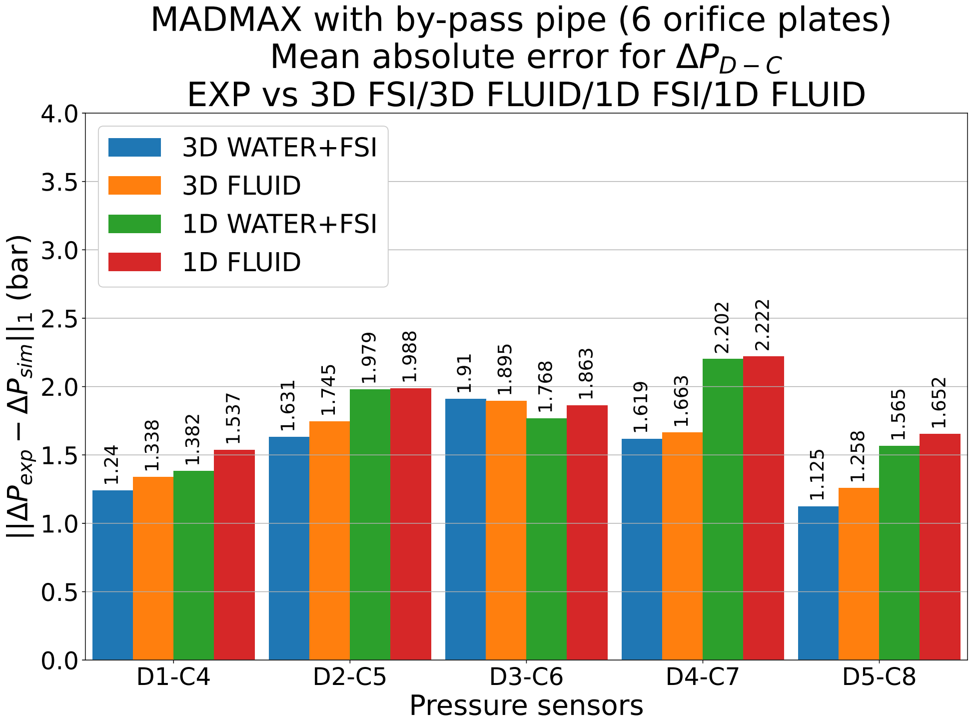

Figure 5.23: Configuration 1 mean absolute error for pressure differences between core and by-pass pipe sensors.

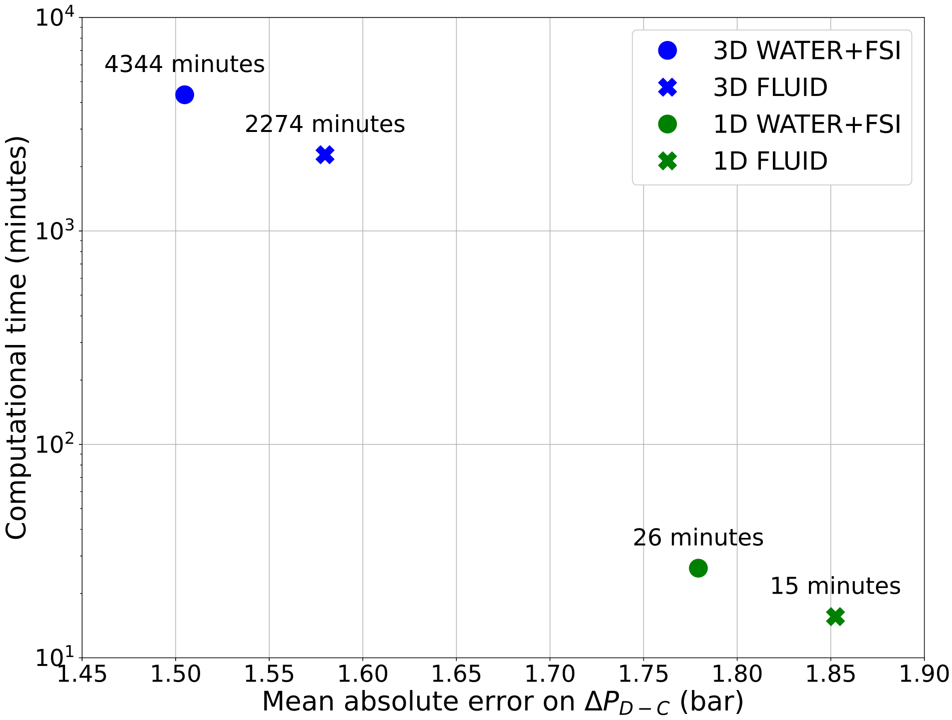

Figure 5.24: Configuration 1 computational cost of the four calculations with respect to their precision.

5.4 Conclusions

This chapter explored the complete configuration of the MADMAX experiment, focusing on Configuration 1, which includes a free core pipe and six orifice plates in the by-pass pipe.

Experimental results show the pressure evolution within the system, highlighting the delays and pressure drops associated with the presence of orifice plates in the by-pass pipe. The numerical simulations, conducted using EUROPLEXUS, encompass 3D and 1D models with and without Fluid-Structure Interaction (FSI). These simulations capture the complex dynamics of the experiment, including rarefaction wave propagation and pressure differentials between the core and by-pass pipes.

Comparison between experimental data and simulation results reveals overall good agreement, particularly in capturing the initial transient behavior. However, discrepancies arise in replicating pressure steps and finer features in the signals recorded by sensors in the by-pass pipe, indicating potential areas for model refinement. Notably, 3D models, especially those incorporating FSI, exhibit higher accuracy than 1D models.

The chapter provides valuable insights into the performance of numerical models in simulating the MADMAX experiment, laying the groundwork for further analysis in subsequent chapters.

Chapter 6

Alternative configurations of MADMAX with by-pass pipe

In this chapter, numerical and experimental experiments are performed and analyzed for two alternative versions of MADMAX with by-pass pipes that have never been tested before: Configurations 2 and 3, presented in Chapter 2 and also briefly mentioned and positioned at the beginning of Chapter 5 with respect to Configuration 1 analyzed in the previous chapter. Numerical simulations are again carried out with EUROPLEXUS following the hierarchy presented in Chapter 3. The purpose this time is two-folded:

- to evaluate with Configuration 2 the effect of a different number of obstacles in the by-pass compared to the full Configuration 1 with 6 orifice plates;
- to evaluate with Configuration 3 the effect of the simultaneous presence of obstacles in the core pipe and the by-pass pipe. This configuration incorporates the same number of orifice plates in the by-pass as Configuration 1, but an additional orifice plate is added in the core pipe, thus approaching even closer to the real industrial case (see Figure 1.2). In the actual industrial case, there is the simultaneous presence of perforated plate-type obstacles in the by-pass zone and fuel assemblies with mixing grids in the core zone. The orifice plate in the core pipe of Configuration 3 of MADMAX is intended to represent the core zone's geometry in a simplified manner.

6.1 Experimental campaign

The results of the experimental campaign carried out on MADMAX Configuration 2 and Configuration 3, realized between January and February 2024, are summarized in this section.

Let us recall the two configurations (described in Paragraph 2.2.2) are characterized as follow:

1. **Configuration 2:** free core pipe and 4 orifice plates in the by-pass,
2. **Configuration 3:** 1 orifice plate [$e = 10\,\text{mm}$, $d = 30\,\text{mm}$] in the core pipe and 6 orifice plates in the by-pass.

The corresponding bursting pressures of the two experiments are collected in Table 6.1.

Table 6.1: Experimental bursting pressure for MADMAX complete set-up (alternative configurations).

EXP	**Configuration 2** (4 o.p. in by-pass)	**Configuration 3** (6 o.p. in by-pass + 1 o.p. e10d30 in core)
P_{burst} (bar)	**68.0**	**76.5**

6.1.1 Analysis of measurements for Configuration 2

Figure 6.1 displays the experimental results of Configuration 2 for all the sensors. As previously mentioned, this experiment differs from Configuration 1 solely due to the absence of two orifice plates in the by-pass pipe, specifically the bottom and top ones. Comparing the results of Configuration 2 in Figure 6.1 with those of Configuration 1 in Figure 5.1, it can be observed that, apart from the different bursting pressure, the results are very similar for all sensors except sensor D1.

We can clearly see, particularly from the zoom-in Figure 6.2, the effect of the absence of the lower orifice plate on the pressure drop recorded at sensor D1: in Configuration 2, the pressure at sensor D1 experiences only the delay due to the crossing of the elbow pipe compared to sensor C4, but no difference is observed between the pressure levels at the first step (at 2 ms) as was seen for Configuration 1. This effect at sensor D1 is reflected at sensors D2 and D3, which show a lower pressure difference with sensors C5 and C6, respectively, compared to Configuration 1. Furthermore, in Configuration 2, the pressure at sensor D1 even drops below the pressure at sensor C4, suggesting that during that transient phase, this section of the by-pass pipe undergoes a faster transient phenomenon. At the same time, we do not observe any significant effect of the absence of the upper orifice plate on sensor D5, which practically shows the same behavior as Configuration 1.

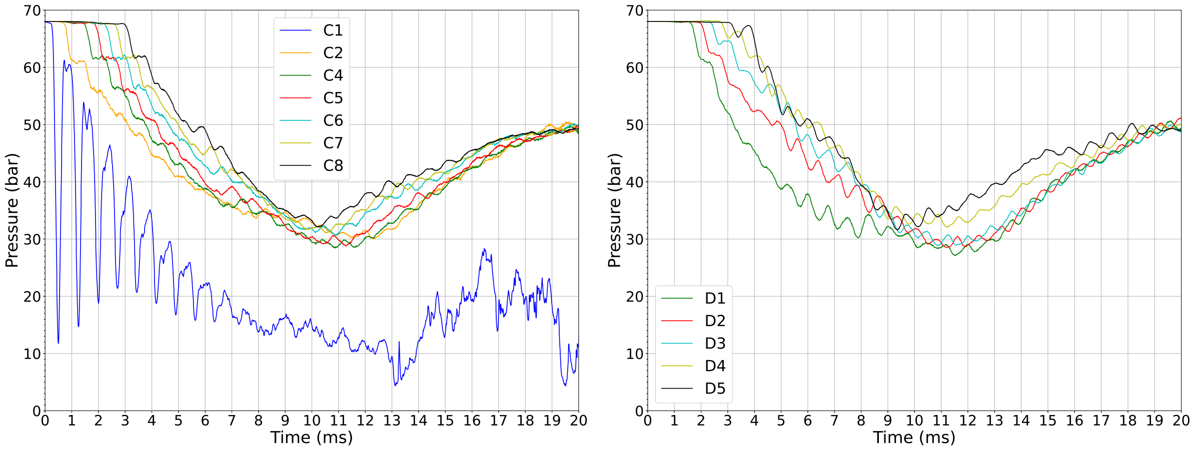

(a) Junction pipe (C1) and core pipe (C2-C8).

(b) By-pass pipe (D1-D5).

Figure 6.1: Experimental pressure evolution for all sensors for Configuration 2.

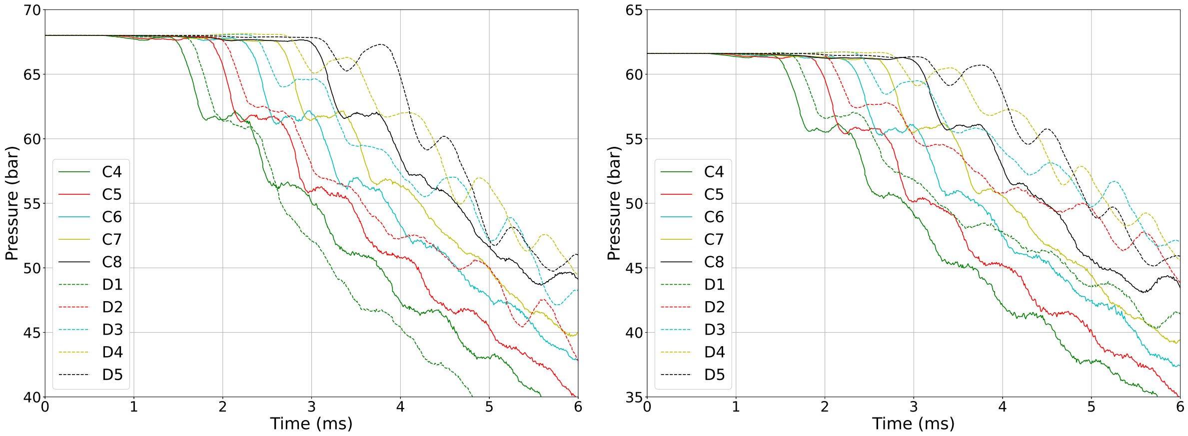

(a) Configuration 2

(b) Configuration 1

Figure 6.2: Experimental pressure evolution for sensors C4-C8 and D1-D5 for $t \leq 6\,\mathrm{ms}$. Comparison between Configuration 2 (a) and Configuration 1 (b).

6.1.2 Analysis of measurements for Configuration 3

Figure 6.3 depicts the experimental results obtained for Configuration 3. This time, owing to the presence of an orifice plate in the core pipe as well, the results notably differ from those of the two previous configurations. We can observe in this configuration the combined effect of the simplified setup presented in Chapter 4 (no by-pass pipe, with one orifice plate in the core pipe) and Configuration 1 (by-pass pipe with 6 orifice plates and free core pipe). The pressure trend for sensors C1-C8 closely resembles that of the experiment [$e = 10\,\mathrm{mm}$, $d = 30\,\mathrm{mm}$], shown in Section 4.1, wherein exactly the same orifice plate was used in the core pipe (see Figure 4.1 (c)), with the exception of the bursting pressure.

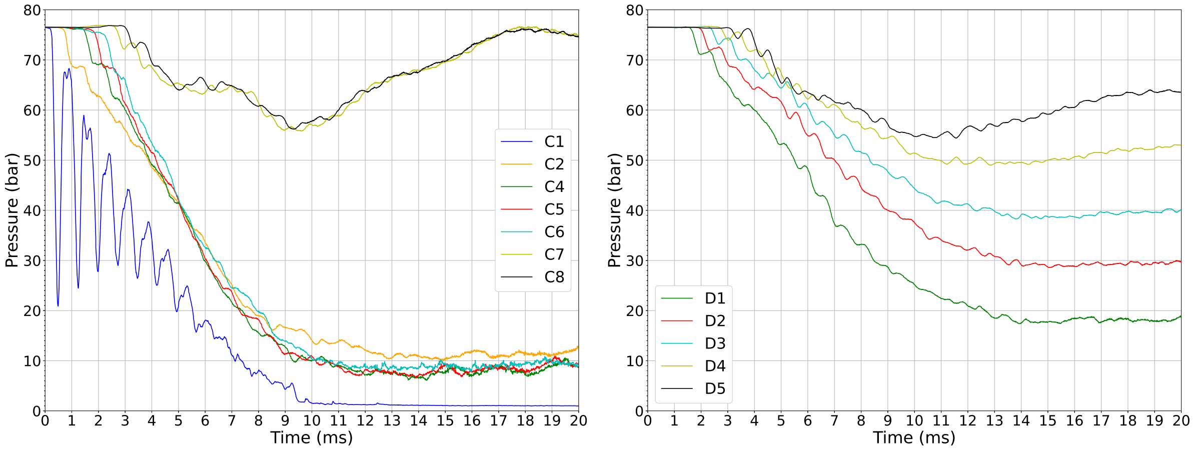

(a) Junction pipe (C1) and core pipe (C2-C8).

(b) By-pass pipe (D1-D5).

Figure 6.3: Experimental pressure evolution for all sensors for Configuration 3.

A notable transient pressure differential emerges between the sensors situated upstream (C2-

C6) and those downstream (C7 and C8) of the orifice plate, resembling the scenario observed without a by-pass pipe. This pressure differential is almost evenly dispersed across the sensors within the by-pass pipe: starting with the lowest pressure level at sensor D1 (close to that measured at sensor C4), followed by a gradual increase in pressure levels from sensor D2 to D4, culminating at sensor D5 with values aligning closely with those of sensor C8.

6.2 Simulation-experiment comparison

In this section, following the approach adopted in the previous chapter for Configuration 1, we present a sensor-by-sensor comparison between the experimental results of Configurations 2 and 3 and their corresponding numerical simulations. Once again, four numerical models are employed: two reference models, namely 3D FLUID and 3D WATER+FSI, and two simplified models, 1D FLUID and 1D WATER+FSI. The characteristics of these models are similar to those detailed in Chapter 5 for Configuration 1; hence, they are not reviewed again in this chapter and the reader is directed to Section 5.2 for further details. The only modifications made to these models in the present chapter involve minor mesh manipulation: for Configuration 2, the lower and upper orifice plates were removed from the by-pass pipe, while for Configuration 3, the same mesh as Configuration 1 was used, albeit with the addition of an orifice plate in the core pipe.

6.2.1 Configuration 2: MADMAX with 4 orifice plates in by-pass pipe

Here, we present the comparison between the experimental results of Configuration 2 and their corresponding numerical simulations. Overall, there are no significant differences compared to the observations made for Configuration 1 in the preceding chapter. The absence of the lower orifice plate in the by-pass pipe results in a nearly negligible transient pressure differential between sensors D1 and C4 (see Figure 6.4 (c) and (d)). Additionally, as previously noted in Section 5.2 of the preceding chapter, the pressure signal reaching sensor D1 appears more diffused in the numerical simulations compared to the experimental measurement, which exhibits the characteristic pressure step at approximately 2 ms. Given the absence of the orifice plate upstream of sensor D1 in this case, we can conclude that the numerical diffusion effect is attributed to the double change in direction of the elbow tube and a potentially insufficient refinement of the mesh in the intersection zone with the core pipe.

If we compare with Configuration 1, the absence of the lower orifice plate in the by-pass pipe also leads to a reduction in the transient pressure differential between the remaining sensor pairs D-C above the D1-C4 pair, as shown in Figures 6.5 and 6.6. Specifically, upon comparing Figure 6.6 with the corresponding results of Configuration 1 in Figure 5.20, it can be observed that for ΔP_{D2-C5}, the range shifts from $[-5, 10]$ bar for Configuration 1 to $[-4, 6]$ bar for Configuration 2, while for ΔP_{D4-C7}, it shifts from $[-5, 10]$ bar to $[-2.5, 7.5]$ bar, based on the experimental curves.

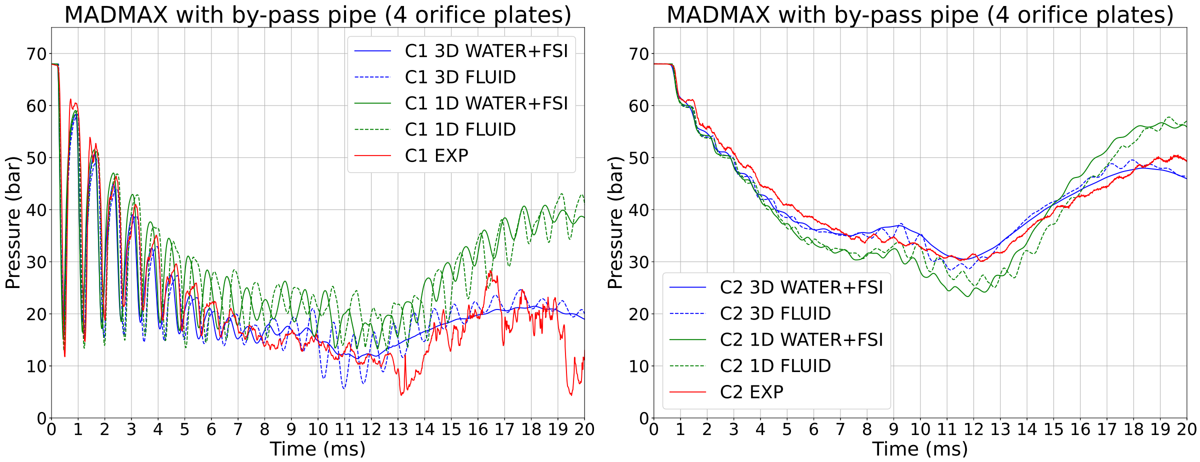

(a) C1 (b) C2

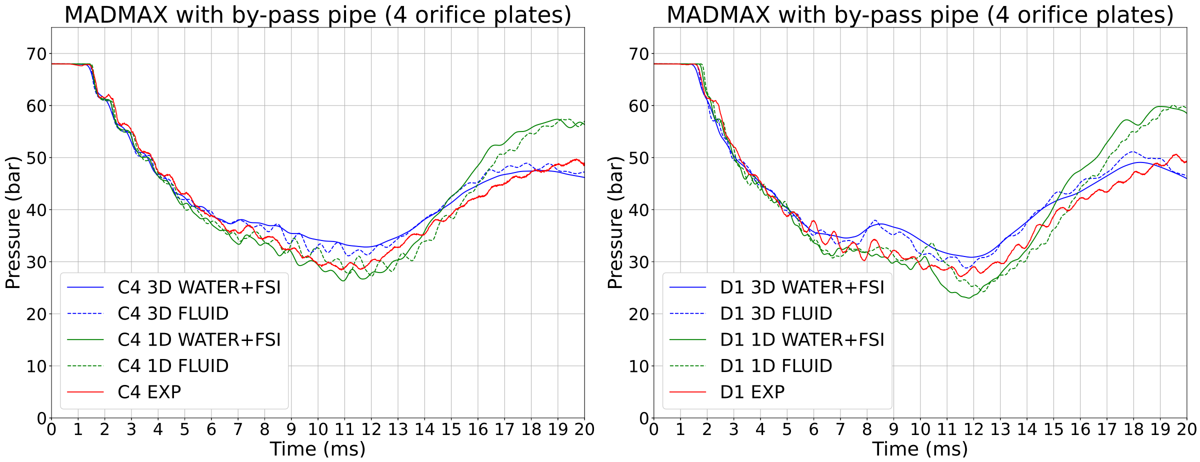

(c) C4 (d) D1

Figure 6.4: Configuration 2 pressure evolution comparison for sensors C1, C2, C4 and D1.

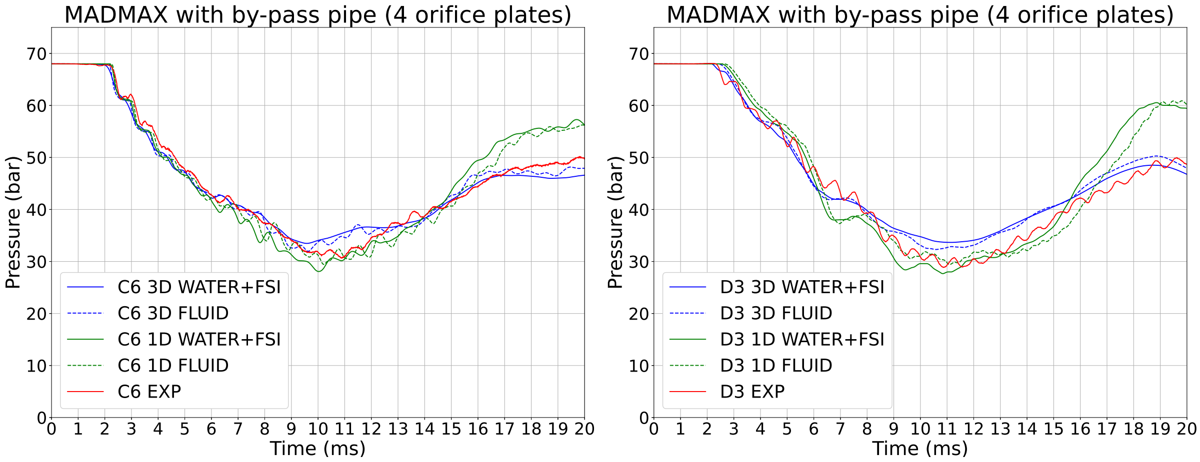

(a) C6 (b) D3

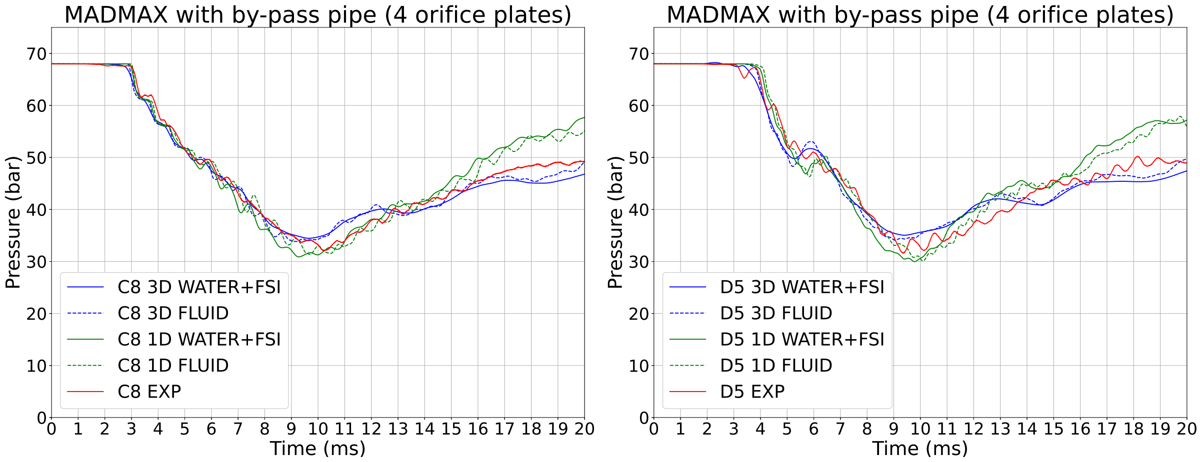

(c) C8 (d) D5

Figure 6.5: Configuration 2 pressure evolution comparison for sensors C6, D3, C8 and D5.

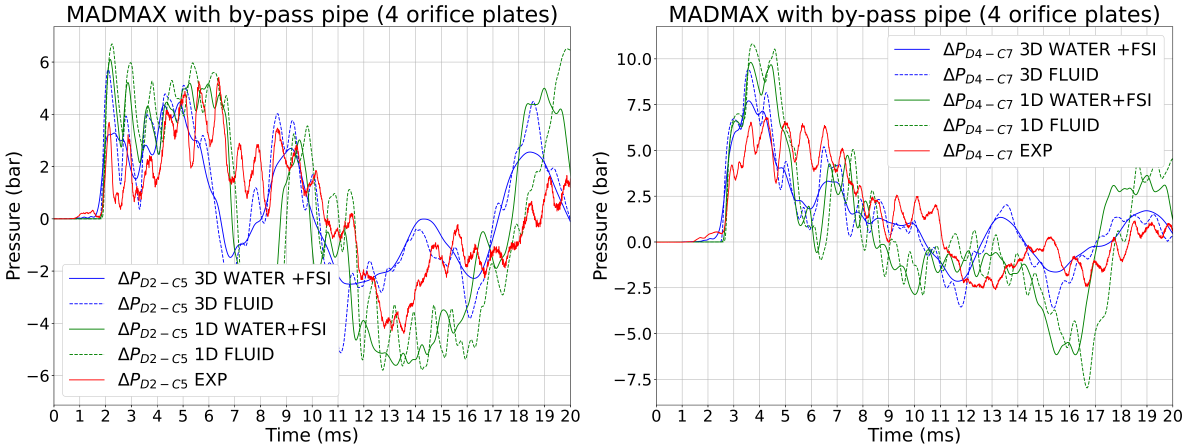

(a) D2-C5

(b) D4-C7

Figure 6.6: Configuration 2 pressure difference between sensors D2 and C5, ΔP_{D2-C5}, and sensors D4 and C7, ΔP_{D4-C7}.

Concerning the numerical models, a more substantial alignment is generally observed between the 3D/3D FSI models and the experimental data, in contrast to the 1D/1D FSI models. This observation holds particularly true when evaluating the mean absolute errors across all sensors depicted in Figures 6.7, 6.8, and 6.9. When compared to the corresponding mean absolute errors calculated for Configuration 1 (Figures 5.21, 5.22, and 5.23), the following observations can be made: for each individual sensor (Figures 6.7, 6.8 for Configuration 2, and Figures 5.21, 5.22 for Configuration 1), there is a slight increase in the mean absolute error for Configuration 2 compared to Configuration 1 across all numerical models. However, there is also a concurrent reduction in the mean absolute error relative to ΔP_{D-C} (Figure 6.9 for Configuration 2 and Figure 5.23 for Configuration 1). This observation might suggest that a lower number of obstacles in the by-pass (Configuration 2) results in a reduced statistical error in reproducing the transient pressure difference between the two branches of the experiment, as the numerical simulations are less perturbed by geometric singularities.

Regarding the trade-off between computational cost and model accuracy, similar conclusions to those presented for Configuration 1 can be drawn for Configuration 2: in a plane “Computational time vs Error or Accuracy”, the 4 models form a set of non-dominated choices, with the 3D WATER+FSI approach providing the best accuracy for the highest cost and the 1D FLUID approach providing the lowest accuracy for the lowest cost.

The choice of one approach over another can be consequently determined, for example, by the level of precision deemed acceptable (or conversely, by the maximum cost one is willing to bear). In the context of nuclear safety, where a conservative approach is often adopted, the fact that the 1D models overestimate transient pressure differentials between the core pipe and the by-pass pipe might not necessarily be problematic as long as this overestimation remains within certain limits.

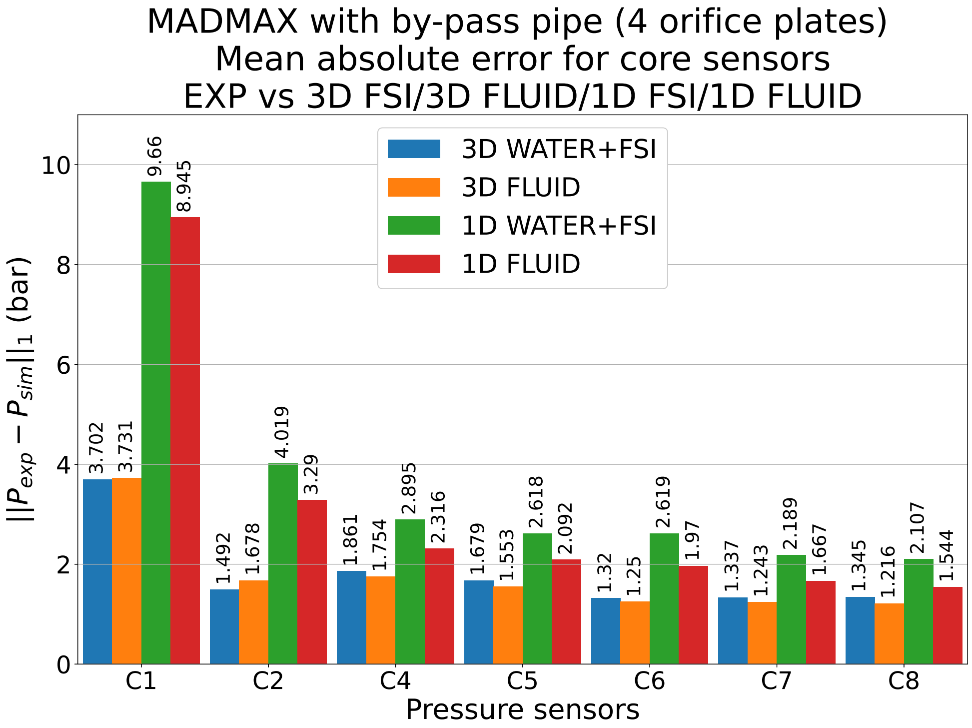

Figure 6.7: Configuration 2 mean absolute error for the junction pipe sensor and the core pipe sensors.

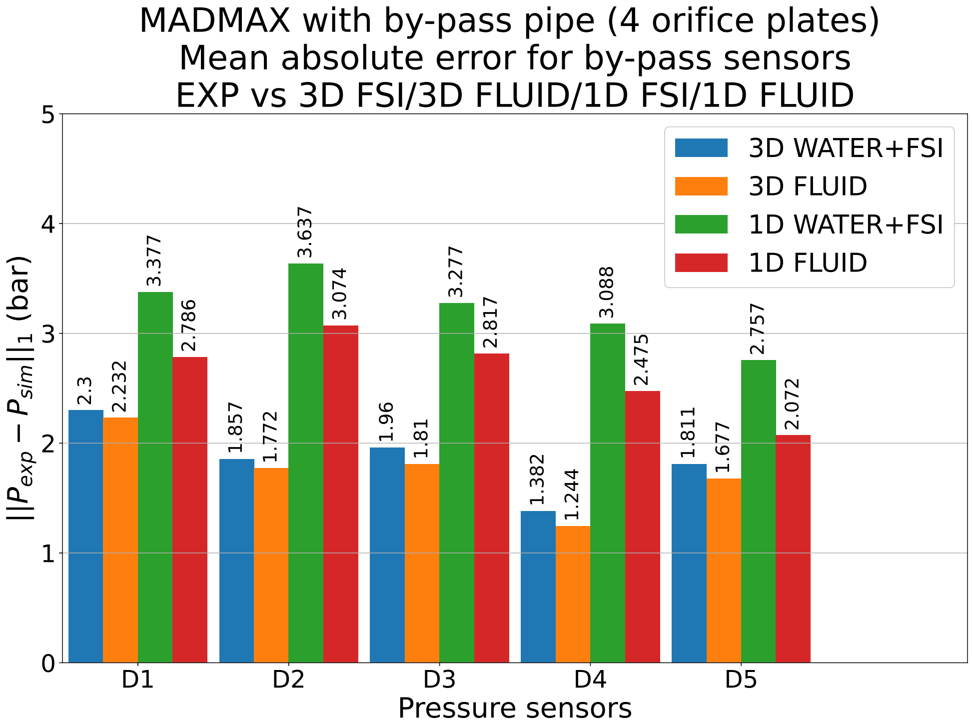

Figure 6.8: Configuration 2 mean absolute error for the by-pass pipe sensors.

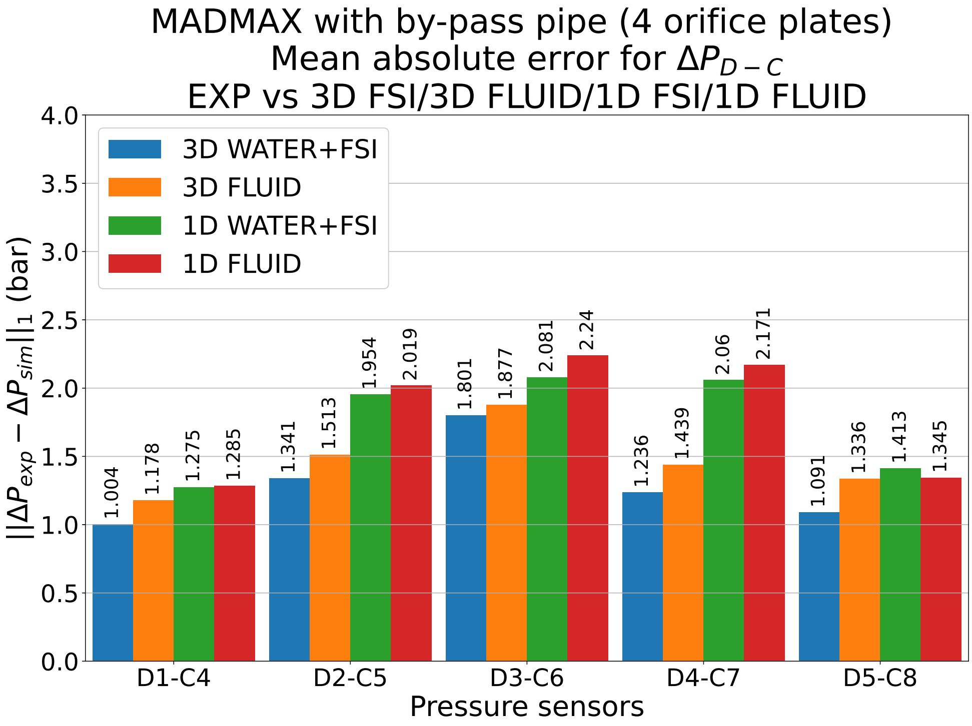

Figure 6.9: Configuration 2 mean absolute error for pressure differences between core and by-pass pipe sensors.

6.2.2 Configuration 3: MADMAX with 6 orifice plates in by-pass pipe and 1 orifice plate in core pipe

The Configuration 3 of MADMAX undoubtedly represents the most significant novelty among all the experiments conducted in the experimental campaigns carried out during this thesis work. Indeed, it is the first time that an experiment has been conducted on MADMAX simultaneously incorporating the presence of orifice plates in the by-pass pipe and an orifice plate in the core pipe.

The presence of the orifice plate with a thickness $e = 10\,\text{mm}$ and an orifice diameter $d = 30\,\text{mm}$ is reflected in the significant transient pressure differential generated in the core pipe between the upstream (sensors C2-C6) and downstream (sensors C7-C8) of the orifice plate, as discussed earlier in the chapter. This pressure differential is almost evenly dispersed across the sensors within the by-pass pipe, D1-D5.

Figures 6.10 and 6.11 depict the pressure evolution for sensors C1, C2, C4, D1, C6, D3, C8, and D5, comparing experimental measurements with the results from the four numerical models. While the 3D/3D FSI models generally exhibit excellent agreement with the experimental results, the 1D/1D FSI models demonstrate limitations in accurately reproducing the pressure plateau for $t \geq 9\,\text{ms}$ for sensors C2-C6 in the core pipe. Both the experiment and the 3D/3D FSI models reach a plateau around 10 bar (the pressure does not drop to ambient pressure levels due to the accumulator thrust and the presence of the junction pipe, which limits the outflow), whereas the 1D/1D FSI models seem to undergo complete depressurization, thus showing a plateau at around 1 bar. This effect reflects on the sensors of the by-pass pipe, becoming progressively less significant from the lowest sensor (D1) to the highest sensor (D5). For sensors C7 and C8, beginning at $t \geq 11\,\text{ms}$, there is a notable overestimation in the pressure levels calculated by the 1D/1D FSI models compared to both the experimental data and the 3D/3D FSI models.

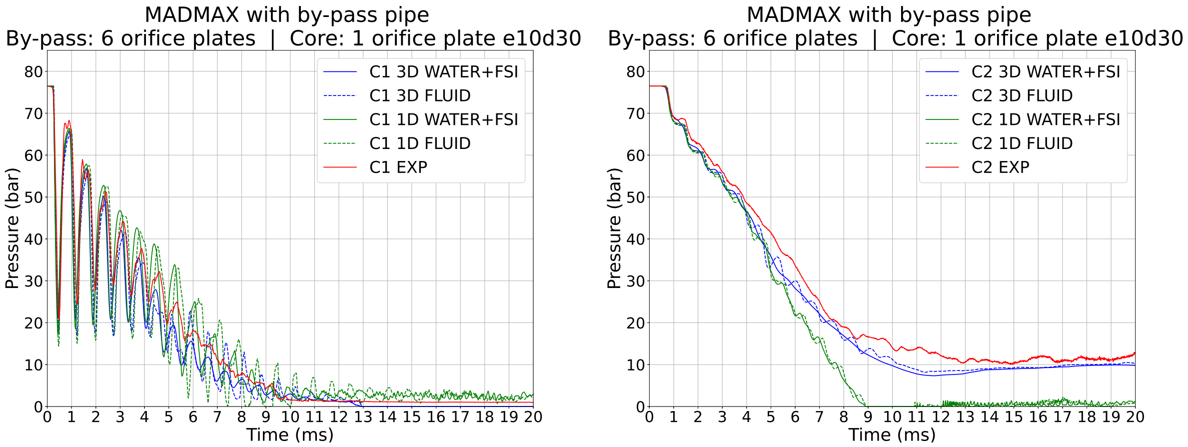

(a) C1

(b) C2

Figure 6.10: Configuration 3 pressure evolution comparison for sensors C1 and C2.

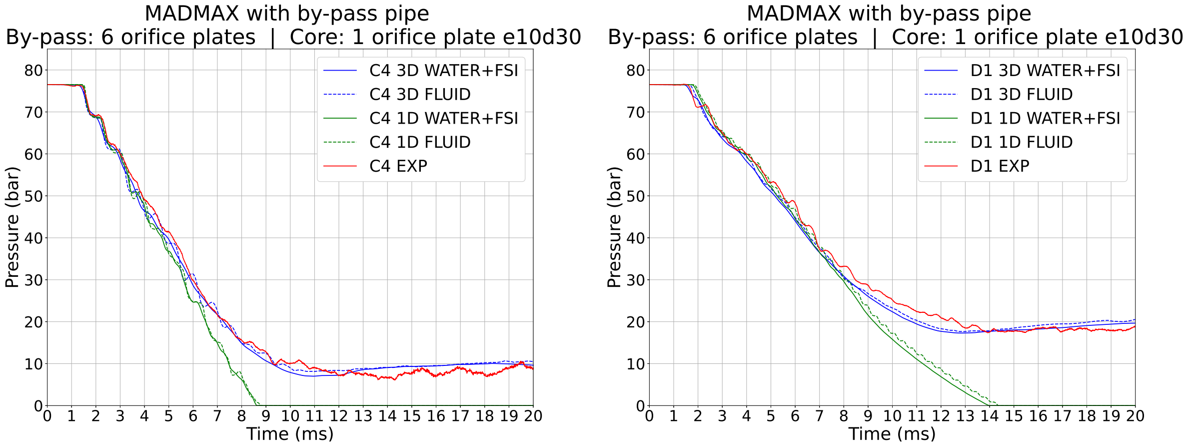

(a) C4 (b) D1

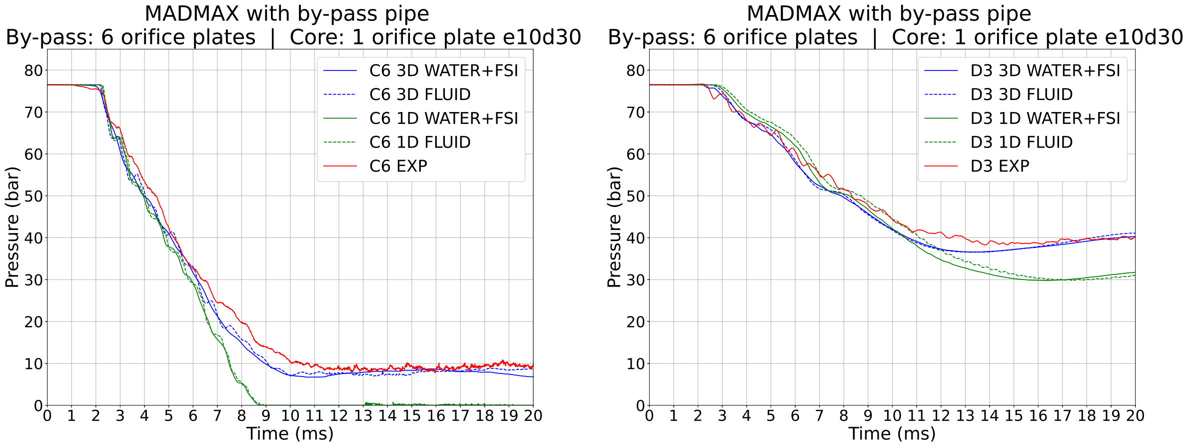

(c) C6 (d) D3

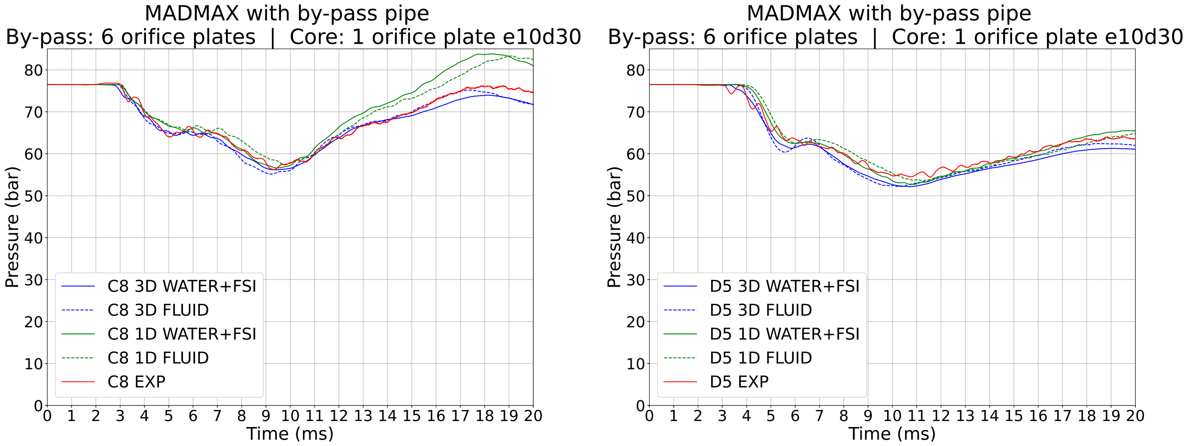

(e) C8 (f) D5

Figure 6.11: Configuration 3 pressure evolution comparison for sensors C4, D1, C6, D3, C8 and D5.

For completeness, Figure 6.12 illustrates the transient pressure differentials between sensors

D2 and C5, ΔP_{D2-C5}, and sensors D4 and C7, ΔP_{D4-C7}. In line with the earlier discussion, the transient pressure differences for the sensor pairs D1-C4, D2-C5, and D3-C6 (all upstream of the core pipe's orifice plate) are positive, indicating that the pressure in that section of the device is higher in the by-pass pipe compared to the core pipe, as the by-pass pipe encounters more difficulty in emptying due to the presence of the six orifice plates. For these sensor pairs, the peaks of the transient differential pressure are approximately 30 bar according to experimental measurements and 3D/3D FSI calculations, while the 1D/1D FSI models show a significant overestimation, with peaks reaching up to 40 bar.

For the sensor pairs D4-C7 and D5-C8, both downstream of the orifice plate in the core pipe, the behavior of the transient pressure differential is diametrically opposite. Apart from the transient zone for $t \leq 6\,\text{ms}$, the trend is consistently negative, indicating a higher pressure in the core pipe than in the by-pass pipe for this area of the experimental setup. This suggests that the orifice plate in the core pipe alone presents more resistance to the emptying of the upper part of the device compared to the six orifice plates arranged in the by-pass pipe. Furthermore the thrust from the accumulators is more significant in the core pipe than in the by-pass pipe, given that by design, they direct the flow along the same axis as the core pipe. The peak of the transient pressure differential is approximately -25 bar according to both experimental results and 3D/3D FSI calculations, while it is again overestimated at around -38 bar by the 1D/1D FSI calculations.

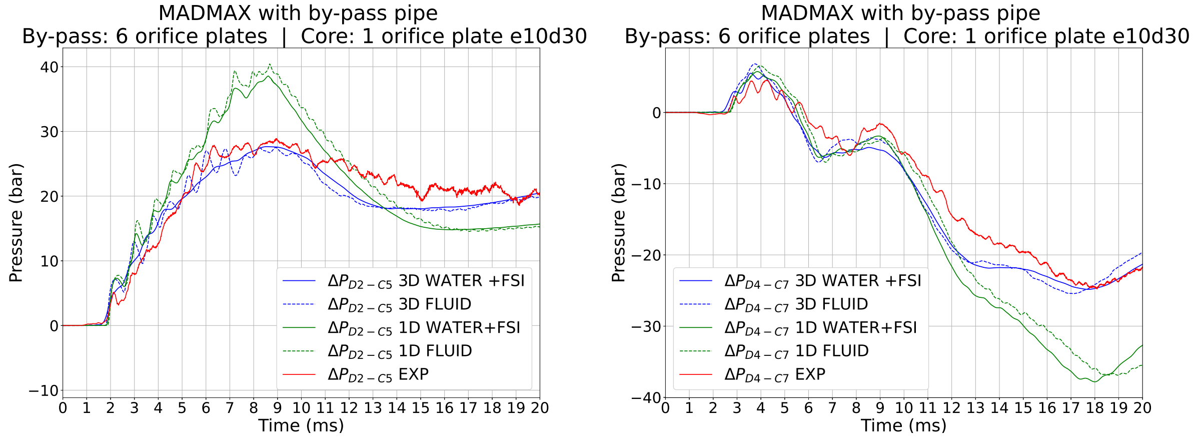

(a) D2-C5 (b) D4-C7

Figure 6.12: Configuration 3 pressure difference between sensors D2 and C5, ΔP_{D2-C5}, and sensors D4 and C7, ΔP_{D4-C7}.

In line with the previous discussion, the mean absolute error between the simulations and experimental results for sensors C1-C8 (see Figure 6.13) falls within the range $[1, 3]$ bar for the 3D/3D FSI models, with higher errors observed for sensors C1 and C2, lower errors for sensors C7 and C8, and intermediate errors for sensors C4-C6. The situation deteriorates significantly for the 1D/1D FSI models, which exhibit errors in the range $[6, 10]$ bar for sensors C2-C6 and errors in the range $[2, 4]$ bar for sensors C1, C7, and C8.

For sensors D1-D5 (see Figure 6.14), the mean absolute error falls within the range $[1.4, 2.5]$ bar for the 3D/3D FSI models, with a peak observed for sensor D4. In contrast, for the 1D/1D FSI models, the error decreases nearly linearly from sensor D1 to sensor D5, ranging from a maximum around 9 bar to a minimum around 1 bar.

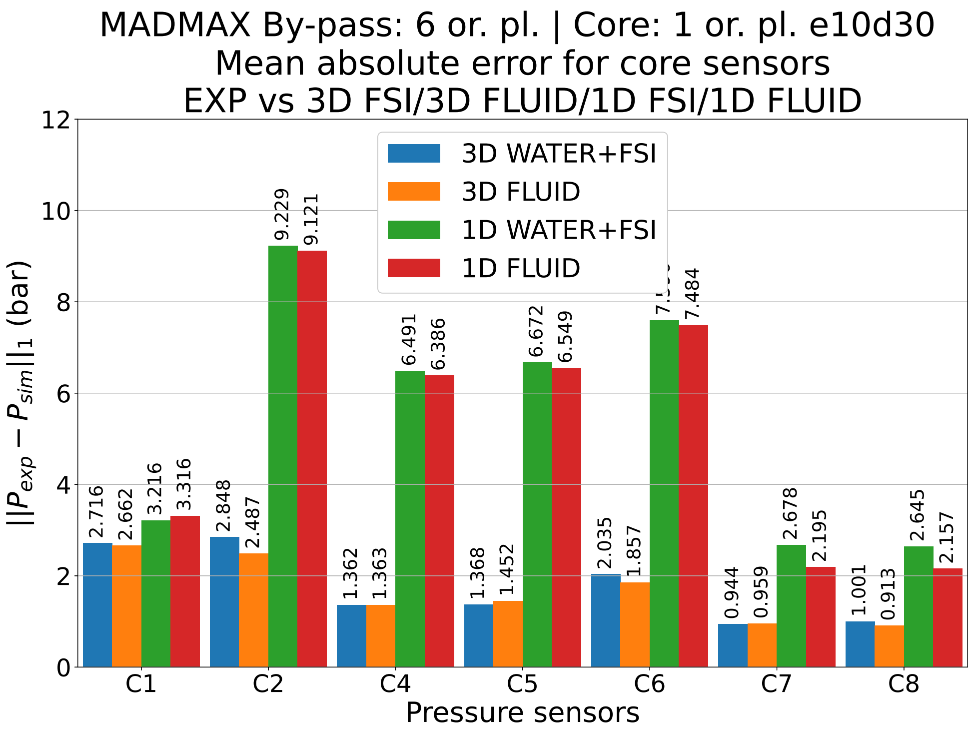

Figure 6.13: Configuration 3 mean absolute error for the junction pipe sensor and the core pipe sensors.

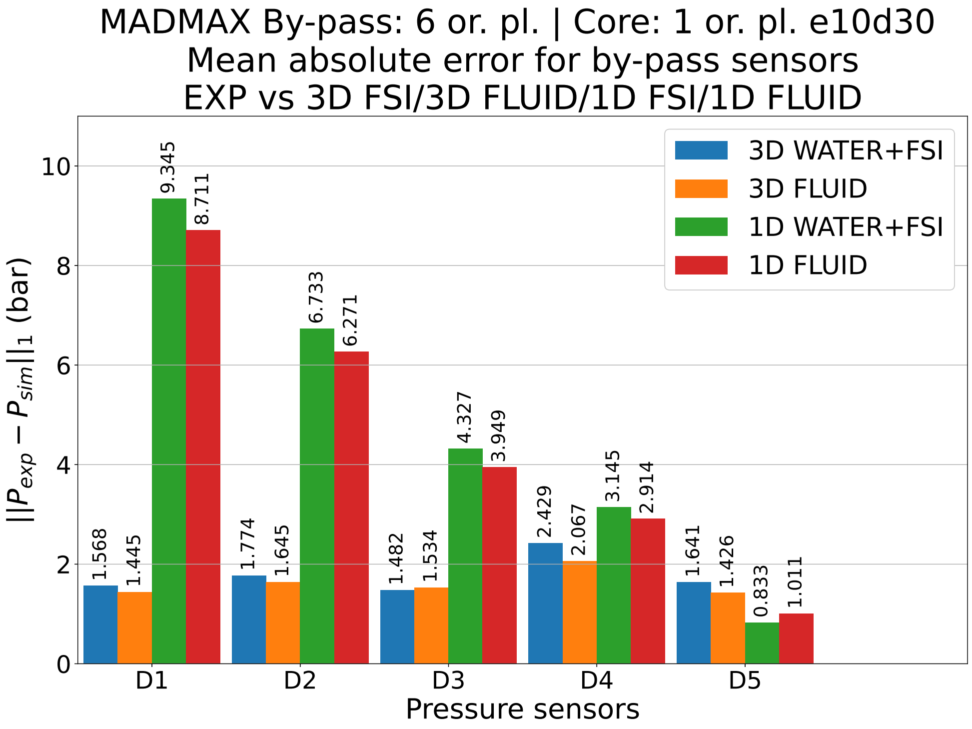

Figure 6.14: Configuration 3 mean absolute error for the by-pass pipe sensors.

Regarding the transient pressure differentials between the sensors of the by-pass pipe (D1-D5) and the sensors of the core pipe (C4-C8), it can be observed from Figure 6.15 that the mean absolute error for the 3D/3D FSI models falls within the range $[1, 3]$ bar, with the FSI case consistently slightly more accurate. For the 1D/1D FSI models, the error range is $[2, 6]$ bar, with values around 5 bar for the pairs D1-C4, D2-C5, D3-C6, and D4-C7, which decrease to approximately 2.5 bar for the pair D5-C8. The 1D WATER+FSI calculation is more accurate than the 1D FLUID calculation for the pairs D1-C4, D2-C5, D3-C6, while the opposite is observed for the pairs D4-C7 and D5-C8.

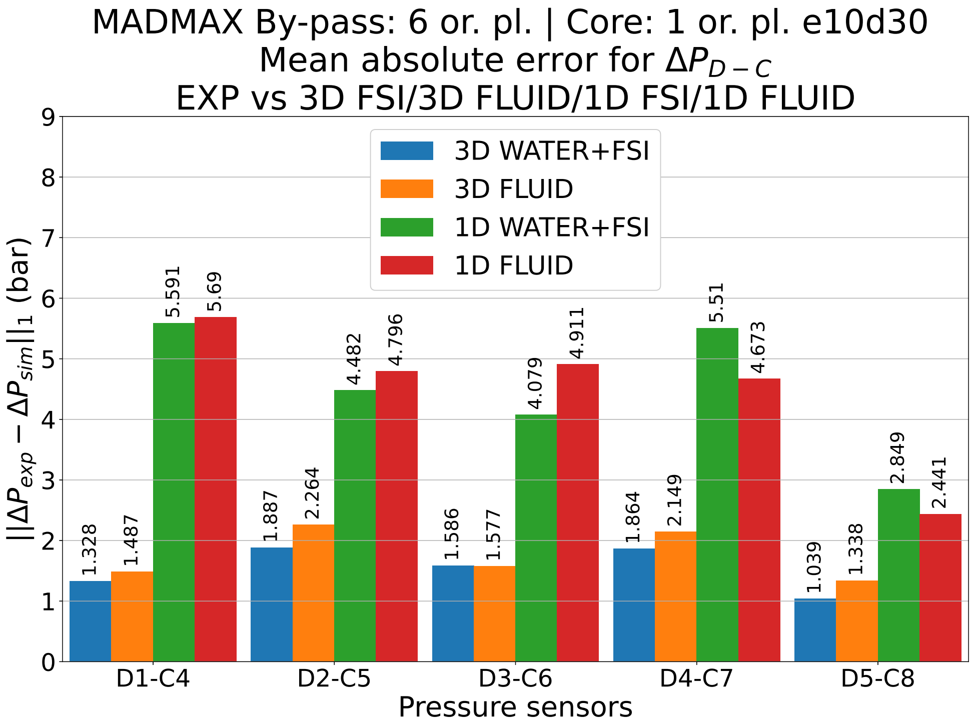

Figure 6.15: Configuration 3 mean absolute error for pressure differences between core and by-pass pipe sensors.

Regarding the trade-off between computational cost and model accuracy, similar conclusions to those presented for Configuration 1 and Configuration 2 can be drawn also for Configuration 3. In a plane “Computational time vs Error or Accuracy”, the 4 models form again a set of non-dominated choices, with the 3D WATER+FSI approach providing the best accuracy for the highest cost and the 1D FLUID approach providing the lowest accuracy for the lowest cost.

In this case, regarding the choice of one approach over another, we can make considerations similar to those made previously for Configuration 2. Everything depends on the level of precision deemed acceptable or the maximum computational cost one is willing to incur. By adopting a conservative approach, as previously mentioned, the 1D models, which tend to overestimate certain results, could be considered favorable. However, in this last analyzed configuration, the discrepancies with the reference models are more significant compared to the two previous configurations. This suggests that a more accurate approach might be necessary to meet specific tolerance limits.

6.3 Conclusions

This chapter has presented an investigation into two alternative configurations of MADMAX featuring the presence of the by-pass pipe, denoted as Configurations 2 and 3. These configurations were previously introduced in Chapter 2 and briefly mentioned at the beginning of Chapter 5.

Experimental campaigns were conducted to examine the behavior of these configurations, providing valuable insights into the understanding of their physical features. Configuration 2, characterized by a free core pipe and 4 orifice plates in the by-pass, exhibited similarities with Configuration 1, except for minor variations due to the absence of two orifice plates in the by-pass pipe. Configuration 3, which incorporated an orifice plate in the core pipe along with 6 orifice plates in the by-pass pipe, represented a novel setup that closely resembled real industrial scenarios.

Comparative analyses between experimental data and numerical simulations were performed, revealing notable findings. The 3D/3D FSI models generally demonstrated better agreement with experimental results compared to the 1D/1D FSI models. In Configuration 2, the absence of the lower orifice plate in the by-pass pipe led to a reduction in transient pressure differentials, while Configuration 3 displayed unique pressure distribution patterns due to the combined effects of orifice plates in both pipes.

The mean absolute errors between simulations and experiments varied across sensors and models, with generally higher errors observed in the 1D/1D FSI simulations compared to the 3D/3D FSI simulations. Additionally, the trade-off between computational cost and model accuracy remained consistent with previous observations, highlighting the advantages of 3D/3D FSI models in capturing complex fluid-structure interactions accurately. However, it is worth noting that despite the higher precision of 3D/3D FSI models over 1D/1D FSI models, the significantly reduced computational cost of the latter makes them highly competitive. Furthermore, the overestimated results provided by 1D/1D FSI models can be considered conservative in the field of nuclear safety.

In summary, the experimental and numerical investigations presented in this chapter offer valuable insights into the behavior and performance of alternative MADMAX configurations, contributing to the comprehension of rarefaction wave propagation phenomena in systems involving multiple obstacles in different configurations.

Conclusions and Perspectives

The investigation presented in this work provides a comprehensive understanding of rarefaction wave propagation phenomena in Pressurized Water Nuclear Reactors (PWRs) during Loss of Coolant Accidents (LOCAs). Through a combination of experimental campaigns conducted on the MADMAX (Modélisation de l'Accident de Dépressurisation - Maquette Analytique-eXpérimentale) facility and numerical simulations using EUROPLEXUS software, various configurations and scenarios were explored to assess the predictive capabilities of simulation models and enhance understanding of fluid-structure interactions in complex systems.

The initial focus on the simplified configuration of MADMAX, without a by-pass pipe and featuring a single modular orifice plate, enabled a detailed parametric study of obstacle geometry and its influence on rarefaction wave propagation. The numerical models employed, ranging from 1D simplified representations to more detailed 2D axisymmetric and 3D reference models, exhibited good agreement with experimental results, demonstrating their reliability in capturing pressure dynamics and deformations within the system. Furthermore, the incorporation of Fluid-Structure Interaction (FSI) effects in the simulations provided valuable insights into cavitation phenomena and structural response, enhancing the fidelity of predictions.

Expanding on this groundwork, configurations involving the by-pass pipe and multiple orifice plates were investigated, offering insights into more complex scenarios resembling real industrial conditions. Comparative analyses between experimental data and numerical simulations revealed the capabilities and limitations of different simulation models, highlighting the trade-offs between computational efficiency and accuracy. While 3D/3D FSI models demonstrated higher accuracy in capturing complex fluid-structure interactions, 1D/1D FSI models offered competitive computational efficiency, albeit with slightly overestimated results. These findings underscore the importance of selecting appropriate simulation models based on the specific requirements of the analysis, balancing computational resources with desired accuracy.

Moreover, the exploration of alternative configurations, such as varying the number and arrangement of orifice plates in the by-pass pipe, provided valuable insights into system behavior and performance under different conditions. These investigations contribute to the broader understanding of rarefaction wave propagation phenomena in nuclear reactor systems and provide valuable data for validating simulation codes used in nuclear safety assessments.

Overall, this work aims to contribute to the field of nuclear reactor analysis and transient flow simulations, offering insights into the complex dynamics of rarefaction wave propagation and FSI in PWRs. By combining experimental data with advanced numerical simulations, this study advances our understanding of LOCA scenarios and provides a foundation for further research aimed at enhancing the safety and reliability of nuclear reactor systems.

Perspectives From both a numerical and experimental perspective, this work opens up significant avenues for scientific and industrial interests. One of the primary prospects is to investigate the influence of different obstacles such as plates with multiple holes or pseudo fuel assemblies and mixing grids in the core pipe.

From a purely **numerical standpoint** we would like to: i) to investigate the use of the Finite Volume Method (FVM) for carrying out the 1D simulations, anticipating that the Finite Element Method does not ensure as well as FVM conservation properties which are critical in other more complex applications; this includes a development step for a Finite Volume acoustic impedance model to be implemented in EUROPLEXUS; ii) to develop and implement a porosity model for representing the central core zone (fuel assemblies and mixing grids).

From the **experimental standpoint**, new configurations may allow us to investigate the influence of different obstacles such as plates with multiple holes or pseudo fuel assemblies and mixing grids in the core pipe. Technical modifications of the experimental device, such as the installation of new sensors (pressure, force, and deformation sensors), will enable a more in-depth and precise investigation of the propagation dynamics of the rarefaction wave both in the fluid and within the structure.

Several alternative configurations or experiment modifications have been proposed during the course of this PhD work; unfortunately, due to time constraints, they could not be implemented. However, they certainly remain among the primary prospects for future developments of the experiment, especially since after completing the PhD, I will continue to work as a research engineer at the DYN laboratory of CEA Saclay. Consequently, I will be overseeing future work on the experiment myself, likely supervising future interns/PhD candidates.

From a scientific standpoint, the following advancements have been proposed:

- Testing on plates with multiple orifices, akin to those depicted in Figure 6.16, to assess the reliability and precision of simplified numerical models for this type of configuration.

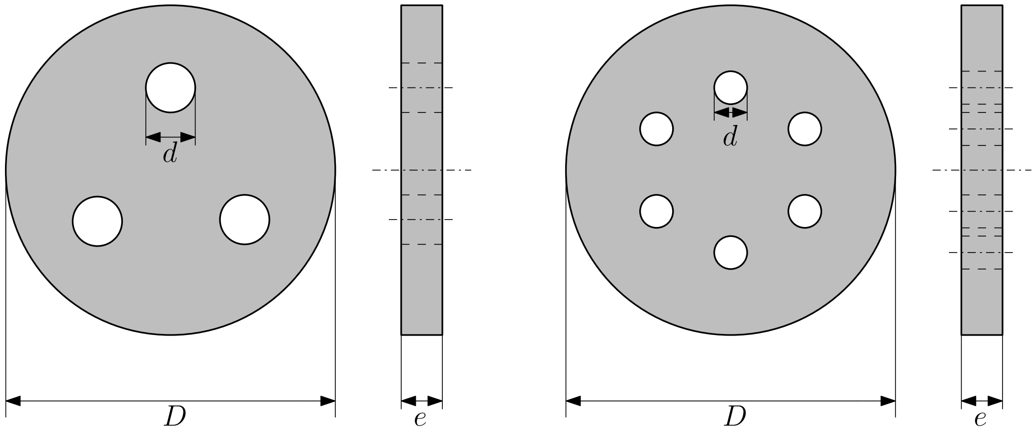

Figure 6.16: Multi-orifice plates examples.

- Installation of a structure in the core pipe that more faithfully reproduces the central zone of a nuclear reactor core, including fuel assemblies and mixing grids, as shown in Figure 6.17. This configuration, requiring a preliminary study for the design of the new component, would bring us closer to the real industrial case outlined at the beginning of Chapter 1. In this case, from a numerical perspective, the implementation of a porosity model for representing the zone is being considered.

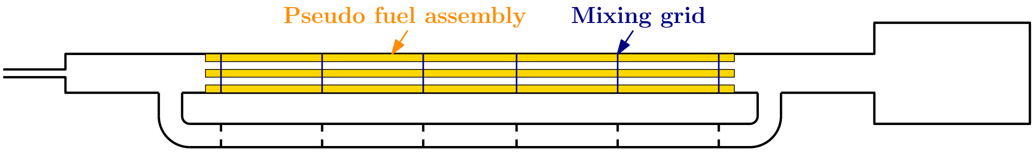

Figure 6.17: MADMAX configuration with pseudo fuel assembly and mixing grids.

From a technical standpoint, the following advancements are anticipated:

- Installation of new piezoresistive pressure sensors in parallel with the existing piezoelectric sensors. The purpose can be summarized into two objectives: 1. duplicating the pressure measurement with a different technology for each measurement point; 2. accurately measuring longer transients (beyond 100 ms) to analyze the complete emptying phase of the device (piezoelectric sensors, by their operational nature, do not allow for measuring long transients as they rely on rapid voltage variations recorded by the sensor following the passage of the pressure wave; piezoresistive sensors, on the other hand, are capable of providing continuous measurement of absolute pressure). This evolution involves mechanical modifications to the device to accommodate the installation of the new sensors. Such modifications will be carried out by an external entity, and it is anticipated to complete them by the end of 2024.

- Installation of force and deformation sensors on the structure to assess the mechanical stresses it undergoes and to provide experimental validation for Fluid-Structure Interaction (FSI) simulations.

- During the thesis, brief consideration was given to the possibilities of measuring fluid velocity within the experimental device. The main techniques used in this field can be summarized into two groups: Eulerian methods such as Particle Image Velocimetry (PIV), Laser Doppler Velocimetry (LDV), or Hotwire, and Lagrangian methods such as Particle Tracking Velocimetry (PTV), Ultrasound Doppler Velocimetry (UDV), or Smart particles. All techniques requiring the use of high-speed cameras (PIV, PTV) are not suitable due to the absence of a sufficiently large observation porthole on the experimental device. LDV was tested through a small porthole present on the central section of the by-pass pipe, but it did not yield any satisfactory results because the transient develops too rapidly, resulting in a very low probability of detecting a particle as it passes through the lasers. UDV might seem like the most reasonable solution, but it risks encountering the same issues as LDV, in addition to having limitations in acquisition frequency with existing technologies and the fact that attempting to observe an acoustic phenomenon using a method based on emitting acoustic waves could in turn cause interference in the measurements. Furthermore, the sensors used in UDV are essentially microphones that measure particle velocity using the acoustic Doppler effect, and the commercially available devices we found do not withstand high pressures.

  As a result of the various technical limitations encountered, the idea of performing velocity measurements on the experiment has been temporarily set aside but may be revisited in the future.

Bibliography

[1] V. Faucher, F. Crouzet, P. Piteau, P. Galon, and P. Izquierdo. Numerical and experimental analysis of transient wave propagation through perforated plates for application to the simulation of LOCA in PWR. *Nuclear engineering and design*, 253:1–11, 2012.

[2] H. Bung. *Méthodes Numériques en Dynamique Rapide*. CEA-Saclay. XCollège de Polytechnique : Interaction Fluide-Structure, 18-20 juin 2013. Présentation.

[3] T. Brandt, V. Lestinen, T. Toppila, J. Kähkönen, A. Timperi, T. Pättikangas, and I. Karppinen. Fluid-structure interaction analysis of large-break loss of coolant accident. *Nuclear engineering and design*, 240(9):2365–2374, 2010.

[4] P. Hermansky and M. Krajčovič. The numerical simulation of the WWER440/V213 reactor pressure vessel internals response to maximum hypothetical Large-break Loss of Coolant Accident. *Nuclear Engineering and Design*, 241(4):1177–1183, 2011.

[5] F. Casadei and S. Potapov. Permanent fluid–structure interaction with non-conforming interfaces in fast transient dynamics. *Computer methods in applied mechanics and engineering*, 193(39-41):4157–4194, 2004.

[6] EUROPLEXUS Website, 2021. URL `http://www-epx.cea.fr`.

[7] F. Bentivegna, A. Beccantini, P. Galon, and C. Corre. Numerical and experimental parametric investigation of rarefaction wave propagation across an orifice plate. *The Proceedings of the International Conference on Nuclear Engineering (ICONE)*, 2023.30:1313, 2023. doi: 10.1299/jsmeicone.2023.30.1313.

[8] F. Bentivegna, A. Beccantini, P. Galon, and C. Corre. Experimental and numerical analysis of rarefaction wave propagation across an orifice plate with varying thickness and diameter. *Mechanical Engineering Journal*, 11(2):23–00474–23–00474, 2024. doi: 10.1299/mej.23-00474.

[9] V. Faucher, F. Crouzet, and F. Debaud. Mechanical consequences of LOCA in PWR: Full scale coupled 1D/3D simulations with fluid-structure interaction. *Nuclear Engineering and Design*, 270:359–378, 2014.

[10] R. J. Gibert and B. Schawb. Reaction Sodium-Eau : étude de l'élément absorbant (CL2D ou CL3D) de plexus en vue de représenter des plaques perforés traversées par une onde plane. *Rapport DEMT/SMTS/LAMS/83-11*, 1983.

[11] P. Izquierdo and T. Valin. Propagation d'une onde de dépressurisation au travers de singularités - Résultats expérimentaux de la *Maquette APRP* - Comparaison au calcul EUROPLEXUS sur une configuration simplifiée. *Rapport DEN/DANS/DM2S/SEMT/DYN/RT/10-029/A*, 2011.

[12] I. E. Idel'Cik. Memento des pertes de charge. *Collection de la Direction des Etudes et Recherches d'Electricité de France*, 1969.

[13] G. Baylac, R. J. Gibert, and M. Livolant. Calcul de l'amplification acoustique dans les circuits complexes: application aux vibrations des échangeurs du réacteur CHINON III. *La Houille Blanche*, 5:407–428, 1971.

[14] R. J. Gibert. *Vibrations des Structures-Interactions Avec les Fluides.* Eyrolles, 1988.

[15] L. J. Pedroso. *Qualification experimentale des methodes de calculs des interactions fluide-structure dans les circuits tubulaires des reacteurs nucleaires.* PhD thesis, INSTN, 1986. URL https://inis.iaea.org/search/search.aspx?orig_q=RN:18095174.

[16] V. Daru and C. Tenaud. Numerical simulation of the viscous shock tube problem by using a high resolution monotonicity-preserving scheme. *Computer and Fluids*, 38 (3):664–676, 2009. doi: 10.1016/j.compfluid.2008.06.008.

[17] S. Radman, C. Fiorina, and A. Pautz. Development of a novel two-phase flow solver for nuclear reactor analysis: algorithms, verification and implementation in OpenFOAM. *Nuclear Engineering and Design*, 379, 8 2021. ISSN 00295493. doi: 10.1016/j.nucengdes.2021.111178.

[18] C. Feuchter. Direct aeroacoustic simulation with a cumulant lattice-boltzmann model. *Computers and Fluids*, 224:104970, 2021. ISSN 00457930. doi: 10.1016/j.compfluid.2021.104970. URL https://doi.org/10.1016/j.compfluid.2021.104970.

[19] S. Mokhtari, G. Ricciardi, V. Faucher, P. Argoul, and L. Adélaide. Multiscale Filtering of Compressible Wave Propagation in Complex Geometry through a Wavelet-Based Approach in the Framework of Pressurized Water Reactors Depressurization Transient Analysis. *Fluids*, 5, 2020. ISSN 23115521. doi: 10.3390/fluids5020064.

[20] M. I. Radaideh, T. Kozlowski, and Y. M. Farawila. Loss of coolant accident analysis under restriction of reverse flow. *Nuclear Engineering and Technology*, 51:1532–1539, 2019. ISSN 2234358X. doi: 10.1016/j.net.2019.04.016. URL https://doi.org/10.1016/j.net.2019.04.016.

[21] V. Faucher, G. Ricciardi, R. Boccaccio, K. Cruz, T. Lohez, and S.A. Clément. Numerical implementation and validation of a porous approach for fluid–structure interaction applied to pressurized water reactors fuel assemblies under axial water flow and dynamic excitation. *International Journal for Numerical Methods in Engineering*, 122:2417–2445, 2021. ISSN 10970207. doi: 10.1002/nme.6626.

[22] S. W. Rienstra and A. Hirschberg. An introduction to acoustics. Eindhoven University of Technology, Netherlands, pp. 86-98, 2004.

[23] G. C. J. Hofmans, R. J. J. Boot, P. P. J. M. Durrieu, Y. Aurégan, and A. Hirschberg. Aeroacoustic response of a slit-shaped diaphragm in a pipe at low Helmholtz number, 1: Quasi-steady results. *Journal of sound and vibration*, 244(1):35–56, 2001.

[24] B. Brunone, U. M. Golia, and M. Greco. International Meeting on Hydraulic Transients with Column Separation, 9th Round Table. IAHR, Valencia, Spain, 1991.

[25] W. Zielke. Frequency-dependent friction in transient pipe flow. *Journal of Basic Engineering*, ASME 90(1):109–115, 1968.

[26] A. Adamkowski and M. Lewandowski. Experimental examination of unsteady friction models for transient pipe flow simulation. *J. Fluids Eng.*, 128, 2006.

[27] J. P. Vítkovskỳ, A. Bergant, A. R. Simpson, and M. F. Lambert. Systematic evaluation of one-dimensional unsteady friction models in simple pipelines. *Journal of Hydraulic Engineering*, 132(7):696–708, 2006.

[28] A. M. Mohsen, M. Z. Yusoff, and A. Al-Falahi. The effects of area contraction on the performance of uniten's shock tube: Numerical study. *IOP Conference Series: Earth and Environmental Science*, 16, 2013. ISSN 17551315. doi: 10.1088/1755-1315/16/1/012111.

[29] A. Britan, O. Igra, G. Ben-Dor, and H. Shapiro. Shock wave attenuation by grids and orifice plates. *Shock Waves*, 16:1–15, 2006. ISSN 09381287. doi: 10.1007/s00193-006-0019-0.

[30] A. Dadone and M. Pandolfi. Interaction of travelling shock waves with orifices inside ducts. *International Journal of Mechanical Sciences*, 13:1–16, 1971. ISSN 00207403. doi: 10.1016/0020-7403(71)90098-1.

[31] T. Schunck and D. Eckenfels. Blast mitigation by perforated plates using an explosive driven shock tube : study of geometry effects and plate numbers. *SN Applied Sciences*, 2021. ISSN 2523-3971. doi: 10.1007/s42452-021-04720-3. URL `https://doi.org/10.1007/s42452-021-04720-3`.

[32] S. Meniconi, B. Brunone, M. Ferrante, and C. Massari. Energy dissipation and pressure decay during transients in viscoelastic pipes with an in-line valve. *Journal of Fluids and Structures*, 45:235–249, 2014. ISSN 08899746. doi: 10.1016/j.jfluidstructs.2013.12.013. URL `http://dx.doi.org/10.1016/j.jfluidstructs.2013.12.013`.

[33] P. Laffay, S. Moreau, M. C. Jacob, and J. Regnard. Experimental investigation of the noise radiated by a ducted air flow discharge though diaphragms and perforated plates. *Journal of Sound and Vibration*, 472, 2020. ISSN 10958568. doi: 10.1016/j.jsv.2020.115177.

[34] G. Ciccarelli, Q. Li, and C. Metrow. The three-dimensional structure of a detonation wave propagating in a round tube with orifice plates. *Shock Waves*, 28:1019–1030, 2018. ISSN 09381287. doi: 10.1007/s00193-018-0839-8.

[35] O. Igra, X. Wu, J. Falcovitz, T. Meguro, K. Takayama, and W. Heilig. Experimental and theoretical study of shock wave propagation through double-bend ducts. *Journal of Fluid Mechanics*, 437:255–282, 2001. ISSN 00221120. doi: 10.1017/S0022112001004098.

[36] O. Igra, J. Falcovitz, H. Reichenbach, and W. Heilig. Experimental and numerical study of the interaction between a planar shock wave and a square cavity. *Journal of Fluid Mechanics*, 313:105–130, 1996. ISSN 00221120. doi: 10.1017/S0022112096002145.

[37] C. Colas, M. Ferrand, J.M. Hérard, J.C. Latché, and E. Le Coupanec. An implicit integral formulation to model inviscid fluid flows in obstructed media. *Computers and Fluids*, 188: 136–163, 2019. ISSN 00457930. doi: 10.1016/j.compfluid.2019.05.014.

[38] G. Abate and W. Shyy. Dynamic structure of confined shocks undergoing sudden expansion. *Progress in Aerospace Sciences*, 38:23–42, 1 2002. ISSN 0376-0421. doi: 10.1016/S0376-0421(01)00016-1.

[39] E. Romenski, G. Reshetova, I. Peshkov, and M. Dumbser. Modeling wavefields in saturated elastic porous media based on thermodynamically compatible system theory for multiphase mixtures, 10 2019. ISSN 00457930. URL `http://arxiv.org/abs/1910.04207`.

[40] D. Igra and O. Igra. Shock wave mitigation by different combination of plate barriers; A numerical investigation. *European Journal of Mechanics, B/Fluids*, 59:115–123, 2016. ISSN 09977546. doi: 10.1016/j.euromechflu.2016.05.002. URL `http://dx.doi.org/10.1016/j.euromechflu.2016.05.002`.

[41] Z. Jiang, K. Takayama, H. Babinsky, and T. Meguro. Transient shock wave flows in tubes with a sudden change in cross section. *Shock Waves*, 7:151–162, 1997. ISSN 09381287. doi: 10.1007/s001930050072.

[42] D. Kröner and M.D. Thanh. Numerical Solutions to Compressible Flows in a Nozzle with Variable Cross-Section. *SIAM J. Numer. Anal.*, 43:796–824, 2005.

[43] G. Rudinger. Passage of shock waves through ducts of variable cross section. *Physics of Fluids*, 3:449–455, 1960. ISSN 10706631. doi: 10.1063/1.1706058.

[44] M. D. Salas. Shock wave interaction with an abrupt area change. *Applied Numerical Mathematics*, 12:239–256, 1993.

[45] M. Schulze, M. Wagner, and T. Sattelmayer. Linearized Euler equations for the determination of scattering matrices for orifice and perforated plate configurations in the high Mach number regime. *Aerospace*, 3, 2016. ISSN 22264310. doi: 10.3390/aerospace3040033.

[46] O. Igra and J. J. Gottlieb. Interaction of rarefaction waves with area enlargements in ducts. *AIAA Journal*, 23:1014–1020, 1985. ISSN 00011452. doi: 10.2514/3.9032.

[47] G. Emanuel, U.S. Satyanand, and F.K. Lu. Performance of a shock tube with a large-area contraction. *AIAA Journal*, 43:1995–1999, 2005. ISSN 00011452. doi: 10.2514/1.12786.

[48] J. Falcovitz and O. Igra. Model for shock interaction with sharp area reduction. *Proceedings of the Institution of Mechanical Engineers, Part G: Journal of Aerospace Engineering*, 222: 789–800, 2008. ISSN 09544100. doi: 10.1243/09544100JAERO321.

[49] S. Alligne, P. Rodic, J. Arpe, J. Mlacnik, and C. Nicolet. Determination of Surge Tank Diaphragm Head Losses by CFD Simulations. *Advances in Hydroinformatics*, 2014. doi: 10.1007/978-981-4451-42-0.

[50] R. Menina, R. Saurel, M. Zereg, and L. Houas. Modelling gas dynamics in 1D ducts with abrupt area change. *Shock Waves*, 21:451–466, 2011. ISSN 09381287. doi: 10.1007/s00193-011-0321-3.

[51] F. Payri, J. Galindo, J. R. Serrano, and F. J. Arnau. Analysis of numerical methods to solve one-dimensional fluid-dynamic governing equations under impulsive flow in tapered ducts. *International Journal of Mechanical Sciences*, 46:981–1004, 2004. ISSN 00207403. doi: 10.1016/j.ijmecsci.2004.07.014.

[52] D. Rochette and S. Clain. Two-dimensional computation of gas flow in a porous bed characterized by a porosity jump. *Journal of Computational Physics*, 219:104–119, 2006. ISSN 00219991. doi: 10.1016/j.jcp.2006.03.013.

[53] L. Erez, O. Sadot, D. Oron, G. Erez, L. A. Levin, D. Shvarts, and G. Ben-Dor. Study of the membrane effect on turbulent mixing measurements in shock tubes. *Shock Waves*, 10: 241–251, 2000. ISSN 09381287. doi: 10.1007/s001930000053.

[54] S. Berger, G. Ben-Dor, and O. Sadot. Experimental and numerical investigations of shock-wave attenuation by geometrical means: A single barrier configuration. *European Journal of Mechanics, B/Fluids*, 50:60–70, 2015. ISSN 09977546. doi: 10.1016/j.euromechflu.2014.11.006. URL `http://dx.doi.org/10.1016/j.euromechflu.2014.11.006`.

[55] O. Ram, G. Ben-Dor, and O. Sadot. On the pressure buildup behind an array of perforated plates impinged by a normal shock wave. *Experimental Thermal and Fluid Science*, 92: 211–221, 2018. ISSN 08941777. doi: 10.1016/j.expthermflusci.2017.11.014. URL `https://doi.org/10.1016/j.expthermflusci.2017.11.014`.

[56] S. Sha, Z. Chen, X. Jiang, and J. Han. Numerical investigations on blast wave attenuation by obstacles. *Procedia Engineering*, 45:453–457, 2012. ISSN 18777058. doi: 10.1016/j.proeng.2012.08.185. URL `http://dx.doi.org/10.1016/j.proeng.2012.08.185`.

[57] S. Berger, G. Ben-Dor, and O. Sadot. Experimental and Numerical Investigation of Shock Wave Attenuation by Dynamic Barriers. *Journal of Fluids Engineering*, 138:031103, 2015. ISSN 0098-2202. doi: 10.1115/1.4031375.

[58] V. Faucher, P. Galon, and P. Izquierdo. Groupe de travail 'Analyse de la traversée d'une plaque perforée par une onde de dépressurisation' – Rapport de synthèse. *Rapport DEN/DANS/DM2S/SEMT/DYN/RT/10-027/A*, 2010.

[59] P. Galon and M. Lepareux. Documentation théorique : modélisation des tuyauteries dans Europlexus. *Rapport DM2S/SEMT/DYN/RT/01-021*, 2001.

[60] A. Letellier. *Contribution à la modélisation des impacts d'oiseaux sur les aubes des réacteurs d'avions*. PhD thesis, Evry-Val d'Essonne, 1996. URL `http://www.theses.fr/1996EVRY0008`.

[61] R. Courant and K.O. Friedrichs. *Supersonic flow and shock waves*, volume 21. Springer Science & Business Media, 1999.

[62] EUROPLEXUS: User's Manual, 2021. URL `http://www-epx.cea.fr/index.php/epx-docs`.

[63] E. Schmidt. Properties of Water and Steam in SI-Units, ed. U. Grigull. Springer Verlag, Berlin, 1979.

[64] F. Casadei, J. P. Halleux, A. Sala, and F. Chille. Transient fluid–structure interaction algorithms for large industrial applications. *Computer methods in applied mechanics and engineering*, 190(24-25):3081–3110, 2001.

[65] L. Allievi. Teoria generale del moto perturbato dell'acqua nei tubi in pressione. *Annali della Societa degli Ingegneri ed Architette Italiani*, 1902.

[66] A. Wood. *A Textbook of Sound*. G. Bell and Sons LTD, London, 1930.

[67] G. B. Wallis. *One-dimensional Two-phase Flow*. McGraw-Hill, New York, 1969.

[68] C. Geuzaine and J. F. Remacle. Gmsh: a three-dimensional finite element mesh generator with built-in pre- and post-processing facilities. `http://gmsh.info`, 2022.

[69] A. Barraco, B. Cuny, A. Hoffmann, P. Jamet, A. Combescure, M. Lepareux, and H. Bung. PLEXUS - Software for the Numerical Analysis of the Dynamical Behavior of Rigid and Flexible Mechanisms. In *Multibody Systems Handbook*, pages 403–425. Springer, 1989.

[70] F. Casadei and J. P. Halleux. Binary spatial partitioning of the central-difference time integration scheme for explicit fast transient dynamics. *International Journal for Numerical Methods in Engineering*, 78(12):1436–1473, 2009.

Appendix A

Finite Element Method

In the description given below, the Finite Element Method is used to handle fluids and structures. Below, we outline the method applied solely to the fluid part. For the structural part, please refer to the literature ([69] and in particular Section 2 - Table I in [70]). The domain is subdivided into elements that are connected by nodes: certain quantities (such as density, internal energy, pressure, etc.) are defined at the Gauss points of the element (in the case of EUROPLEXUS fluid FE, there is only one Gauss point located at the element's centroid), while other quantities (typically velocity, acceleration, etc.) are defined at the nodes.

A.1 Spatial Discretization

The spatial discretization method used for the three conservation equations presented in the previous chapter is described below.

Mass Conservation Equation

Assuming that the mass density ρ is uniform within the element, Equation (3.5) can be written as follows:

$$\frac{\delta M^{\mathrm{e}}}{\delta t} = \frac{\delta}{\delta t}\int_{V_{\mathrm{e}}} \rho \, dV = \sum_{k=1}^{\mathrm{nface}} \rho^k \oint_{S_k} \left(\underline{w}^k - \underline{v}^k\right) \cdot \underline{n}^k \, dS = \sum_{k=1}^{\mathrm{nface}} \rho^k \left(\underline{w}^k - \underline{v}^k\right) \cdot \underline{n}^k \cdot S^k \tag{A.1}$$

where M^{e} is the mass of the element, V_{e} is the volume of the element, $\underline{n}^k$ is the normal to the k-th face of the element, $\underline{w}^k$ and $\underline{v}^k$ are respectively the "average" grid velocity and the "average" fluid velocity of the k-th face of the element (obtained after integration over this face), S^k is the surface of the k-th face of the element, ρ^k is the weighted mass density at the k-th interface, nface is the number of faces of the element.

The mass density ρ^k at interface "k" is the weighted average of the mass densities of the two elements adjacent to face k:

$$\rho^k = \frac{1}{2}\left[\left(1 - \alpha^k\right) \cdot \rho^{\mathrm{e}} + \left(1 + \alpha^k\right) \cdot \rho^{\mathrm{e'}}\right] \tag{A.2}$$

where α^k is the convective flux off-centering parameter. If $(\underline{w} - \underline{v}) \cdot \underline{n} \leq 0$, we take $\alpha^k > 0$. This favors the density of the "donor" element, which stabilizes the numerical scheme. In Europlexus, the default choice is to use $\alpha^k = 1$ (full off-centering or Upwind scheme).

Momentum Equation

Taking into account the variational formulation of the momentum equation (Eq. (3.12)), the following can be written for each element:

$$\underline{v}^*(\underline{x},t) = \sum_{I=1}^{\text{nbnoe}} N^I(\underline{x}) \cdot \underline{v}^{*I}(t) \qquad\qquad \underline{v}(\underline{x},t) = \sum_{I=1}^{\text{nbnoe}} N^I(\underline{x}) \cdot \underline{v}^{I}(t) \tag{A.3}$$

where $\underline{v}$ and $\underline{v}^*$ (respectively the material velocity field and the virtual velocity field, see Section 3.1.2.2 for details) are velocity vectors that depend on the type of discretized element, “nbnoe” is the number of element nodes, N^I corresponds to the shape functions of the considered element for node I, $\underline{v}^I$ and $\underline{v}^{*I}$ are the velocity values at node I of the element.

Depending on the type of element considered (beam, tube, etc.), a certain number of degrees of freedom may be associated with each node I. Denoting by i a degree of freedom associated with node I, we can write the relative velocities as follows:

$$v_i^*(\underline{x},t) = \sum_{I=1}^{\text{nbnoe}} N^I(\underline{x}) \cdot v_i^{*I}(t) \qquad\qquad v_i(\underline{x},t) = \sum_{I=1}^{\text{nbnoe}} N^I(\underline{x}) \cdot v_i^{I}(t) \tag{A.4}$$

The variational formulation of the momentum equation is recalled as follows:

$$\begin{aligned}\int_V \rho(\underline{x},t)\frac{\delta \underline{v}}{\delta t}\cdot \underline{v}^*\,dV = \int_V \rho(\underline{x},t)\underline{g}\cdot \underline{v}^*\,dV + \oint_S \underline{\underline{\sigma}}\cdot \underline{n}\cdot \underline{v}^*\,dS - \int_V \underline{\underline{\sigma}} : \frac{\partial \underline{v}^*}{\partial \underline{x}}\,dV \\ + \int_V \rho(\underline{x},t)\left((\underline{w}-\underline{v})\cdot\frac{\partial \underline{v}}{\partial \underline{x}}\right)\cdot \underline{v}^*\,dV\end{aligned} \tag{A.5}$$

Using relations (A.3), for each element, we can rewrite this equation as follows:

$$\begin{aligned}\sum_{\text{e}}\left[\int_{V_\text{e}} \rho(\underline{x},t)\sum_{J=1}^{\text{nbnoe}} N^J\frac{\delta \underline{v}^J}{\delta t}\cdot\sum_{I=1}^{\text{nbnoe}} N^I\cdot\underline{v}^{*I}\,dV\right] = \sum_{\text{e}}\Bigg[\int_{V_\text{e}} \rho(\underline{x},t)\underline{g}\cdot\sum_{I=1}^{\text{nbnoe}} N^I\cdot\underline{v}^{*I}\,dV \\ + \oint_{S_\text{e}} \underline{\underline{\sigma}}\cdot\underline{n}\cdot\sum_{I=1}^{\text{nbnoe}} N^I\cdot\underline{v}^{*I}\,dS \\ - \int_{V_\text{e}} \underline{\underline{\sigma}} : \left(\sum_{I=1}^{\text{nbnoe}}\frac{\partial N^I}{\partial \underline{x}}\right)\underline{v}^{*I}\,dV \\ + \int_{V_\text{e}} \rho(\underline{x},t)\left((\underline{w}-\underline{v})\cdot\frac{\partial \underline{v}}{\partial \underline{x}}\right)\cdot\sum_{I=1}^{\text{nbnoe}} N^I\cdot\underline{v}^{*I}\,dV\Bigg]\end{aligned} \tag{A.6}$$

This equation must be true for any $\underline{v}^*_j$. We then obtain (for $I = 1, ..., \text{nbnoe}$) vector equations:

$$\begin{aligned}\sum_{\text{e}}\left[\sum_{J=1}^{\text{nbnoe}}\int_{V_\text{e}} \rho(\underline{x},t)N^I N^J\,dV\frac{\delta \underline{v}^J}{\delta t}\right] = \sum_{\text{e}}\Bigg[\int_{V_\text{e}} \rho(\underline{x},t)\underline{g}N^I\,dV + \oint_{S_\text{e}} N^I\underline{\underline{\sigma}}\cdot\underline{n}\,dS - \int_{V_\text{e}}\underline{\underline{\sigma}} : \frac{\partial N^I}{\partial \underline{x}}\,dV \\ + \int_{V_\text{e}} \rho(\underline{x},t)\left((\underline{w}-\underline{v})\cdot\frac{\partial \underline{v}}{\partial \underline{x}}\right)\cdot N^I\,dV\Bigg]\end{aligned} \tag{A.7}$$

After discretization within each elemental volume (element), we can write more precisely:

$$\boxed{\sum_{\mathrm{e}} \left[\left[M_{ij}^{IJ}\right]^{\mathrm{e}} \frac{\delta \left\{v_j^J\right\}^{\mathrm{e}}}{\delta t} \right] = \sum_{\mathrm{e}} \left[\left\{F_i^I\right\}_g^{\mathrm{e}} + \left\{F_i^I\right\}_{\mathrm{ext}}^{\mathrm{e}} - \left\{F_i^I\right\}_{\mathrm{int}}^{\mathrm{e}} + \left\{F_i^I\right\}_{\mathrm{t}}^{\mathrm{e}} \right]} \tag{A.8}$$

where:

- $\left[M_{ij}^{IJ}\right]^{\mathrm{e}}$ is the consistent mass matrix of the element (upper index e):

$$\left[M_{ij}^{IJ}\right]^{\mathrm{e}} = \int_{V\mathrm{e}} \rho(\underline{x}, t) N_i^I N_j^J \, dV \tag{A.9}$$

This matrix is then made diagonal by condensation in Europlexus, i.e., by summing each row and assigning this sum to the diagonal term.

$$\left[\widetilde{M}_{ij}^{IJ}\right]^{\mathrm{e}} = \sum_{J=1}^{\mathrm{nbnoe}} \sum_{j=1}^{\mathrm{nddl}} \left[M_{ij}^{IJ}\right]^{\mathrm{e}} \tag{A.10}$$

where nbnoe is the number of nodes of the element and nddl is the number of degrees of freedom per node.

- $\left\{F_i^I\right\}_g^{\mathrm{e}}$ corresponds to the discretization of the volume forces on the element. Its expression is:

$$\left\{F_i^I\right\}_g^{\mathrm{e}} = \int_V \rho(\underline{x}, t) \underline{g} N^I \, dV \tag{A.11}$$

- $\left\{F_i^I\right\}_{\mathrm{ext}}^{\mathrm{e}}$ corresponds to the discretization of external forces other than volume forces:

$$\left\{F_i^I\right\}_{\mathrm{ext}}^{\mathrm{e}} = \oint_{S_{\mathrm{e}}} N^I T_i \, dS \quad \text{with} \quad T_i = \sigma_{ij} \cdot n_j \tag{A.12}$$

- $\left\{F_i^I\right\}_{\mathrm{int}}^{\mathrm{e}}$ corresponds to internal forces:

$$\left\{F_i^I\right\}_{\mathrm{int}}^{\mathrm{e}} = \int_{V_{\mathrm{e}}} \underline{\underline{\sigma}} \frac{\partial N^I}{\partial x_i} \, dV \tag{A.13}$$

In our case, the stress tensor depends only on a scalar field, which is the pressure p in the fluid:

$$\underline{\underline{\sigma}} = -p\underline{\underline{I}} \quad \text{where } I \text{ is the identity tensor} \tag{A.14}$$

- $\left\{F_i^I\right\}_{\mathrm{t}}^{\mathrm{e}}$ corresponds to the elemental contributions of the momentum transport terms:

$$\left\{F_i^I\right\}_{\mathrm{t}}^{\mathrm{e}} = \int_{V_{\mathrm{e}}} N^I \rho(\underline{x}, t) \left(w_j - v_j\right) \cdot \frac{\partial v_i}{\partial x_j} \, dV \tag{A.15}$$

After assembly over all elements, we can finally write the momentum equation in the following form:

$$\boxed{\left[\widetilde{M}_{ij}^{IJ}\right] \frac{\delta \left\{v_j^J\right\}}{\delta t} = \left\{F_i^I\right\}_g + \left\{F_i^I\right\}_{\mathrm{ext}} - \left\{F_i^I\right\}_{\mathrm{int}} + \left\{F_i^I\right\}_{\mathrm{t}}} \tag{A.16}$$

Energy Conservation Equation

For the energy conservation equation (Eq. (3.16)), we assume that the density ρ and pressure p are uniform within the element.

$$\frac{\delta E^{\mathrm{e}}}{\delta t}=\frac{\delta}{\delta t}\int_{V_{\mathrm{e}}}\rho(\underline{x},t)\left(i+\frac{1}{2}v^2\right)dV=\sum_{k=1}^{\mathrm{nface}}\rho^k\left(i+\frac{1}{2}v^2\right)\oint_{S_k}(\underline{w}^k-\underline{v}^k)\cdot\underline{n}^k\,dS-p^{\mathrm{e}}\oint_{S_k}\underline{v}^k\cdot\underline{n}^k\,dS \tag{A.17}$$

Similarly, the equation written in terms of internal energy (Eq. (3.17)) can be discretized as follows:

$$\frac{\delta I^{\mathrm{e}}}{\delta t}=\frac{\delta}{\delta t}\int_{V_{\mathrm{e}}}\rho(\underline{x},t)i\,dV=\sum_{k=1}^{\mathrm{nface}}\rho^k i\oint_{S_k}(\underline{w}^k-\underline{v}^k)\cdot\underline{n}^k\,dS-p^{\mathrm{e}}\oint_{S_k}\underline{v}^k\cdot\underline{n}^k\,dS \tag{A.18}$$

Where:

- E^{e}: energy in the element
- I^{e}: internal energy in the element
- $e=i+\frac{1}{2}v^2$: specific total energy
- i: specific internal energy
- ρ: density
- V_{e}: volume of the element
- $\underline{n}^k$: normal to the k-th face of the element
- $\underline{w}^k$: average grid velocity of the k-th face of the element
- $\underline{v}^k$: average fluid velocity for the k-th face of the element
- S_k: surface of the k-th face of the element
- ρ^k: density weighted at the k-th interface
- p^{e}: pressure in the element

Equation A.18 is the one solved by EPX when using the Finite Element Method.

The energy $(\rho e)^k$ at interface k is defined as the weighted average of the energies of the two adjacent elements:

$$(\rho e)^k=\frac{1}{2}\left[\left(1-\alpha^k\right)(\rho e)^{\mathrm{e}}+\left(1+\alpha^k\right)(\rho e)^{\mathrm{e'}}\right] \tag{A.19}$$

where α^k is the convective flux offset parameter. If $(\underline{w}-\underline{v})\cdot\underline{n}\leq 0$, we take $\alpha^k>0$. This favors the density of the "donor" element, stabilizing the numerical scheme. In Europlexus, the default choice is to use $\alpha^k=1$ (full offset or Upwind scheme).

A.2 Temporal Discretization

The method used for temporal discretization (in the ALE description) is the **centered difference** method.

At time step n, we know the *grid geometry* $\underline{x}^n$, the *grid velocity* $\underline{w}^n$, the *fluid velocity at the previous half-step* $\underline{v}^{n-1/2}$, the *element density* ρ^n, the *internal energy* i^n, the *interior* and *exterior forces* applied to this element F^n_{int} and F^n_{ext}, and the *acceleration* $\underline{\gamma}^n = d\underline{v}^n/dt$.

Calculation of New Geometry

Knowing the acceleration at time step n, $\underline{\gamma}^n$, and the fluid velocity at the previous half-time step $\underline{v}^{n-1/2}$, the fluid velocity at the next half-time step $\underline{v}^{n+1/2}$ can be calculated, considering a time interval Δt:

$$\left\{v_j^J\right\}^{n+1/2} = \left\{v_j^J\right\}^{n-1/2} + \Delta t \left\{\gamma_j^J\right\}^n \tag{A.20}$$

where the acceleration can be determined from Equation (A.16):

$$\left\{\gamma_j^J\right\}^n = \frac{\delta \left\{v_j^J\right\}^n}{\delta t} = \left(\left[\widetilde{M}_{ij}^{IJ}\right]^n\right)^{-1} \cdot \left(\left\{F_i^I\right\}_g^n + \left\{F_i^I\right\}_{\text{ext}}^n - \left\{F_i^I\right\}_{\text{int}}^n + \left\{F_i^I\right\}_{\text{t}}^n\right) \tag{A.21}$$

In the case of the **ALE description**, the grid velocity at the next half-time step $\underline{w}^{n+1/2}$ is now calculated (we will not go into the details of this calculation), and therefore, the new geometric configuration $\underline{x}^{n+1}$ can be calculated:

$$\left\{x_j^J\right\}^{n+1} = \left\{x_j^J\right\}^n + \Delta t \left\{w_j^J\right\}^{n+1/2} \tag{A.22}$$

In the case of the **Eulerian description** the geometric configuration remains unchanged.

Calculation of Element Mass

Knowing the new domain configuration at time t^{n+1}, we calculate for each element the new volume of the element:

$$\left|V^{\text{e},\,n+1}\right| = f\left(\underline{x}^{n+1}\right) \tag{A.23}$$

The new mass of the element is obtained from Equation (A.1):

$$\begin{aligned} M^{\text{e},\,n+1} &= M^{\text{e},\,n} + \Delta t \sum_{k=1}^{\text{nface}} \rho^{k,\,n} \oint_{S_k^{n+1}} \left(\underline{w}^{k,\,n+1/2} - \underline{v}^{k,\,n+1/2}\right) \cdot \underline{n}^{k,\,n+1}\, dS \\ &= M^{\text{e},\,n} + \Delta t \sum_{k=1}^{\text{nface}} \rho^{k,\,n} \left(\underline{w}^{k,\,n+1/2} - \underline{v}^{k,\,n+1/2}\right) \cdot \underline{n}^{k,\,n+1} \cdot S^{k,\,n+1} \end{aligned} \tag{A.24}$$

Here, the mass increment is calculated from the material velocity and the previously calculated grid velocity at time step $n + 1/2$. Since the new geometry is known, here we take the normal and surface of the k-th face for time step $n + 1$. The density used to calculate the mass flux for each of the element's interfaces is determined from the densities of the two adjacent elements, e and e', using Equation (A.2).

Increment Calculation of Internal Energy

First, we calculate the first term of the internal energy increment ΔI_1 using the following discretization:

$$\begin{aligned}\Delta I_1^{\mathrm{e}} &= \Delta t \sum_{k=1}^{\mathrm{nface}} \rho^{k,\,n}\, i^{\,k,\,n} \oint_{S_k^{n+1}} \left(\underline{w}^{k,\,n+1/2} - \underline{v}^{k,\,n+1/2}\right) \cdot \underline{n}^{k,\,n+1}\, dS \\ &= \Delta t \sum_{k=1}^{\mathrm{nface}} \rho^{k,\,n}\, i^{\,k,\,n} \left(\underline{w}^{k,\,n+1/2} - \underline{v}^{k,\,n+1/2}\right) \cdot \underline{n}^{k,\,n+1} \cdot S^{k,\,n+1}\end{aligned} \tag{A.25}$$

Similarly to before, it can be weighted based on the internal energies of two adjacent elements to calculate the internal energy flux through an interface:

$$(\rho\, i)^{k,\,n} = \rho^{k,\,n}\, i^{\,k,\,n} = \frac{1}{2}\left[\left(1-\alpha^k\right)\cdot(\rho\, i)^{\mathrm{e,\,n}} + \left(1+\alpha^k\right)\cdot(\rho\, i)^{\mathrm{e',\,n}}\right] \tag{A.26}$$

We then determine the intermediate specific internal energy:

$$\widetilde{i} = \frac{\Delta I_1^{\mathrm{e}} + I^n}{\left|M^{\mathrm{e},\,n+1}\right|} \tag{A.27}$$

Calculation of Density, Pressure, and Nodal Masses

The new density is determined from the element mass and its volume calculated from the new grid geometry at step $n+1$:

$$\rho^{\mathrm{e},\,n+1} = \frac{M^{\mathrm{e},\,n+1}}{\left|V^{\mathrm{e},\,n+1}\right|} \tag{A.28}$$

The pressure is then determined by the equation of state and is calculated from the intermediate specific internal energy and the density at step $n+1$:

$$p^{\mathrm{e},\,n+1} = F\left(\widetilde{i},\, \rho^{\mathrm{e},\,n+1}\right) \tag{A.29}$$

Knowing the new density at time $n+1$, we then calculate for the element the masses to be associated with the nodes using a condensation technique (to have only diagonal terms).

Calculation of Internal Forces and Convective Transport

The internal forces at step $n+1$ are calculated as follows:

$$\left\{F_i^I\right\}_{\mathrm{int}}^{\mathrm{e},\,n+1} = -\int_{V^{\mathrm{e},\,n+1}} p^{\mathrm{e},\,n+1} \frac{\partial N^I}{\partial x_i}\, dV \tag{A.30}$$

The transport forces at time $n+1$ are determined by the discretized equation:

$$\left\{F_i^I\right\}_{\mathrm{t}}^{\mathrm{e},\,n+1} = \int_{V^{\mathrm{e},\,n+1}} N^I \rho^{\mathrm{e},\,n+1} \left(\underline{w}^{n+1/2} - \underline{v}^{n+1/2}\right) \cdot \left(\frac{\partial v_i}{\partial x_i}\right)^{n+1/2} dV \tag{A.31}$$

The integration is done over the volume in configuration $n+1$. The grid velocity and material velocity are those determined at the half-time step. Integrals are numerically determined using the Gauss integration method.

Calculation of Internal Energy

The internal energy of the element can be calculated as follows (Eq. (A.18)) at step $n+1$:

$$I^{n+1} = I^n + \Delta I_1 - \Delta t \oint_{S^{n+1}} p^{\mathrm{e},\, n+1} \cdot \underline{v}^{k,\, n+1/2} \cdot \underline{n}^{k,\, n+1} \, dS \tag{A.32}$$

This last integral is transformed into an integral over the volume of the element. The previous relation is approximated as follows:

$$I^{n+1} = I^n + \Delta I_1 - \Delta t \int_{V^{n+1}} p^{\mathrm{e},\, n+1} \cdot \left(\frac{\partial v_i}{\partial x_i} \right)^{n+1/2} dV \tag{A.33}$$

Integration over the volume is done using the Gauss integration method.

Calculation of External Forces, Volume Forces, and New Accelerations

The external forces are calculated as follows:

$$\left\{F_i^I\right\}_{\mathrm{ext}}^{n+1} = \oint_S N^I T_i^{n+1} \, dS \qquad \text{with} \qquad T_i = \sigma_{ij} \cdot n_j$$

as well as the volume forces:

$$\left\{F_i^I\right\}_g^{n+1} = \int_V \rho^{n+1} \underline{g} N^I \, dV \tag{A.34}$$

We then calculate:

- The mass matrix at time $n+1$
- The new internal nodal forces
- The new transport nodal forces

We then determine the new acceleration:

$$\left\{\gamma_j^J\right\}^{n+1} = \frac{\delta \left\{v_j^J\right\}^{n+1}}{\delta t} = \left(\left[\widetilde{M}_{ij}^{IJ} \right]^{n+1} \right)^{-1} \cdot \left(\left\{F_i^I\right\}_g^{n+1} + \left\{F_i^I\right\}_{\mathrm{ext}}^{n+1} - \left\{F_i^I\right\}_{\mathrm{int}}^{n+1} + \left\{F_i^I\right\}_{\mathrm{t}}^{n+1} \right) \tag{A.35}$$

Stability

The scheme being explicit, it is conditionally stable. The CFL stability condition (Courant, Friedrichs, Levy stability condition) imposes a maximum time step to ensure convergence of the scheme.

The stability step is calculated for each element. The selected calculation step is then taken as less than or equal to the smallest stability step of the considered domain (associated with each element). For "massive" elements, it can be shown that:

$$\Delta t_{\mathrm{stab}} \leq \min \left(\frac{L^{\mathrm{e}}}{C^{\mathrm{e}} + \max\left(v_i^{\mathrm{e}}\right)} \right) \tag{A.36}$$

Where:

- L^{e} is the smallest dimension of element e
- C^{e} is the speed of sound in element e
- v_i^{e} is the component of the material velocity of element e

Since the calculations are often highly nonlinear, a safety factor α is taken to impose the stability step. This coefficient generally depends on the problem being addressed. It can be modified using the OPTION directive. By default, this coefficient is 0.8 in Europlexus.

$$\Delta t_{\mathrm{stab}}^{\mathrm{calcul}} = \alpha \Delta t_{\mathrm{stab}} \tag{A.37}$$

Appendix B

Finite Volume Method

Similarly to what was done in the previous annex on FEM, here we present the main characteristics of the other numerical method used in this work only for the fluid numerical treatment, the Finite Volume Method (FVM). The conservation equations to be satisfied are exactly the same as those used for FEM, except for the energy conservation equation, where total energy (Eq. 3.16) will be used instead of internal energy.

In both FEM and FVM, the domain is divided into elements connected by nodes. In FEM, certain quantities (such as density, internal energy, pressure, etc.) are defined at the mesh Gauss points within the elements, while others (typically velocity, acceleration, etc.) are defined at the nodes. Conversely, in FVM, all quantities are defined at the Finite Volume centroid. For a schematic view, refer to Fig. 3.6.

We use the conservation law for a general vector quantity U. We can therefore write the integral form of the governing equations as:

$$\frac{\partial}{\partial t}\iiint_V \mathrm{U}\cdot dV + \iint_S \mathcal{F}_{C}^{\mathrm{ALE}}\cdot\vec{n}dS = \iiint_V \mathrm{H}dV \tag{B.1}$$

The time derivative of the conservative variable can be cast in the form:

$$\frac{\partial}{\partial t}\iiint_V \mathrm{U}\cdot dV = \frac{\partial}{\partial t}(\bar{U}V) \tag{B.2}$$

where:

$$\bar{U} = \frac{1}{V}\iiint_V U(x,y,z)dV \qquad \mathcal{F}_{\mathrm{C}}^{\mathrm{ALE}} = \mathcal{F}_{\mathrm{C}} - U\cdot\vec{v}_{\mathrm{Grid}} \qquad \mathrm{U} = \begin{bmatrix}\rho\\ \rho u\\ \rho v\\ \rho w\\ \rho(e+\vec{u}^2/2)\end{bmatrix} \tag{B.3}$$

The surface integral in Equation B.1 is approximated by the sum of the fluxes crossing the faces. We suppose that the flux is constant along each individual face (sufficient for a second-order scheme):

$$\frac{\partial}{\partial t}(\bar{U}V) = -\left[\sum_{k=1}^{\mathrm{Nface}} \mathcal{F}_{\mathcal{C}}^{\mathrm{ALE}}\cdot\vec{n}_k S_k - V\cdot H\right] = -\mathrm{R} \tag{B.4}$$

In Europlexus, the time derivative of the conservative variables U use an explicit Euler scheme (for first-order accuracy):

$$\bar{U}^{t+\Delta t}V_{\text{vol}}^{t+\Delta t} - \bar{U}^{t}V_{\text{vol}}^{t} = -\Delta t \left[\sum_{k=1}^{\text{Nface}} \left(\mathcal{F}_{\text{C}} - U^{*} \cdot \vec{v}_{\text{Grid}}\right) \cdot \vec{n}_k S_k\right] = -\text{R}\Delta t \tag{B.5}$$

thus:

$$\bar{U}^{t+\Delta t} = \frac{\bar{U}^{t}V_{\text{vol}}^{t}}{V_{\text{vol}}^{t+\Delta t}} - \frac{\Delta t}{V_{\text{vol}}^{t+\Delta t}}\left[\sum_{k=1}^{\text{Nface}} \left(\mathcal{F}_{\text{C}} - U^{*} \cdot \vec{v}_{\text{Grid}}\right) \cdot \vec{n}_k S_k\right] \tag{B.6}$$

where V_{vol}^{t} and $V_{\text{vol}}^{t+\Delta t}$ are the volumes at t and $t+\Delta t$, while U_{vol}^{t} and $U_{\text{vol}}^{t+\Delta t}$ are the conservative variables at t and $t+\Delta t$

The Courant–Friedrichs–Lewy condition (CFL) is a parameter for obtaining the stability inside the calculus of a model in Computational Fluid Dynamics (CFD). Its value lies between 0.1 and 1, and the conditions for respecting this range are the following ones: for a set of iterations i, the condition of CFL is defined as in equation B.7, where u_i is the velocity of fluid, c_i the sound speed, L_i the total length of the space iterated, and Δt_i the time step iterated, counting Δt_i as the minimal obtainable within the condition of CFL_i:

$$\forall i \qquad \Delta t_i < \frac{\text{CFL}_i L_i}{\|u_i\| + c_i} \tag{B.7}$$

This time step can be minimized maximizing the coefficient CFL_i, letting it being equal to 1. At this value, it is possible to assume that the CFL is equal to another coefficient; the stability coefficient CSTA.

To satisfy the Geometric Conservation Law (GCL) an intermediate frame is used for the fluxes computation:

$$\bar{U}^{t+\Delta t} = \frac{\bar{U}^{t}V_{\text{vol}}^{t}}{V_{\text{vol}}^{t+\Delta t}} - \frac{\Delta t}{V_{\text{vol}}^{t+\Delta t}}\left[\sum_{k=1}^{\text{Nface}} \left(\mathcal{F}_{\text{C}} - U^{*} \cdot \vec{v}_{\text{Grid}}^{\,t+\Delta t/2}\right) \cdot \vec{n}_k^{\,t+\Delta t/2} S_k^{t+\Delta t/2}\right] \tag{B.8}$$

Introduction of numerical fluxes for the discretization:

$$\bar{U}^{t+\Delta t} = \frac{\bar{U}^{t}V_{\text{vol}}^{t}}{V_{\text{vol}}^{t+\Delta t}} - \frac{\Delta t}{V_{\text{vol}}^{t+\Delta t}}\left[\sum_{k=1}^{N/ace} \mathcal{F}_k^{\text{ALE}} \left(U_{\text{L}}, U_{\text{R}}, \vec{v}_{\text{Grid}}^{\,t+\Delta t/2}\right) \cdot \vec{n}_k^{\,t+\Delta t/2} S_k^{t+\Delta t/2}\right] \tag{B.9}$$

with Left and Right States U_{L} and U_{R}.

Several numerical solvers are available in Europlexus (see EPX manual [62] and references therein):

- Rusanov,
- HLLE,
- Godunov (for perfect gaz),
- HLLC (by default, used in our simulations),
- AUSM+ and variants,

- Specific Low-Mach solvers,
- ...

In EPX two orders regarding the space discretization are implemented:

- Order 1, in which the unknown variables are constant and the values of U_{L} and U_{R} are the same.
- Order 2, where the solution is linear on the control volume. This leads to a better precision for the calculations.

First-order schemes are known to be too diffusive for many problems involving complexes geometries. Therefore more accurate methods are required for this kind of flows. In FSI problems the structure imposes the time steps and the solution compute with first order methods are stable but not accurate enough.

Order 2 is the one used in this manuscript. U_{L} and U_{R} are rebuilt supposing a solution linear on the control volume.

Appendix C

Implementation of the IMPEDANCE GRID model in EUROPLEXUS

We aim to describe here how the IMPEDANCE GRID model presented in Paragraph 3.1.4 is numerically implemented in EUROPLEXUS using the Finite Element Method in 1D.

Geometric obstacles can be represented by means of an impedance called GRID, which enables to model the influence of grids or rigid perforated plates on a fluid [62]. Initially, under the acoustic assumption (non-linear entrainment terms and viscosity terms are neglected), it can be shown that the pressure difference between the two sides of the obstacle, Δp, is related to the acceleration effect of the fluid at the hole of the orifice plate [15]. This effect can be represented by means of an equivalent length L_{eq} such that:

$$\Delta p = -\frac{L_{\mathrm{eq}}}{s}\dot{q} \tag{C.1}$$

where s is the cross-sectional area of the orifice and $\dot{q} = dq/dt$ where q is the mass flow rate.

Considering, in addition, the effects of drag and viscosity and assuming that the methods used for permanent flows at a singularity still apply, we can write (superposition of the effects):

$$\Delta p = -\frac{L_{\mathrm{eq}}}{s}\dot{q} - \frac{1}{2}k\frac{q^2}{\rho_0 S_{\mathrm{t}}^2} \tag{C.2}$$

where k is the head loss coefficient, ρ_0 is the average density of the fluid, S_{t} is the cross-sectional area of the pipe.

We are interested in an acoustic fluctuation around a steady flow with a flow rate Q_0. The previous equation can be written as:

$$\Delta p = -\frac{L_{\mathrm{eq}}}{s}\dot{q} - \frac{1}{2}k\frac{qQ_0}{\rho_0 S_{\mathrm{t}}^2} \tag{C.3}$$

We then define:

$$\tau = \frac{S_{\mathrm{t}}}{s}\frac{L_{\mathrm{eq}}}{2c} \qquad M_0 = \frac{Q_0}{\rho_0 c S_{\mathrm{t}}} \qquad \alpha = \frac{1}{2}kM_0 \tag{C.4}$$

The previous equation becomes:

$$\Delta p = -2\frac{c\tau}{S_{\rm t}}\dot{q} - \alpha c\frac{q}{S_{\rm t}} = -2c\tau\rho_0\frac{dv_{\rm r}}{dt} - \alpha c\rho_0 v_{\rm r} \tag{C.5}$$

The two parameters τ and α, assumed constant during the calculation, depend on the material (fluid) properties and geometric characteristics of the singularity. The first term of the previous equation is inertial while the second one is dissipative. For $q = Q_0$, we recover the singular head loss in steady flow.

$L_{\rm eq}$ can be calculated using

$$L_{\rm eq} = 2\left[0.85 - \frac{r}{R} + 0.15\left(\frac{r}{R}\right)^2\right] r + e \tag{C.6}$$

where r is the radius of the orifice plate hole, R is the inner radius of the pipe and e is the thickness of the orifice plate (see Fig. C.1). In the case of a single cross-sectional change (sudden enlargement or shrinkage), $L_{\rm eq}$ reduces to:

$$L_{\rm eq} = \left[0.85 - \frac{r}{R} + 0.15\left(\frac{r}{R}\right)^2\right] r \tag{C.7}$$

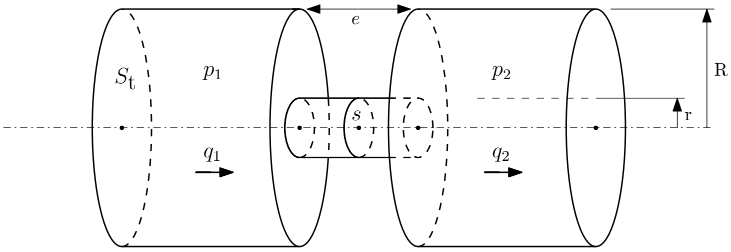

Figure C.1: Orifice plate scheme.

The head loss coefficient k can be obtained from Idel'Cik correlations [12] for an orifice plate or for single cross-sectional changes.

In summary, it can be said that the modeling of the singularity consists of two terms: an inertial acoustic term and a classic head loss term. In the calculations, we must provide as input to the model, in addition to the fluid density and the speed of sound, two fundamental parameters: the characteristic time τ and the head loss coefficient k.

The term for the **linearized head loss** with respect to the mean flow rate Q_0 is discretized as follows:

$$\Delta p_1 = -\alpha\rho_{\rm donor}^{n+1} c v_{\rm r}^{n+1/2} \tag{C.8}$$

where $\rho_{\rm donor}^{n+1}$ is the density of the donor element, c is the speed of sound (provided by the user and constant), $v_{\rm r}^{n+1/2}$ is the relative velocity of the fluid with respect to the piping, and α is the dissipative impedance.

The **inertial term** is modeled simply by adding mass (constant throughout the calculation) to the variable part of the nodal mass of the node associated with the boundary condition element. It is shown that this additional mass is given by [10]:

$$m_{\rm add} = (2+\alpha)\,\frac{\pi D_{\rm min}^2}{4}\rho_0 c\tilde{\tau} \qquad \text{where} \qquad \tilde{\tau} = \frac{\tau}{1+\alpha/2} \tag{C.9}$$

where D_{min} is the diameter of the passage section associated with the node connecting the two neighboring elements.

Here, we describe in detail the procedure to obtain equation (C.9) from equation (C.5), following the approach adopted by Gibert and Schwab [10].

Equation (C.5) represents an acoustic impedance that can be made dimensionless using the Laplace transform (L.T.): $\left[\dot{q}(t) \xrightarrow{\text{L.T.}} \tilde{p}\, q(\tilde{p})\right]$ and $\left[q(t) \xrightarrow{\text{L.T.}} q(\tilde{p})\right]$, where $\tilde{p}$ is the Laplace variable and has the dimension of frequency (s^{-1}).

Let's recall equation (C.5):

$$\Delta p = -2\tau \frac{c}{S_{\mathrm{t}}} \dot{q}(t) - \alpha \frac{c}{S_{\mathrm{t}}} q(t)$$

By using the Laplace transform, we obtain:

$$\Delta p = -2\tau \frac{c}{S_{\mathrm{t}}} \tilde{p}\, q(\tilde{p}) - \alpha \frac{c}{S_{\mathrm{t}}} q(\tilde{p}) \tag{C.10}$$

And in dimensionless form:

$$\frac{\Delta p}{\frac{c}{S_{\mathrm{t}}} q} = -(2\tau\tilde{p} + \alpha) \qquad \text{with} \qquad \tau = \frac{S_{\mathrm{t}}}{s} \frac{L_{\mathrm{eq}}}{2c} \qquad \text{and} \qquad \alpha = \frac{1}{2} \frac{k\, Q_0}{\rho_0\, c\, S_{\mathrm{t}}} = \frac{1}{2} k M_0 \tag{C.11}$$

To evaluate the effect of a orifice plate (see Fig. C.1) on a progressive wave, we consider $S(\tilde{p})$, $R(\tilde{p})$, and $T(\tilde{p})$: the Laplace transforms of the incident wave, the wave reflected by the orifice plate, and the wave transmitted through the orifice plate, respectively.

To write the following equations, we consider an even simpler diagram (see Fig. C.2), where the orifice plate's geometry is "removed" because its effect will be replaced by the acoustic impedance model. Let x be the direction of wave propagation, and we place the axes' origin at the singularity level.

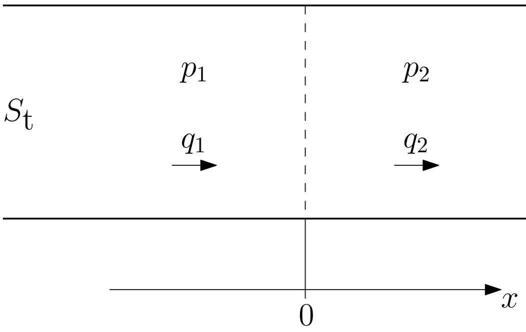

Figure C.2: Simplified scheme of the orifice plate.

The pressure p_1 to the left of the orifice plate is the result of the sum of the incident wave and the reflected wave, taking into account the propagation time at the speed of sound c:

$$p_1 = S(\tilde{p})\, e^{-\frac{\tilde{p}x}{c}} + R(\tilde{p})\, e^{\frac{\tilde{p}x}{c}} \tag{C.12}$$

The pressure p_2 to the right of the orifice plate is equal to the transmitted wave shifted by the propagation time:

$$p_2 = T(\tilde{p})\, e^{-\frac{\tilde{p}x}{c}} \tag{C.13}$$

The flow rates q_1 and q_2 associated with these waves can be calculated using Euler's equation:

$$\frac{\partial q}{\partial t} + S_\mathrm{t}\frac{\partial p}{\partial x} = 0 \tag{C.14}$$

which, using the Laplace transform, can be written as:

$$\tilde{p}\, q + S_\mathrm{t}\frac{\partial p}{\partial x} = 0 \qquad \Longrightarrow \qquad q = -\frac{S_\mathrm{t}}{\tilde{p}}\frac{\partial p}{\partial x} \tag{C.15}$$

Now, let's compute the derivative with respect to x of equations (C.12) and (C.13):

$$\frac{\partial p_1}{\partial x} = \frac{\tilde{p}}{c}\left[-S(\tilde{p})\, e^{-\frac{\tilde{p}x}{c}} + R(\tilde{p})\, e^{\frac{\tilde{p}x}{c}}\right] \qquad \frac{\partial p_2}{\partial x} = -\frac{\tilde{p}}{c}T(\tilde{p})\, e^{-\frac{\tilde{p}x}{c}} \tag{C.16}$$

Next, we calculate q_1 and q_2 on both sides of the orifice plate (at $x = 0$):

$$q_1 = \frac{S_\mathrm{t}}{c}\left[S(\tilde{p}) - R(\tilde{p})\right] \qquad q_2 = \frac{S_\mathrm{t}}{c}T(\tilde{p}) \tag{C.17}$$

Assuming that the flow rate is conserved through the orifice plate and using equation (C.11), the following system of equations can be written:

$$\begin{cases} q_1 = q_2 = q \\ p_2 - p_1 = -\frac{c}{S_\mathrm{t}}q(2\tau\tilde{p} + \alpha) \end{cases} \tag{C.18}$$

By replacing p_1, p_2, and q_2 with their expressions from equations (C.12), (C.13), and (C.17), respectively, at $x = 0$, we obtain:

$$\begin{cases} S(\tilde{p}) = R(\tilde{p}) + T(\tilde{p}) \\ p_2 - p_1 = T(\tilde{p}) - S(\tilde{p}) - R(\tilde{p}) = -(2\tau\tilde{p} + \alpha)T(\tilde{p}) \end{cases} \tag{C.19}$$

Solving this system allows us to express T and R in terms of the source S:

$$T(\tilde{p}) = \frac{S(\tilde{p})}{1 + \alpha/2 + \tau\tilde{p}} = \frac{S(\tilde{p})}{1 + \alpha/2}\cdot\frac{1}{1 + \tilde{\tau}\tilde{p}} \qquad \text{with} \qquad \tilde{\tau} = \frac{\tau}{1 + \alpha/2} \tag{C.20}$$

$$R(\tilde{p}) = \frac{\alpha/2 + \tau\tilde{p}}{(1 + \alpha/2)(1 + \tilde{\tau}\tilde{p})}S(\tilde{p}) \tag{C.21}$$

We then obtain:

$$p_2 - p_1 = -\frac{\alpha + 2\tau\tilde{p}}{(1 + \alpha/2)(1 + \tilde{\tau}\tilde{p})}S(\tilde{p}) = -2R(\tilde{p}) \tag{C.22}$$

and the ratio p_2/p_1, at $x = 0$, is:

$$\frac{p_2}{p_1} = \frac{T(\tilde{p})}{S(\tilde{p}) + R(\tilde{p})} = \frac{1}{1 + \alpha + 2\tau\tilde{p}} \tag{C.23}$$

Application: Added Mass at Node

Let's consider two identical 1D elements of length L (Fig. C.3) and denote by S_t the section corresponding to the node P separating the two elements. In our case, S_t is equivalent to the section of the pipe.

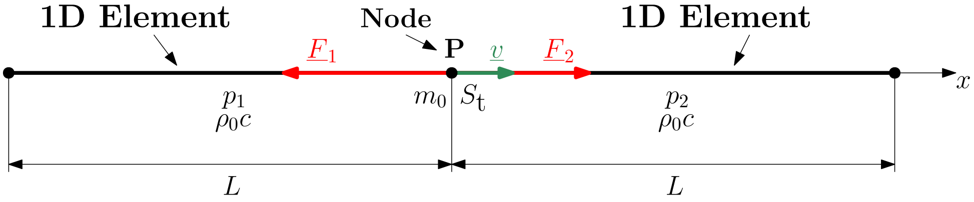

Figure C.3: Elements extracted from the 1D mesh.

Each 1D element has two nodes, so the mass assigned to each of the two nodes for a single element is $\frac{\rho_0 \cdot S_\mathrm{t} \cdot L}{2}$, which is half of the total mass of the element. Therefore, the total mass m_0 assigned to node P for the two elements is:

$$m_0 = \rho_0 \cdot S_\mathrm{t} \cdot L \tag{C.24}$$

For a planar wave propagating from left to right, the pressure p is related to the velocity v by:

$$p = \rho_0 c v \tag{C.25}$$

This means that a force F_2 is applied to the mass m_0:

$$F_2 = p S_\mathrm{t} = \rho_0 c v S_\mathrm{t} \tag{C.26}$$

The reaction of the element is a force F_1 such that:

$$F_1 - F_2 = m_0 \frac{dv}{dt} \tag{C.27}$$

Using the Laplace transform $\left(\frac{dv}{dt} \xrightarrow{\text{L.T.}} \tilde{p} v\right)$, we get:

$$F_1 - F_2 = m_0 \tilde{p} v = m_0 \tilde{p} \frac{F_2}{\rho_0 c S_\mathrm{t}} \tag{C.28}$$

$$\frac{F_2}{F_1} = \frac{1}{1 + \frac{m_0}{\rho_0 c S_\mathrm{t}} \tilde{p}} \tag{C.29}$$

Comparing equation (C.29) with equation (C.23) by taking $\alpha = 0$

$$\frac{p_2}{p_1} = \frac{1}{1 + 2\tau \tilde{p}} \tag{C.30}$$

We deduce by analogy the time constant τ:

$$\tau = \frac{m_0}{2 \rho_0 c S_\mathrm{t}} \tag{C.31}$$

Replacing m_0 with its value, we find $\tau = \frac{L}{2c}$, which is half of the wave transit time through the element.

An increase in mass m_0 will result in an increase in the time constant, corresponding to an increase in the length of the wave path. The mass m_{add} added to node P is equal to:

$$m_{\text{add}} = 2\rho_0 c S_{\text{t}} \tau \tag{C.32}$$

If we now consider $\alpha \neq 0$ and the definition of $\tilde{\tau}$

$$\tilde{\tau} = \frac{\tau}{1 + \alpha/2} \tag{C.33}$$

It follows that

$$m_{\text{add}} = (2 + \alpha)\rho_0 c S_{\text{t}} \tilde{\tau} \tag{C.34}$$

Since $S_{\text{t}} = \frac{\pi D_{\text{min}}^2}{4}$, we recover equation (C.9) (as desired):

$$m_{\text{add}} = (2 + \alpha)\,\frac{\pi D_{\text{min}}^2}{4}\rho_0 c \tilde{\tau} \tag{C.35}$$